SECONDARY ION ENERGY EFFECTS ON QUANTITATIVE SIMS

by

Paul M. Gough

Department of Materials Engineering

Graduate Program
In
Engineering Science

Submitted in Partial fulfillment
of the requirements for the degree of
Master of Engineering Science

Faculty of Graduate Studies
The University of Western Ontario
London, Ontario

September, 1997

© Paul M. Gough 1998

National Library of Canada

Bibliothèque nationale du Canada

Acquisitions and Bibliographic Services

Acquisitions et services bibliographiques

395 Wellington Street
Ottawa ON K1A 0N4
Canada

395, rue Wellington
Ottawa ON K1A 0N4
Canada

Your file Votre référence

Our file Notre référence

The author has granted a non-exclusive licence allowing the National Library of Canada to reproduce, loan, distribute or sell copies of this thesis in microform, paper or electronic formats.

L'auteur a accordé une licence non exclusive permettant à la Bibliothèque nationale du Canada de reproduire, prêter, distribuer ou vendre des copies de cette thèse sous la forme de microfiche/film, de reproduction sur papier ou sur format électronique.

The author retains ownership of the copyright in this thesis. Neither the thesis nor substantial extracts from it may be printed or otherwise reproduced without the author's permission.

L'auteur conserve la propriété du droit d'auteur qui protège cette thèse. Ni la thèse ni des extraits substantiels de celle-ci ne doivent être imprimés ou autrement reproduits sans son autorisation.

0-612-32481-8

Canada

ABSTRACT

This paper investigates the effect of secondary ion energy selection upon the quantitative analysis of NBS stainless steel standards using the Relative Sensitivity Factors approach and the Bond Breaking Model. Five standards were analyzed using an O_2^-, 12.5 KeV, primary ion beam by measuring positive secondary ion count rates. The oxygen saturation plateau required for bond breaking model analysis was determined and all specimens were analyzed in the plateau region under essentially identical analysis conditions. Ionic intensity measurements were taken at 40 eV offset intervals from the secondary ion distribution peak.

Two data sets were collected for comparative analysis. Both data sets exhibited characteristic curve shapes for both relative sensitivity factors (RSF's) and bond breaking relative emission coefficients for individual element combinations when these values were plotted against secondary ion energy offset. Values obtained for RSF's were most stable in the 80 to 120 eV energy offset range where a global set of averaged RSF's also yielded the most accurate composition predictions for the alloys studied. Bond Breaking emission coefficients yielded the most reliable results in the 0 eV energy offset region while exhibiting the least reliability in the 80 eV offset range. Although bond breaking results performed better at a 0 eV energy offset than any of the RSF results, a general trend of increasing error with energy offset was observed. Comparison of the two models indicated that the Bond Breaking model while superior when using a 0 eV offset, offered no measurable benefit for its increased complexity for energy offsets significantly above this. Relative error in predicted elemental composition was found to decrease with increased concentration, particularly in the low concentration range.

ACKNOWLEDEMENTS

The author would like to thank Dr. J.D. Brown for his continued guidance and support without which this project would not have been possible. Dr. Browns valued input and professionalism served as a source of inspiration throughout the duration of the project. The author would also like to extend his sincere thanks to Dr. N.S. McIntyre and Dr. P. Van der Heide of Surface Science Western for their support and valued input into this project. The help of Gary Mount, ShiFeng Lou, David Kingston, Dietmar Fichter and Ross Davidson of Surface Science Western is also appreciated for their aid in training and technical help.

Just as this work could not have been completed without the help of the aforementioned people, a number of family and friends have also been instrumental in bringing this project to fruition. For this reason I would like to thank my family, friends, and colleagues at MITEL Corporation, all of whose ongoing support have made completion of this project a reality. Last but certainly not least the author would like to thank the late Dr. I. J. Duerden. Dr. Duerden represented the authors first exposure to Materials Engineering, he made the field both interesting and exciting. Dr. Duerden was not only a source of inspiration but also a valued friend - his presence will be sorely missed by many.

TABLE OF CONTENTS

Page

CERTIFICATE OF EXAMINATION ii
ABSTRACT iii
ACKNOWLEDGEMENTS iv
TABLE OF CONTENTS v
LIST OF TABLES ix
LIST OF FIGURES x
LIST OF APPENDICES xiv

CHAPTER 1 - INTRODUCTION TO SIMS 1

1.1 INTRODUCTION 1
1.2 HISTORICAL DEVELOPMENT OF SIMS 3
1.3 CHARACTERISTICS OF SIMS 7
1.4 DISADVANTAGES OF SIMS 8
1.5 MATERIALS ANALYSIS USING SIMS 9
1.6 SEMI-QUANTITATIVE SIMS ANALYSIS 10

CHAPTER 2 - SIMS INSTRUMENTATION 12

2.1 INTRODUCTION 12
2.2 ION SOURCES 16
2.2.1 Duoplasmatron Ion Source 16
2.2.2 Cesium Surface Ionization Source 17
2.3 PRIMARY BEAM PURIFICATION 19
2.4 PRIMARY ION LENSES AND BEAM SCANNING 20
2.5 SECONDARY ION COLLECTION 22
2.6 MASS ANALYZERS 25
2.7 ION DETECTORS AND COUNTING 29
2.8 VACUUM SYSTEM 32

TABLE OF CONTENTS- CONTINUED

Page

CHAPTER 3 - QUANTITATIVE SIMS ANALYSIS 33

3.1 INTRODUCTION.. 33
3.2 SURFACE PROCESSES... 34
3.3 QUANTITATIVE SIMS: THE RELATIVE SENSITIVITY FACTORS APPROACH AS DERIVED FROM CALIBRATION CURVES.. 35
3.4 RELATIVE SENSITIVITY FACTORS VERSUS ENERGY OFFSET: MASS INTERFERENCE EFFECTS........... 44
3.5 BOND BREAKING MODEL.. 45
3.6 NUMERICAL REGRESSION... 51
3.7 THE ISOTOPE EFFECT: MASS FRACTIONATION........................ 53
3.8 INSTRUMENTAL EFFECTS.. 53
3.9 STATISTICAL AND SYSTEMATIC ERRORS................................ 54
3.10 A PROMISING NEW MODEL... 55

CHAPTER 4 - EXPERIMENTAL METHODS.. 57

4.1 SAMPLE PREPARATION.. 57
4.2 SAMPLE ANALYSIS... 57
4.3 OXYGEN PLATEAU DETERMINATION....................................... 59
4.4 ENERGY WINDOW CENTERING AND STANDARDIZATION OF ANALYSIS CONDITIONS.. 60
4.5 DATA ANALYSIS.. 60
4.6 COMPOSITION OF ALLOYS.. 61
4.7 SELECTION OF ISOTOPES FOR INVESTIGATION.................... 64

TABLE OF CONTENTS-CONTINUED

Page

CHAPTER 5 - RESULTS AND DISCUSSION... 67

5.1 CORRECTION FOR RELATIVE ISOTOPIC ABUNDANCE............ 67
5.2 CORRECTION FOR VARIATIONS IN PRIMARY ION
IN PRIMARY ION BEAM CURRENT.. 67
5.3 OXYGEN SATURATION PLATEAU DETERMINATION................ 68
5.4 IONIC INTENSITY MEASUREMENTS FOR ALLOYS
AND PURE METALS.. 71
5.5 RELATIVE SENSITIVITY FACTORS RESULTS............................ 71
5.5.1 Validity of Relative Sensitivity Factors Determined.............. 71
5.5.2 Relationship Between Relative Sensitivity
Values And Secondary Ion Energy....................................75
5.5.3 Specimen Composition Prediction Using Global
RSF Values.. 79
5.5.4 Relationship Between Error In Calculated Composition
Using Global RSF Values And Elemental Composition 87
5.6 BOND BREAKING MODEL RESULTS... 92
5.6.1 Relationship Between Relative Emission Coefficients
And Secondary Ion Energy.. 92
5.6.2 Relationship Between Relative Emission Coefficients
Calculated Using Top Three Versus Top Five
Most Abundant Elements.. 95
5.6.3 Prediction of Specimen Composition Based Upon
Average Global Emission Coefficients For The
Bond Breaking Model... 98
5.6.4 Relationship Between Error In Calculated Composition
Using Average Emission Coefficients And Elemental
Composition.. 108
5.6.5 Validity of The Bond Breaking Model Specimen D 850
Composition Calculated Using Relative
Emission Coefficients For Three Elements
Determined Experimentally... 113
5.6.6 Specimen D 850 Composition Calculated Using Relative
Emission Coefficients For Three elements
Determined Experimentally.. 117
5.6.7 Comparison of Relative Error In Prediction of Specimen
D850 Composition: Five Element Model Versus
Three Element Model... 120

TABLE OF CONTENTS

Page

CHAPTER 5 - RESULTS AND DISCUSSION

5.6.8 Comparison of Relative Error In Prediction of Specimen D850 Composition: Five Element bond Breaking Model Versus Relative Sensitivity Factors Model 121

CHAPTER 6 - CONCLUSIONS AND RECOMMENDATIONS 122

6.1 CONCLUSIONS 122
6.2 RECOMMENDATIONS 127

APPENDIX A 128

APPENDIX B 134

APPENDIX C 188

BIBLIOGRAPHY 223

VITA 228

LIST OF TABLES

Table	Description	Page
4.1	Certified Elemental Compositions Of Alloys	63
4.2	Non-Certified Elemental Compositions Of Alloys	63
4.3	Isotopes And Relative Isotopic Abundance Of Elements Studied	66
5.4.1	RSF Values From This Study And From Piven et. al.	74

LIST OF FIGURES

Figure	Description	Page
1.1.1	Schematic Diagram Illustrating Primary Ion Induced Interactions	2
1.1.2	SIMS Spectra For Specimen D850	5
2.1.1	Schematic Diagram of a Cameca Ims-3f Ion Microscope	13
2.1.2	Direct Imaging Ion Microscope	15
2.2.1	Schematic representation of a Hollow Cathode Duoplasmatron Ion Source	18
2.2.2	Schematic Diagram of a Surface Ionization Cesium Ion Gun	18
2.4.1	Ion Optics of The Cameca Ims-3F	21
2.5.1	Maxwellian Secondary Ion Energy Distribution For Monatomic Ions	24
2.5.2	Variation of Secondary Ion Beam Processing in the Cameca Ims-3f Using the Three Lenses of The Transfer Optics	26
2.6.1	Trajectory Of An Ion Through The Electrostatic Sector	28
2.6.2	Trajectory Of An Ion Through The Seconday Magnet	28
2.7.1	Faraday Cup And Electron Multiplier Ion Detectors	31
3.3.1	Calibration Curve For Element A, Reference Element R	38
5.3.1	Oxygen Saturation Plot For Iron And Nickel	70
5.5.2.1	RSF Values Versus Energy Offset For Alloy S846 Ratiod Against Iron	78
5.5.2.2	RSF Values Versus Energy Offset For Alloy D849 Ratiod Against Iron	78
5.5.3.1	Calculated Average Global RSF Value	80
5.5.3.2	Predicted Composition of D847 Using Average Global RSF Values	80

LIST OF FIGURES-CONTINUED

Figure	Description	Page
5.5.3.3	Error In Predicted D845 Composition Using Global RSF Values	83
5.5.3.4	Error In Predicted D846 Composition Using Global RSF Values	83
5.5.3.5	Error In Predicted D847 Composition Using Global RSF Values	84
5.5.3.6	Error In Predicted D849 Composition Using Global RSF Values	84
5.5.3.7	Error In Predicted D850 Composition Using Global RSF Values	85
5.5.3.8	Sum of Error In Predicted Composition of D846	86
5.5.3.9	Sum of Error In Predicted Composition of D847	86
5.5.4.1	Variation of Error In Fe Content With Composition: Data Set 1	89
5.5.4.2	Variation of Error In Cr Content With Composition: Data Set 1	89
5.5.4.3	Variation of Error In Ni Content With Composition: Data Set 1	90
5.5.4.4	Variation of Error In Mn Content With Composition: Data Set 1	90
5.5.4.5	Variation of Error In Si Content With Composition: Data Set 1	91
5.6.1.1	Iron Relative Emission Coefficient Values Versus Energy Offset For Data Set 1	94
5.6.1.2	Iron Relative Emission Coefficient Values Versus Energy Offset For Data Set 2	94
5.6.2.1	Three Element Model Iron Relative Emission Coefficient Values Versus Energy Offset For Data Set 1	97
5.6.2.2	Three Element Model Iron Relative Emission Coefficient Values Versus Energy Offset For Data Set 2	97
5.6.3.1	Predicted Composition of Specimen D846 Using Global Alpha Values and Data Set 1	102
5.6.3.2	Elemental Error Composition of D845 Using Average Alpha Values	102

LIST OF FIGURES-CONTINUED

Figure	Description	Page

5.6.3.3 Elemental Error Composition of D846 Using Average Alpha Values 103

5.6.3.4 Elemental Error Composition of D847 Using Average Alpha Values 103

5.6.3.5 Elemental Error Composition of D849 Using Average Alpha Values 104

5.6.3.6 Elemental Error Composition of D850 Using Average Alpha Values 104

5.6.3.7 Sum Of Error In Composition of D845 Using Average Alpha Values 105

5.6.3.8 Sum Of Error In Composition of D846 Using Average Alpha Values 105

5.6.3.9 Sum Of Error In Composition of D847 Using Average Alpha Values 106

5.6.3.10 Sum Of Error In Composition of D849 Using Average Alpha Values 106

5.6.3.11 Sum Of Error In Composition of D845 Using Average Alpha Values 107

5.6.4.1 Error in Fe Content Vs. Composition Using Average Alphas 110

5.6.4.2 Error in Cr Content Vs. Composition Using Average Alphas 110

5.6.4.3 Error in Ni Content Vs. Composition Using Average Alphas 111

5.6.4.4 Error in Mn Content Vs. Composition Using Average Alphas 111

5.6.4.5 Error in Si Content Vs. Composition Using Average Alphas 112

5.6.5.1 Predicted Composition of Specimen D850 Using Bond Breaking Data From Data Set 1 115

LIST OF FIGURES-CONTINUED

Figure	Description	Page
5.6.5.2	Predicted Composition of Specimen D850 Using Bond Breaking Data From Data Set 2	115
5.6.5.3	Relative Error in Predicted Composition of Specimen D850 Bond Breaking Data From Data Set 1	116
5.6.5.4	Relative Error in Predicted Composition of Specimen D850 Bond Breaking Data From Data Set 2	116
5.6.6.1	Predicted Composition of Specimen D850 Using Three Element Model Bond Breaking Data From Data Set 1	118
5.6.6.2	Predicted Composition of Specimen D850 Using Three Element Model Bond Breaking Data From Data Set 2	118
5.6.6.3	Relative Error in Predicted Composition of Specimen D850 Using Three Element Model Bond Breaking Data From Data Set 1	119
5.6.6.4	Relative Error in Predicted Composition of Specimen D850 Using Three Element Model Bond Breaking Data From Data Set 2	119

LIST OF APPENDICES

Appendix		Page
APPENDIX A	Measured Intensity Values Corrected For Isotopic Abundance And Primary Ion Beam Intensity	128
APPENDIX B	Relative Sensitivity Factors Results Presented In Graphical Form	134
APPENDIX C	Bond Breaking Model Results Presented In Graphical Form	188

CHAPTER 1
INTRODUCTION TO SIMS

1.1 INTRODUCTION

Secondary Ion Mass Spectrometry (SIMS) is the study of mass spectra of charged atomic and molecular particles emitted from the surface and near surface regions of a condensed phase subjected to heavy particle bombardment [1]. An ion beam of charged particles in the energy range of some KeV incident on a surface results in a phenomena known as sputtering of the target surface. This process consists of the ejection of atoms and molecules from the target specimen via energy and momentum transfer to a limited volume around the primary particle impact zone (in a billiard ball fashion). Unfortunately this transfer not only yields secondary particles used for mass spectometrical analysis, but also results in a disturbance of the specimen surface. This modification fits into three categories:

1) loss of material by sputtering
2) distortion of the material's structure
3) some primary species implantation

Particles sputtered from the specimen surface may be electrically neutral or ionized. Neutrals are swept away by the vacuum system while ionized particles are accelerated and focused by electromagnetic electrodes and lenses into a secondary ion beam which is analyzed by a mass spectrometer. This is the basis of SIMS analysis.
Figure 1.1.1 illustrates the processes which occur upon primary particle impact subsequently leading to the ejection of target species. These atomic scale elastic collisions are the cause of the afore mentioned structure modification of the target

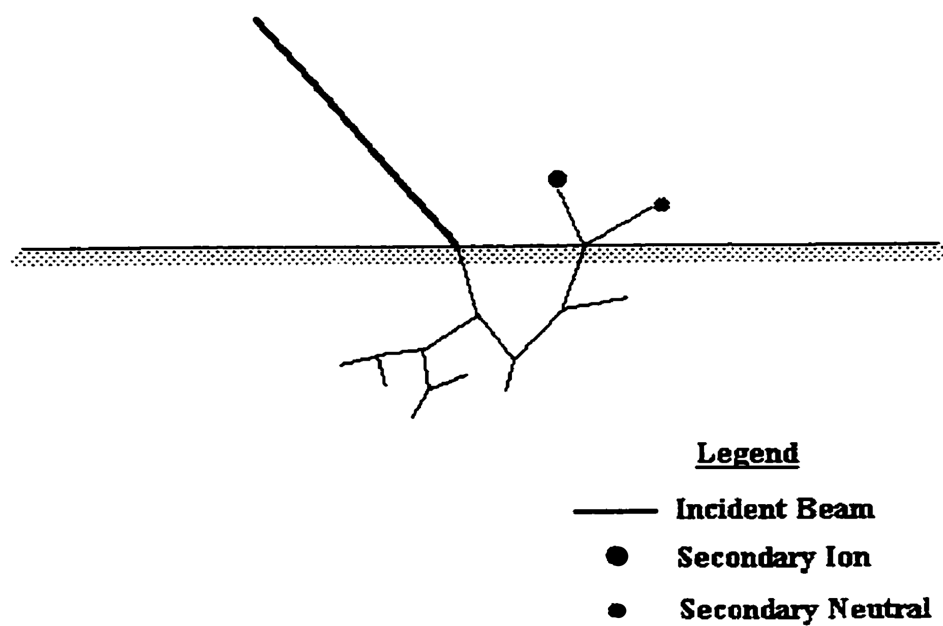

Figure 1.1.1: Schematic Diagram Illustrating Primary Ion Induced Interactions

material. These changes occur by a variety of processes discussed later in this thesis.

Examination of a sample SIMS spectra provides insight into the complexity of the surface ionization process and subsequent data analysis (Figure 1.1.2). In order to derive any practical SIMS information, a quantitative description of the ionization processes and transport mechanisms leading to detection of secondary ions by the mass spectrometer is required. A knowledge of the surface modification phenomena is also essential. The purpose of this thesis is to add further understanding to some such aspects of SIMS analysis.

1.2 HISTORICAL DEVELOPMENT OF SIMS

In 1910 Sir J.J. Thompson first observed secondary ions emitted from a condensed solid phase. This discovery occurred during the study of charge-mass ratios of both neutral and charged Canalstrahlen particle rays [2]. The identified ions were positively charged secondaries emitted (along with neutrals) by a metal electrode bombarded by Canalstrahlen generated in a discharge tube. Later, in 1931 Woodcock correctly identified negative secondaries using Dempsters 180° mass spectrometer [3]. These first known negative ion spectra were obtained by bombardment of sodium fluoride and calcium fluoride targets with 500 eV primary lithium ions. It was not until 1949 however, that instrumentation which would yield a steady beam for reliable analysis was first developed. Herzog and Viehbock [4] used negative ions emitted from a sputtered cathode during the discharge of a Canal ray tube as a primary source. This was also the first instrument to utilize the novel concept of using separate electric fields for acceleration of the primary and secondary ions. Secondary ions were analyzed in a Thompson parabola apparatus designed by Herzog.

In the 1960's SIMS activity intensified and rapid progress began. Until 1963 secondary ions were mostly generated by either electron impact, surface ionization, or

spark sources. However, in that year Liebl and Herzog [5] unveiled a new sputter ion source for the analysis of solids. This "Duoplasmatron" source provided a stable argon beam with many desirable characteristics. One included the complete separation of the primary ion source from the target region. Hence a high intensity primary beam could be used while maintaining a very low gas pressure at the target. Consequently, use of considerably higher energy primary ions was possible thus resulting in a high yield of secondary ions and reduced discrimination. Secondary beam currents of 10^{-8} amperes were now available, quite adequate for routine analysis.

In contrast to the previously popular spark sources, the sputtering source provided stable operation facilitating electrometric recording of the mass spectrum and henceforth simple spectra of singly charged species. Also of benefit was the ability to use the source to study insulators in addition to metals and semiconductors.

Advances made in the nineteen sixties resulted in the development of three basic types of instruments: mass analyzers with moderate lateral resolution, ion microprobes, and ion microscopes [6]. Mass analyzers were combined with high yield sources such as the duoplasmatron to provide high surface erosion rates and secondary flux for trace and depth profiling analysis. This mode of operation used mainly for the analysis of inorganics is known as "Dynamic SIMS".

In 1960 Castaing and Slodzian [7] produced the first prototype ion microscope. This design used a broad primary ion beam to irradiate a sample surface. The beam was subsequently rastered across the specimen surface in order to ensure uniform illumination. A high lateral resolution on the order of 1 μm was then achieved by the use of a dedicated ion optics and mass filter system using a narrow beam of secondary ions to form a magnified image of the object. Here uniform illumination was of paramount importance while primary beam quality was of secondary importance. This instrument was the forerunner of such commercial instruments as the Cameca Ims-3f used in this study.

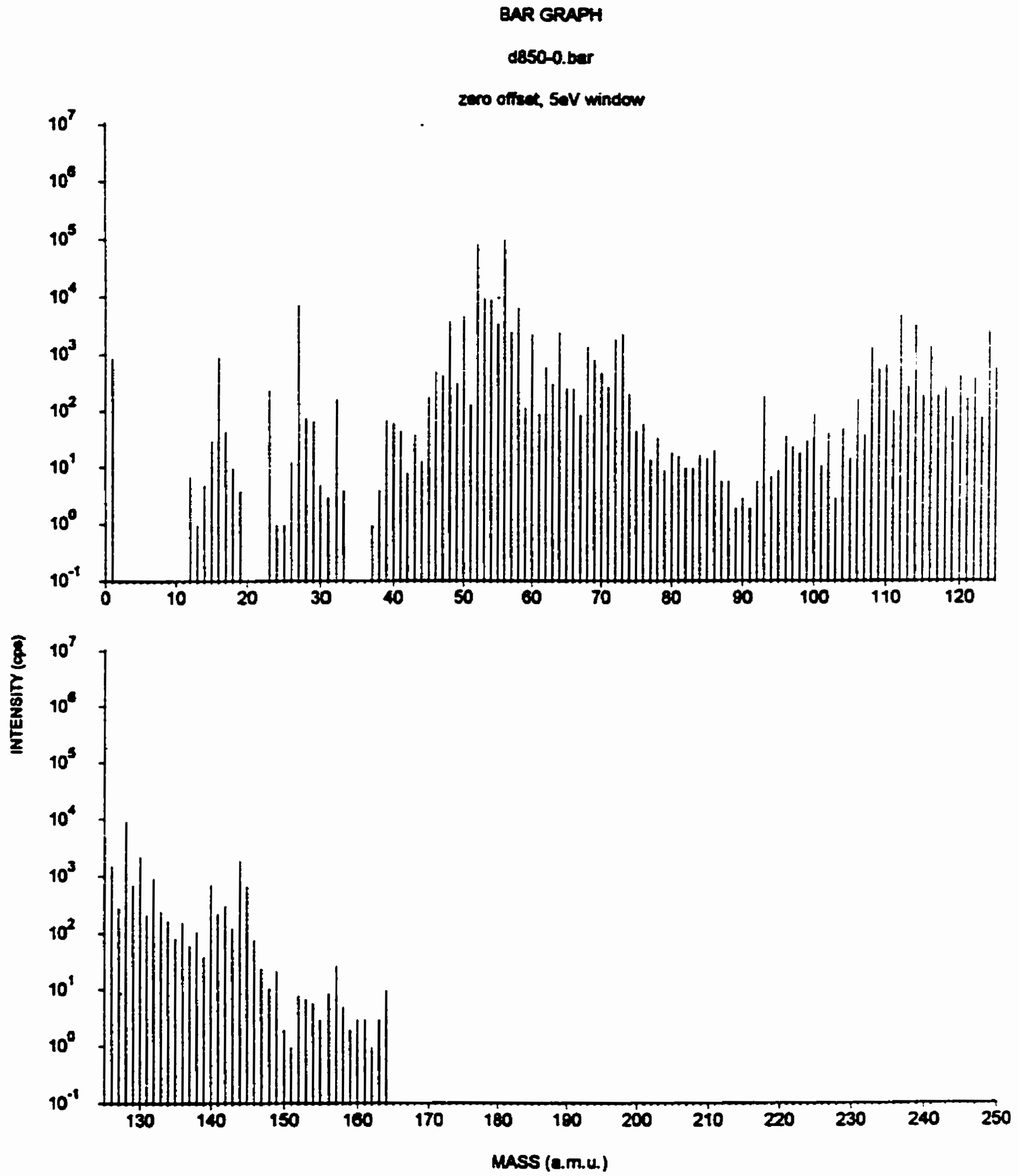

Figure 1.1.2: SIMS Spectra For Specimen D850

Several years after the introduction of the ion microscope (1967) Liebl introduced the "IMMA" ion microprobe. This instrument used a rastered primary primary beam on the order of μm in diameter generated by a duoplasmatron. Here, the secondary ions were analyzed by a mass filter and a suitable detection system. Again, lateral resolution determined by the primary beam diameter was on the order of 1μm [8].

A major milestone in Dynamic SIMS analysis was the development of the liquid metal ion source by Krohn and Ringo in 1975 [9]. Capable of providing a primary beam of less than 0.1 μm in diameter, this source greatly improved lateral resolution in ion microprobe analysis. In newer instruments lateral resolutions of about 0.2 and 0.1 μm have been attained with Ga^{-} ions of 10 and 27 KeV energy respectively. Levi-Setti et. al. (1974) [10] reported a further improvement in resolution to approx. 20 nm using a 47 KeV primary beam. The resulting improved lateral resolution is however attained at the cost of lost depth resolution resulting from the higher beam energies used. The available current limitations resulted in a lack of sensitivity when imaging, thus limiting analysis to major elements [1]. The development of higher transmission secondary optics, improved detection systems, and digital image processing, have subsequently allowed direct imaging with single ion sensitivity.

In order to improve quantitative analysis by SIMS efforts have progressed since 1959 to reduce or remove matrix effects caused by secondary ion yield variations. One method has seen the use of post ionized secondary neutrals instead of ions. Early experiments [11] employed a low voltage plasma which required planar sample surfaces of mm dimensions making microanalysis difficult. As a result, other techniques such as electron impact [12], high temperature thermalization [13], and laser post-ionization [14,15] have been pursued. High temperature thermalization appears free of matrix effects and is strictly quantitative but cannot detect some elements such as C, B, and O. Laser post ionization is still being investigated for its quantitative abilities. These techniques,

termed Secondary Neutral Mass Spectrometry (SNMS) have now become an area of study in themselves.

Since the early 1970's an interest in SIMS analysis of organic systems has become increasingly popular. In 1970 Benninghoven et. al. introduced a "Static SIMS" approach which made possible the analysis of organic systems without destruction of desorbed molecules. This preserves the chemical structure information of surface organics. Static SIMS incorporates typical current densities on the order of 10^{-9} A cm^{-2}, and analysis times approaching 1000 seconds. Since total doses are in the range of 10^{12} to 10^{13} cm^{-2} this yields aggregate bombarded areas from 1 to 10 percent of the total area. Here, large sample areas are used to increase sensitivity. Initially quadropole mass analyzers were used, but over the last decade time of flight spectrometers have become prevalent for static SIMS. Their collection efficiency and mass resolution offer superior results. Today SIMS is still a growing field for analytical applications and research. The field continues to evolve at an ever increasing rate and in the future is destined to become more and more prevalent in the field of surface and near surface analysis as more becomes known about matrix effects and quantitation.

1.3 CHARACTERISTICS OF SIMS

The wide dynamic range, high sensitivity, isotopic differentiation, and ability of SIMS to detect the entire periodic table make SIMS an extremely attractive surface analysis technique. Combined with a high signal to background ratio and detection limits as low as 10^{14} - 10^{16} atoms cm^{-2} (parts per billion range) for many elements, SIMS is an increasingly attractive analysis tool, particularly in the semiconductor and metallurgical industries. More specifically, the positive attributes of SIMS include: [1,16].

- Detection limits are on the order of parts per million to parts per billion atomic

- All elements of the periodic table are detectable
- Isotopes can be distinguished
- Depth resolution of 1 nm is possible, but 10-20 nm is typical
- Lateral resolution varies from 20 nm to 1 μm, depending on primary ion source
- Composition of specimens can be quantified using standards and/or Relative Sensitivity Factors (RSFs)
- Most insulators in addition to semiconductors and metals can be analyzed
- Limited chemical information may be obtained from relative molecular ion abundances

1.4 DISADVANTAGES OF SIMS

As with any other technique, secondary ion mass spectrometry has its limitations. The primary disadvantage of SIMS is the variation of the secondary ion yields and subsequent elemental sensitivity for a given material or matrix depending on the sample composition. This "Matrix Effect" complicates SIMS data, resulting in the requirement of models such as the Bond Breaking Model in order to achieve semiquantitative analysis. In order to achieve this an extensive base of standards for empirical calibration of instruments for elemental sensitivities had to be developed. Similarly other negative aspect of SIMS which must be accounted for in sample analysis include [16]:

- Mass Interferences may be present, particularly at higher masses
- Secondary ion yields vary by more than six orders of magnitude over the periodic table
- Secondary ion yields are often found to be matrix dependent
- Numerous standards required for data quantification
- Flat surfaces are required for optimal depth resolution and ion microscopic analysis
- Destructive nature of analysis technique

1.5 MATERIALS ANALYSIS USING SIMS

The ionization processes of SIMS analysis are complicated in nature and data must be interpreted with care. As all secondary ions originate from the near surface regions of the analyzed sample, all modes of analysis, including bulk, are in effect surface analyses. The secondary ions reflect either the chemical composition or a modified chemical composition of the near surface region. As such one must consider the interaction of the bombarding particles with the sample, and the resulting changes arising from this interaction.

SIMS analysis of metals in particular may be complicated by nonuniform sputtering arising from their complex chemical composition and heterogeneous microstructure. This may lead to a loss of depth resolution, or misleading chemical information. Analysis of metals may be subject to more difficulties than semiconductors or dielectrics due to the presence of multiple phases, polycrystalline regions, inclusions, precipitates, impurities, and grain boundaries. [16] The surface is different from the bulk, and the bulk itself may contain any of the above morphologies, in addition to possible intermetallic compounds [17] .

Bombardment of polycrystalline regions can result in cone formation as a consequence of differential sputter rates, especially when inert primary ions are used. An oxygen primary beam reduces this as the oxygen causes an amorphous oxide surface to form on the specimen. [16] Otherwise some models used in quantitative analysis of multiphase structures are made difficult to employ as the sputter yield and ionization probability change locally. Similarly, problems may be encountered arising from enhancement or suppression effects on the secondary ion yield resulting from small phases and precipitates. In general, such analytical artifacts can be minimized by oxygen flooding to saturate the surface and impose a constant oxide stoichiometry. [17] Even so, standard samples of a similar structure and homogeneous nature such as those used in this study are recommended for analysis purposes.

In specimen analysis further consideration should be given to the effect of a transfer of the specimen from its original environment to the ultra high vacuum chamber. Drastic changes in the surface chemistry of a specimen can take place as a consequence of removal of the specimen from the ambient gas or liquid into a reduced atmosphere dominated by O_2, CO, and H_2O. Surface contamination or desorption of surface chemistries can result.

1.6 SEMI-QUANTITATIVE SIMS ANALYSIS

The goal of quantitative elemental SIMS analysis is to determine the fractional atomic concentration of an element or elements in the surface region or bulk volume of a sample from a measurement of the sputtered particle currents. A representative analysis of the bulk volume only holds if the composition of the sputtered volume, V, is identical to that of the bulk volume. This sputtering equilibrium is possible in spite of the selective sputtering effect sometimes encountered. It is indeed the definition of sputtering equilibrium that the composition of the atomic beam leaving the sample surface is identical to that of the bulk [1]. That is after a time period is allotted to allow the primary beam to sputter through layers of surface contaminants and the prior surface oxide, the secondary ion signal stabilizes. Further this time period must be sufficient to allow the sputter front to catch up with the primary ion implant front thus allowing a more consistent secondary ion signal without perturbations usually associated with the beginning of a new analysis site [1]. Under these conditions as long as there is not a change in secondary ion counts due to build the up of one element in the surface region due to preferential sputtering then sputtering equilibrium is usually attained and the signal varies with composition. This is true for the iron, nickel, chromium system investigated in the study.

Only a fraction of the secondary ions ejected from the target are subsequently measured at the detector. The value completing this journey ranges from 10^{-5} to 10^{-3},

depending on the instrument [1]. The instrumental transmission factor is a combination of the efficiencies of collection into the mass spectrometer, transmission through the mass analyzer, and ion detection. The transmission in magnetic sector instruments such as the Cameca Ims-3f decreases with increasing mass resolution. Here a balance must be struck in order to avoid mass interferences in complicated materials such as alloys. In addition, ionic intensities must be corrected for mass fractionation and relative isotopic abundances.

Any dependence of the transmission factor on the actual ion measured arises from differences in the initial ejection energies and emission angles of the secondary ions and on the mass dependent transmission and detection capabilities of the instrument [1]. Here, differences in initial kinetic energy of secondary ions reflected in the mass dependent instrument transmission can result in a large contribution to systematic errors. The position and width of the energy window will effect measured secondary ion intensity ratios between elements due to varying distribution widths and peak shapes. Hence the use of standards with constant analysis parameters is required for analysis. Herein lies the basis of this study - to investigate the effect of variance in secondary ion distributions on quantitative analysis.

CHAPTER 2

SIMS INSTRUMENTATION

2.1 INTRODUCTION

SIMS analysis of specimens is achieved via a three step process. Initially the sample surface is bombarded by a beam of focused primary ions resulting in a sputtering of the sample surface layers. The sputtered species (atoms, molecules, polyatomic clusters) which are ionized in nature are then separated and mass filtered spectrometrically by their mass/charge ratio and respective energy. The selected species are then collected and counted or imaged for a variety of analysis techniques. In this study, this process was performed using a Cameca Ims-3f ion microscope located at Surface Science Western, the University of Western Ontario. This instrument is illustrated in Figure 2.1.1 [18]. The Ims-3f is a "Direct Imaging Microscope" and as such it maintains the spatial relationships of secondary ions through the secondary column to the dual microchannel plate detector (Figure 2.1.2). This allows the use of laterally space resolved information for ion mapping for quantitative or imaging analysis.

The Ims-3f uses two ion sources, a hollow cathode douplasmatron source capable of generating both positive or negative primary ions, and a surface ionization source used for Cs^+ generation for analysis of electronegative elements. The two sources are mounted to ports on the primary beam electromagnet which uses magnetic field strength and polarity to direct the selected primary beam into the primary column [1].

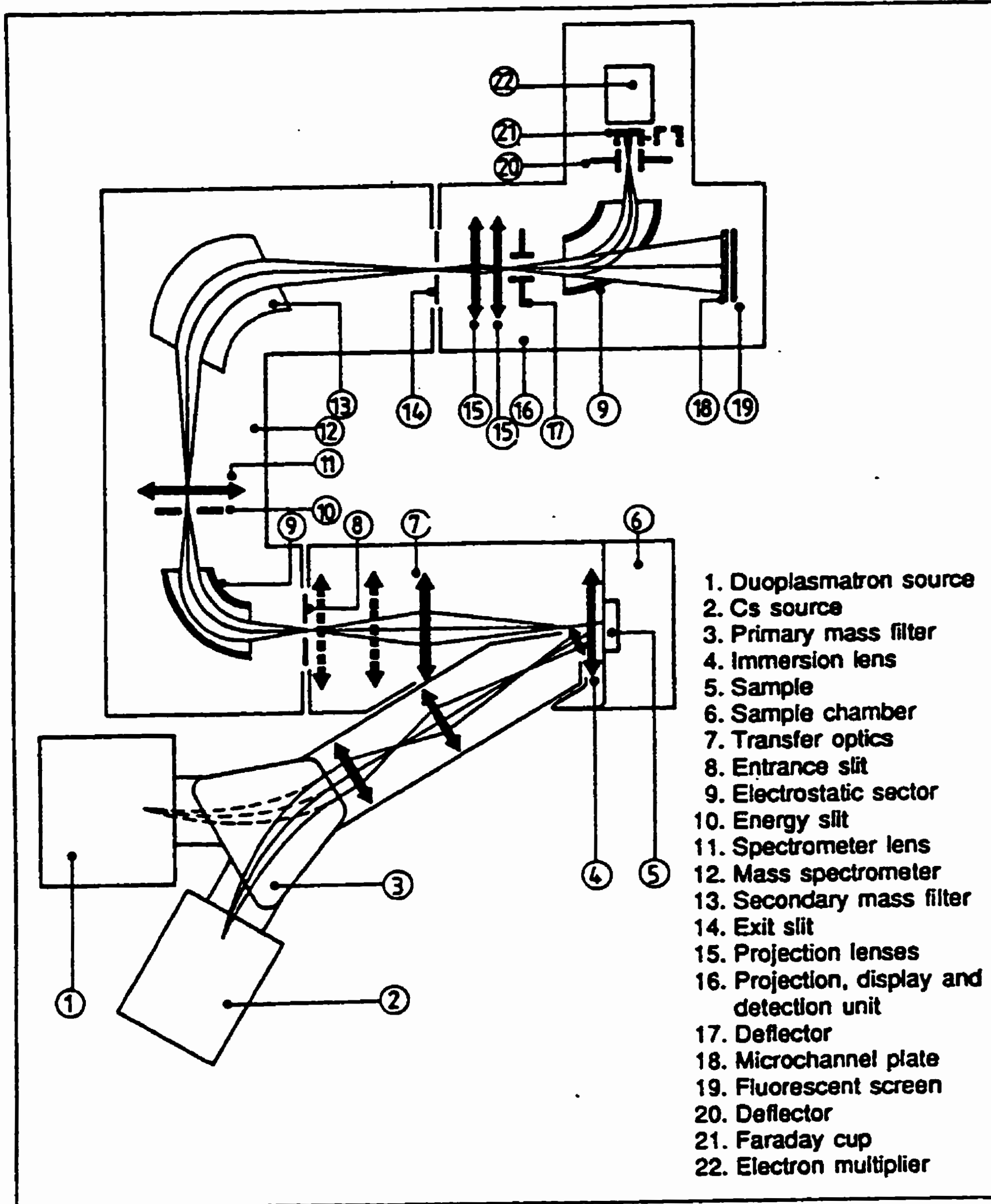

Figure 2.1.1: schematic Diagram of Cameca Ims-3f Ion microscope [19]

The primary column is composed of three sets of electrostatic lenses, a stigmator, and deflection plates which focus and shape the primary beam to a diameter of 1 to 500 μm at the sample surface [1]. As the Ims-3f is a direct imaging microscope, the entire imaged field is illuminated simultaneously by the primary beam as illustrated in Figure 2.1.2 [18].

As stated earlier the impact of a primary ion at the sample surface results in a reshuffling of matrix atoms [20] and subsequent emission of secondary particles which may be neutral or ionized in nature. The Ims-3f uses a dual magnetic sector mass spectrometer for mass analysis, via an electrostatic sector for energy focussing, and a magnetic sector for focussing by mass. This geometry allows energy discrimination in order to prevent low energy polyatomic ions from entering the mass analyzer, thus simplifying some analyses [20].

The spatial point to point microscopic function is achieved by use of ion optic lenses in the secondary column, initially this is preserved by the strong electrostatic accelerating field of 4500 volts present between the specimen and the immersion lens [18]. The transfer optics of the secondary column optimize the global, non-mass resolved image of the sample surface [1]. This is achieved via the use of one of three lenses which is energized in order to cross-over the first virtual global image at the entrance slit. The image itself is focused to form a second virtual image at a fixed distance beyond the slit at a point in the electrostatic sector . The electrostatic sector refocuses this virtual image to crossover at a plane between the electrostatic and the magnetic sectors at which place the energy slit limits the energy bandwidth used for analysis. Another transfer lens

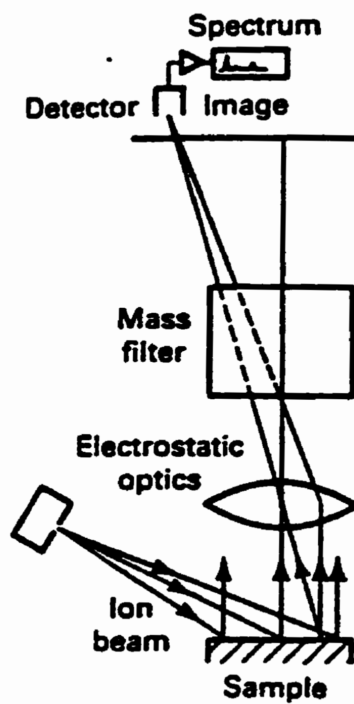

Figure 2.1.2: Schematic Representation of a Direct Imaging Ion Microscope [18]

located just beyond the energy slit transfers the second image to a third virtual image located inside the magnetic sector where mass filtering takes place. The then mass resolved image is projected by a post accelerating lens system in such a manner that the image crosses over at a point inside an electrostatic sector which directs the secondary beam to a dual microchannel plate detector, or, a faraday cup or electron multiplier. The dual channel plate detector is used for image analysis. This channel plate detector is composed of an array of electron multiplying capillaries which convert energy from an incident ion into a localized electron shower which illuminates a phosphor screen [20]. During quantitative analysis the mass separated secondary beam is directed toward a faraday cup or an electron multiplier. An attached computer collects and stores information based on measured ion currents for mass spectral analysis, depth profiles or surface ion distributions along a line [20].

2.2 ION SOURCES

2.2.1 Duoplasmatron Ion Source

There are several types of ion sources used for noble gas and/or reactive ion beam generation. These vary in available current output, brightness, gas efficiency, and spread in energy of ions generated [21]. The duoplasmatron ion source developed in 1956 by von Ardenne [22] is a high intensity source which maintains a very low gas pressure at the target. Moreover, this source maintains a stable beam of high intensity and high energy thus yielding a high secondary ion intensity and reduced discrimination [23]. Secondary currents of up to 10^{-8} generated by such a source are more than adequate for routine analysis. The douplasmatron source illustrated in Figure 2.2.1 operates by burning a

discharge between the anode and cathode through the intermediate (Zwischen) electrode at a pressure of 10 to 100 Pascals. The gas plasma is constricted by a magnetic field and ions are extracted via a small axial bore in the anode. Switching between positive and negative ion extraction is accomplished by reversing polarity of the extraction field at the extraction electrode. Suppression of electron emission necessary during negative ion generation is achieved by ensuring that the bore in the intermediate electrode is eccentric.

2.2.2 Cesium Surface Ionization Source

The second ion source on the Cameca Ims-3f is a Cesium surface ionization source. This source is characterized by a low energy spread (approximately 0.2 eV) and a high brightness. These properties allow a much smaller spot size than the duoplasmatron while maintaining the same ion current [1].

The surface ionization source is supplied with cesium by introducing an ampoule of pure cesium into the heater resvoir (Figure 2.2.2) and breaking the ampoule under vacuum. The cesium is then heated in the reservoir to a temperature of approximately 250°C to provide the correct vapor pressure of cesium [24]. The cesium vapor is then fed into a porous tungsten ionizer plug by a thin heated feed tube. The cesium vapor subsequently diffuses through the plug to its front surface which is heated radiatively by a coil heater to a temperature of approximately 1000°C [1]. Ionization of the cesium occurs at the plug surface by thermal ionization with about 99% efficiency [26].

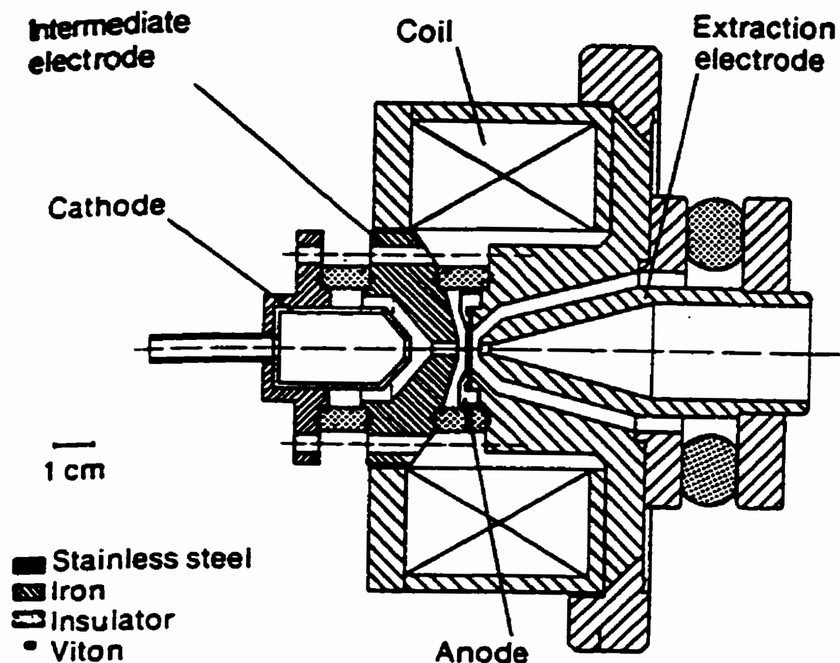

Figure 2.2.1: Schematic Diagram of a Hollow Cathode Duoplasmatron Ion [25]

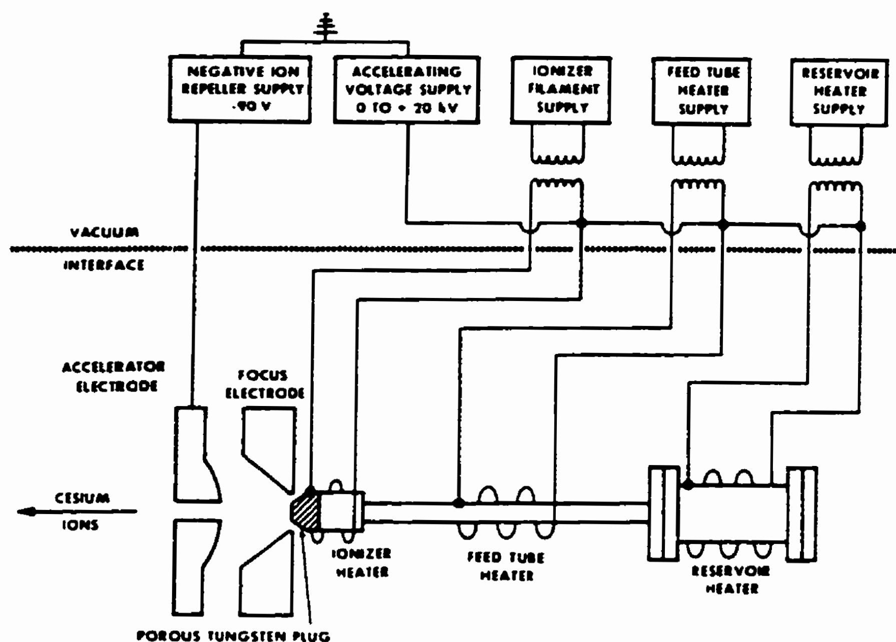

Figure 2.2.2: Schematic Diagram Of a Surface Ionization Cesium Ion Source [26]

The ionized atoms are then accelerated into the primary filter by a potential difference of up to 20,000 volts between the focus and accelerator electrodes. An additional negative voltage of 90 volts is applied to the accelerator electrode to prevent backstreaming of electrons and negative ions.

Such a cesium source offers the benefit of increased ion yields of electronegative elements such as phosphorous, selenium, and telerium used in semiconductors. Hydrogen, carbon, oxygen, and noble metals are similarly enhanced [26].

2.3 PRIMARY BEAM PURIFICATION

Primary ion beams emitted from gas discharge sources such as the duoplasmatron usually contain impurity ions (often stemming from inner source walls or gas memory effect) and energetic neutrals. These neutrals arise from charge exchange processes that occur either during or after primary beam acceleration. Further, undesired polyatomic or multiply charged molecules may also be present, resulting in contamination of the specimen and subsequent secondary ion spectra. Such contamination may alter secondary yields or, erroneously appear as a sample constituent. For this reason primary beam purification is performed using a magnetic sector in the Ims-3f. This magnetic sector not only selects and purifies the primary ion beam based on the mass-charge ratio but it also utilizes a bend in the primary beam column to remove energetic neutrals not deflected by the magnetic field [21].

2.4 ION LENSES AND BEAM SCANNING

As previously mentioned the primary column uses three sets of electrostatic lenses, a stigmator, and deflection plates (Figure 2.4.1) to focus and shape the primary ion beam to a diameter of 1 to 500 μm at the sample surface [1]. In order to avoid the mass dependent focussing nature of magnetic lenses, ion beams are focused using electrostatic lenses instead. The effective focussing of ions of the energies required for SIMS analysis is not possible using magnetic lenses the effective field strength is orders of magnitude too low. Electrostatic lenses are mechanically simpler, and consume no power, but unfortunately are also of poorer optical quality than their magnetic counterparts.

Most SIMS instruments whether they be of an imaging nature or not are usually provided with the ability to raster the primary beam across the sample surface in two mutually perpendicular directions. This is true of the Ims-3f when the primary beam is focused to a small spot size. Here, a uniform fluence is achieved over an area of the specimen surface usually larger than the analyzed area in order to avoid crater edge effects. This scanning motion is achieved via the use of two pairs of quasi electrostatic deflection plates arranged either before or after the final lens [27].

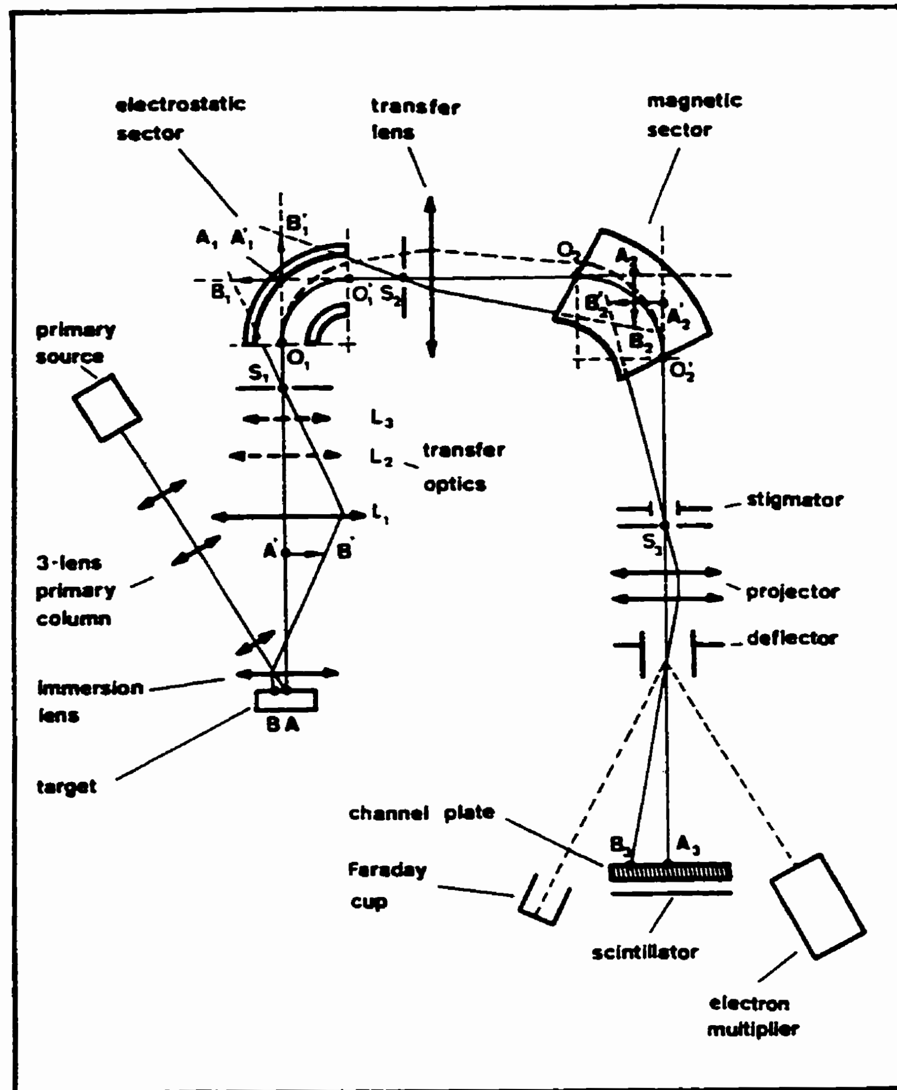

Figure 2.4.1: Ion Optics Of The Cameca Ims-3f [28]

2.5 SECONDARY ION COLLECTION

In order to make SIMS a viable analysis technique it is important to maximize instrumental sensitivity via a high secondary ion collection efficiency. Typically bombardment of a sample with a reactive primary ion species, such as oxygen used in this study, results in the emission of secondary ions with an energy distribution which is Maxwellian in shape (Figure 2.5.1). For monatomic ions the most probable energy is approximately 10 eV while molecular ions will have a lower most probable energy and a narrower energy distribution. It is this difference in ion distributions which creates interest in studying the effects of using different secondary ion energies for quantitative SIMS. For optimal SIMS analysis the most effective method of collecting secondary ions with little energy discrimination is to accelerate them immediately from the sample surface, as is done in the Cameca Ims 3f. The reduced discrimination in collection efficiency allows a more accurate study of the effect of secondary ion energy on quantitative analysis. The transfer optics of the Cameca are designed to produce a low aberration, high magnification, global real image of the analyzed surface which can be processed by the mass spectrometer to filter out one ionic image from the global image. The transfer optics must shape and limit the dispersion of the secondary ion beam so that the mass spectrometer can provide appropriate mass resolution. The Ims-3f transfer optics are flexible enough to allow lateral image resolution, mass resolution and magnification to be optimized for individual analyses. This is accomplished using an immersion lens for ion extraction and one of three Einzel transfer lenses (only one of which is energized at a time) to select the analyzed field size and mass resolution, when used in conjunction with an appropriate mass spectrometer entrance slit size (Figure 2.5.2) [1]. Here, the field of view

is selected for a constant collection angle, Φ, from the target. Due to the properties of the optics with increased magnification, there is an accompanying increase in mass resolution due to the smaller mass spectrometer entrance slit used and the

reduced angular magnification [1].

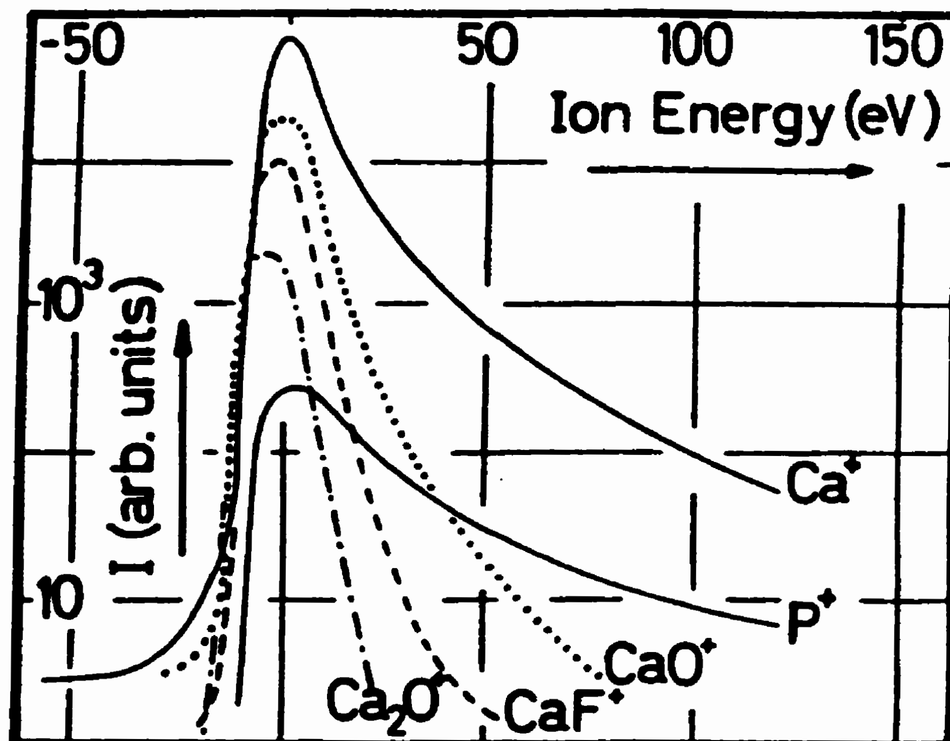

Figure 2.5.1: Maxwellian Secondary Ion energy Distributions For Monatomic And Polyatomic Ions [20]

2.6 MASS ANALYZERS

The Cameca Ims 3f uses a double focussing magnetic sector mass analyzer. The mass analyzer itself is preceded by an electrostatic energy analyzer which narrows the energy dispersion of the secondary ions and focuses the ions such that the energy dispersion of the energy analyzer is matched to cancel that of the magnetic field mass analyzer. This is the origin of the term "double focussing". Such a spectrometer can transmit a broad enough energy range to allow analysis of the most significant portion of the secondary ion energy distribution (0 to 130 eV) [29].

Before mass separation can be performed in the magnetic sector, the secondary ion beam must be constricted to a small energy bandwidth. The energy bandwidth selected usually corresponds to the peak of the Maxwellian distribution at an energy of approximately 10 eV. This process of energy filtering is performed in the electrostatic sector (in conjunction with the energy slit). Here two torroidally shaped electrodes deflect an ion through a circular path via an induced electric field between the plates (Figure 2.6.1).

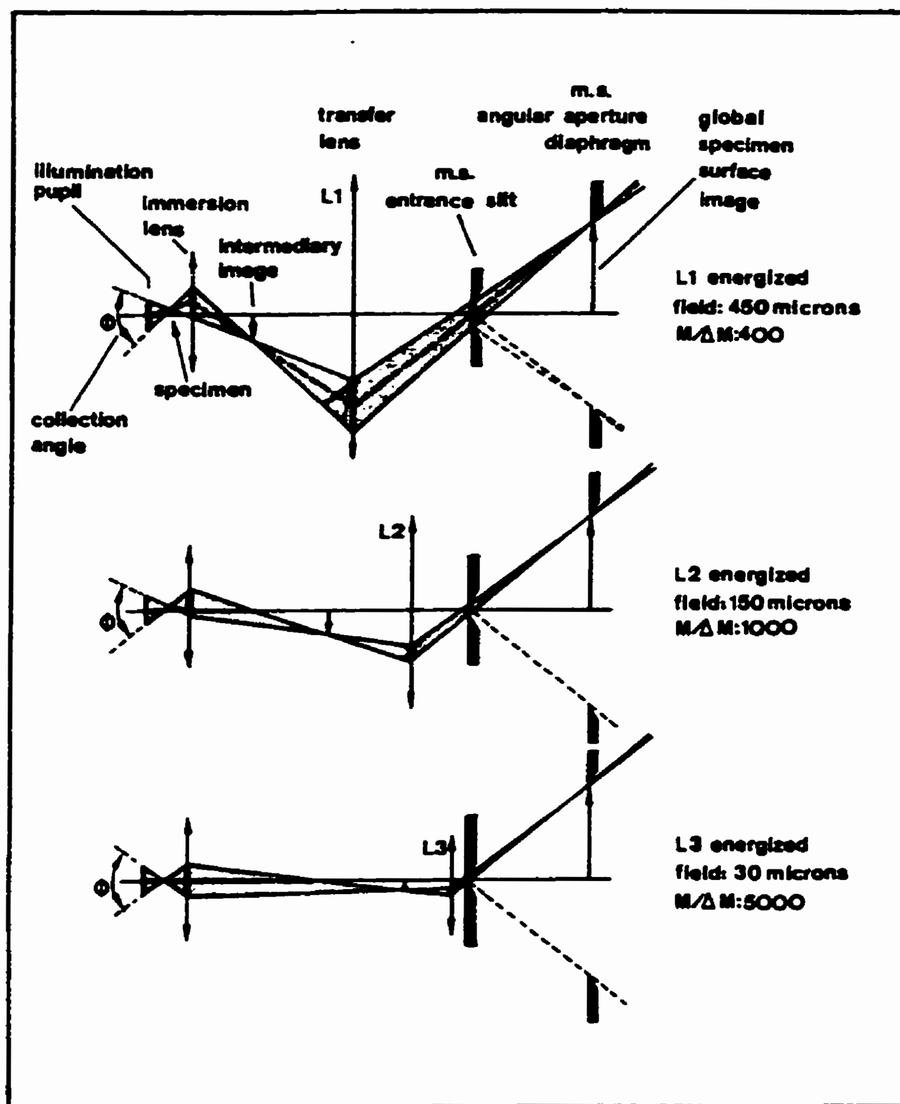

Figure 2.5.2: Variable Secondary Ion Beam Processing in the Cameca Ims-3f Based on Transfer Optics Lens Selection [1]

For this circular transmission to be successful, the centripetal force acting on the ion given by

$$F_c = mv^2 / R_0$$

Where: m = ionic mass
v = ionic velocity
R_0 = radius of curvature

must balance the force imposed by the electric field given by

$$F = q\,\varepsilon$$

Where: q = charge on ion
ε = Electric Field Strength

Then,

$$\text{Kinetic energy} = (mv^2)/2 = (q\,\varepsilon\,R_0)/2$$

and the ion energy passed by the electrostatic sector is selected by varying the voltage imposed electric field, ε.

After energy filtering in the electrostatic sector, the secondary ion beam passes through the energy slit (which aids in ion energy selection)to the magnetic sector for mass filtering. Here the ions are deflected by the magnetic field in the secondary magnet by their mass/charge ratio. The path traveled by by ions in the magnet is determined as they undergo a magnetic field imposed tunable deflection in a manner analogous to that for the electrostatic sector. Again the ion must traverse a circular path (Figure 2.6.2) with an acting centripetal force given by:

$$F_c = mv^2 / R_m$$

Where: m = ionic mass
v = ionic velocity
R_m = radius of curvature

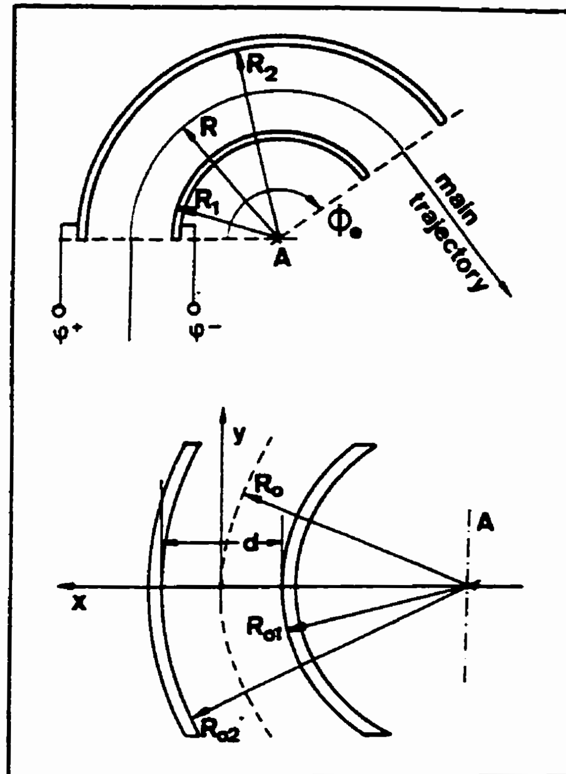

Figure 2.6.1: Ion Trajectory Through an Electrostatic Sector [1]

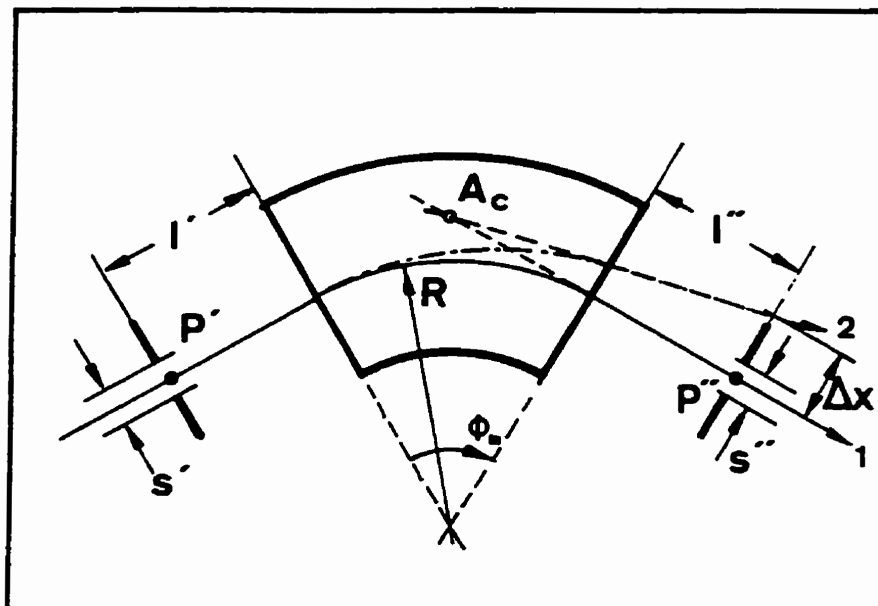

Figure 2.6.2: Ion Trajectory In The Secondary Magnet [1]

In order for the ion to successfully navigate the magnetic fieldin the spectrometer, the centripetal force must be equal to the magnetic field induced force of :

$$F_m = q\,v\,B$$

Where: q = charge on ion
v = ionic velocity
B = magnetic field strength

Since $F_c = F_m$, this can be reduced to

$$mv/q = R_m B$$

Hence, by changing the magnetic field, ions can be selected based on their mass/charge ratio [1].

2.7 ION DETECTORS AND COUNTING

The Cameca Ims 3f uses two types of detectors for counting ion fluence, a Faraday cup, and an Electron multiplier. The Faraday cup illustrated in Figure 2.10 utilizes DC amplification of the incident ion current to detect currents as low as the 10^{-8} to 10^{-14} Amp ran ge. Here, a positive or negative incident ion current causes a drop in the voltage, U_s, measured across the resistor R given by:

$$U_s = IR$$

Since the ion fluence is measured across the resistor, the input noise voltage from the amplifier, A, thus determines the minimum reliably detectable ion current.

The electron multiplier used in the Ims-3f is an open electron multiplier, usually operated in the pulse counting mode. In such a system an incident ion impacts the first

(conversion) dynode causing the ejection of secondary electrons (Figure 2.7.1). The ejected electrons are then accelerated by an electrical potential of 200 to 300 eV toward a second dynode where the release electron impact induced secondary electrons. This process continues from dynode to dynode in a cascading effect which increases the electron fluence. With a conversion yield of two electrons per incident particle, typical gains of 10^4 to 10^8 can be realized depending on the number of dynodes, their material and the total multiplier voltage. Due to this signal amplification the input resistance R' of the electron multiplier can be factors smaller than that of a Faraday cup while still measuring the same current. In the multiplier the minimum detectable current is not determined by amplifier noise, rather, it is a function of of the spurious emission of electrons by the conversion or multiplication dynodes in the electron multiplier. Minimum detectable ion currents are as low as 10^{-20} to 10^{-21} Amps in pulse counting mode.

Pulse counting is a process whereby each electron current pulse generated from an individual ion impact at the conversion dynode is amplified and counted on a high speed electronic counter. For this process there is an upper ion current detection limit which is determined by detector dead time losses. These losses typically limit the dependable maximum count rate to an average of 10^8 counts per second. For this reason, primary ion currents used in this study were limited such that secondary ion count rates would not significantly exceed 10^7 counts per second in order to avoid nonlinear response of the detector.

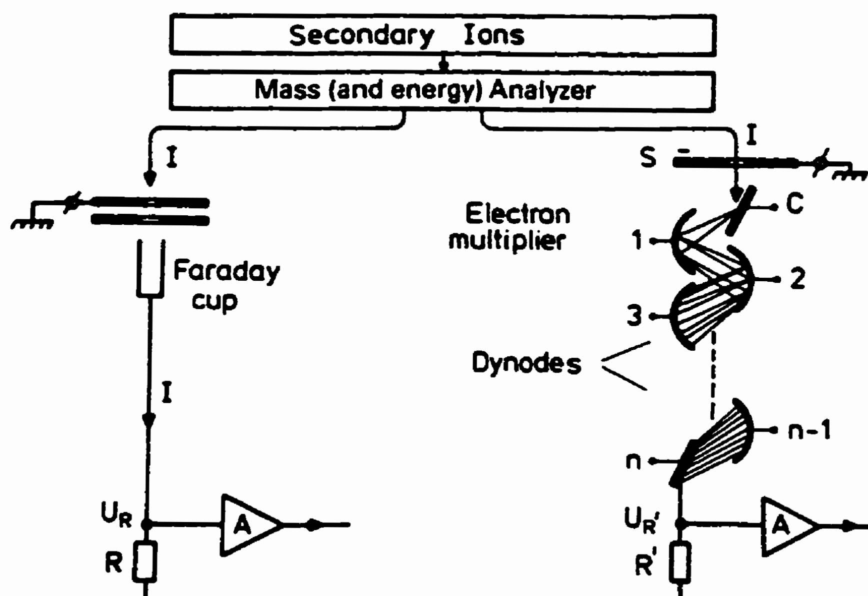

Figure 2.7.1: Faraday Cup And Electron Multiplier Ion Detectors [30]

2.8 VACUUM SYSTEM

The Cameca Ims-3f vacuum system is pumped by a combination of turbomolecular pumps, cryogenic pumps, and ion pumps. There are three turbomolecular pumps, two pumping the primary column and ion gun region, and one pumping the the sample introduction chamber. These pumps are used as high pumping rate removes contamination originating from primary ion generating sources, and specimen introduction vacuum losses.

The specimen analysis chamber is evacuated by a cryogenic pump which is capable of removing most gases with the exception of hydrogen (H_2). This property facilitates the reduction of sample contamination and reduces memory effect in the sample chamber. Finally the secondary column and detection regions of the IMS-3f are pumped by ion pumps which typically achieve pressures on the order of 5×10^{-10} torr [31].

CHAPTER 3

QUANTITATIVE SIMS ANALYSIS

3.1 INTRODUCTION

A thorough understanding of SIMS analysis demands the knowledge of phenomena occurring during the surface ionization process and how these processes influence the quantitative interpretation of ion intensities. Since secondary ion emission is very sensitive to the state of the surface, the sample matrix, and primary ion beam induced effects, the ratio of measured secondary ion intensities of an element at different points on a sample or samples are not necessarily a measure of relative element concentration [32]. Theoretical SIMS modeling requires the consideration of many experimental observables including relative ion yields, energy and angular distribution of ejected particles, the effect of primary beam energy and angle of incidence, cluster formation processes, crystal structure effects, not to mention the ionization process itself [33]. Furthermore, machine effects on secondary ion detection levels such as transmission factor and detector efficiency must also be considered. Empirical analysis using consistent machine parameters can remove from direct consideration the contributions of many of these parameters. For SIMS results to be considered at least semiquantitative some sort of correction must be applied to compensate for experimental effects and preferences. This chapter introduces some of the phenomena which are involved in the ionization process and hence affect quantitative analysis. The models used in this investigation are then introduced and explained.

3.2 SURFACE PROCESSES

In order to obtain compositional information on the surface and near surface regions of a specimen SIMS analysis utilizes the mass-charge ratio of atomic and molecular ions emitted from a specimen subjected to bombardment by a primary ion beam. To facilitate correct interpretation of secondary ion mass spectra the sputter emission process and near surface volume modifications resulting from ion bombardment must be considered [32]. Ion yields are influenced by effects dependant on the chemical nature and crystal structure of the material surface (such as relative grain size and orientation). Resulting effects include primary ion channeling, radiation induced damage and recrystallization, differences in the angular distribution of ejected particles, and variations in the implanted oxygen concentration, all of which act to affect secondary ion signal intensity. Intensity variations measured between grains are approximately equal for all elements [32] thus if measured intensities are ratioed to those of a major constituent at each analysis point, grain orientation effects are reduced if not eliminated [32]. From this observation, quantitation procedures based upon relative ion yields (such as the Relative Sensitivity Factors approach and Bond Breaking Model) are likely superior to those based upon absolute yields. Differences in SIMS instrument designs which affect angles of primary beam incidence, secondary ion collection efficiencies, transmission and detection, when combined with the complexity of the emission process make the derivation of a purely theoretical model applicable to all SIMS instruments for a variety of analysis conditions and sample types barely short of unimaginable. Alternative approaches such as

RSF's and the Bond Breaking Model which provide an empirical solution appear much more practical.

3.3 QUANTITATIVE SIMS: THE RELATIVE SENSITIVITY FACTORS APPROACH AS DERIVED FROM CALIBRATION CURVES

If instrumental parameters such as primary species, primary ion energy, primary beam current density, secondary ion extraction potentials, and secondary ion bandpass are all controlled reproducibly as are experimental conditions such as sample location and orientation, residual vacuum pressure, detector efficiency, and sample preparation and cleaning, it is possible to reproduce SIMS measurements with a precision of better than 5% [1,32]. A prerequisite to this statement being true is of course the requirement that sputtering equilibrium has been attained prior to analysis in order to remove selective sputtering effects [1]. Once these conditions are fixed meaningful sample analyses are possible using Relative Sensitivity Factors derived from standards of similar composition to that of an unknown sample given that all materials are homogeneous on a microscale as are the NBS standards used in this investigation [32].

In such a case the detected ionic isotopic yield of an element M in a specimen will be proportional to the respective ionic abundance of the element [1]. this may be expressed as

$$I^q_M(A,M_i) = I_P\, Y^q_M(A,M_i)\, f^q_M(A,M_i) \qquad (3.3.1)$$

Where: $I^q_M(A,M_i)$ = Detected ion current of M in charge state q (Amps)
I_P = Primary ion current (Amps)
$Y^q_M(A,M_i)$ = Specific Yield of M in charge state q
$f^q_M(A,M_i)$ = Instrumental transmission factor of M in charge state q

And the specific Yield, $Y^q_M(A,M_i)$ is given by

$$Y^q_M(A,M_i) = Y^q_M(A) \bullet a(A,M_i) \qquad (3.3.2)$$

Where: Y^q_M = Total Elemental Yield of the Element A containing isotope M_i
$a(A,M_i)$ = Fractional isotopic abundance of isotope M_i of element A

then these two expressions can be combined to yield

$$I^q_M\,(A,M_i) = I_P\, Y^q_M(A) \bullet a(A,M_i)\, f^q_M(A,M_i) \qquad (3.3.3)$$

Here the instrument transmission factor compensates for mass dependent spectrometer transmission and both elemental and isotopic effects on detector efficiency. The above relationships hold true both for atomic and molecular species thus allowing the use of molecular species for quantitative analysis in the presence of weak or noninterference free atomic distributions.

If the variation of mass dependant isotopic detector efficiency and spectrometer mass transmission are ignored, then equation (3.4.3) can be simplified and the Total elemental detected ionic current of element A, I(A), can be written

$$I^q\,(A) = I_P\, Y^q(A)\;\; f^q(A,\boldsymbol{M}) \qquad (3.3.4)$$

Where: $\boldsymbol{M}$ is the mean mass number of element A.

By taking the ratio's of equation (3.4.4) applied to an element A, and a reference element, R, present in the matrix in significant quantity the relation

$$\frac{I^q(A)}{I^q(R)} = \frac{Y^q(A)}{Y^q(R)} \frac{f^q(A,M_A)}{f^q(R,M_R)} \qquad (3.3.5)$$

can be written. If the element A is always referred to the same reference element, R, then the ratio of elemental instrumental transmission factors will be constant. Now, if the concentration of R is constant then the ratio of detected intensities can be written as

$$\frac{I^q(A)}{I^q(R)} = g[c(A)] \qquad (3.3.6)$$

where g is a function of the concentration of A. Thus if the above stated assumptions are followed, then a "Calibration Curve" for element A for a specific sample matrix can be derived. Here the total detected ion current for a test element is then a function of the test element only. Generation of such a curve requires analysis under identical experimental conditions of a set of samples of differing compositions of the test element, A, while maintaining all other compositions as identical as possible. The ratios of $I^q(A)/I^q(R)$ are then measured to plot a calibration curve similar to that in Figure 3.3.1. The shape of the calibration curve is determined by the sample matrix, the reference element, and the element of interest. Generally the curve increases monotonically with concentration except when discontinuities from phase transitions are present.

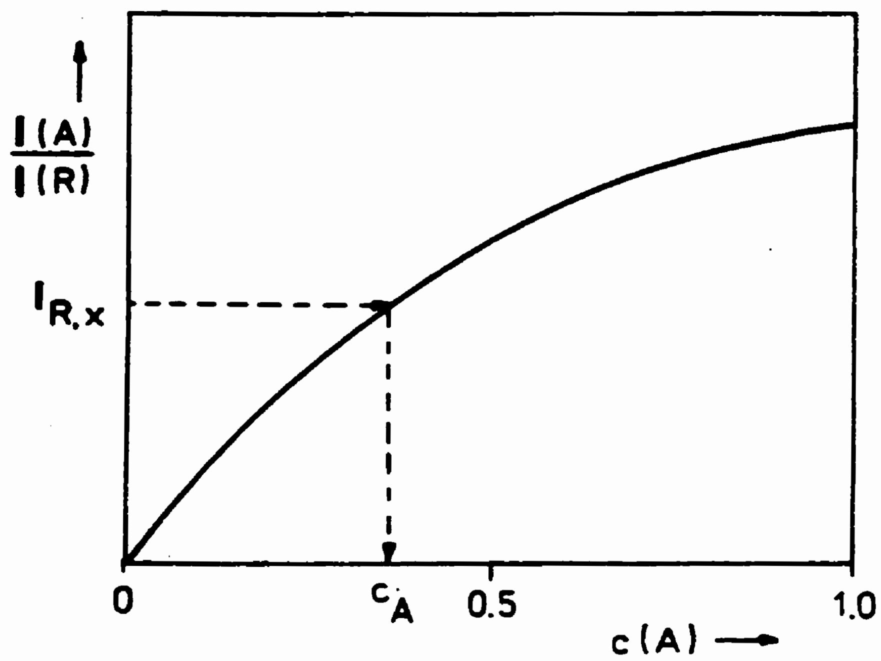

Figure 3.3.1: Calibration Curve For Element A, Reference Element R. [1]

Calibration curves are generally known to be linear in concentration ranges below1% [1]. Under such conditions the detected ion

$$I^{q} = I_{P}\, S_{p}(A)\, c(A) \qquad (3.3.7)$$

Where: Sp is the Practical Sensitivity of A given by

$$Sp = \frac{N^{q}(A)}{I_{p}\, c(A)} \quad [cps/nA] \qquad (3.3.8)$$

Where: $N^{q}(A)$ = Detected Current Measured in cps
Ip = Primary Current (nA)

Now, if the practical sensitivities are assumed to be independent of the atomic concentration, then it can be written that

$$\frac{I^{q}(A)/c(A)}{I^{q}(R)/c(R)} = \frac{S_{p}(A)}{S_{p}(R)} = \text{constant} = S_{r}(A) \qquad (3.3.9)$$

Where: $S_r(A)$ = Relative Sensitivity Factor (RSF) of element A with respect to Element R in the sample matrix.

Then the concentration of A in the sample matrix can be calculated from the ratio of detected ion currents and the known concentration of the reference element by rearranging the equation to obtain

$$c(A) = \frac{I(A)\ c(R)}{I(R)\ S_r(A)} \qquad (3.3.10)$$

Thus it can be said that the relative ion signals when divided by the relative sensitivity factor, $S_r(A)$, form a set of values proportional to the atomic concentration of the element in the sample. Quantitative analysis of multielemental specimens using relative sensitivity factors can be performed without the use of an internal reference element of known concentration if a complete set of relative sensitivity factors for all the elements in a matrix are known for that specific matrix type. If all the total elemental ion currents are measured then the sum of concentrations can be normalized to 100% and equation (3.4.10) may be written as

$$c(X) = \frac{I(X)\ /\ S_r(X)}{\Sigma\ I(X_i)/S_r(X_i)} \quad \text{For all X} \qquad (3.3.11)$$

Thus if an unknown sample is analyzed under controlled conditions and all ion currents and relative sensitivity factors for that matrix type are known the composition of the specimen can be determined if the SIMS instrument is capable of detecting all major constituents with sufficient sensitivity. In a well behaved matrix, quantitative accuracies on the order of ten percent can be realized through this model given adequate standards and sample homogeniety [32].

The Relative Sensitivity Factors approach has enjoyed fairly wide acceptance throughout recent years. This model has been used in analysis of a number of different types of materials including semiconductors [34,35,36], trace metallic contaminants on wafer surfaces [37], brain tissue [38], and cultured animal cells [39]. Some other materials

studied include trace elemental analysis of high purity copper [40], chemical vapor deposited diamond films and natural diamonds [41], and a variety of glasses. Part of the reason for the success of the RSF approach is the degree of accuracy of results obtained using this relatively simple model. The major inconvenience of this model is the initial derivation of applicable RSF values from known standards. Much work has been performed in studying the day to day variability of these values in an instrument and also the transferability of RSF values from one instrument to another and the associated accuracy. Round-robin studies have been performed to this end. Gries [42] stated that for truly accurate work, RSF values must be considered as non-transferable between instruments. In fact, the RSF value may change from day to day on the same instrument. Homma [43] investigated the origin of variation of RSF values using RSF data from his own and a series of other labs and concluded that day to day variation for a given instrument arises from variations in primary ion energy, beam density, and the contrast aperture diameter which determines the transmission of the mass spectrometer. For a five year period Homma observed variations in RSF's which possessed a standard deviation of less than 30% for positive secondaries and 35% for negative secondaries for a Cameca Ims-3f instrument. Using a newer Cameca Ims-4f instrument deviations of 14% were observed over a one year period. Variations in RSF values measured between different instruments of the same type tend to be larger - typically +/- 50% or less [44] . In contrast RSF variations between different types of instruments are typically an order of magnitude [43]. This large difference of RSF's was thought to depend mostly on the difference of impact angles of primary ions between instruments. Impact angle acts to effect the surface concentration of primary ions which in turn effects the ionization probability of secondary

ions. Homma found that RSF's measured at various incidence angles of O_2^+ using an Atomika 6500 instrument increase with angle of incidence for positive secondaries. When RSF's measured using three different instruments with different incidence angles were compared their results were in close agreement with the results from the Atomika experiment. Different mass spectrometers and bandpass will also influence RSF values as their mass transmission function will directly influence the relative intensities of impurity and matrix ions.

Simons et. Al performed a round-robin study of a variety of elements implanted in Si. Analysis was performed in three magnetic sector instruments m the same manufacturer and two different quadropole SIMS [45]. RSF values were plotted against ionization potential. Comparison of RSF values showed remarkably close agreement between the magnetic sector instruments. The average standard deviation among the magnetic sector labs for the RSF data set was 22% - which Simons stated is only a factor of two larger than the results achieved by carefully controlled repetitive measurements of a single lab and is in close agreement with variations which Homma found within his own lab over a five year basis. Results obtained for the two quadropole instruments were more discrepant. This is not surprising due to their differing geometries and operating conditions. Based upon these two works it is apparent that tabular RSF values should only be applied to SIMS data taken on the same make and model of instrument if errors of 50% or less are to be desired. For more accurate results RSF values must be determined for the individual instrument.

As SIMS is widely applied to the semiconductor industry it was only a matter of time before quantification of boron in silicon was given priority in SIMS standardization

for ISO certification by the Technical Committee if the International Organization for Standardization (ISO). As such a round robin study was initiated to obtain information for boron quantification using boron doped and implanted silicon crystals. Analyses were performed using Kratos S1030, Cameca Ims-3f, 4f, 5f and Hitachi IMA-3 instruments. Boron to matrix intensity ratios were measured and Relative standard deviations calculated. Standard deviations were all less than 18% for each individual instrument, even for low concentration samples. Relative sensitivity factors were used to examine the linearity of the SIMS ion intensity ratio to concentration. Calculated values showed a deviations of between 5 and 13% for ten measurements at each lab thus confirming that resistivity reference materials of the type used in the study can be used to evaluate linearity of SIMS instruments. The correlations between SIMS ion intensity ratio and resistivity based concentration was good (linear), and repeatable as determined by the deviation of the RSFs thus a correlation was present and suitable for meaningful analysis. Use of the results to evaluate an unknown using an average RSF value and measured intensities yielded a close agreement (deviation of 6 to 7%) with the resistivity based boron concentration thus the standardizing method was effective [46].

Closer to this study, Yamamoto et. al investigated the repeatability of RSF values for impurities in steel using three different instruments. All three instruments were magnetic sector type the instruments being a Kratos S1030, a VG 1X70S, and an ARL IMMA. These instruments possessed primary beam incidence angles of 59°, 48°, and 0° respectively. NIST standard SRM 600 low alloy alloy steels and VSS standard FXS low alloy steels were analyzed using an O_2^+ primary beam. The measured RSFs for the Kratos (incidence angle 59°) and the VG (48°) exhibited similar periodic trends corresponding to

the ionization potential of the impurity element studied. The RSFs measured for the VG were greater than those for the Kratos due to differences in the spectrometer design and incidence angles. The mean coefficients of repeatability (standard deviation devided by mean) were 7.9% and 20.5% for the Kratos and the VG respectively. Conversely when repeatability coefficients for measurements of boron, phosphorus, and arsenic measured in silicon using the Kratos were 2.7, 1.4 and 1.0 percent. The repeatabilities in steel were significantly worse due to the large sputtered surface irregularity and complicated structure observed on the steel surfaces when compared to silicon. This was considered the main cause of the poor repeatability in the steel samples. This theory was further backed up by the lower coefficients of variation observed for the ARL IMMA results whose samples exhibited a smoother surface topography [47]. Due to this phenomenon repeatability of RSF values between data sets in this study may be variable.

3.4 RELATIVE SENSITIVITY FACTORS VERSUS ENERGY OFFSET: MASS INTERFERENCE EFFECTS

For secondary ion distributions where a molecular interference is present a curve for RSF versus energy offset voltage may be plotted. Since the kinetic energy distribution of molecular ions is generally narrower than that of atomic species a test species suffering from molecular interference will exhibit a more rapid decrease in detected ion current than a noninterfered atomic species as the energy acceptance window progresses up the kinetic energy tail. This will result in an additional variance of the RSF value with energy offset [16]. (Some variance would be likely due to differences in the energy distributions of

different elements.) If the test element suffers molecular interference while the reference element does not this effect will result in a decrease in the RSF value with increased energy offset. Conversely if it is the reference element that suffers molecular interference then an increase in the RSF value of the test element with energy is likely [32].

3.5 BOND BREAKING MODEL

The bond breaking model is an empirical model which links the dependance of secondary ion emission yields to the chemical environment of atoms in a matrix. the model holds true for metals and their oxides flooded with oxygen and for complex silicates subjected to oxygen bombardment. Under such conditions the elemental composition of the specimen controls the ionization yields thus complicating quantitative analysis [48]. The relation is based on the postulation that the ionization of a sputtered atom, M, is controlled by electronic exchanges between the atom, M, and one of its neighbors during a collision which results in the ejection of the atom, M [49]. Here, the atom M, is resident on or near the surface of the specimen and is surrounded with oxygen atoms when it is ejected after a collision with an N atom. If we assume that as the atom M leaves the target it breaks a "bond" with the complex anion A composed of an atom N and the neighboring oxygen atoms, then A^{M}_{N} will be the Ionization Probability of M during this process. If however M is ejected after a collision with another M atom then A^{M}_{M} will be its ionization probability during the bond breaking process with the complex anion A' composed of an M atom and its the surrounding oxygen atoms. If the flux of particles moving inside the target towards the surface and being efficient in the sputtering process has the same

composition as the bulk material then the probability for M to be ejected by an M or N atom are respectively equal to the concentrations C_M and C_N. The total ionization probability is then given by

$$P(M+) = A^M_M \bullet C_M + A^M_N \bullet C_N \qquad (3.5.1)$$

After some modifications to account for different ionization processes, the presence of both energy and angular distributions and the correlated discrimination of secondary ions by the collecting and filtering optics, the ionization probabilities A^M_M and A^M_N may be replaced by ion emission yields P^M_M and P^M_N.

The emission yields are equal to the ratio of the number of emitted M+ ions to the total number of M atoms in the sputtered volume $S_{NM} \bullet C_M$ whose atoms may be ejected as monatomic species or as cluster constituents. In these studies the emission yield, P^M_{NM}, of the species M+ in the matrix MN varied linearly with the bulk atomic concentrations C_M, C_N in accordance with the equation

$$P^M_{NM} = P^M_M \bullet C_M + P^M_N \bullet C_N \qquad (3.5.2)$$

where P^M_M and P^M_N are the M+ emission yields of a pure M matrix and an infinite dilution of M in N respectively under oxygen flooding conditions. At concentrations of C_M less than 5 percent the measured value of P^M_N is essentially correct (based upon the consideration that at these concentrations C_M is less than P^M_N/P^M_M and thus that the emission yield of M+ is P^M_N based on the supression coefficients measured on numerous alloys) [49]. From measurements of the ionic intensities of well defined alloys and pure

metals under identical experimental conditions subjected to Ar+ bombardment Piven, Roque-Charmes, and Slodzian [50] found that the intensities followed the pattern

$$\frac{I(M+)_{NM}}{I(M+)_{M}} = \frac{C^{M}_{NM}}{1} \bullet \frac{P^{M}_{NM}}{P^{M}_{M}} \bullet \frac{S_{NM}}{S_{M}} \qquad (3.5.3)$$

where the sputter yields S_{NM} and S_M represent the total number of sputtered atoms from the binary alloy NM and the pure metal M respectively. The group also verified that for Fe, Ni, and Cr alloys analyzed under oxygen flooding that the ratio of sputter yields was approximately unity, that is S_{MN} was independent of composition and was approximately equal to S_M and S_N. In their investigations Piven et. al. also showed that NiCr and FeCr alloys flooded with oxygen under Ar+ bombardment were covered with an oxide film. Further, an oxide sample of the same NiCr or FeCr ratio sputtered under identical conditions although not necessarily possessing the same stoichiometry due to oxygen depletion in alloys did produce the same emission yield coefficients P^{M}_{M} ,P^{M}_{N}. The Bond Breaking Model accounts for many experimental results on the variation of ionization probabilities with composition of materials [48,50,51,52] and with the mass of isotopes[53]. In all cases the matrix materials tested were oxides or alloys whose surface was covered by a thin oxide layer at oxygen partial pressures sufficiently high to achieve a complete oxygen coverage of the surface. In such cases atomic ionization of atoms involves electronic exchange in transient $M_2(O)_n$ or $MN(O)_n$ clusters [49]. This situation is critical to the accuracy of the bond breaking model, in fact the equation is only valid if oxygen content of the oxides formed is at a maximum, and is directly related to the nature

and content of the metallic species of the sample. In order to achieve this condition and maintain the validity of the model (equation 3.5.3) for metallic materials sputtered by O_2^+ additional flooding is required to saturate the specimen surface and maximize oxygen adsorption (see determination of oxygen saturation plateau in Chapter 4). Without complete oxygen saturation the implanted oxygen content of the sample surface region is a function of the incident ion energy, the sample composition and crystallography of the specimen [49]. Moreover, without oxygen saturation experiments on alloys bombarded with O_2^+ ions showed that the M+ emission yields varied in a nonlinear fashion with concentration, but rather depended more upon the angle of incidence of the primary O_2^+ species with respect to the surface [49].

Later, Piven et al. proved that the bond breaking model could be applied to ternary alloy systems involving Fe, Ni, and Cr the same three major constituents used in the alloys in this study. Here they confirmed the sputter yield ratios $\langle S_{Alloy} \rangle / \langle S_M \rangle$ were close to unity both for the oxygen flooded metals and their oxides [51]. Moreover, the emission yields of Fe+, Ni+, and Cr+ were found to be linear functions of their atomic concentrations in the bulk material. Further, the similarity of the emission coefficients P^M_M, P^M_N, and P^M_Q found in the binary and ternary alloy systems and their oxides (less than a 10% variation) suggest that the emission of M+ ions does obey a binary process determined by independent interactions between M and each type of neighbor M,N, or Q of which the specimen is composed [51]. Hence for a ternary alloy the relationship

$$P^M_{MNQ} = P^M_M \bullet C_M + P^M_N \bullet C_N + P^M_Q \bullet C_Q \qquad (3.5.4)$$

was found to be valid where the values P^M_M, P^M_N, and P^M_Q are similar to those found in binary alloys of M,N,Q suggesting the validity of the assumption of individual contributions of each of the alloy constituents. The model is only valid if the total number of monatomic particles (ionized and neutral) sputtered from the sample surface is approximately constant over the whole range of concentrations studied, otherwise a compensation factor must be applied to the emission yield, P^M, to obtain the true ionization probability [51]. The fact that the ejected particles originate primarily in the inner layers of the specimen may explain the dependance of P^M on the bulk concentration of M,N, and Q. The equation would not be valid if the ionization of M was determined by electronic exchanges with atoms at rest in the surface layer as P^M would depend upon changes in the surface composition due to sputtering effects [49]. In the presence of preferential sputtering due to the presence of atoms of very different masses in the sample, then superficial concentrations determined by added proportionality constants must be used to alter the ionization probability equation [51].

Since the determination of emission yields depends upon the comparison of ionic intensities measured for samples of different compositions, and these intensities are also dependent upon other factors such as the intensity of the primary ion beam, I_p, the collection efficiency of secondary ions, β, and the target sputtering yield , S_{MNQ}, these factors must all be kept constant or be accounted for.

Although, generally the sputtering yield varies with composition as a consequence of changes in the fraction of incident energy deposited in the outer layers and changes in the binding energy of atoms at the sample surface this is not the case in Fe-Ni, Fe-Cr, and Ni-Cr alloys thus simplifying the analysis [49]. In more general cases, the sputter yield

must be measured for each alloy in order to avoid error based on the assumption of the sputter yield being an atomic property being independent of the matrix or composition. For the purpose of analysis in this study the emission yield of an alloy in a multielement system is given by

$$P^M_{MNQ...} = P^M_M \bullet C_M + P^M_N \bullet C_N + P^M_Q \bullet C_Q + \ldots \qquad (3.5.5)$$

This alloy emission yield can be allied in a manner similar to equation (3.5.3) in order to remove the consideration of sputter yields since they are essentially the same for the alloys and major constituents studied [51]. Then (3.5.3) becomes

$$\frac{I(M+)_{MNQ...}}{I(M+)_M} = \frac{C^M_{NMQ...}}{1} \bullet \frac{P^M_{NMQ...}}{P^M_M} \bullet \frac{S_{NMQ...}}{S_M} \qquad (3.5.6)$$

Substituting in equation (3.5.5) gives

$$\frac{I(M+)_{MNQ...}}{I(M+)_M} = \frac{C^M_{NMQ...}}{P^M_M} \bullet \{ P^M_M \bullet C_M + P^M_N \bullet C_N + P^M_Q \bullet C_Q + \ldots \} \qquad (3.5.7)$$

which can be manipulated to yield

$$\frac{I(M+)_{MNQ...}}{I(M+)_M} = C^M_{NMQ...} \{ 1 + \alpha_{MN} C^N_{MNQ} + \alpha_{MQ} C^Q_{MNQ} + \ldots \} \qquad (3.5.8)$$

where the relative emission coefficient, $\alpha_{MN} = P^M_N / P^M_M$. Now this relation holds true for each element in the alloy, therefore if the number of alloys studied is equal to or greater

than the number of elements of interest then the number of equations is equal to or greater than the number of unknowns and a system of equations can be solved to determine the relative emission coefficients.

In recent years, the main proponents of the Bond Breaking Model have moved on to other areas of study. - J.C. Piven has studied diamond and diamond like films, diffusion phenomena, titanium carbides, and nano indentors. In the meantime Slodzian has moved on to study imaging and parallel detection, imaging of human chromosomes, and the "Contribution of the LZS Model to the Understanding of Positive Secondary Ion Emission" [54]. As this study unfolds we may find out why the Bond Breaking Model does not enjoy the popularity of the Relative Sensitivity Factors approach.

3.6 NUMERICAL REGRESSION

Calculation of bond breaking relative emission coefficients and elemental compositions both required the use of a numerical regression technique. In both cases least squares regressions were performed using the solver utility in Microsoft Excel™. This solver uses an iterative process which changes designated cell values to recalculate the worksheet while considering any constraints added and optimize the results in a given target cell - the square of the error in this case. This process stopped when a solution was found to an acceptable precision. The minimum square of the error is found using a derivative of the Newton method.

The method used my Excel™ is that of the Generalized Reduced Gradient (GRG) algorithm [55]. This program first evaluates any constraints given by the user for any

conflicts subsequently incorporating them into the equations to be solved. The basis and gradient functions of the equation set are then calculated. The GRG code then solves the original problem by solving a sequence of reduced problems. These are the minimizations of a number of directional searches corresponding to the number of variables (and the basis) present. These reduced problems are solved by the Broyden-Fletcher-Goldfarb-Shannon (BFGS) gradient method [55,56]. This method calculates a direction vector, d, based upon the local gradient of the function to be solved and initiates a one dimensional search to solve the problem:

$$\text{Minimize:} \qquad F(x+\beta d) \qquad \text{For } \beta > 0$$

Where d = direction vector for direction of descent. This is done by finding three β values A,B,C, which satisfy:

$$0 \leq A < B < C$$

$$\text{and} \qquad F(x+Ad) \geq F(x+Bd) \leq F(x+Cd)$$

Then, the interval [A,C] contains a local minimum of $F(x+\beta d)$. This minimum is approximated by passing a quadratic in β through A,B,C with its minimum at D. The best point B or D is taken as an estimate of the optimal β. This minimum may be refined by a subsequent closer approximation by using optimal β point and the two bracketing points to further fit another quadratic in an iterative process until a preassigned tolerance is met. Once this condition is fulfilled the function to be solved, F(x), is recalculated at the minimum point using the β value and the tangent vector. At this point, a new gradient function and direction vector are then calculated. The new direction vector is used to begin another minimization search in the new direction. This process continues until a

number of iterations equal to the number of unknowns has been performed, or, until the problem converges to a solution of acceptable precision.

3.7 THE ISOTOPE EFFECT: MASS FRACTIONATION

Any quantitative procedure that does not include signal comparison to a standard is susceptible to variation based on the susceptibility of the matrix to surface and bulk element fractionation caused by sputtering and ion implantation effects caused by the primary beam. Here, fractionation in the primary ion implant zone is dependant on the matrix, the element studied, its mobility, electric field gradients arising from surface charging, and upon the chemical nature of the primary species [32]. Studies of many different samples suggest that this phenomena is not a threat to experimental accuracy in most instances, however, some situations have been noted where anomolous effects have been observed and mass fractionation was considered a reasonable explanation.

3.8 INSTRUMENTAL EFFECTS

As the SIMS instrument is by nature a rather complex analytical instrument there are a number of effects or parameters which are characteristic of a given SIMS instrument that may effect quantitative analysis using the said instrument. These effects include [32,57]:

- Uniformity of primary ion current density
- Consistency of primary ion current

- Primary beam impurities
- Charging of insulators (not applicable in this investigation)
- Memory Effect
- Peak interferences
- Mass dependant transmission and detector efficiency
- Counting Losses
- Dynamic Range
- Minimum detectable concentration
- Consistent oxygen flooding pressure
- Residual gas impurities

By performing impirical quantitative analysis rather that applying a totally theoretical model, and by keeping count rates below 10^6 counts per second and performing complete analysis under identical operating conditions many of these effects can be reduced or removed.

3.9 STATISTICAL AND SYSTEMATIC ERRORS

Statistical and systematic errors can be divided into two categories - those that effect the repeatability or precision of a result and those that effect the accuracy of a result. Precision or what is commonly referred to as the degree of scatter in a series of results is largely influenced by a number of factors including [1]:

- Sampling error associated with sample homogeneity, grain orientation

- Fluctuations in electrode voltages
- Instability in electron multiplier gain
- Secondary ion signal strength
- Sample holder vibration

Accuracy is not a measure of the degree of scatter in a series of results - it is rather, a measure of how closely the grouping of results reflects the actual value to be determined. Sources of error which effect the accuracy of a series of data include [1]:

- Erroneous meter reading or recording
- Incorrect model coefficients or calibration curves
- Confusion of samples

3.10 A PROMISING NEW MODEL

Since the inception of this project a new model has gained momentum and popularity for predicting the composition of an unknown specimen. This model, known as the "Infinite Velocity Model", extrapolates secondary ion yield via a modified or "corrected" intensity versus kinetic energy data to a point at which the velocity is infinite. This process is followed because matrix effects are theoretically and empirically shown to be removed at this velocity limit as the secondary ion yield per unit concentration of all elements becomes the same. The model requires no calibration materials or sputter yield measurements in order to determine the concentrations of major and trace elements in a conductive or made to be conductive sample. Under these conditions the relative concentration per unit volume is given by

$$C_e = i_e / \Sigma i_{x,y,z}$$

where all i are the corrected secondary ion intensities for e, the element of interest, and the matrix elements x,y,z. Corrected intensity values are obtained by dividing measured intensities by the instrument transmission function, and the relative isotopic abundance, and by correcting for the sputter yield. [58,59,60,61,62].

CHAPTER 4

EXPERIMENTAL METHODS

4.1 SAMPLE PREPARATION

All reference elements used in this study were certified at 99.99% pure or better. The said samples were prepared for analysis by mounting in bakelite, followed by grinding on silicon-carbide paper and final polishing using 0.1 μm diamond grit. Grinding was performed using 180, 320, 400, and 600 grit silicon-carbide paper using water flush. Grind direction was rotated by 90° with each subsequent paper grade in order to ensure removal of all remnants of the previous step.

Final polishing was performed on a napped cloth using 1μm diamond paste and varsol lubricant. The polished samples were washed with soap, rinsed thoroughly with distilled water then acetone to remove contamination.

4.2 SAMPLE ANALYSIS

All samples were analyzed using an O_2^- primary ion beam and measuring positively charged secondary ion spectra. Primary beam currents ranged from 39 to 175 nA for all analyses while the alloys studied were done so using primary currents of 108 to 175 nA. The primary ion beam was rastered over a 250 μm square area, and the analyzed area was limited to 150 μm in diameter by the transfer optics with a contrast aperture setting of 3 and a field aperture of setting of 2.

A 5 eV energy window was used to collect data at energy offsets of from the energy distribution peak of 0, 40, 80, 120, and 160 eV respectively. Elements analyzed were Mo, Nb, Fe, Ni, Cr, Mn, Cu, Si, and Ti. Secondary ion counts were measured using an electron multiplier. A minimum of 17 data points were measured and averaged for alloy specimens and 15 for pure metals. In the case of less intense signals such as pure Ni the number of measurements taken was increased to a number as high as 37. Count rates were kept below 10^7 in order to prevent non-linear dead time losses in the detector. All specimens were analyzed after the secondary ion signal had reached sputtering equilibrium conditions. That is, a time period was allotted to allow the primary beam to sputter through layers of surface contaminants and the prior surface oxide. Further, this time period was sufficient to allow the sputter front to catch up with the implant front and to obtain a more consistent secondary ion signal without perturbations usually associated with the beginning of a new analysis site. Sample chamber pressure was maintained at 2.9×10^{-7} torr with a partial pressure of oxygen of 1.4×10^{-7} torr as determined for oxygen saturation conditions (section 4.3). Under these conditions oxygen saturation was present and uniform reproduceable secondary ion intensities were measured.

4.3 OXYGEN PLATEAU DETERMINATION

After start-up the SIMS instrument was optimized for primary and secondary beam alignment and focus. The instrument was allowed to settle into steady state conditions with NBS standard D 850 in the chamber (for a complete description of the standards used refer to chapter 4.6.) . The steady state count rates for iron and nickel were measured

at energy offsets of 0, 80, 160 eV from the secondary ion energy distribution peak. The elements iron and nickel were chosen as iron is the main constituent in the alloys studied, and nickel the major element which requires a higher oxygen partial pressure to reach the saturation plateau when compared to chromium [63]. Nickel also generally possesses a relatively low positive ion yield when compared to the other major elements present [26].

Prior to investigation of oxygen flooding conditions the specimen surface was scanned and the elemental count rates monitored until surface oxides were completely removed from the specimen surface and count rates stabilized. Residual oxygen pressure (PO_2) was then increased via flooding with oxygen of 99.999% purity through a needle admit valve opened incrementally by 1/8 of a turn. This introduced oxygen into the sample analysis chamber via a capillary tube. After each increase in oxygen pressure the elemental count rates were allowed to reach equilibrium before readings were taken. This procedure was continued as the count rate increased with PO_2 until increased PO_2 pressure no longer yielded an increase in elemental count rates for both elements. At pressures above the saturation plateau count rates begin to drop as residual pressure in the chamber is such that oxygen flooding atoms begin to interfere with the sputtering and collection processes.

4.4 ENERGY WINDOW CENTERING AND STANDARDIZATION OF ANALYSIS CONDITIONS

All experimental results were measured on the SIMS instrument consecutively. No other analyses were performed between the samples in this report. Hence there was no disruption in settings used. Initial alignment and energy window centering was performed

on NBS sample D850. When not in use the SIMS instrument was left running with only the primary ion beam turned off. Upon restart the primary beam intensity was maximized by optimization of the duoplasmatron source and only minor changes to the primary beam settings achieving similar primary, secondary beam currents. Energy window centering was checked using specimen D850, and the iron distribution. The only changes between analyses were minor changes commonly used to correct for instrumental drift.

Each secondary ion distribution was examined and energy offsets used were in standard increments from the energy peak for each elemental distribution. Each such peak was centered in the energy window to maximize secondary ion signal for the element. All analyses were performed under similar instrumental settings and analysis conditions. Partial pressure of oxygen and total pressure of oxygen were also monitored to ensure that each analysis was performed under similar conditions within the oxygen saturation plateau.

4.5 DATA ANALYSIS

Each specimen was analyzed at energy offsets of 0, 40, 80, 120, and 160 eV from the peak intensity in the secondary ion distribution for that element. All readings of intensity used in this study were taken after the beam had settled down from surface effects and each intensity value used is the average of at least 15 data points recorded as noted earlier. The data points were measured with the electron multiplier by cycling between the elements studied. Here, a wait of 1 to 1.5 seconds was allowed for secondary ion beam, magnetic sector settling before an accumulation time of 1.0 seconds was allowed for each element.

Collected data was corrected for relative isotopic abundance, and normalized to the primary ion current as discussed in Chapter 5 of this report. Data manipulation was performed using Microsoft Excel.

4.6 COMPOSITION OF ALLOYS

The alloys used in this investigation were all spectrographic stainless steel standards of certified homogeneity and composition. The standards, certified by the National Bureau of Standards under the U.S. Department of Commerce are composed of predominantly iron, and certified quantities of Mn, Si, Cu, Ni, Cr, Mo, and Nb. In addition the elements Ti, Ta, W, V, and Sn are present in very low but uncertified concentrations. These compositions are not certified due to minor irregularities in the samples observed during homogeneity testing and because the values are the analytical results of a single laboratory.

The concentrations indicated for certified elements are averages of the results of chemical analyses made by the National Bureau of Standards, the Armco Steel Corporation (Research labs and the Rustless Division), the Wilbur B. Driver Company, and the Allegheny-Ludlem Steel Corporation. Tables 4.1, 4.2 list the elements present in each standard, and their certified concentration.

Alloy #	Mn	Si	Cu	Ni	Cr	Mo	Nb
D 845	0.78	1.03	0.06	0.27	14.23	0.53	0.066
D 846	0.53	2.34	0.16	8.55	19.45	0.25	0.36
D 847	0.23	0.73	0.17	12.47	25.19	0.034	0.018
D 849	1.65	1.35	0.18	6.29	5.88	0.087	0.19
D 850	-	0.24	0.32	23.99	3.26	-	0.031

Table 4.1: Certified Elemental Compositions Of Alloys (In Atom Percent) [64]

Alloy #	Ti	Ta	W	V	Sn
D 845	0.035	6.14 e-6	0.13	0.055	-
D 846	0.39	0.0091	0.012	0.033	0.0093
D847	0.023	6.1 e-6	0.018	0.033	-
D 849	0.13	0.065	0.058	0.011	0.033
D 850	0.059	6.28 e-6	0.065	0.0067	0.043

Table 4.2: Non-Certified Elemental Compositions Of Alloys (Atom Percent) [64]

4.7 SELECTION OF ISOTOPES FOR INVESTIGATION

Not all isotopes studied in this investigation are the most abundant for the elements in question. In some cases the isotope counted is a relatively minor one in order of abundance. Mass interference's from other elemental isotopes, oxides, hydroxides, and multiply charged or polyatomic species must be avoided. Secondary ions from another element or compound may complicate the quantitation process if their mass-charge ratio is similar to the isotope being studied. In this case a superposition of count rates will occur thus distorting quantitative results. At this point several options are available: analysis using high mass resolution to separate the interference, analysis using energy offsets to remove polyatomic secondaries, peak stripping, or a prudent selection of isotopes studied.

Analysis using high mass resolution is time intensive, requires fine tuning of apparatus, and produces uninterfered data at the cost of high count rates. Similarly, use of an energy offset for collecting secondary ions will reduce mass interference from low energy polyatomic secondaries of similar mass-charge ratio. Again, this is at the sacrifice of high count rates for the element studied.

Peak stripping is the process of approximating the number of counts caused by an interfering ion based on an isotopic ratio to a non-interfering peak caused by that ion. That approximate number of counts is then subtracted from the data recorded for the elemental isotope of interest in order to attempt to remove the mass interference effect by eliminating the superposition of the peaks. This process is tedious, approximate, and dependent on the presence of a peak of sufficient count rate for the interfering isotope which itself is not under any external influences.

In order to minimize unnecessary labor and maximize quantitative accuracy, it is essential to judiciously select isotopes studied prior to analysis. To this end, the use of other techniques which complicate analyses may be minimized or avoided.

In this study a chart of all common oxides, hydroxides, diatomic ions, and multiply charged ions was constructed to aid in the selection of isotopes studied. This chart both increased the efficiency of isotope selection, and avoided oversight of potential interference's. Table 4.3 lists the elements studied, the isotopes used, and their relative abundance.

Element	Isotopic Mass	Isotopic Abundance (%)*
Fe	56	91.72
Cr	52	83.789
Mn	55	100
Mo	100	9.63
Nb	93	100
Ni	62	3.634
Si	30	3.10
Ti	46	8.0

Table 4.3: Isotopes And Relative Isotopic Abundance Of Elements Studied [65]

NOTE TO USERS

Page(s) not included in the original manuscript are unavailable from the author or university. The manuscript was microfilmed as received.

UMI

CHAPTER 5

RESULTS AND DISCUSSION

5.1 CORRECTION FOR RELATIVE ISOTOPIC ABUNDANCE

As many elements posses one or more isotopes, this fact must be accounted for during quantitative analysis. Firstly, the choice of isotope studied in analysis must be made with respect to consideration for mass interferences from other elemental isotopes, oxides, hydroxides, and multiply charged or polyatomic species. Secondly the isotope chosen should be detectable with sufficient intensity to allow reliable data collection for quantitative analysis. The data collected must then be corrected for the relative abundance of the isotope used. That is the count rate must be divided by the fraction of the element that naturally occurs as that particular isotope:

$$\text{Corrected Intensity} = \frac{\text{Measured Intensity}}{\text{\% Relative Isotopic Abundance}} \times 100\,\%$$

5.2 CORRECTION FOR VARIATIONS IN PRIMARY ION BEAM CURRENT

Due to the nature of the duoplasmatron ion source used in this analysis, the primary .ion beam current will vary slightly over time. For quantitative analysis this fact must be considered during data manipulation. To this end, the primary ion beam current was measured both prior to and after each analysis of each individual specimen analyzed.

For each such specimen the measured values were averaged to yield a mean ion beam current used for determining the average elemental intensities measured. As total yield is known to vary linearly with primary beam current given a constant sputter yield for a sample, the measured intensities for each pure elemental isotope were normalized to that measured for a 100 nA primary beam current using the equation:

$$\text{Normalized Yield} = \frac{\text{Measured Yield}}{\text{Primary Beam Current (nA)}} \times 100 \text{ (nA)} \qquad \text{Cps}$$

This manipulation allows scaling of relative count rates under uniform analysis conditions for different samples to allow direct comparison. The result is a more accurate interpretation of the concentrations of each element present in a given sample.

5.3 OXYGEN SATURATION PLATEAU DETERMINATION

Determination of the oxygen saturation plateau was accomplished using the method outlined in section 4.3 of this report. Figure 5.3.1 is a graphical representation of the effects of this yield enhancing phenomenon. The figure illustrates that elemental count rates for both iron and nickel measured at energy offsets of 0, 80 and 160 eV respectively from the secondary ion energy distribution peak. These measurements all increase uniformly with the partial pressure, PO_2, measured as oxygen flooding was increased in the sample chamber. All measured intensity curves increased in an approximately parallel and consistent manner for both elements at all ion energies monitored. At the initial

chamber PO_2 partial pressure of 6.0×10^{-9} torr the measured ion count rates were uniform at a base level, above this pressure the count rate began to increase with PO_2. This increase in count rate continued with partial pressure, PO_2, until this pressure reached 2.0×10^{-8} torr. Above this pressure only a slight increase in count rates was recorded with an increase in PO_2. Increased flooding was continued until the partial pressure PO2 was 1.6×10^{-7} torr, and the total pressure 4.0×10^{-7} torr. At this point no further pressure increases were performed as the saturation plateau determined to this point spanned a pressure range sufficiently wide for sample analysis and no desire was present to corrupt the vacuum in the system. The oxygen saturation plateau was thus determined to span from a PO_2 range of approximately 2.0×10^{-8} to 1.6×10^{-7} torr which was present over a range of total pressure which varied from 6.3×10^{-8} to 4.0×10^{-7} torr total pressure. For the experiments performed in this study the partial pressure PO2 was maintained at approximately 6.6×10^{-8} torr and total pressure at 2.0×10^{-7} torr.

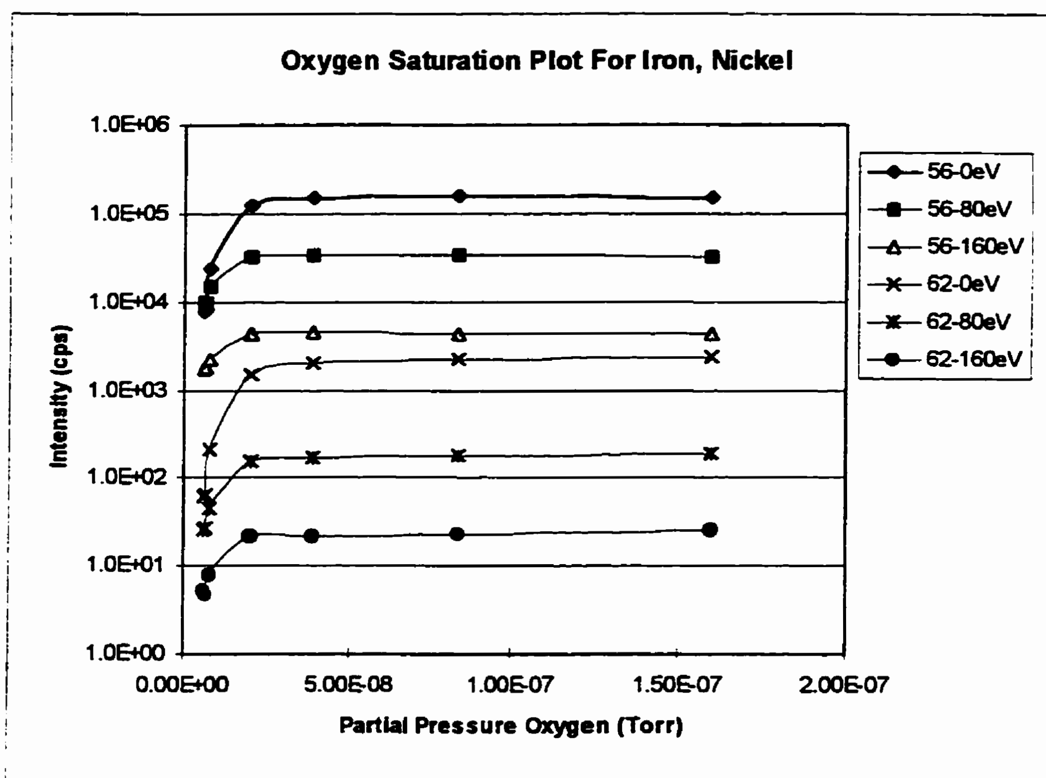

Figure 5.3.1: Oxygen Saturation Plot For Iron and Nickel
Atomic numbers 56 and 62 respectively

5.4 IONIC INTENSITY MEASUREMENTS FOR ALLOYS AND PURE METALS

Plots of measured intensity versus secondary ion energy offset are not included for the sake of brevity. Tables of intensities after correction for relative isotopic abundance and primary ion beam intensity are however provided in Appendix A for consultation.

5.5 RELATIVE SENSITIVITY FACTORS RESULTS

5.5.1 Validity of Relative Sensitivity Factors Determined

Values of Relative Sensitivity Factors (RSF's) determined in this study cannot be directly compared to published values since, to the knowledge of the author, no analyses of certified NBS standards similar to the ones used in this study has been performed using a Cameca IMS-3f. Newbury et. al. studied a low alloy series of Standard Reference Materials (SRM 661, 662, 663, 664, 665) using an IMMA microprobe [66]. These materials typically contained approximately 94 atomic percent iron with the balance of the material consisting of carbon, manganese, silicon, copper, nickel, chromium, vanadium, molybdenum, tungsten, cobalt, titanium, aluminum, niobium, tantalum, and zirconium. Alloying elements were present in the range of from 0.01 to 1.87 atomic percent. Here, analysis was performed using an 18.5 KeV $^{16}O^{+}_{2}$ primary ion beam at a beam current of 5 nA in a chamber with vacuum pressure on the order of 10^{-4} Pa. The samples studied were certified homogeneous on a macroscale but not on a microscale. Concentration gradients for some elements were found on a micrometer scale but analysis was performed by scanning a 250 μm square area with the ion beam to minimize error. The standard reference material 662 was used to determine Relative Sensitivity factors which were in

turn used to approximate the composition of the remaining alloys. In Newbury's study most of the relative errors measured against the certified composition of the studied specimens were less than 50 percent. In some cases relative errors greater than 100 percent were measured, these were attributed to vacuum conditions or inhomogenieties in the specimens. Newbury did conclude that even with well characterized materials and a careful technique that relative errors of calculated composition of 50 percent could be expected.

The Relative Sensitivity Factors calculated by Newbury [66] with respect to iron are presented along with those calculated with respect to iron for specimen D845 in this study (at 0 eV offset) for comparison in Table 5.5.1. Given the differences in sample composition between specimen D845 and Newbury's SRM 662 and in analysis conditions the similarity in Relative Sensitivity Factors is surprisingly good. This close agreement suggests that the values measured are acceptable and are indeed valid. The relative sensitivity factors calculated from this study are listed as specimen D845 and S845 (which represents the data generated based on the second set of analyses performed on the samples). It can be seen that the RSF's calculated for both days differ somewhat from day to day illustrating the limited accuracy of the RSF model, however the values generally agree with each other and are similar to those of Newbury et al. The largest discrepancy in RSF values occurs for the element titanium. This may be due to the lower titanium concentrations present in the specimens and the resulting secondary ion intensities measured. This observation is particularly true for energy offsets greater than 40 eV as the measured titanium signal intensity drops off rapidly with energy offset.

Of note is the fact that comparison of the RSF's calculated from the two data sets of this study at an energy offset of 80 eV from the secondary ion peak shows that although they are not necessarily as close to the values measured by Newbury (which is not really expected) they are however in closer agreement with one another than those measured at 0 eV. More on this will be discussed in the next section.

Element	Composition At. %		SRF's At 0 eV Offset			SRF's At 80 eV Offset		
	Newbury	D 845	Newbury	D 845	S 845	Newbury	D 845	S 845
Si	0.77	1.029	0.24	0.19	0.23	-	0.45	0.33
Ti	0.097	0.035	5.8	3.56	21.20	-	2.19	9.38
Cr	0.32	14.231	2.1	2.46	2.84	-	1.54	1.68
Mn	1.05	0.779	2.0	2.77	3.66	-	1.31	1.58
Ni	0.56	0.265	0.51	1.35	4.74	-	0.44	0.45
Cu	0.44	0.057	0.79	1.08	1.84	-	0.26	0.32
Mo	0.035	0.533	0.38	0.075	0.084	-	0.29	0.27

Table 5.4.1: RSF Values From This Study And From Newbury et. al. [66]

5.5.2 Relationship Between Relative Sensitivity Factor Values And Secondary Ion Energy

Calculated Relative Sensitivity Factors were plotted versus Energy Offset for each alloy for each data set collected. Examples of such distributions are given in Figures 5.5.1 and 5.5.2. A full set of plots of RSF's calculated with respect to the five major elements present in the alloys (Fe, Cr, Ni, Mn, and Si) are provided in Appendix B. Examination of the full data set reveals several trends.

Relative sensitivity factor curves plotted for a particular element combination consistently exhibited a similar curve shape versus energy for all alloys examined even though the actual values differed. This characteristic curve shape was consistent not only from alloy to alloy but also across both sets of data measured thus indicating reproducibility. Generally, RSF curve shapes with respect to secondary ion energy were observed to be almost identical even though there was some difference in measured values for the two sets of data collected on different analysis days (some variation in curve shape was observed in curves associated with less intense signals measured). This characteristic curve shape is determined by the characteristic secondary ion energy distributions and relative intensities of the two elements being ratiod and thus is an intrinsic property of the alloy combination for a given SIMS instrument.

Although the general curve shape is consistent, the actual values on the curve and the curve slope will change depending on the relative alloy composition as this affects the relative intensities of the two characteristic intensity distributions. The relative position of the RSF curves with respect to each other was also observed to change with sample composition confirming that RSF's are valid only over a small composition range. Again,

even though the relative positions of the RSF curves change with composition the curve shapes with respect to energy remain essentially constant over the range of compositions studied.

RSF values for any given element combination when plotted against secondary ion energy offset appear the most stable (exhibit the least variation between energies) in the intermediate energy range of 80 to 120 eV offset from the distribution peak. This trend appeared consistent for any element combination. The RSF curves tended to vary the most between zero and 40 eV offset from the distribution peak. In fact the RSF values calculated at 0 eV offset were often quite different than those calculated at other energies. This change in RSF value may be attributed to many factors including a difference in secondary ion energy distributions, mass interferences not accounted for, and error in location of the distribution peak in the energy window. Due to the rapid drop in intensity on the low energy side of the ion distribution peak even a relatively small change in energy window positioning (for a narrow energy window) will have a pronounced effect on the measured ion intensity and consequent RSF value. Any of these phenomena are good reason to choose an energy offset greater than zero for determination of RSF values.
While many RSF values tended to be quite stable at energy offsets greater than 40 eV some did vary over the entire energy distribution measured. In these cases the RSF values did tend to do so less above the 40 eV range also, again suggesting a reduced error associated with using measured intensities and RSF's in the intermediate energy range to calculate elemental compositions of unknowns. At energy offsets of 160 eV some variation of RSF values from the more stable values measured in the intermediate energy offset range was also observed, particularly in less abundant elements in the alloys. This is

attributed to statistical variations in measured intensities arising from low count rates measured for the less abundant elements. Since these elements are not present in large quantities and count rates drop off at the high energy tail of the elemental ion energy distribution the count rates are low and variable thus the statistical relevance of the measured count rate to the elemental composition becomes suspect as would the measured RSF value.

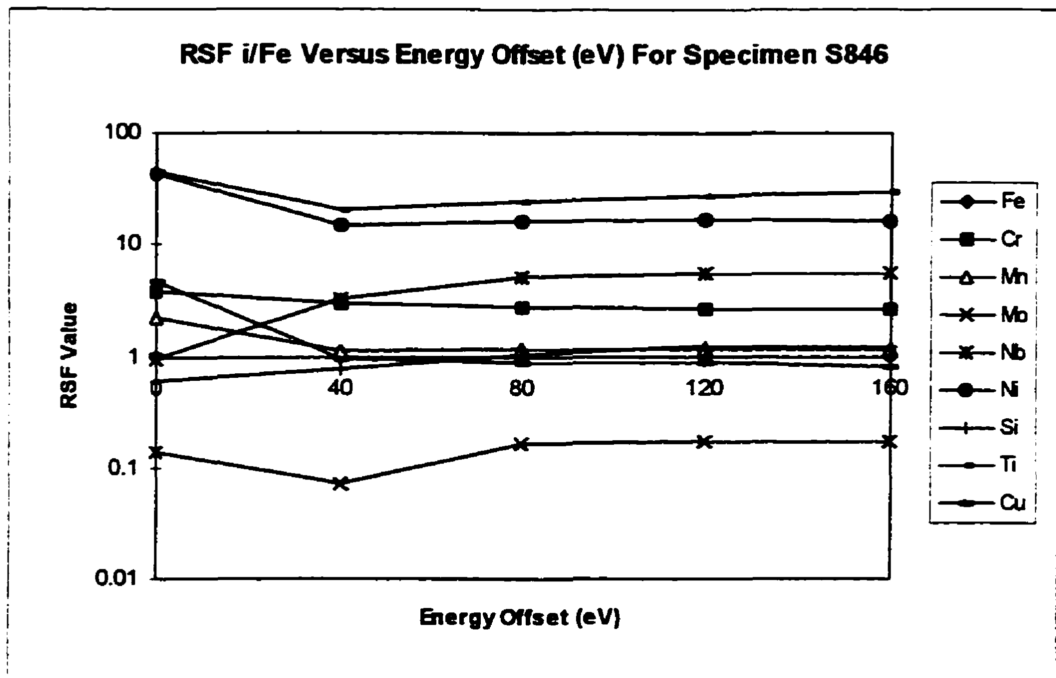

Figure 5.5.2.1: Relative Sensitivity Factor Values Versus Energy Offset For Alloy S 846 Ratiod Against Iron

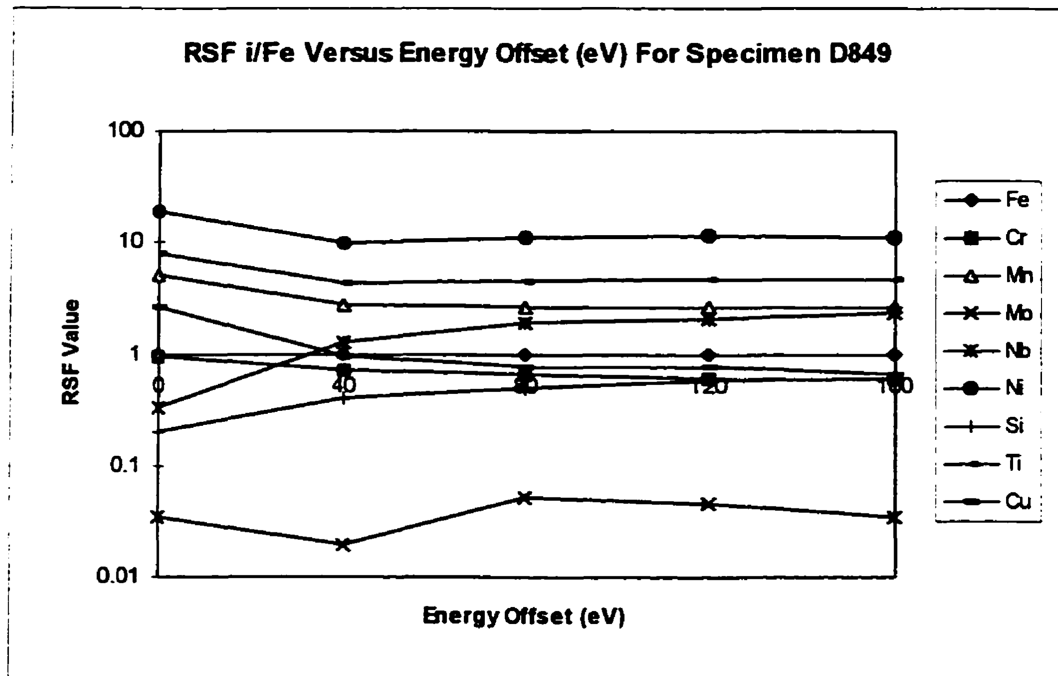

Figure 5.5.2.2: Relative Sensitivity Factor Values Versus Energy Offset For Alloy D 849 Ratiod Against Iron

5.5.3 Specimen Composition Prediction Using Calculated Global RSF Values

An average global set of RSF values was calculated by averaging RSF values, R^i_{Fe} measured for each element across all alloys of each data set at each energy offset. The result is a set of RSF values which average the RSFs measured for a variety of compositions at any given energy offset. Such a set of RSF values may be used for initial composition prediction for an alloy of totally unknown relative elemental compositions using the measured ionic intensities of that alloy.

Calculated global RSF values (illustrated in Figure 5.5.3.1) were in turn used to predict the composition of each of the alloys studied using the two data sets of measured intensities and equation (3.3.11). Figure 5.5.3.2 illustrates the variation of the predicted composition of alloy D847 with energy based upon calculations with the global RSF values. This figure reveals that there is indeed some variation present in the predicted composition of the sample based upon RSF value variations with energy. It is rather difficult to interpret the effect of secondary ion energy selection upon accuracy of quantitative results by examination of figures such as figure 5.5.3.2 alone. For this reason, the relative error in the predicted composition of each element in specimen D850 was plotted versus energy for each element in the sample.

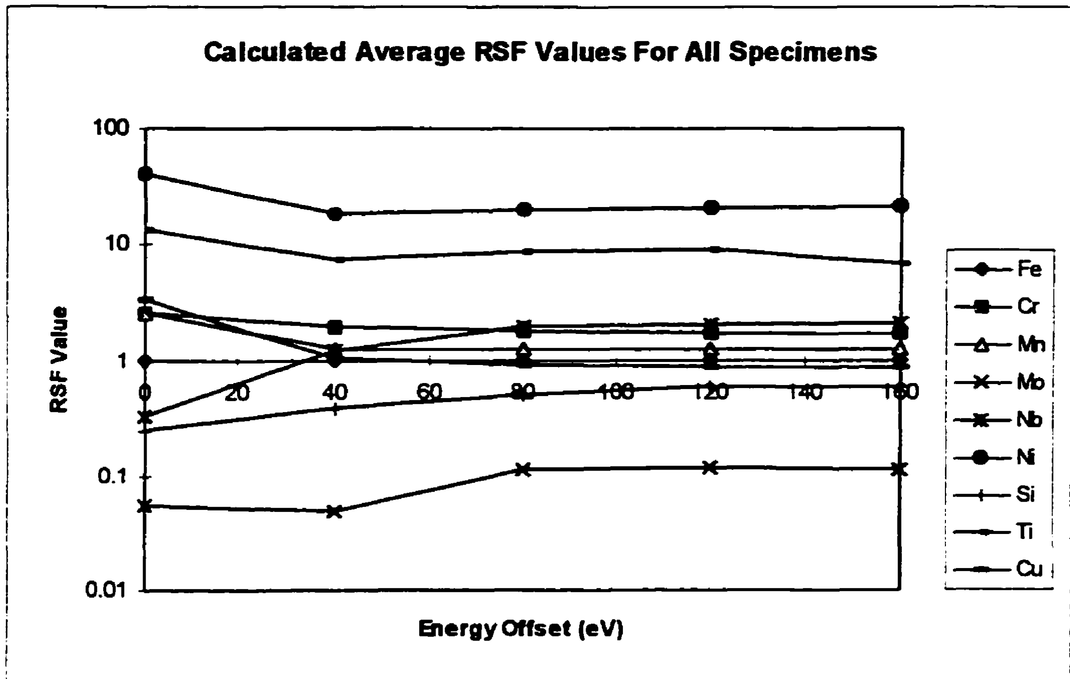

Figure 5.5.3.1: Calculated Average Global RSF Values Versus Energy Offset

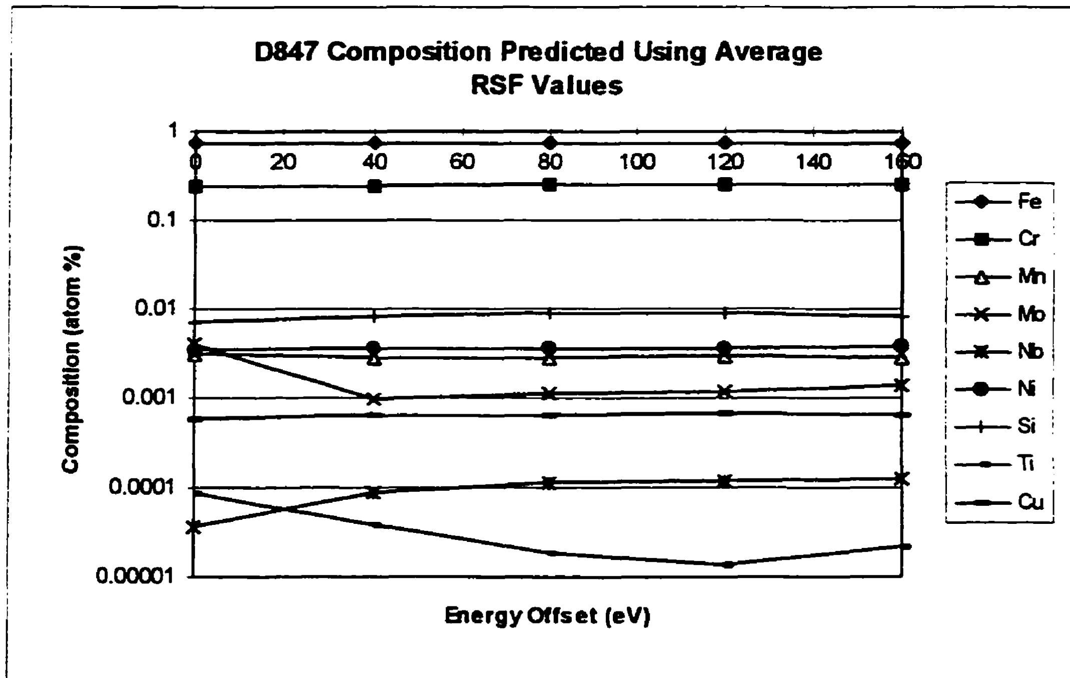

Figure 5.5.3.2: Predicted Composition of D847 Using Average Global RSF Values

For comparative purposes, figures 5.5.3.3 to 5.5.3.7 contain plots of error in the predicted composition of specimens D845, D846, D847, D849 and D850 respectively (for the first data set collected). A full set plots of both predicted composition of all alloy specimens and error in predicted composition are available for both data sets in Appendix B. Relative error values calculated are based upon the equation

$$\text{Rel. Error} = \frac{\text{ABS(Calculated Comp. - Actual Comp.)}}{\text{Actual Composition}} \qquad (5.5.3.1)$$

where compositions are measured in atomic percent. For further ease of analysis, plots of the sum of the relative errors of the elements versus energy offset were generated. In these graphs the sum of the error associated with each of the 3 major elements present (Fe, Cr, Ni) was plotted as was the sum of the squares of the error. The sum of error and sum of squares of error for the five most abundant elements (Fe, Cr, Ni, Mn, Si) are similarly included. Figures 5.5.3.8 and 5.5.3.9 illustrate such curves. A full set of sum or error plots for both data sets is included along with all other RSF data plots in Appendix B.

Examination of graphs of the relative error in calculated composition using the global RSF values versus energy offset reveals characteristic trends, both for individual elements and for the data as a whole. Examination of all alloys for both data sets reveals:

- Error in Fe content was essentially constant regardless of energy offset except at 0 eV where the error was more irregular, but not consistantly better or worse
- Error in Cr content was slightly variable, especially at 0 eV. Error tended to drop with energy offset in data set 1, while dropping only in the 40 to 80 eV offset range for data set two.

- Error in Ni content was essentially constant
- Error in Mn was variable at 0 eV energy offset but otherwise exhibited only a minor improvement in error in the 40 to 120 eV offset range compared to other energies
- Error in Si content prediction was variable at 0 eV with respect to the rest of the error curve. Some improvement in error was observed in the 80 eV offset range in data set 1 while data set two exhibited no clear trend with energy.
- Error associated with Mo content prediction was also variable at 0 eV, again showing some improvement in error in the 48 to 80 eV energy offset range
- Error in predicted Nb content decreased slightly with energy in data set 1. In data set 2 error was a maximum at 0 eV and a minimum in the 40 to 120 eV range
- Ti and Cu content error was essentially constant with energy offset, a mild improvement in error was observed in the 40 to 120 eV range of data set 1 for both elements

In general all relative error values were less than 1 with the exception of those for Mo and Mn. Error in predicted Mo content was consistently high while the Mn error value was high only for specimen D850. Mo content was quite small, thus accounting for increased error as will be seen in section 5.5.4. Error was observed to be highly variable at 0 eV with respect other energy offsets for many given elements when compared from alloy to alloy. For the given element 0 eV results were superior for one alloy , then inferior for the next - no consistent pattern was observed. For the majority of elements at energy offsets greater than 0 eV, error was essentially flat with energy offset, exhibiting only a minor improvement in the mid energy offset range.

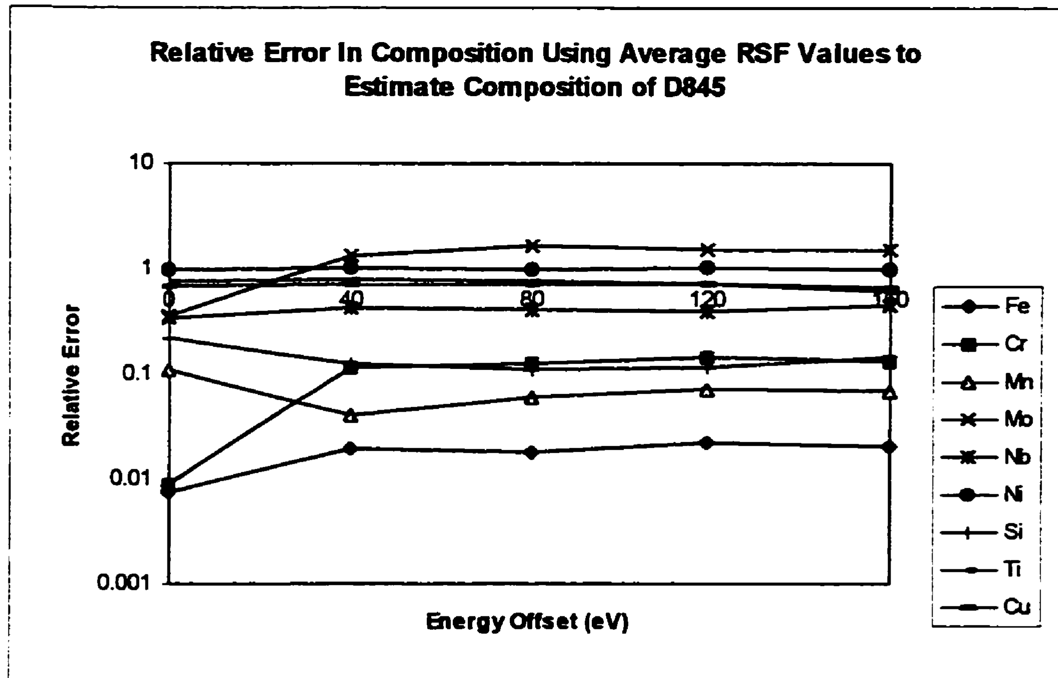

Figure 5.5.3.3: Error In Predicted D845 Composition Using Global RSF Values

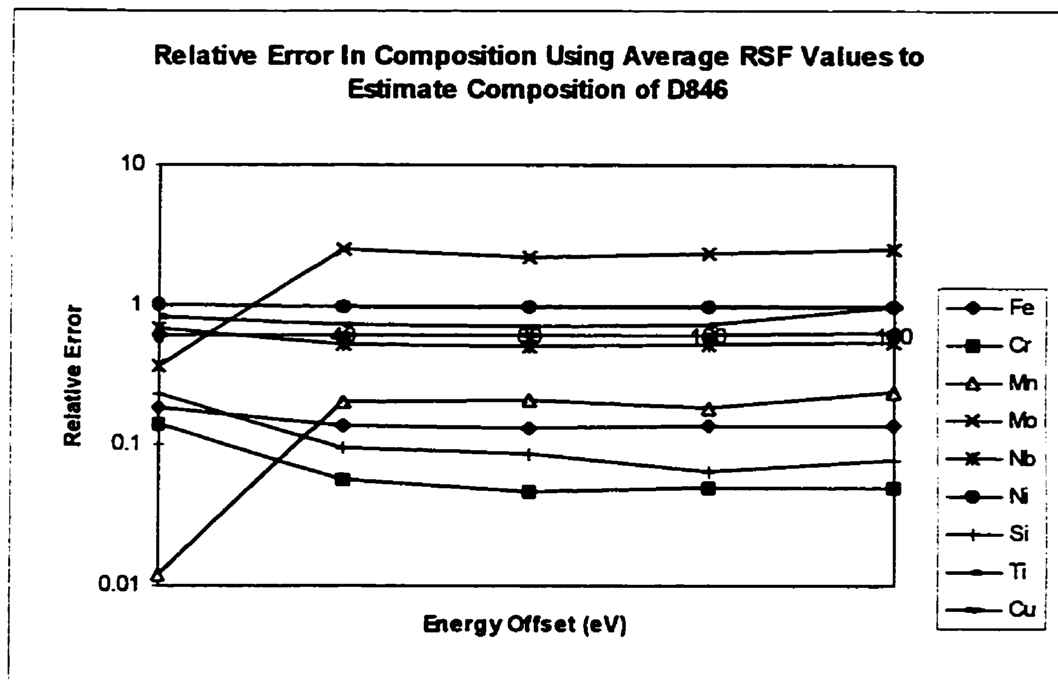

Figure 5.5.3.4: Error In Predicted D846 Composition Using Global RSF Values

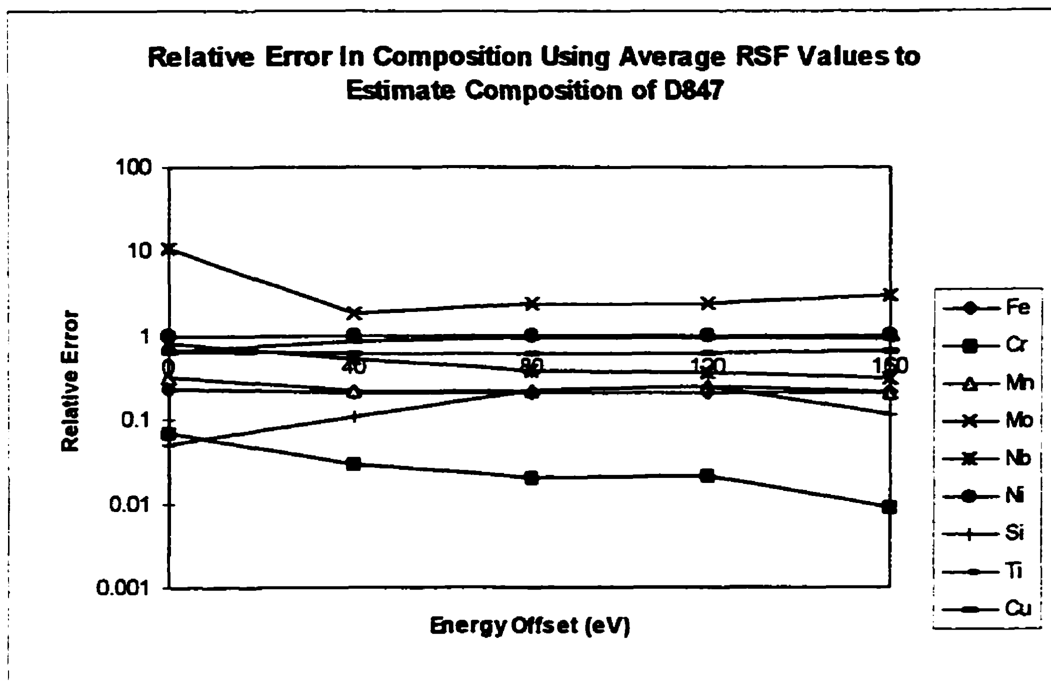

Figure 5.5.3.5: Error In Predicted D847 Composition Using Global RSF Values

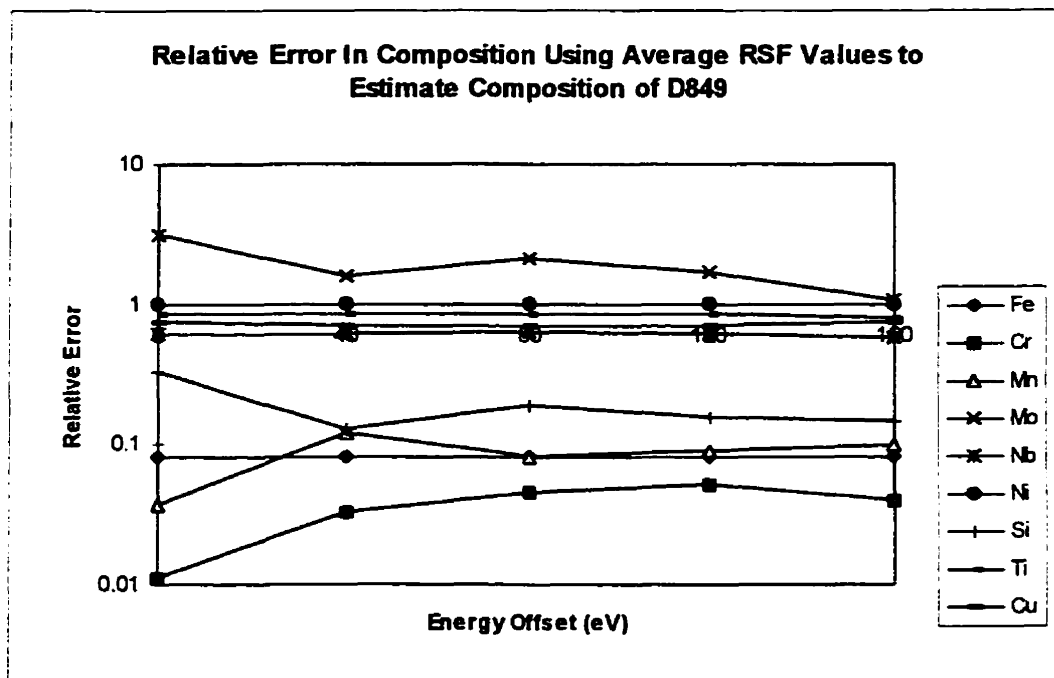

Figure 5.5.3.6: Error In Predicted D849 Composition Using Global RSF Values

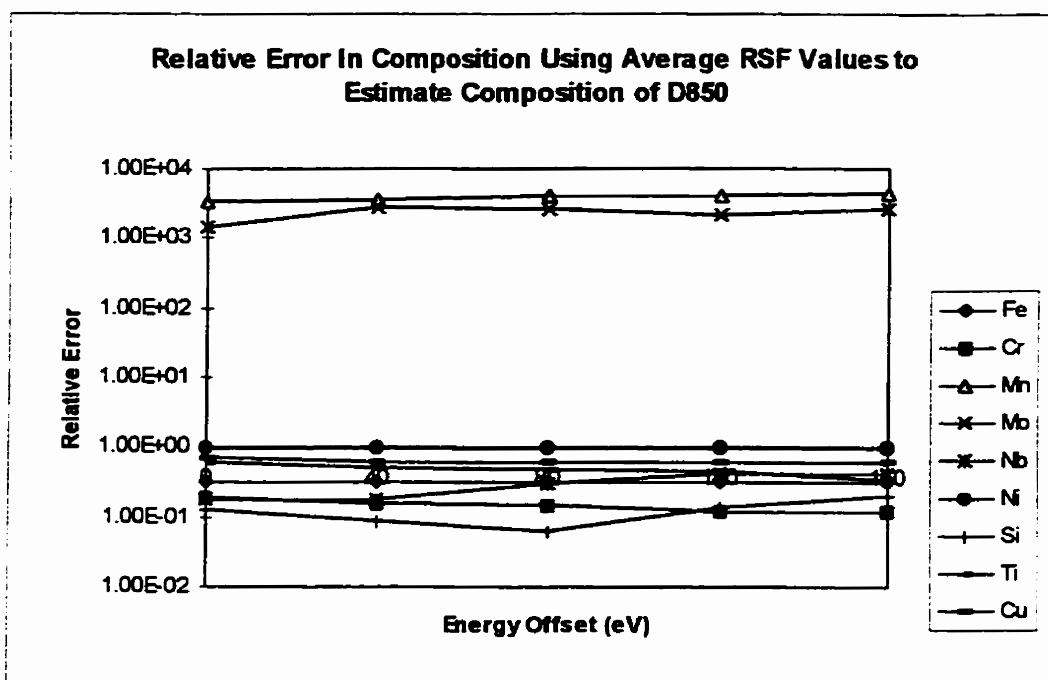

Figure 5.5.3.7: Error In Predicted D850 Composition Using Global RSF Values

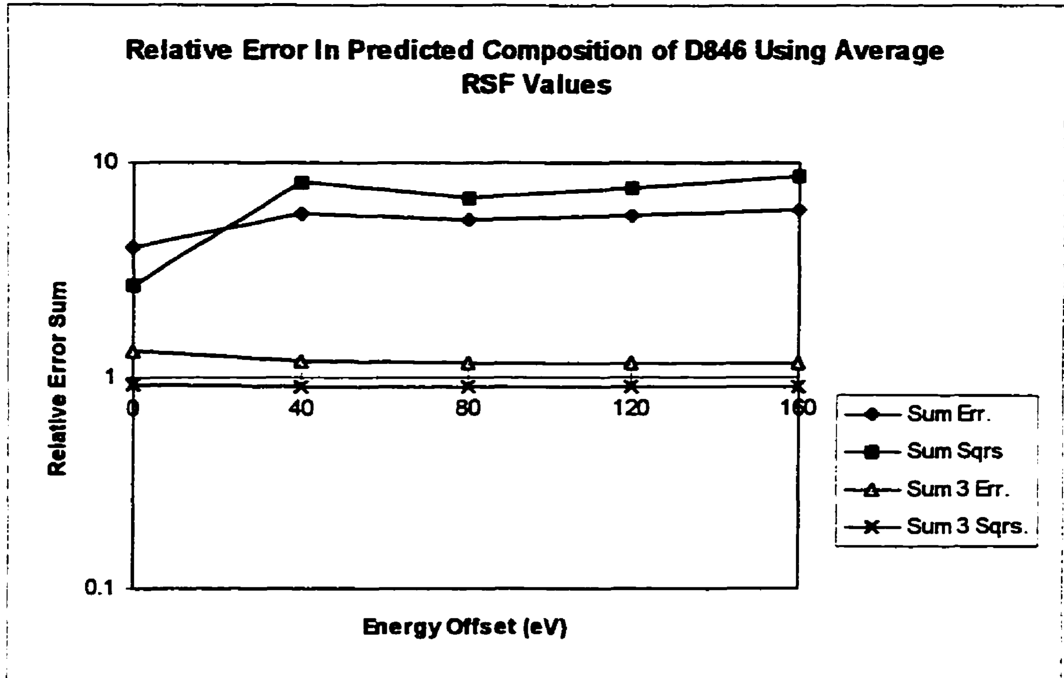

Figure 5.5.3.8: Sum of Error In Predicted Composition of D846

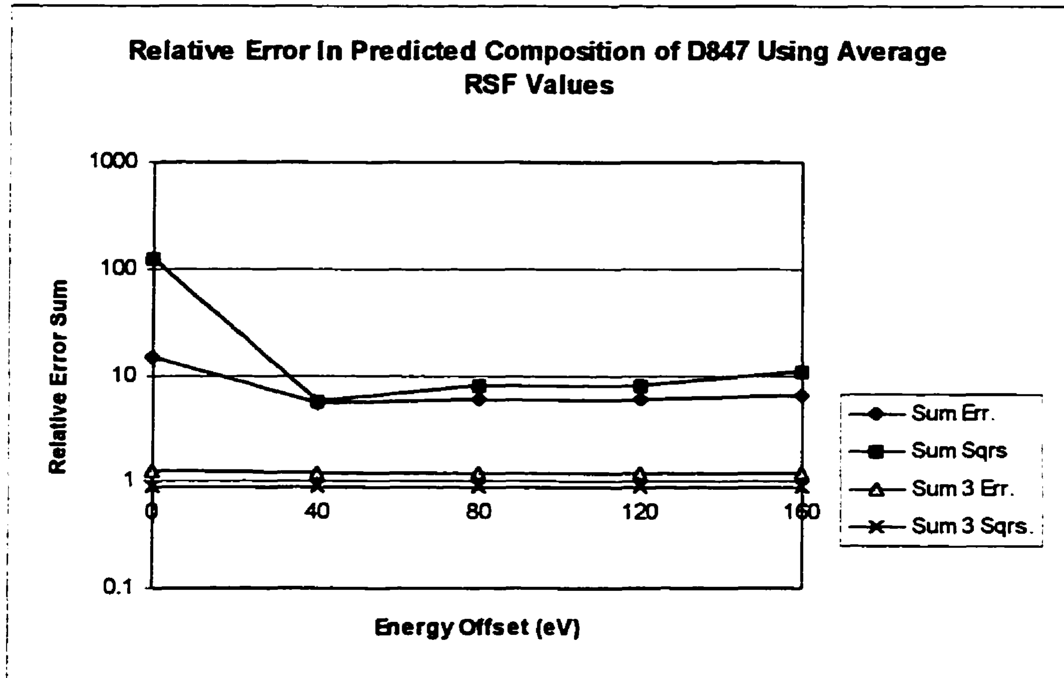

Figure 5.5.3.9: Sum of Error In Predicted Composition of D847

5.5.4 Relationship Between Error In Calculated Composition Using Global RSF Values And Elemental Composition

Relative errors in calculated elemental composition of the alloys based upon the global RSF values from section 5.5.3 were plotted against the certified elemental composition for trend analysis. Figures 5.5.4.1 to 5.5.4.5 illustrate results obtained for each of the five major elements present from data set 1. Appendix B contains the full set of plots used in this study.

Comparative analysis of graphs representing both data sets reveals trends in error prediction for both individual elements and for the overall data as a whole. These include:

- Curve shapes and calculated values of error in Fe content versus composition were very similar in for both data sets. The curve was not smooth but the general trend was that of reduced error with increased composition. The calculated error at the intermediate composition was surprisingly high compared to those for other compositions. The spread in error was however fairly small. Error ranged between close to zero and approximately 30 percent. No energy offset provided consistently superior results.
- Cr curve shapes for the two data sets were not too similar. In both cases error tends to improve roughly with increased concentration but not smoothly. Error was observed to drop sharply from approximately 50% to near 15% as concentration increased between the two lowest concentrations. Optimal results were obtained with the 40 and 80 eV energy offset curves.

• Ni error was noted to reduce slightly with increased concentration. Again 40 and 80 eV energy offsets yielded most consistently superior results. Results obtained for both data sets were similar in curve shapes and values calculated.

• Error versus composition curve shapes and values were quite similar for Mn. Error was observed to decrease quite drastically with the initial increase in concentration. Error was generally observe to be quite small, and again, the 40 and 80 eV curve yielded slightly more consistently good results.

• Curve shapes obtained for Si were not very similar, however, error for both data sets was typically in the range of less than 10% which is quite acceptable. Error in data set 1 increased with Si content while that of data set 2 decreased slightly. Error curves for data set 2 were erratic. No energy offset curve provided clearly superior results.

A general trend of reduced error associated with increased elemental compositions was observed in this study. In low concentration elements a drastic drop in error was observed as the composition increased from its lowest levels. In general the 40 and 80 eV energy offset curves, were most consistent in providing a minimum, or close to minimum, error. The observed irregular curve shapes may be a result of surface roughness of the specimens due to the sputtering process as discussed by Yamamoto [47].

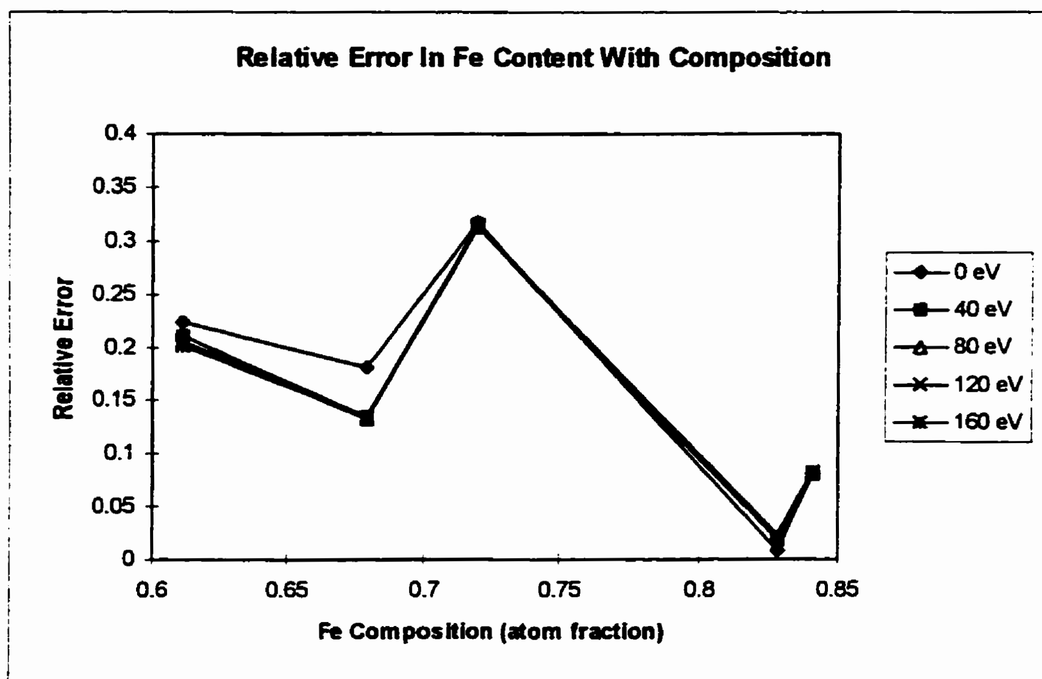

Figure 5.5.4.1: Variation of Error In Fe Content With Composition: Data Set 1

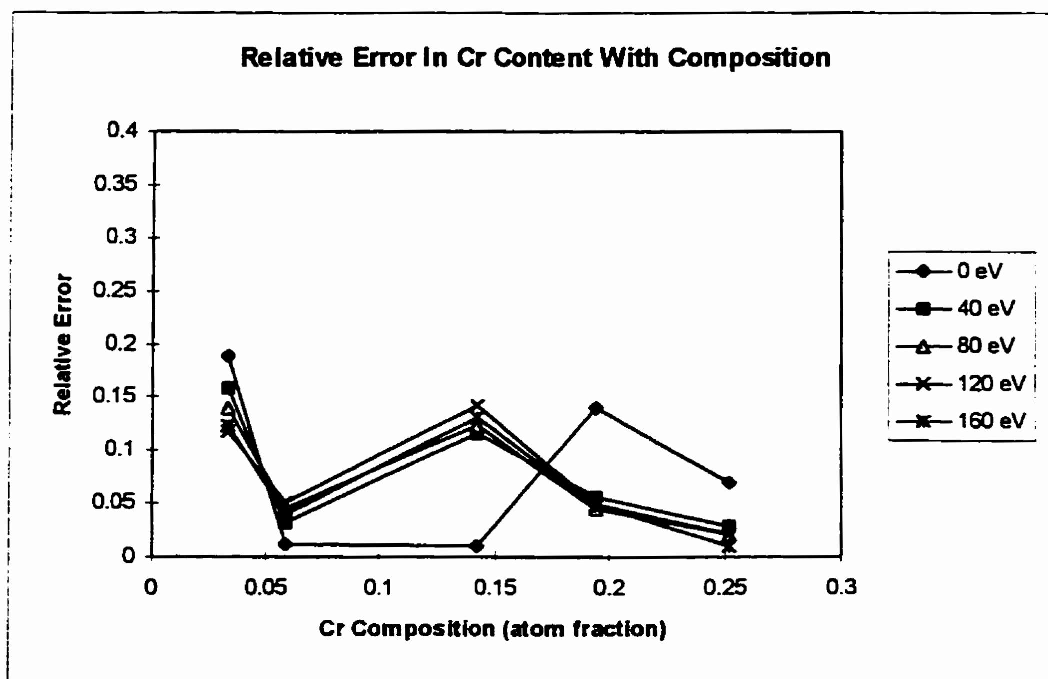

Figure 5.5.4.2: Variation of Error In Cr Content With Composition: Data Set 1

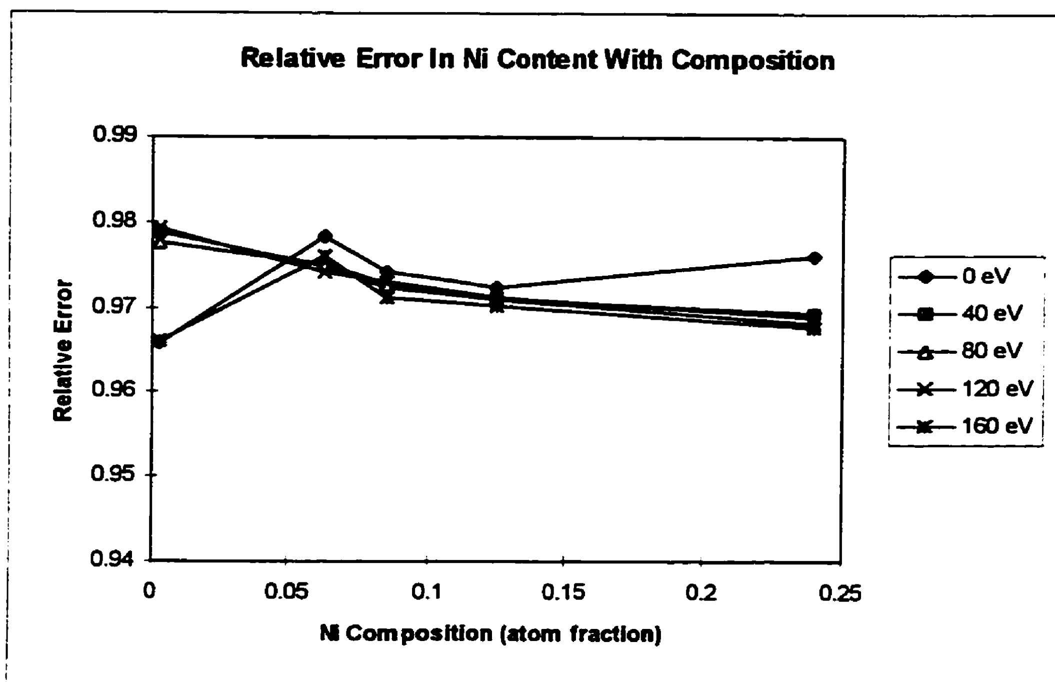

Figure 5.5.4.3: Variation of Error In Ni Content With Composition: Data Set 1

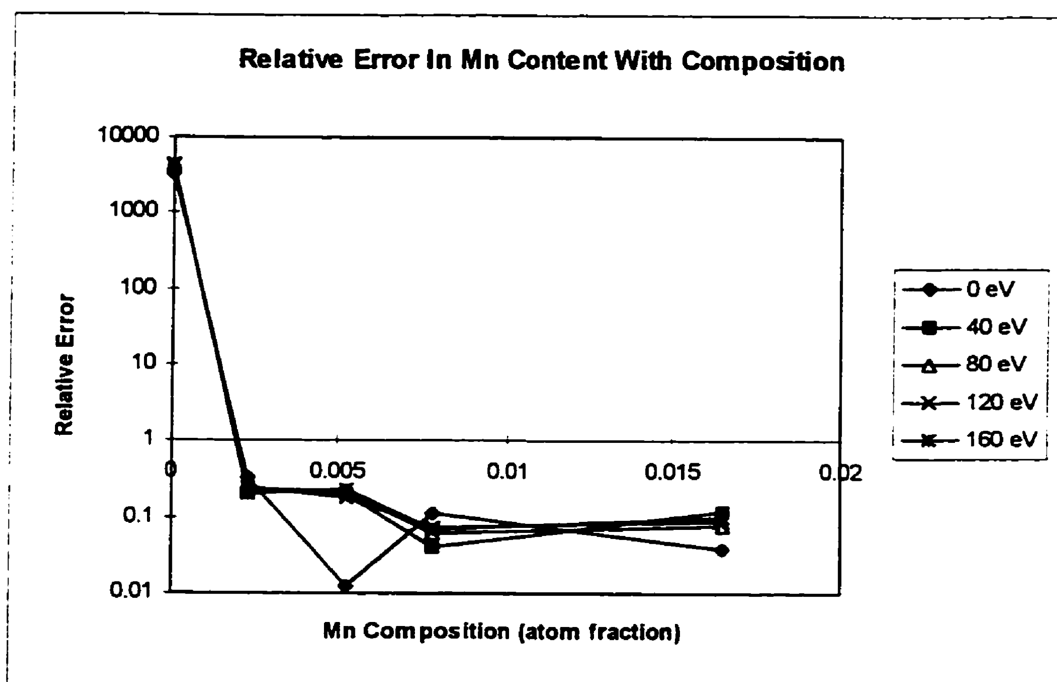

Figure 5.5.4.4: Variation of Error In Mn Content With Composition: Data Set 1

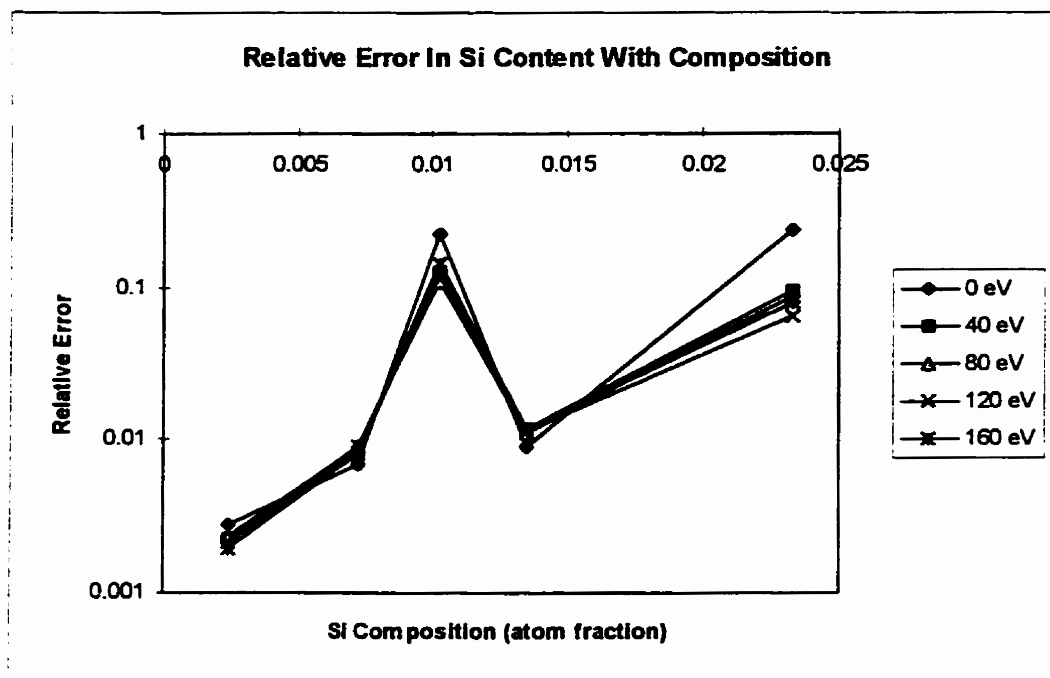

Figure 5.5.4.5: Variation of Error In Si Content With Composition: Data Set 1

5.6 BOND BREAKING MODEL RESULTS

5.6.1 Relationship Between Relative Emission Coefficients And Secondary ion Energy

Elemental relative emission coefficients (α's) were calculated by least squares regression and plotted versus energy offset from the secondary ion distribution peak. Unlike RSF values which are expected to change with composition, α values are expected to remain essentially constant with composition variation in homogeneous alloys unless a phase change occurs. As such the α values were solved using measured intensities from samples of differing composition in order to interpret the effect of individual α coefficients upon the overall emission of individual elements. A complete set of plots of α values for the five major elements (Fe, Cr, Ni, Mn, Si) versus secondary ion energy are provided in Appendix C. Figures 5.6.1.1 and 5.6.1.2 illustrate typical emission coefficient distributions for the two data sets for example.

Calculated elemental relative emission coefficients (α values) for the three most abundant elements (Fe, Cr, Ni) exhibited very similar curve shapes when plotted versus secondary ion energy offset for both data sets even though the actual measured values differed in some cases. Curve shapes obtained for Mn, Si α coefficients were less well behaved. In the majority of cases the curve shapes for the relative emission coefficients of these two less abundant elements were similar in the two data sets, however, in some instances the values obtained were erratic and thus less consistent. This result is attributed to mainly to the lower ionic count rates measured for these elements thus introducing some statistical unreliability, and, also to the effect that the least squares regression has on the approximation of these less intense signals. The overall similarity of calculated α

versus energy distribution curves does however indicate reproducibility. Based upon the underlying theory of the Bond Breaking Model which suggests that each element will have a given enhancement or suppression effect upon the emission of ionized atoms of another element in a matrix, the plotted curve shapes for α versus energy should be an intrinsic property of an element system in a given instrument and thus should indeed be reproducible.

Calculated α values when plotted versus energy offset typically tended to drop in magnitude as energy offset increased from 0 eV toward 80 eV where the α values reached a minimum of/or near to zero. For some element combinations the α values remained low at higher energy offsets while in other instances the α values increased in magnitude again as energy offset neared 160 eV, particularly when Mn was the enhancing element. It is interesting to note that in the majority of cases the calculated α values were a maximum at 0 eV offset for all alloy combinations studied. This would suggest that any enhancement effects are a maximum at zero offset dropping to a minimum in the intermediate energy offset range around 80 eV and in some cases increasing again at higher energy offsets.

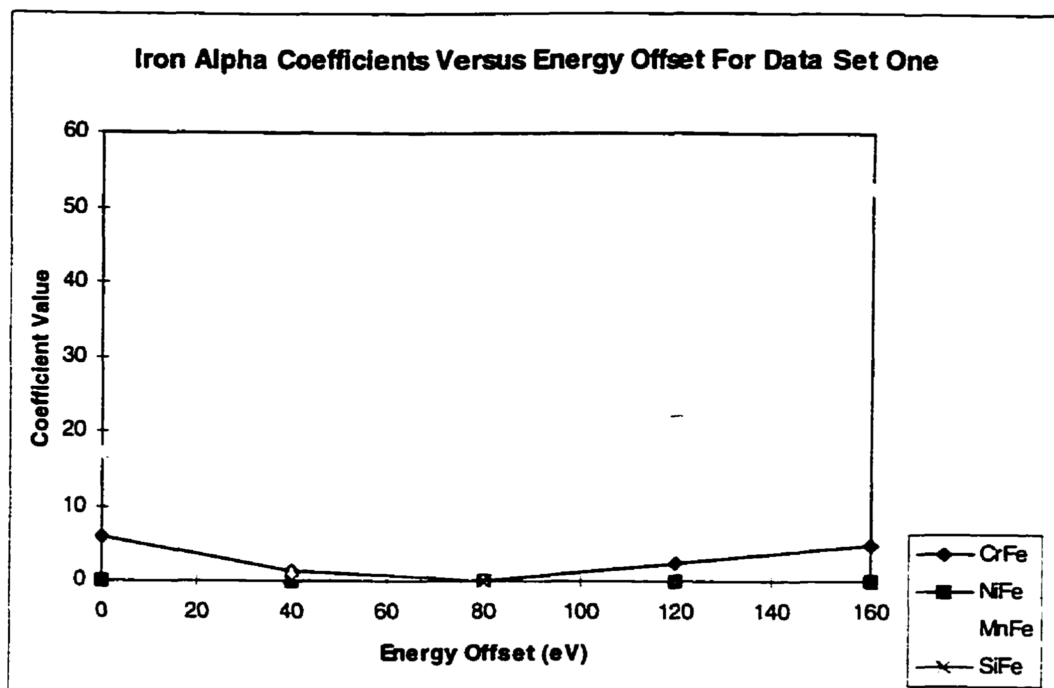

Figure 5.6.1.1: Iron Relative Emission Coefficients Values Versus Energy Offset For Data Set 1

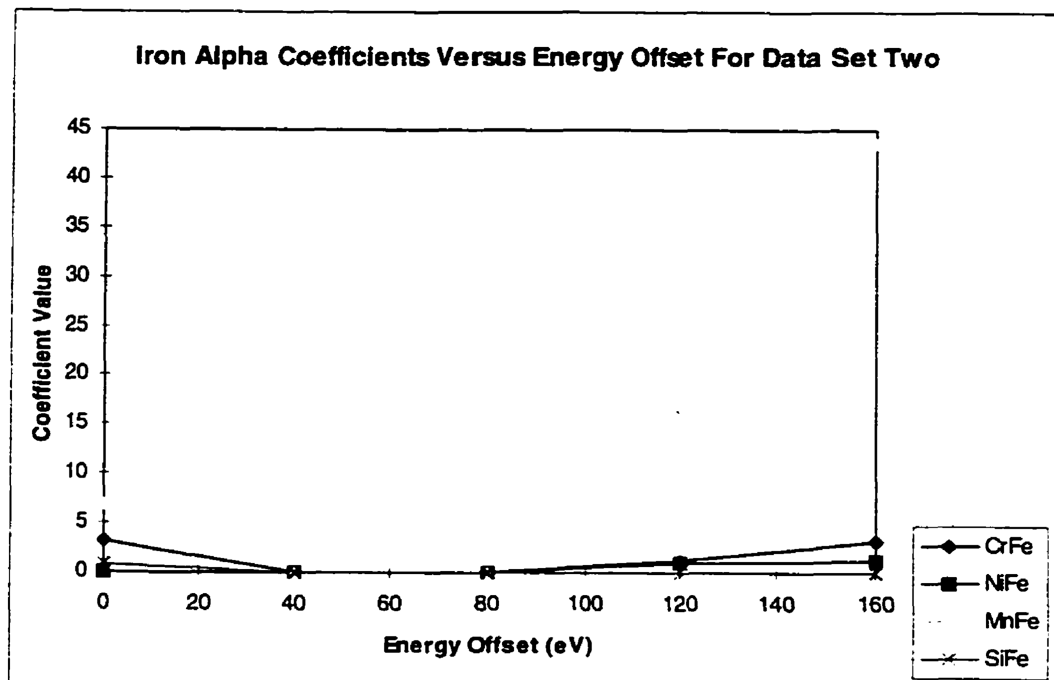

Figure 5.6.1.2: Iron Relative Emission Coefficients Values Versus Energy Offset For Data Set 2

5.6.2 Relationship Between Relative Emission Coefficients Calculated Using Top Three Versus Top Five Most Abundant Elements

Relative emission coefficients were calculated for the 3 major elements Fe, Cr, Ni with the exclusion of Mn and Si in order to study the effect of including these less abundant elements in the analysis and also to check the validity of the five element results. Again, the calculated relative emission coefficients were plotted against their associated energy offset. Examples of the distributions obtained are provided in Figures 5.6.2.1 and 5.6.2.2 with the complete set of results provided in Appendix C.

Comparison of curves obtained for both five and three element results showed that for the majority of the data the curve shapes were very similar for both data sets studied. In many instances the calculated α values were almost identical for both three and five element models while in other cases the coefficients obtained using the three element model were slightly higher - acting to offset any significant contribution calculated for Mn or Si in the five element analysis. Again, calculated coefficients were generally a maximum at 0 eV, dropping as energy increased to 80 eV. Some alpha values remained low out to an energy offset of 160 eV while others increased in magnitude again as energy offset increased in a mode similar to the 5 element results. Again, the patterns obtained were generally very similar for both the three element and five element results. Nickel coefficients tended to exhibit the least similarity between the three and five element models - however, an overall similarity was still observed in their data. Lack of similarity observed for the nickel results was again attributed to lower nickel intensities, particularly at higher energy offsets, and to the effect of these lower intensities upon the least squares regression results for α values.

Overall results obtained indicated that not only did the five element model describe the experimental parameters effectively but also that the similarity of three and five element results for both data sets suggest that the regression technique was both stable and well behaved.

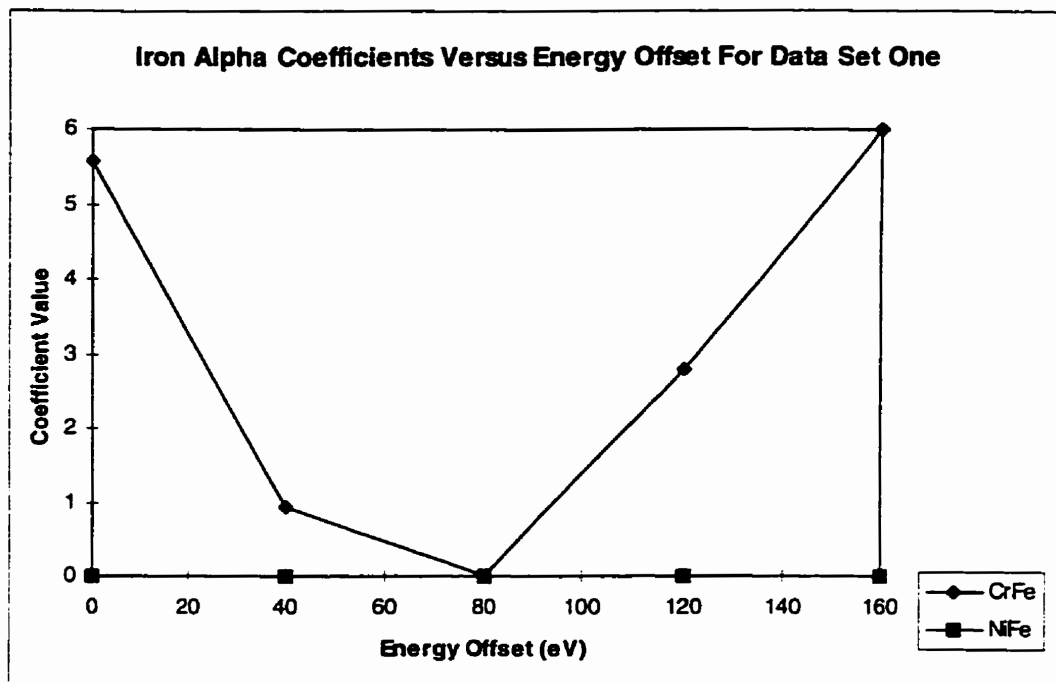

Figure 5.6.2.1: Three Element Model Iron Relative Emission Coefficients Values Versus Energy Offset For Data Set 1

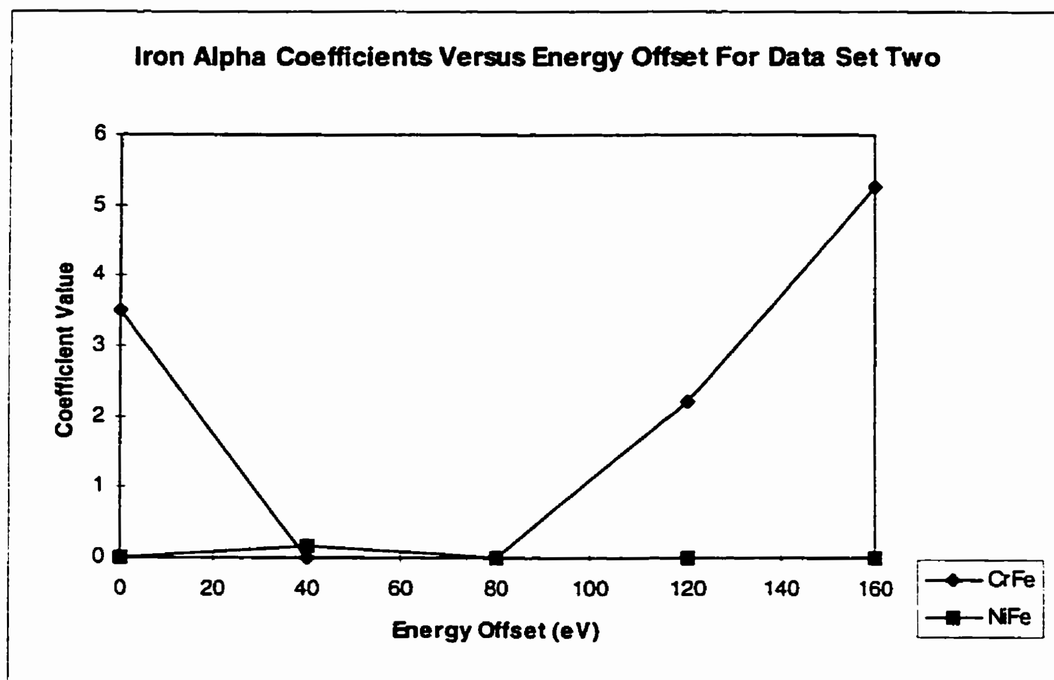

Figure 5.6.2.2: Three Element Model Iron Relative Emission Coefficients Values Versus Energy Offset For Data Set 2

5.6.3 Prediction of Specimen Composition Based Upon Average Global Emission Coefficients For The Bond Breaking Model

An average, global set of emission coefficients was generated by averaging the alpha values calculated for each element at each energy offset from the two data sets. These coefficients were then used to predict the composition of each of the alloys using the method outlined in section 3.5. Figure 5.6.3.1 illustrates the variation of the predicted composition for specimen D846 with energy offset as a result of emission coefficient variation. Examination of this figure reveals that there is indeed some variation in predicted composition with energy offset. Since the composition of each of the alloys is known, the relative error in their predicted composition was calculated using equation (5.5.3.1). To ease analysis a full set of graphs of relative error in predicted composition versus energy offset was generated and are available in Appendix C. For comparative purposes figures 5.6.3.2 to 5.6.3.6 contain plots of error associated the predicted composition of all five alloy specimens using data set 1 intensities. To further aid analysis, plots of the sum of the errors in predicted composition versus energy offset were generated. In these figures the sum of the error associated with the three major elements (Fe, Cr, Ni) was plotted as was the sum of the squares of the error. The sum of error and the sum of the squares of error for the five most abundant elements (Fe, Cr, Ni, Mn, Si) are similarly included. Figures 5.6.3.7 and 5.6.3.11 illustrate typical sum error of plots. A complete set of sum of error plots is available in Appendix C.

Emphasis was placed upon the three most abundant elements due to their statistical reliability arising from their higher measured count rates. Examination of predicted

composition versus energy offset revealed that the three major elements provided relatively stable curve shapes and values for the two data sets. In general the curve shapes and in many cases composition values obtained were similar between data sets but not identical. The minor elements (Mn, Si) exhibited less consistency that the major elements, following similar trends with energy but with a greater variation in values measured. For the two less abundant elements not all the same data points were present in both data sets. Curve shapes versus energy offset for both major and minor elements were in some cases erratic, not exhibiting a clear trend with energy offset.

Examination of graphs of the relative error in calculated elemental composition using the global average emission coefficients versus energy offset revealed that results obtained using the two data sets were similar but not identical. Comparison of the results on an alloy to alloy basis revealed:

• For specimen 845, although values differed, the elemental curve shapes were essentially similar. Fe, Cr exhibited a general trend of increasing error with energy offset while Ni exhibited a reduced erroe in the 80 eV offset range.

• For alloy 846, error curve shapes were similar as were many error values for the individual elements. The trend in error versus energy offset varied with element. Fe, Cr, exhibited an increase with offset, while Ni, Mn were erratic, and Si error dropped with offset from a high value at 40 eV offset.

• For Alloy 847, the three major elements possessed essentially similar error curve shapes between data sets although individual error values varied. Again, Fe, Cr error appeared to increase with energy offset while Ni's curve shape was erratic, showing no clear trend. The minor element curves showed little agreement between the data sets.

• For specimen 849, the Fe, Cr curve shapes were similar, as were the error values, both showing an increase in error with energy offset. Nickel curves for the two data sets possessed similar values except in the intermediate (80 to 120 eV) offset range. Error curves observed for Mn, Si were inconclusive.

• For alloy 850 all curve shapes were quite similar between data sets, as were the error values obtained. Fe and Ni errors were observed to drop with energy offset while the error in predicted Ni and Mn compositions increased. The silicon curve shape was inconclusive. Erratic behavior was noted in many curve shapes in the 80 eV energy offset range.

Overall trends were definitely observed in error in predicted composition versus energy offset on an elemental basis even though error values were different in many cases. Trends were especially apparent for the three major elements. Erratic behavior tended to obscure trends in some curve shapes in the 80 eV offset range. This behavior was likely occurring as a result of the tendency for emission coefficients to approach zero in this regime.

Examination of the sum of error versus energy offset plots adds clarity to the above mentioned results. With the exception of some instability in the intermediate (80 eV) offset range the curve shapes obtained for the two data sets are in general agreement. The sum of error curves which represent the sum of errors associated with the three major elements consistently show a general trend of a slight increase in error with increased energy offset. The sum 5 error curves tend to suggest a smaller increase in error with energy offset, appearing in cases essentially flat with energy overall. The sum of error

results for five elements are not as consistent due to the poorer prediction of the minor elements Mn, Si and the presence of missing data points. Further, the reduced statistical accuracy of the five element results combined with the erratic behavior of the minor elements in the 80 eV offset range suggest that the three element results are more accurate.

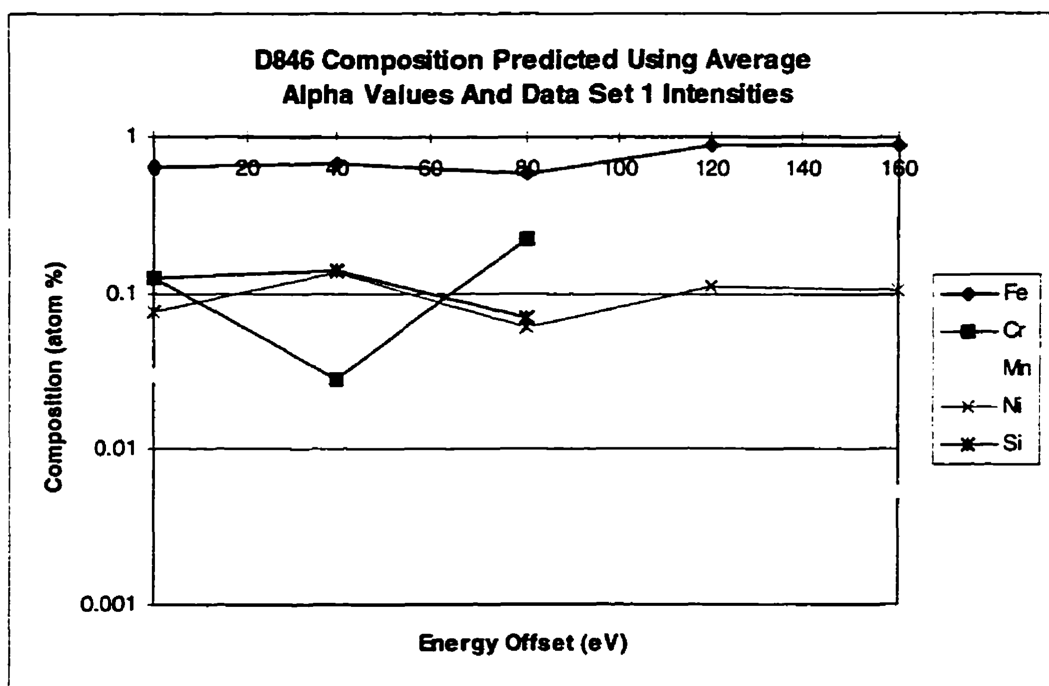

Figure 5.6.3.1: Predicted Composition of Specimen D846 Using Global Alpha Values and Data Set 1 Intensities

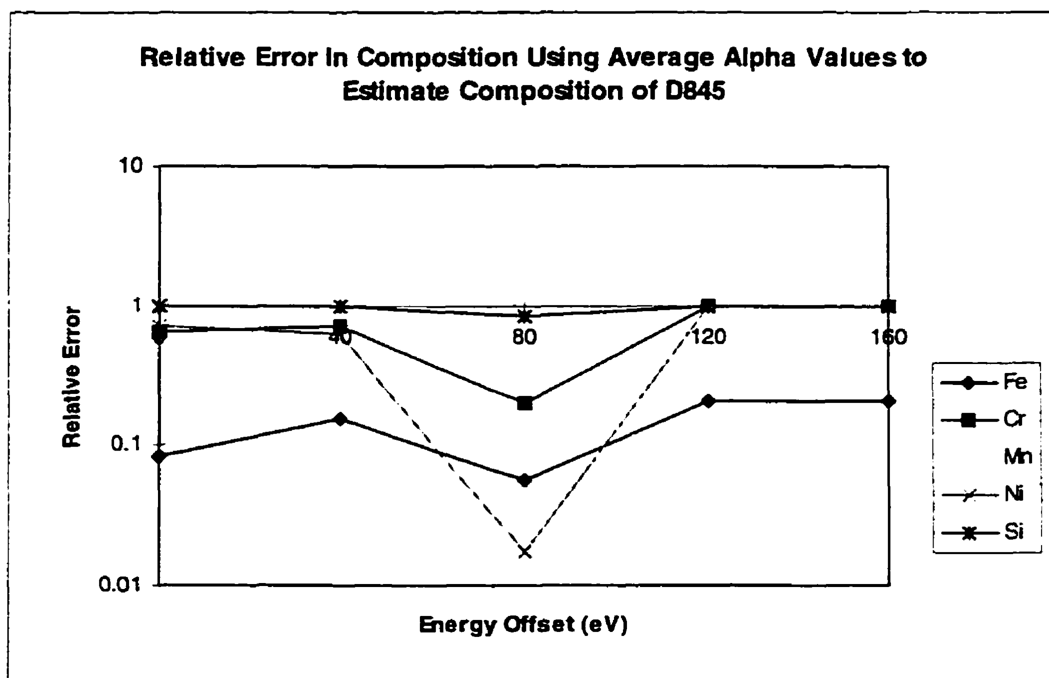

Figure 5.6.3.2: Elemental Error Composition of D845 Using Average Alpha Values

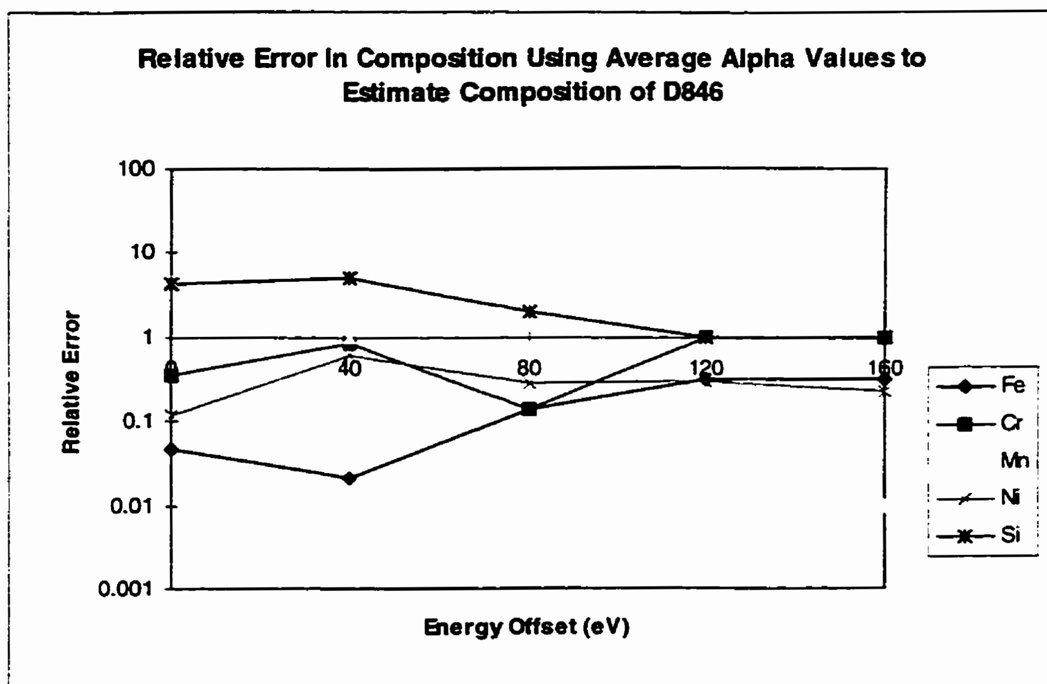

Figure 5.6.3.3: Elemental Error Composition of D846 Using Average Alpha Values

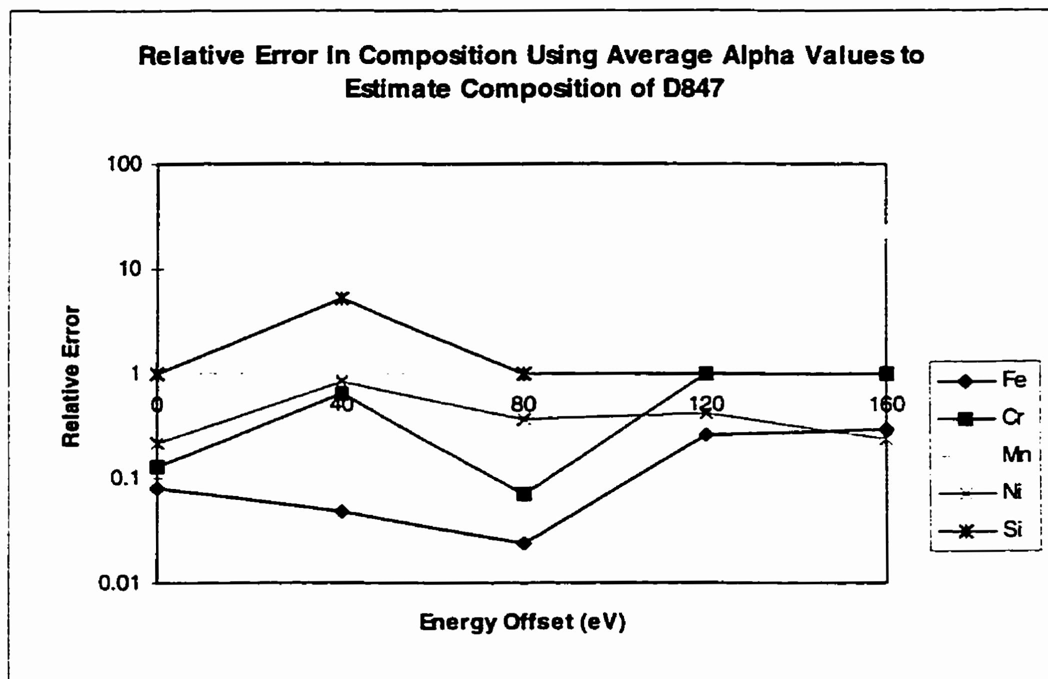

Figure 5.6.3.4: Elemental Error Composition of D847 Using Average Alpha Values

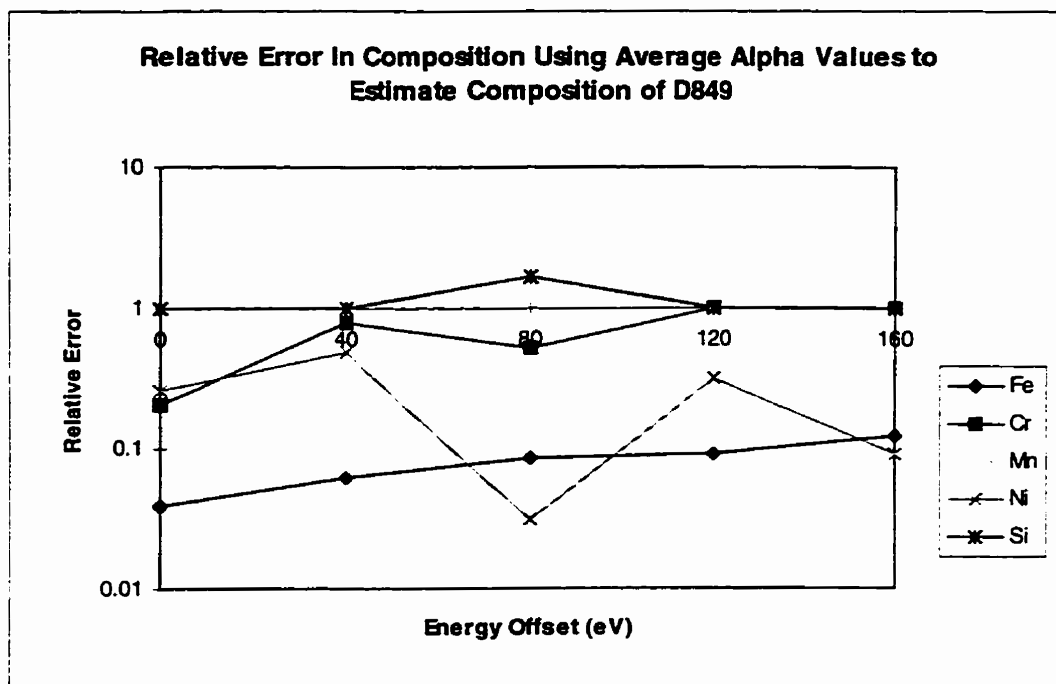

Figure 5.6.3.5: Elemental Error Composition of D849 Using Average Alpha Values

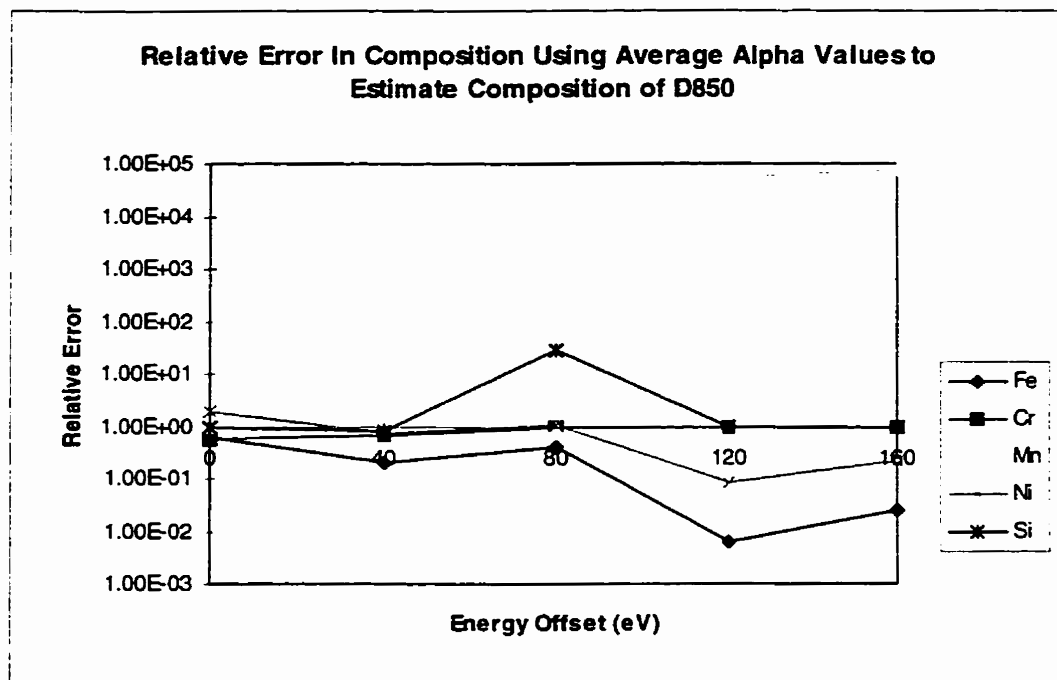

Figure 5.6.3.6: Elemental Error Composition of D850 Using Average Alpha Values

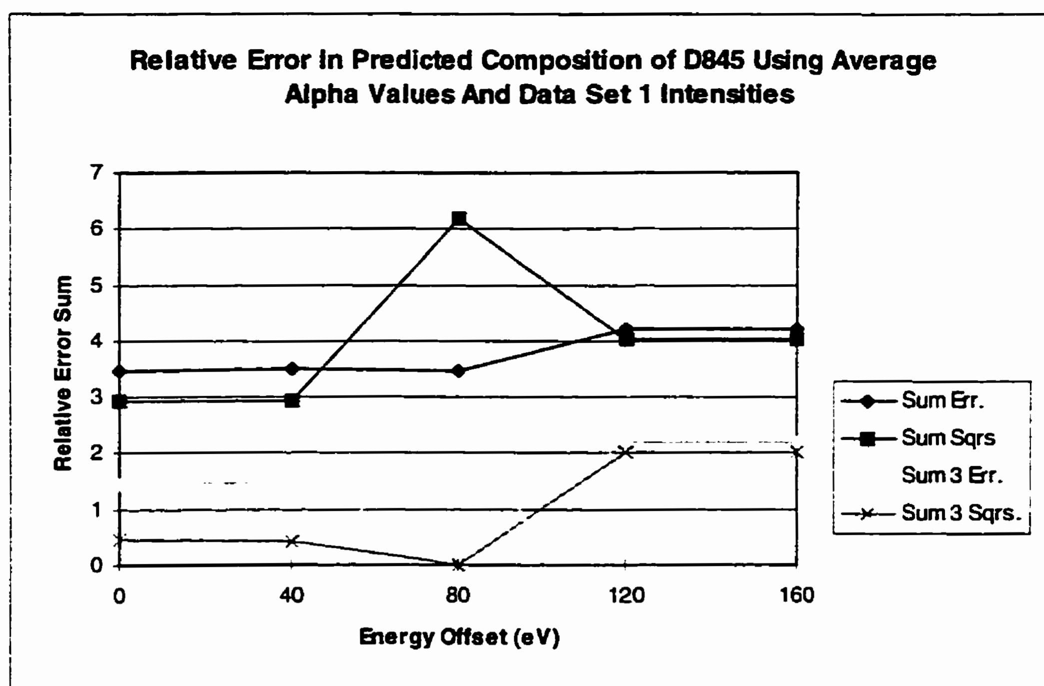

Figure 5.6.3.7: Sum Of Error In Composition of D845 Using Average Alpha Values

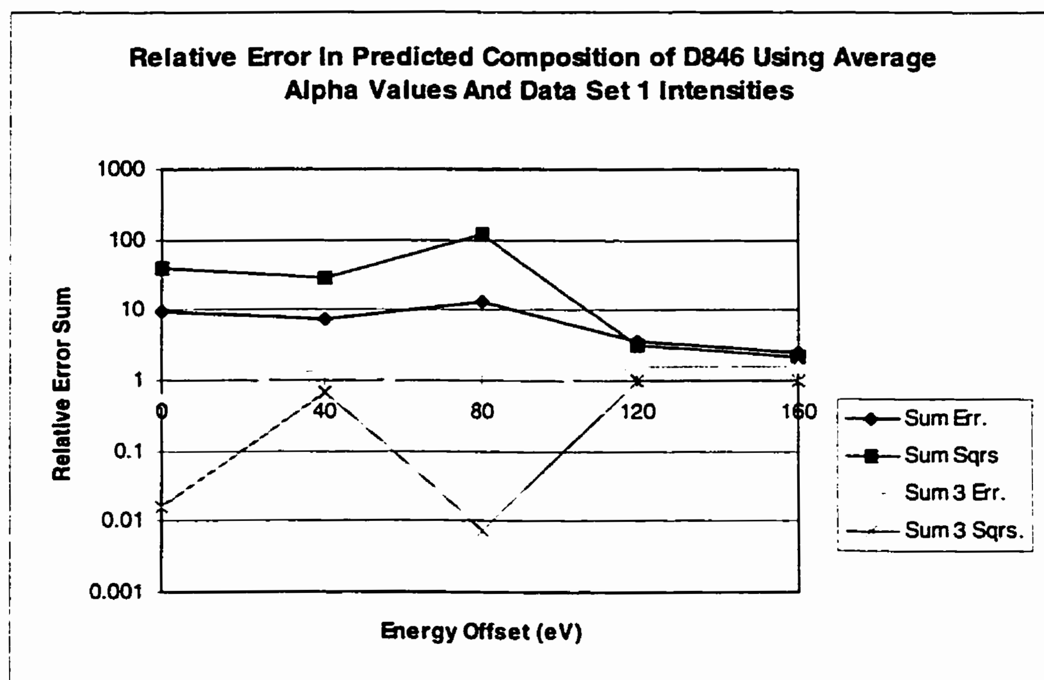

Figure 5.6.3.8: Sum Of Error In Composition of D846 Using Average Alpha Values

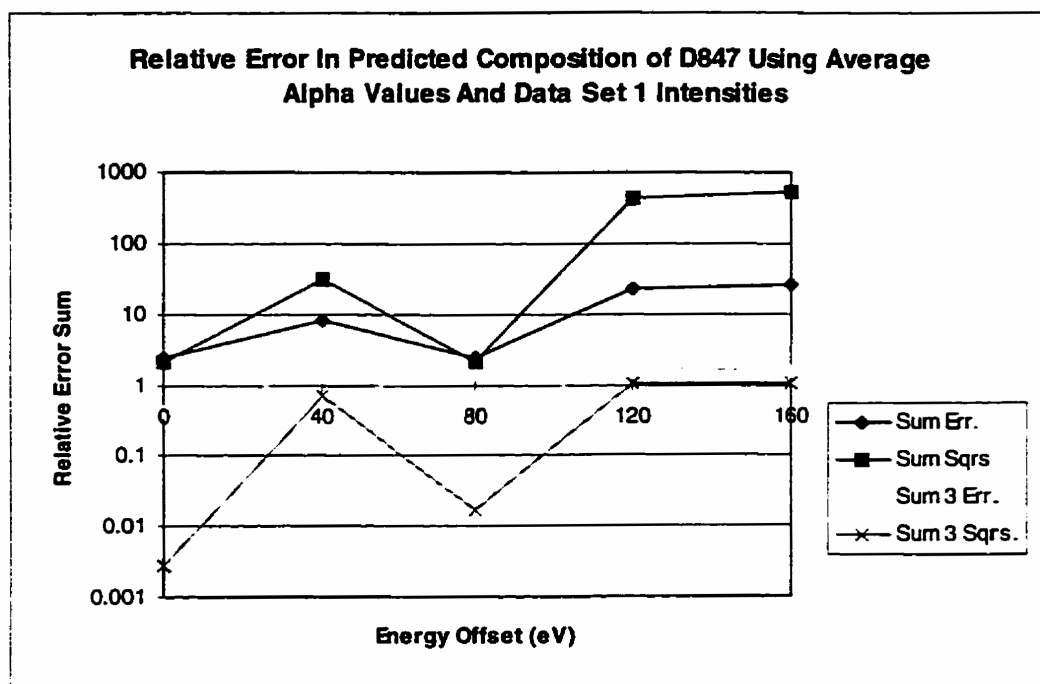

Figure 5.6.3.9: Sum Of Error In Composition of D847 Using Average Alpha Values

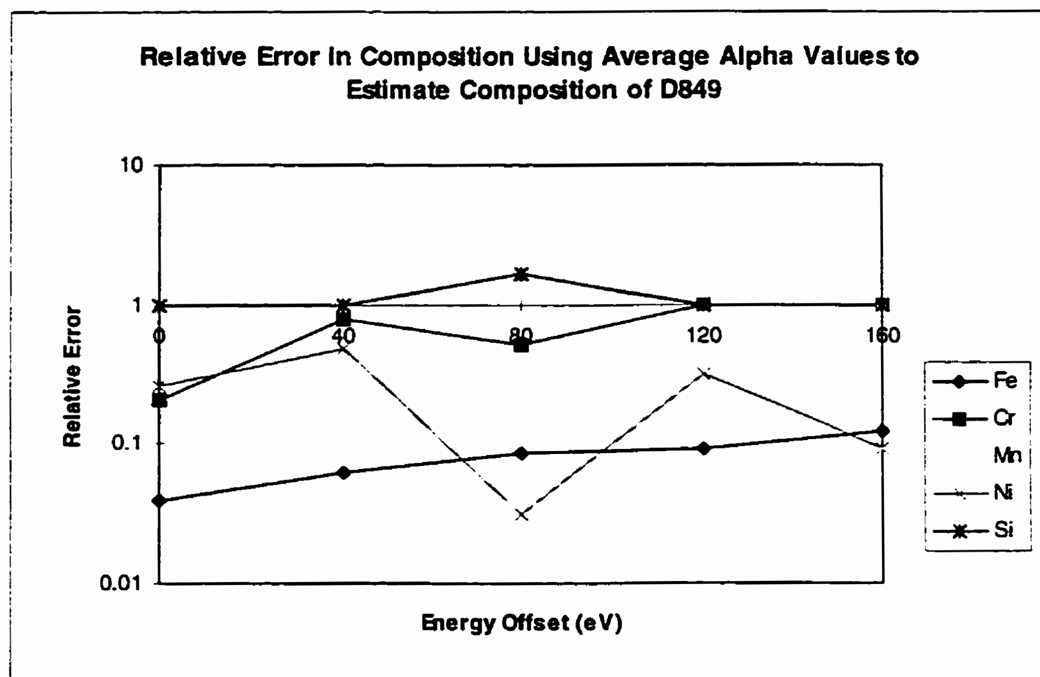

Figure 5.6.3.10: Sum Of Error In Composition of D849 Using Average Alpha Values

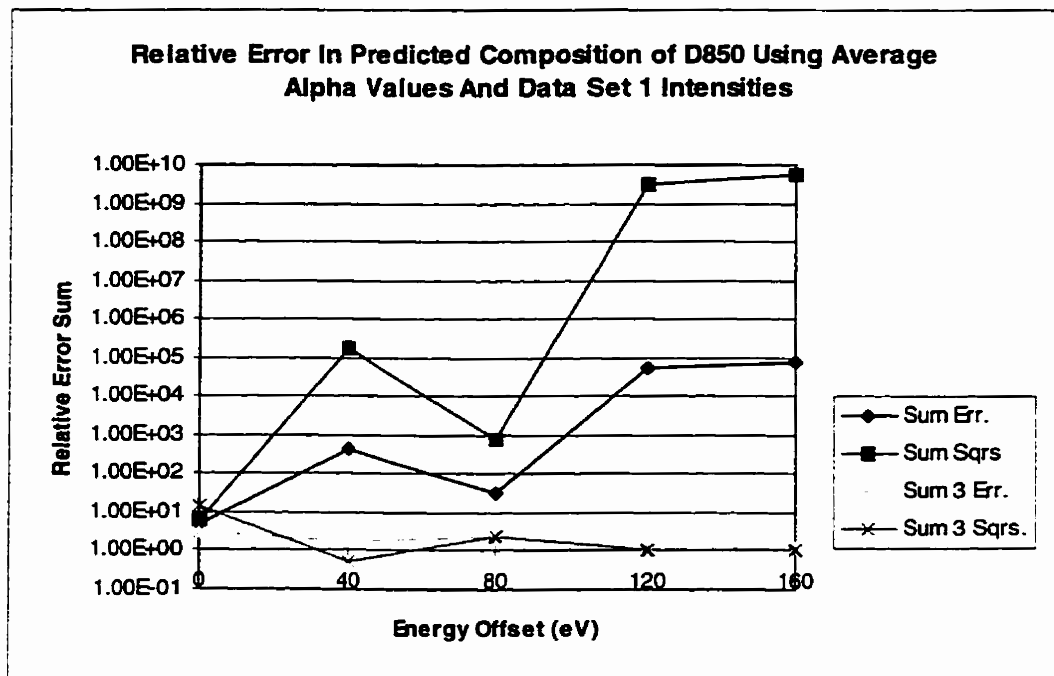

Figure 5.6.3.11: Sum Of Error In Composition of D850 Using Average Alpha Values

5.6.4 Relationship Between Error In Calculated Composition Using Average Emission Coefficients And Elemental Composition

Relative errors calculated for the elemental composition predictions using average alpha emission coefficients were plotted against the certified elemental composition for analysis of trends. Figures 5.6.4.1 to 5.6.4.5 illustrate the results obtained for each of the five alloys studied in using data set 1. Appendix C contains a complete set of plots used in this study.

Comparative analysis of relative error versus elemental composition plots for the two data sets reveals trends in error prediction for the elements, and, for the overall data set. These include:

- Curve shapes and data values for each energy offset representing error in Fe content for both data sets were very similar. Curve shapes varied considerably between energy offsets although the variation in curve shape did show a uniform transition with energy. Variation of relative error with concentration did not follow a smooth trend. No clear trend with composition was observed. Relative enhancement/supression effects of other elements may be acting to obscure any such trend.
- Cr curve shapes were observed to be loosely similar between the two data sets. A general trend of reduced error with increasing composition was observed. The lowest error values were generally attained using the 0 eV energy offset.
- Error in Ni prediction was a maximum at the lowest concentration. The drop in error between the two lowest concentrations was quite significant. Above this second

concentration the error in Ni prediction was relatively stable until the error increased again at the maximum concentration. Shape of the error curve varied with energy offset. The 120 eV energy offset curve consistently provided the minimum error.

• For many instances the Mn composition was predicted to be zero. The errors for the compositions which were predicted exhibit a trend of reduced error with increasing concentration, particularly between the two lowest concentrations. The relative error curves obtained for both data sets were similar.

• For many instances the Si composition was also predicted to be zero due to th low concentration present and accompanying low signal intensity. In both data sets the 80 eV offset curve exhibits a trend of reduced error with increasing concentration. Zero and forty eV energy offset curves are erratic but show a slight decrease in error with concentration but are inconclusive.

In general similarities in curve shapes were observed between both data sets despite differing error values in some cases. Curve shapes tended to be more erratic than those obtained using the RSF model, and tended to show much more variation between results for different energy offsets than the in RSF factors approach. A trend of reduced error with increased concentration was observed, but it was not as consistent as expected. This may be a result of enhancement or suppression effects of other matrix atoms. Energy offsets in the 0 to 80 eV range produced the least error in elemental composition and provided the most data points for the less abundant elements.

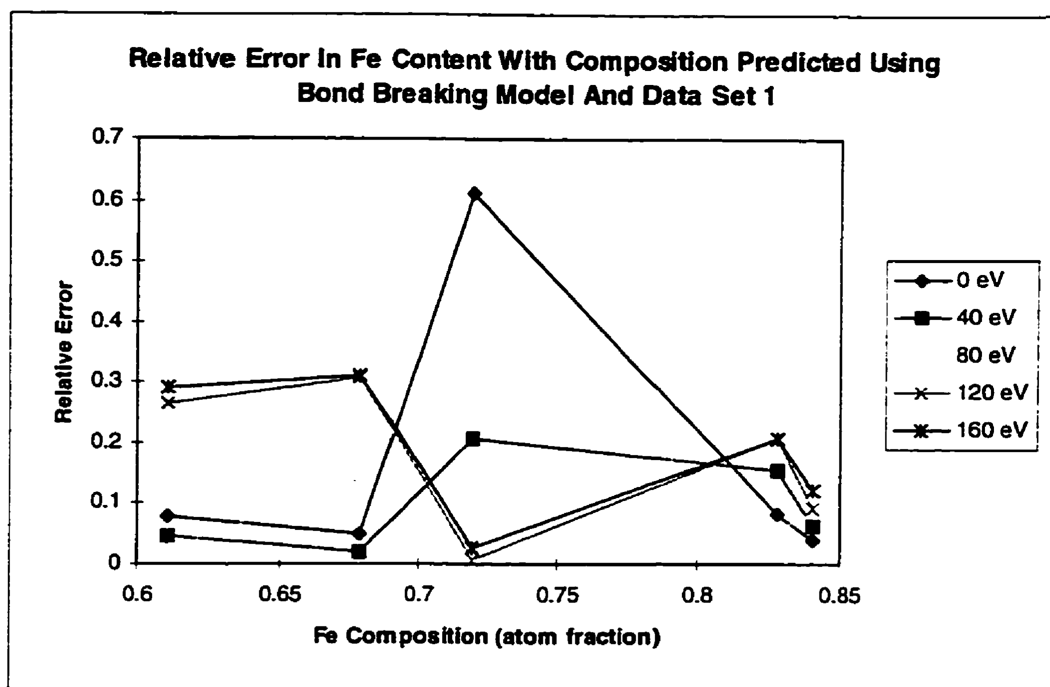

Figure 5.6.4.1: Error in Fe Content Vs. Composition Using Average Alphas

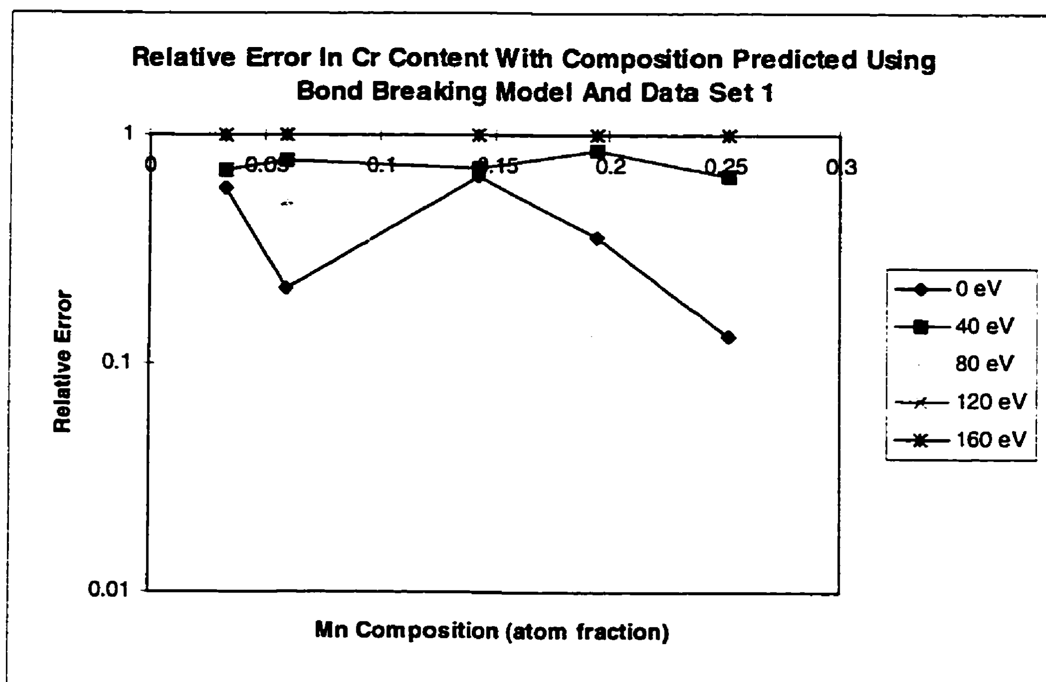

Figure 5.6.4.2: Error in Cr Content Vs. Composition Using Average Alphas

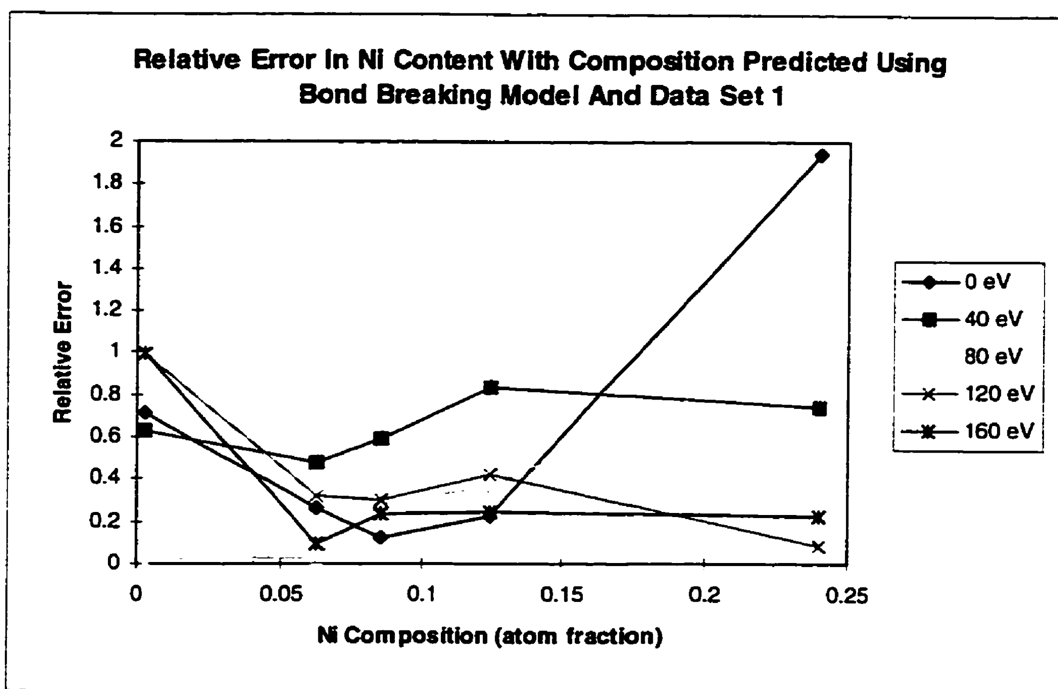

Figure 5.6.4.3: Error in Ni Content Vs. Composition Using Average Alphas

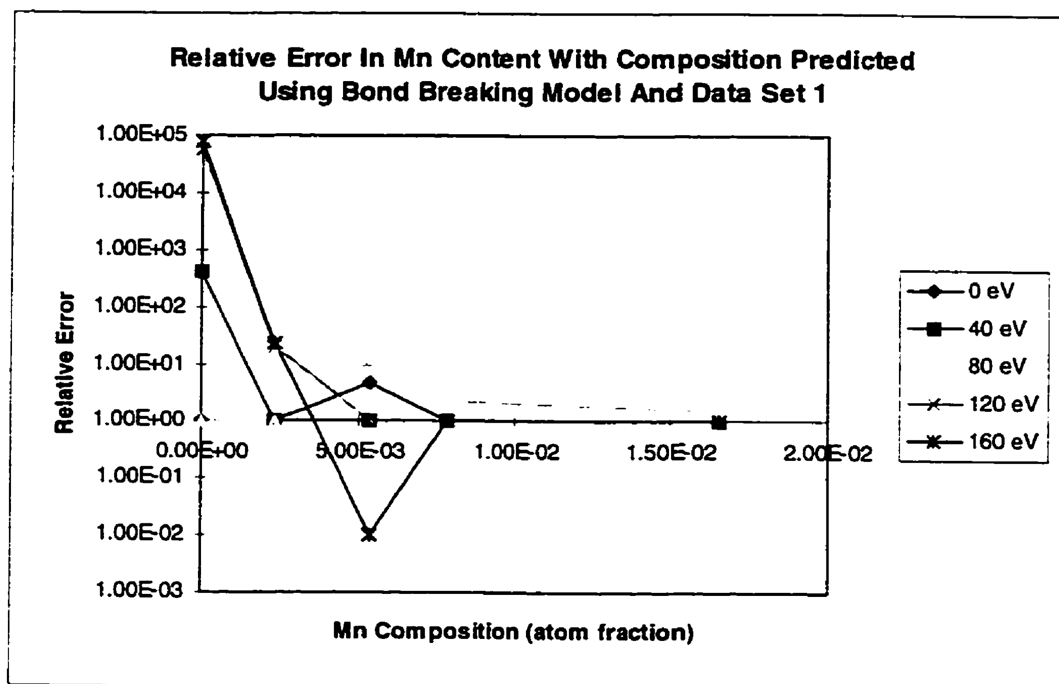

Figure 5.6.4.4: Error in Mn Content Vs. Composition Using Average Alphas

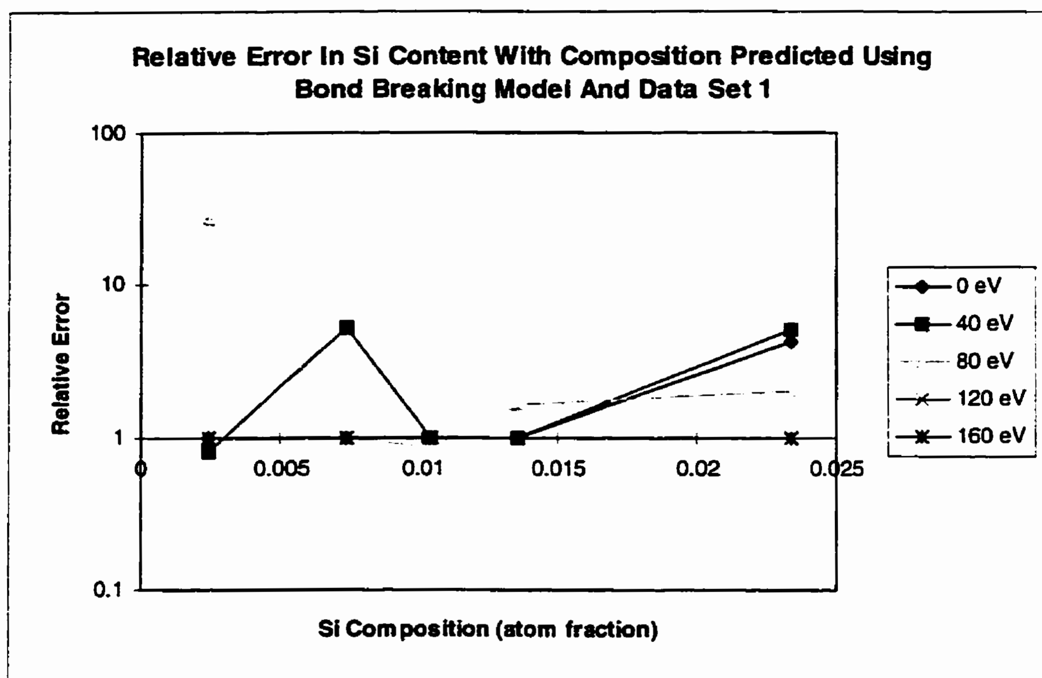

Figure 5.6.4.5: Error in Si Content Vs. Composition Using Average Alphas

5.6.5 Validity of Bond Breaking Model: Specimen D850 Composition Calculated Using Relative Emission Coefficients For Five Elements Determined Experimentally

In order to verify that the bond breaking model was performing properly, and the numerical regressions were well behaved, the composition of specimen D850 was predicted using both the five, and the three most abundant elements. If the model was poorly behaved large discrepancies in the results for these two analysis would arise. Using experimentally derived α coefficients determined from the measured intensities of alloys D845, D846, D847 and D849 at each of the 40 eV energy offset increments, the composition of specimen D850 was predicted using the method outlined in section 3.5. Since the composition of specimen D850 is known the relative error in predicted composition was calculated using equation (5.5.3.1) as in previous sections. Figures 5.6.5.1and 5.6.5.2 illustrate the variation in predicted composition with energy for results obtained for each of the two data sets. Interpretation of the results obtained is rather awkward based on these figures alone. Figures 5.6.5.3 and 5.6.5.4 illustrate the variation of the relative error in the predicted composition of specimen D850 with energy for each data set.

If only the three most abundant elements are emphasized due to their statistical reliability there is an apparent increase in error associated with an increase in offset energy. This is likely a result of a reduction of statistical accuracy as count rate decreases. It is interesting to note however, that the high energy offset results yield the most repeatable sum of error values. That is, the higher energy offset results although not the most accurate, did posses the most precision. This statement is based upon the sums of

the relative error calculated for the three major elements for both the three element and five element analysis results.

Specifically, with regard to the five element model analysis - data set two exhibited a general increase in error with offset energy for all elements studied whereas data set 1 results were not quite as well behaved. Data set one results obtained at 0 ev were unexpectedly poor, but otherwise the sum of error was approximately flat with energy.

Examination of the data gathered as a whole leads to the general observation that for the five element bond breaking model analysis there is a slight increase in error with energy offset for the three major elements. In addition, results obtained in the 80 eV offset interval were erratic, likely resulting from the tendency for α values to approach zero at this energy. Here, the composition may not be as closely approximated since any enhancement or suppression effects, if they are present, are not predicted well. All graphs do suggest that as energy offset approaches 80 ev, the relative emission coefficients do approach zero. This phenomena tends to support the possibility that enhancement is diminished in the intermediate energy offset range, and may also be limited at higher energy offsets. This bears closer scrutiny in the future and may lend some insight into the ionization process itself.

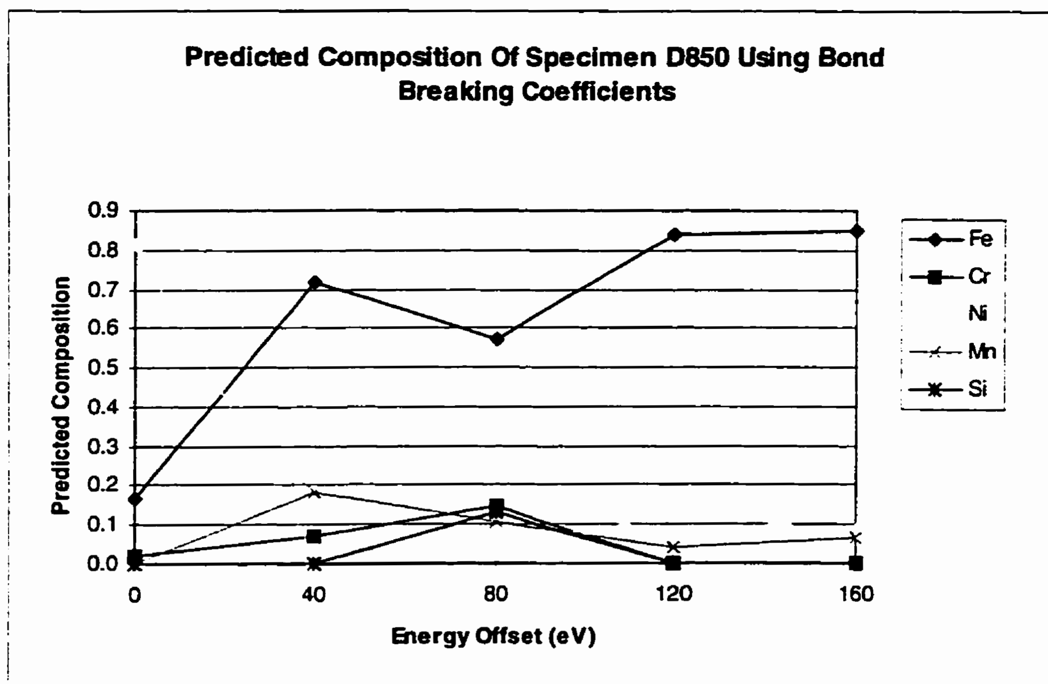

Figure 5.6.5.1: Predicted Composition of Specimen D850 Using Bond Breaking Data From Data Set 1

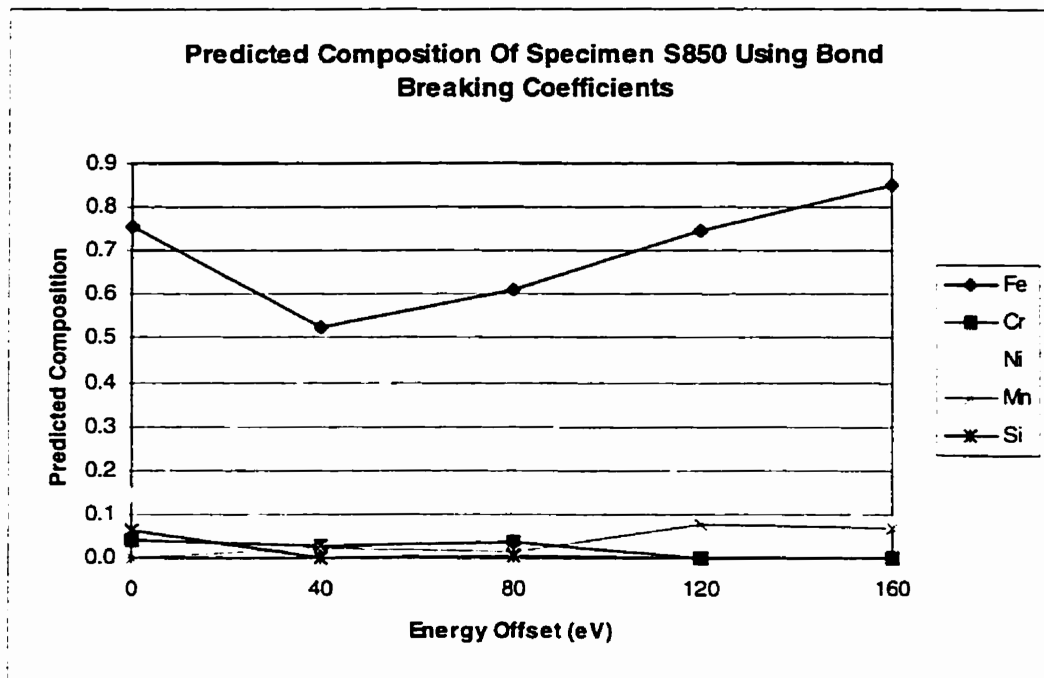

Figure 5.6.5.2: Predicted Composition of Specimen D850 Using Bond Breaking Data From Data Set 2

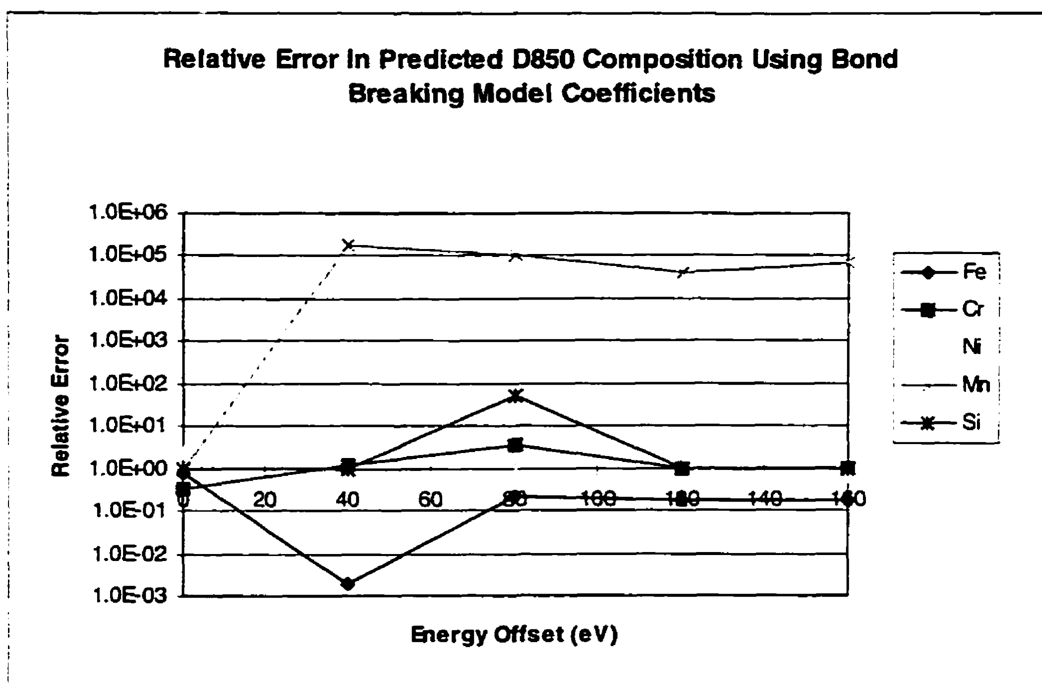

Figure 5.6.5.3: Relative Error in Predicted Composition of Specimen D850 Using Bond Breaking Data From Data Set 1

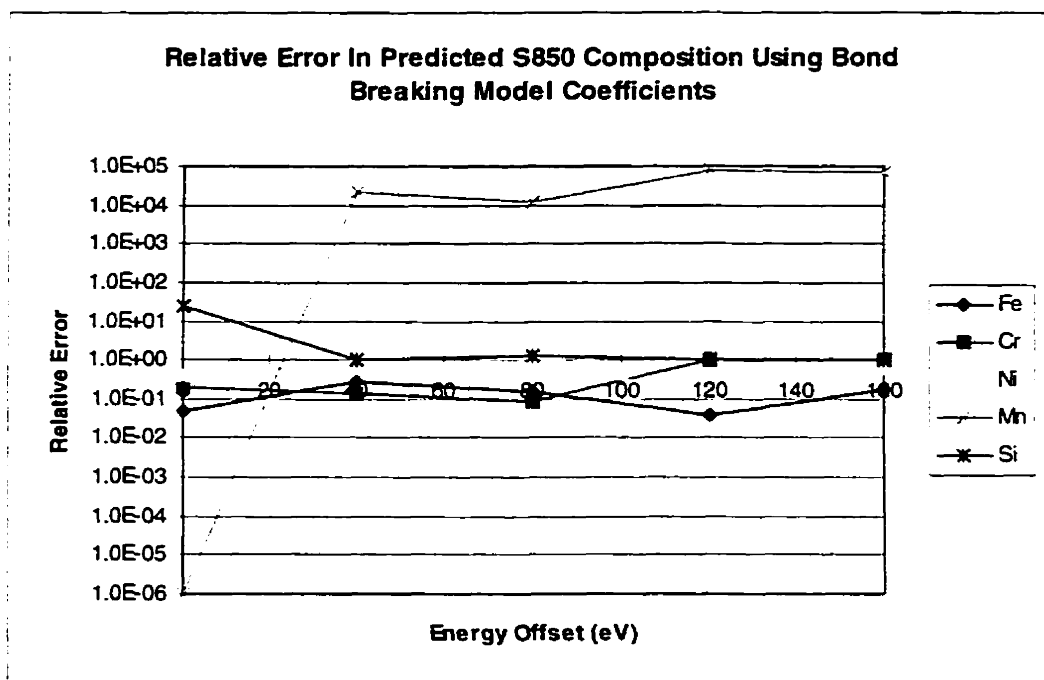

Figure 5.6.5.4: Relative Error in Predicted Composition of Specimen D850 Using Bond Breaking Data From Data Set 2

5.6.6 Specimen D 850 Composition Calculated Using Relative Emission Coefficients For Three Elements Determined Experimentally

Relative emission coefficients determined for Fe, Cr and Ni in the three element model of the composition of specimen D850 based upon the measured intensities of alloys D845, D846, D847 and D849 at each of the 40 eV energy offset increments were used to predict the composition of specimen D850 using the method outlined in section 3.5.

Figures 5.6.6.1 and 5.6.6.2 represent the predicted composition of specimen D850 based upon the two data set results. Figures 5.6.6.3 and 5.6.6.4 show the associated relative error of the predictions in figures 5.6.6.1 and 5.6.6.2 respectively. Although the predicted compositions of specimen D850 at each energy are not that similar to their 5 element counterparts for each data set, the relative sum of error distributions for corresponding analyses are very similar. That is, there appears to be a general trend towards increased error associated with an increase in offset energy used to collect data for modeling. In addition, for the majority of cases the iron content predictions versus energy follow a similar pattern for 5 element results and their 3 element solution counterparts. The comparison of actual values and their trends is complicated by the contributions of Mn and Si in the five model element solutions.

The similarity of relative error values and of distribution shapes between the 3 element and 5 element solutions reinforce the observation that the numerical analysis is generally well behaved.

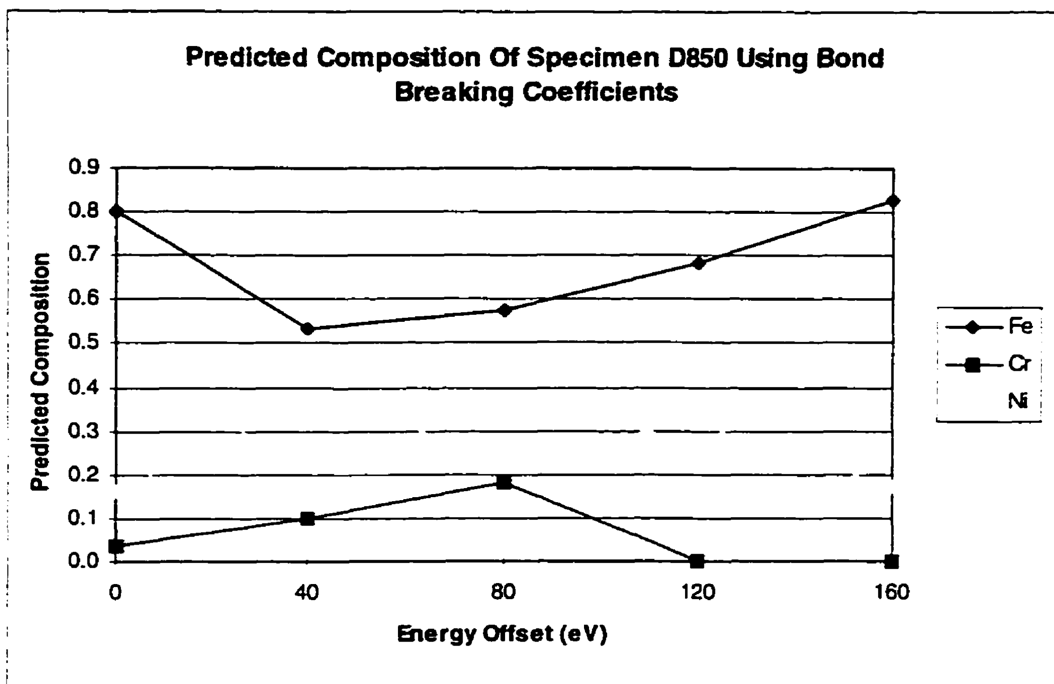

Figure 5.6.6.1: Predicted Composition of Specimen D850 Using Three Element Model Bond Breaking Data From Data Set 1

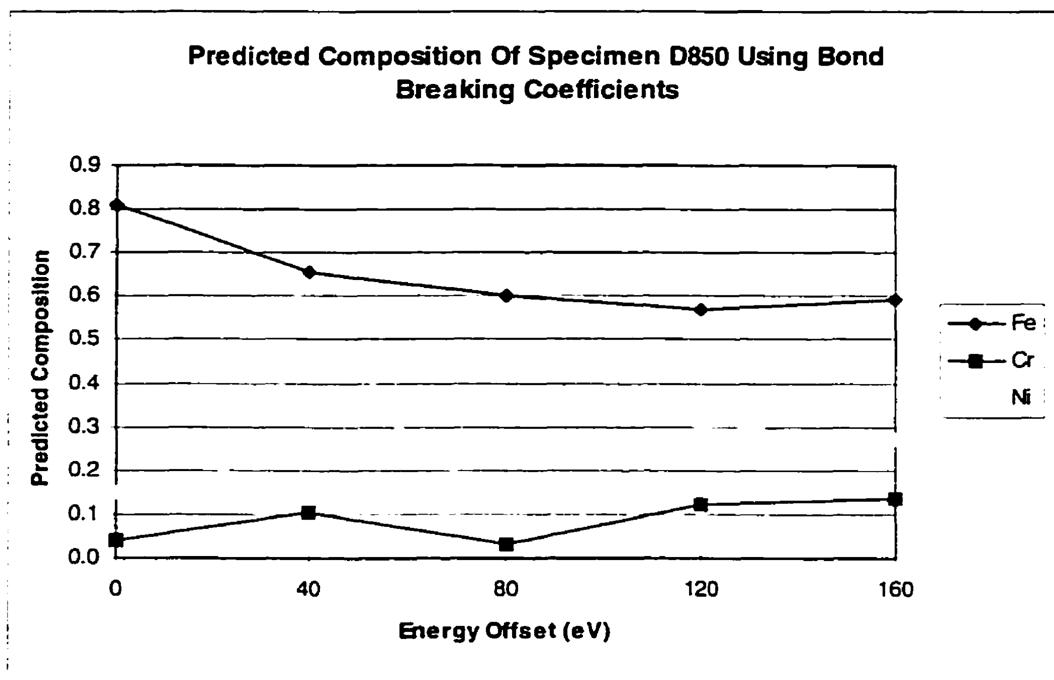

Figure 5.6.6.2: Predicted Composition of Specimen D850 Using Three Element Model Bond Breaking Data From Data Set 2

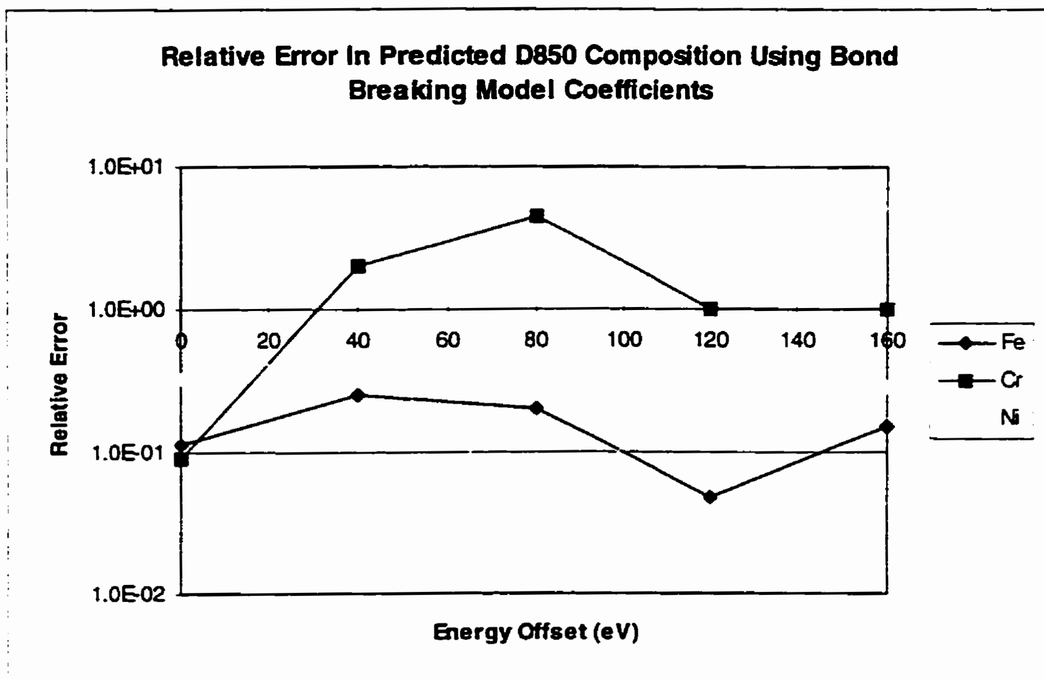

Figure 5.6.6.3: Relative Error in Predicted Composition of Specimen D850 Using Three element Model Bond Breaking Data From Data Set 1

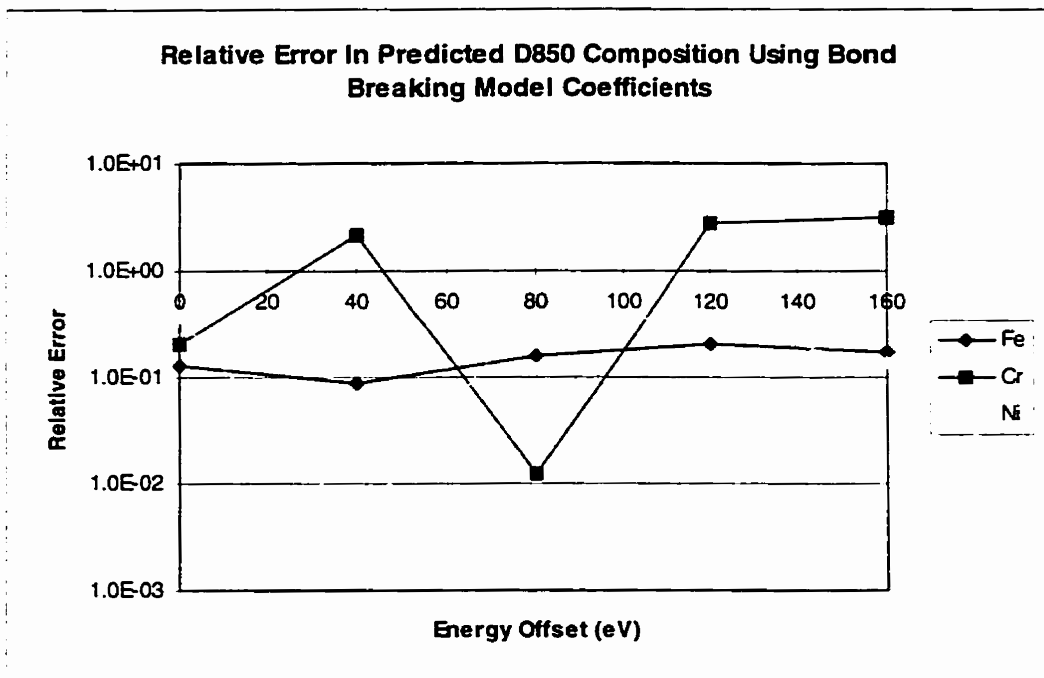

Figure 5.6.6.4: Relative Error in Predicted Composition of Specimen D850 Using Three element Model Bond Breaking Data From Data Set 2

5.6.7 Comparison of Relative Error In Prediction of Specimen D850 Composition:

Five Element Model Versus Three Element Model

Relative error values obtained for composition predictions of both data sets for both the three element and five element prediction models were compared. Each model was represented by data comprised of the prediction of D850 composition by two data sets at five different energy offsets - representing ten different predictions for each of the three and five element models respectively. Comparison of the relative errors associated with the three major elements in the two models revealed that the 5 element results were more accurate in 7 of the ten results, very similar to the 3 element results in two cases and worse in only one case. The case in which the 3 element model yielded superior results was that of 0 eV in data set one - where the results calculated for the five element model were disappointing as mentioned previously. It is relatively safe to conclude that the five element model more accurately predicted the composition of specimen D850 and that the elements Mn and Si do indeed make a measurable contribution to the secondary ion signals collected in this analysis.

5.6.8 Comparison of Relative Error In Prediction of Specimen D850 Composition: Five Element bond Breaking Model Versus Relative Sensitivity Factors Model

Comparison of the relative errors associated with predictions of specimen compositions for the three major elements were made comparing the Relative Sensitivity Factors analysis using global RSF values to the Bond Breaking results using average emission coefficients. The Bond Breaking analysis provided superior results with a lower sum of errors for the three major elements provided the 0 eV energy offset conditions were applied. At higher energy offsets the error in prediction increased to a point where the two models were closely matched. At this point results varied on an alloy to alloy basis.

CHAPTER 6

CONCLUSIONS AND RECOMMENDATIONS

6.1 CONCLUSIONS

Based upon the results of this investigation a number of conclusions may be drawn. These summarize the different aspects of the investigation including experimental procedure, Relative Sensitivity Factors results, and Bond Breaking model results. As such this investigation provided data that allowed the author to conclude:

- The oxygen saturation plateau of the Cameca Ims-3f used in this study for the alloy system investigated spanned the pressure range of 2.0×10^{-8} to 1.6×10^{-7} torr PO_2 (6.3×10^{-8} to 4.0×10^{-7} torr total pressure). No further pressure increases were made for fear of corrupting the system vacuum.
- RSF values were in surprisingly close agreement with those obtained by Newbury et al. given the differences in sample composition and analysis conditions. This agreement confirms the validity of RSF values calculated in this study.
- RSF values obtained for the two data sets in this investigation were in general agreement with each other for all energies but were in closest agreement in the 80 eV offset energy range where the most accurate approximations of the alloy compositions were also obtained.
- RSF's for a given element combination consistently exhibited a characteristic curve shape when plotted versus energy offset for the different alloys in this study.

Although some values of RSF's varied the curves were almost identical in shape for both data sets studied.

- Characteristic RSF versus energy curve shapes are determined by the characteristic secondary on distributions of the two elements being ratiod and are thus an intrinsic property of the element combination for a given SIMS instrument.
- Relative position and slope of the RSF curves with respect to one another is a function of the composition of the sample studied.
- RSF values exhibit the least variation (are the most stable) between energies in the intermediate (80-120 eV) energy range.
- RSF values exhibited the most variation between energies in the 0 to 40 eV energy offset regime. This variation is attributed to mass interferences not accounted for, error in peak location, steep secondary ion distribution shape near 0 eV combined with window centering on the peak and with differences in secondary ion distribution shapes between elements.
- Specimen composition prediction using RSF's was generally most consistently accurate in the 40 to 80 eV energy offset range. This is likely due to reduced mass interferences, the gentle secondary ion distribution curve shapes (reduced energy window centering effects), and sufficiently intense secondary ion signals for statistical reliability.
- Bond breaking relative emission coefficients (α values) exhibited similar curve shapes when plotted versus secondary ion energy offset (particularly true for the three most abundant elements present). Despite some variation in calculated values this indicates reproducibility in nature.

- Relative emission curve shapes for Mn and Si were more erratic than those for Fe, Cr, and Ni. The curves for these less abundant elements did however exhibit similarities. Variations were attributed to lower count rates, and accompanying least squares regression effects.
- Relative emission coefficients were observed to be a maximum at 0 eV energy offset. The magnitude of the α values for most element combinations dropped to zero as energy offset increased to 80 eV. At energy offsets above 80 eV the α values for some element combinations remained at or near zero while others began to increase in magnitude as energy approached 160 eV.
- Relative emission coefficient curve shapes for the three major elements present (Fe, Cr, Ni) were observed to be similar for bond breaking analyses based both upon the 3 element model and the 5 element model which includes Mn and Si. This similarity confirms the validity of results obtained and also the stability and reproducibility of the regression technique.
- The overall trend in relative error in the predicted composition of specimen D850 is believed to be a result of the superposition of two effects. Relative error is thought to increase with energy offset - likely as a result of signal strength effects on statistical accuracy. Secondly, results in the 80 eV energy offset range appear erratic, likely as a result of α values approaching zero. The reduced enhancement effect observed at higher energy offsets in conjunction with these observations may yield some insight to the ionization process.

- Trends observed in the relative error of predicted composition versus energy are similar for both the three and five element predictions for each data set again reflecting stability and reproducibility of the numerical analysis.
- Approximations of the composition of the alloys using the bond breaking model with average emission coefficients were more accurate than those performed using the relative sensitivity factors approach at the 0 Ev enrgy offset. At higher energy offsets the errors became more closely matched, possibly due to the reduced enhancement effect at and above intermediate energy offsets and the two numerical best fits required. Low count rate induced error for less abundant elements, particularly at high energy offsets may compound this problem during regression. These sources of error then begin to match the error in the RSF model introduced by using an average set of global RSF values.
- The bond breaking model appears more "fragile" as it is more susceptible to magnification of errors during analysis due to the extensive modeling required - however, if used carefully in the low energy offset range where it performs best the results attained are superior the RSF method using global RSF values.
- Bond breaking results tend to become more erratic at intermediate energy offsets whereas relative sensitivity factors results tend to improve at intermediate energies.
- For both models, the relative error in predicted composition improved with an increase in elemental composition, particularly in the low concentration range. This improvement was not as consistent or as smooth with increasing concentration as expected. This erratic improvement may be a result of differing enhancement, supression effects arising from different quantities of alloying elements present.

Surface roughness may also play a role in this erratic behaviour.

6.2 RECOMMENDATIONS

The conclusions of this study are based upon the results of two data sets based upon the analysis of a set of stainless steel standards and thus bear further investigation. A repeat analysis of the alloy system performed while ensuring similar total counts for each element will reduce statistical influences on the numerical analysis and results gathered. Even though longer count times were used for less intense signals in this study such an investigation would further remove any statistical influences and may expose any systematic or experimental errors that may have been present in this investigation.
Analysis of other alloy systems possessing a variety of matrix types will determine if the observations made in this investigation are unique or can be applied to other investigations.

Based upon the results of this study it appears evident that in order to optimize numerical analysis for quantitative SIMS investigations the effects of secondary ion energy upon the model used in the analysis is an experimental parameter which should be given full consideration. Relative sensitivity factors investigations may indeed benefit from the use of an energy offset from the distribution peak while such an offset may be detrimental to a bond breaking analysis.

APPENDIX A:

MEASURED INTENSITY VALUES CORRECTED FOR ISOTOPIC ABUNDANCE AND PRIMARY ION BEAM INTENSITY

Corrected Intensity Values For Specimen D845 Using Normalized Intensities

Element	Correction Factor	0 eV Offset Average	40 eV Offset Average	80 eV Offset Average	120 eV Offset Average	160 eV Offset Average
Cr	1.193474	925775.47	96017.862	14345.136	4149.7793	1743.6655
Fe-a	1.090275	2192370.1	335718.89	54296.08	16886.564	7048.5637
Mn	1	57136.088	4029.7647	668.29412	205.79412	86.088235
Mo	10.38422	1061.814	240.36258	101.33898	30.265207	12.301263
Nb	1	366.27049	185.02498	48.681878	16.133276	6.3461313
Ni	27.51789	9499.0556	407.63023	77.303828	22.663371	16.143771
Si	32.25806	5274.0031	1363.1877	300.56922	105.50283	44.022764
Ti	12.5	3284.8529	233.08824	50	17.647059	7.9411765
Fe-b	1.090275	2192369.3	335513.03	54606.939	16750.875	6966.5082
Cu	1.4457135	1620.1275	66.343184	9.664004	2.9359	1.46795

Correction Ratio For B Sample = 2192370 / 2159159 = 1.0153814

Figure A.1: Corrected Elemental Intensity Values For Specimen D845

Corrected Intensity Values For Specimen D846 Using Normalized Intensities

Element	Correction Factor	0 eV Offset Average	40 eV Offset Average	80 eV Offset Average	120 eV Offset Average	160 eV Offset Average
Cr	1.193474	586757.87	92539.025	15270.781	4658.1992	1972.2509
Fe-a	1.090275	1124185.9	202480.61	35452.536	11400.364	4859.5481
Mn	1	18572.647	2098.5	372.70588	115.11765	51.294118
Mo	10.38422	262.16906	110.09505	40.790884	14.059124	5.9403911
Nb	1	526.3805	550.03516	158.40326	51.056305	21.795465
Ni	27.51789	123767.62	11313.366	2158.2102	710.58796	333.72762
Si	32.25806	6304.743	2557.1154	594.68682	213.2827	94.876647
Ti	12.5	13148.237	2227.6471	465.29412	142.20588	7.9411765
Fe-b	1.090275	1124185.9	212505.23	37676.223	12127.264	5133.5673
Cu	1.4457135	3106.588	172.89147	26.382386	8.0635819	3.3494879

Correction Ratio For B Sample = 1124186 / 1091753 = 1.029707

Figure A.2: Corrected Elemental Intensity Values For Specimen D846

Corrected Intensity Values For Specimen D847 Using Normalized Intensities

Element	Correction Factor	0 eV Offset Average	40 eV Offset Average	80 eV Offset Average	120 eV Offset Average	160 eV Offset Average
Cr	1.193474	1563962.3	174744.95	27849.365	8360.496	3504.3907
Fe-a	1.090275	1996081	275336.06	46566.222	14660.671	6102.0768
Mn	1	20589.441	1307.1765	224.32353	70.705882	28.705882
Mo	10.38422	602.66081	17.427522	8.1055272	2.6341596	1.2158595
Nb	1	30.852483	39.458394	13.728477	4.6249453	2.10757
Ni	27.51789	368214.91	24535.798	4641.2814	1493.7161	659.54203
Si	32.25806	4620.8722	1139.2788	284.25043	104.36431	40.227698
Ti	12.5	3081.7647	102.05882	10	2.3529412	1.1764706
Fe-b	1.090275	1996081.8	286769.29	49519.724	15624.229	6511.3506
Cu	1.4457135	5160.1238	236.09571	34.997518	11.129803	4.4011389

Correction Ratio For B Sample = 1996081 / 1950479 = 1.0537846

Figure A.3: Corrected Elemental Intensity Values For Specimen D847

Corrected Intensity Values For Specimen D849 Using Normalized Intensities

Element	Correction Factor	0 eV Offset Average	40 eV Offset Average	80 eV Offset Average	120 eV Offset Average	160 eV Offset Average
Cr	1.19	246712.77	33498.639	5549.5839	1722.3936	748.23799
Fe-a	1.09	1509219.5	278625.1	50395.397	16492.462	7139.6338
Mn	1.00	71828.147	7117.9706	1242.7059	403.64706	176.55882
Mo	10.38	332.84316	33.907929	16.953965	4.8716341	1.5591801
Nb	1.00	392.51547	277.04656	75.384138	26.488601	13.089479
Ni	27.52	90285.426	8807.0349	1747.2161	610.39469	254.69261
Si	32.26	3781.7832	1380.2655	308.15935	120.30359	54.269442
Ti	12.50	4964.7059	502.5	93.382353	31.911765	13.970588
Fe-b	1.09	1509219.1	296372.98	53606.728	17492.663	7410.0625
Cu	1.45	2705.6322	177.88217	27.022138	8.83103	3.1335913

Correction Ratio For B Sample = 1509219 / 1489294 = 1.0133792

Figure A.4: Corrected Elemental Intensity Values For Specimen D849

Corrected Intensity Values For Specimen D850 Using Normalized Intensities

Element	Correction Factor	0 eV Offset Average	40 eV Offset Average	80 eV Offset Average	120 eV Offset Average	160 eV Offset Average
Cr	1.19	116290.14	14510.257	2313.5845	716.0142	304.47628
Fe-a	1.09	1137527.6	188970.7	32897.701	10916.346	4650.6001
Mn	1.00	9686.9706	887.32353	176.35294	58.441176	25.882353
Mo	10.38	91.837882	26.701822	9.9118376	2.8322137	1.4158034
Nb	1.00	96.456137	86.901106	26.415131	10.080996	4.3538214
Ni	27.52	275713.71	26856.285	5370.2921	1794.3858	817.26731
Si	32.26	820.87275	168.88043	40.227698	14.041744	5.6925988
Ti	12.50	3601.1765	452.20588	94.852941	34.705882	13.088235
Fe-b	1.09	1137527.5	202472.93	36684.519	11957.188	5073.7271
Cu	1.45	3806.2823	259.37907	40.047453	12.039582	5.111542

Correction Ratio For B Sample = 1137528 / 1081372 = 1.0519302

Figure A.5: Corrected Elemental Intensity Values For Specimen D850

Corrected Intensity Values For Specimen S845 Using Normalized Intensities

Element	Correction Factor	0 eV Offset Average	40 eV Offset Average	80 eV Offset Average	120 eV Offset Average	160 eV Offset Average
Cr	1.19	683885.59	75825.194	12372.745	3800.0212	1578.2641
Fe-a	1.09	1403028.2	237435.34	42962.286	13849.763	5896.9127
Mn	1.00	48328.294	3609.0294	637.58824	197.5	81.294118
Mo	10.38	761.88458	191.16987	73.598722	25.712906	9.8754328
Nb	1.00	589.80861	227.18694	52.914289	17.037002	6.8901618
Ni	27.52	21300.68	337.72983	61.324628	18.367763	7.1101018
Si	32.26	4080.4548	779.12703	178.3681	67.172666	28.842501
Ti	12.50	12505.001	910	169.41176	49.264706	19.264706
Fe-b	1.09	1403027.8	226744.97	40896.26	13011.139	5514.99
Cu	1.45	1769.4748	51.868278	9.5720903	3.035053	1.2840609

Correction Ratio For B Sample = 1403028 / 1448019 = 0.9689293

Figure A.6: Corrected Elemental Intensity Values For Specimen S845

Corrected Intensity Values For Specimen S846 Using Normalized Intensities

Element	Correction Factor	0 eV Offset Average	40 eV Offset Average	80 eV Offset Average	120 eV Offset Average	160 eV Offset Average
Cr	1.19	841968.04	107664.48	18192.405	5616.4184	2334.0841
Fe-a	1.09	1270918.9	211610.64	38163.922	12313.309	5215.2343
Mn	1.00	26669.559	2179.6176	408.32353	131.64706	56.029412
Mo	10.38	1122.0359	98.058383	39.636438	13.525294	5.6355393
Nb	1.00	938.25074	531.82104	153.34051	53.022007	22.495007
Ni	27.52	169888.81	10008.78	1940.5266	639.47474	260.15063
Si	32.26	9295.6344	1993.5481	483.49139	180.64514	79.316877
Ti	12.50	23166.472	1770.7353	382.20588	138.52941	64.117647
Fe-b	1.09	1270919.2	198942.83	36812.698	11743.127	5014.7306
Cu	1.45	4111.0654	138.5197	22.557017	7.179016	2.9029901

Correction Ratio For B Sample = 1270919 / 1301020 = 0.9768638

Figure A.7: Corrected Elemental Intensity Values For Specimen S846

Corrected Intensity Values For Specimen S847 Using Normalized Intensities

Element	Correction Factor	0 eV Offset Average	40 eV Offset Average	80 eV Offset Average	120 eV Offset Average	160 eV Offset Average
Cr	1.19	1030117.7	136691.88	23185.409	7253.2329	3068.0706
Fe-a	1.09	1242705.3	198892.65	36015.567	11649.46	4979.9914
Mn	1.00	12842.676	1012.2941	200.23529	64.647059	27.088235
Mo	10.38	337.75351	13.579175	4.7811411	2.4861016	0.5737599
Nb	1.00	23.454922	26.714852	8.481344	2.6245201	1.4918325
Ni	27.52	214625.75	14122.221	2851.7513	955.44921	410.82492
Si	32.26	3529.4113	685.7684	163.94685	57.305495	23.529408
Ti	12.50	2173.5294	33.970588	5	2.7941176	6.7647059
Fe-b	1.09	1242705	181776.45	33836.42	11010.312	4672.0529
Cu	1.45	2713.207	129.3658	21.727383	6.470287	3.1153234

Correction Ratio For B Sample = 1270919 / 1301020 = 0.9945553

Figure A.8: Corrected Elemental Intensity Values For Specimen S847

Corrected Intensity Values For Specimen S849 Using Normalized Intensities

Element	Correction Factor	0 eV Offset Average	40 eV Offset Average	80 eV Offset Average	120 eV Offset Average	160 eV Offset Average
Cr	1.19	233008.11	29813.893	5147.313	1636.3933	688.28348
Fe-a	1.09	1236088.1	238100.8	45637.052	15155.656	6558.9661
Mn	1.00	65116.735	6015.7353	1117.8235	361.41176	155.5
Mo	10.38	441.252	28.860033	14.050376	3.9872151	2.8480108
Nb	1.00	376.01503	213.95283	64.534162	23.696352	10.559138
Ni	27.52	81123.996	6380.9629	1342.1848	459.47038	204.37677
Si	32.26	4354.4586	909.67729	242.88422	90.702075	45.161284
Ti	12.50	5769.2647	380.58824	87.5	30.882353	13.382353
Fe-b	1.09	1236087.5	221502.8	43175.314	14238.612	6201.9051
Cu	1.45	2310.6795	122.79797	18.516839	5.9872435	2.6169409

Correction Ratio For B Sample = 1270919 / 1301020 = 0.9873485

Figure A.9: Corrected Elemental Intensity Values For Specimen S849

Corrected Intensity Values For Specimen S850 Using Normalized Intensities

Element	Correction Factor	0 eV Offset Average	40 eV Offset Average	80 eV Offset Average	120 eV Offset Average	160 eV Offset Average
Cr	1.19	160617.1	18297.431	3033.1791	944.17834	397.42684
Fe-a	1.09	1230286.1	229546.43	43401.731	14008.751	5941.3574
Mn	1.00	11731.706	1019.2647	211.97059	69.176471	30.441176
Mo	10.38	261.31919	27.62996	12.842184	4.0861496	0.5837357
Nb	1.00	87.271804	52.728471	15.346346	5.6494791	2.2766558
Ni	27.52	354495.48	26356.101	5361.8059	1825.0126	768.18211
Si	32.26	1208.7285	151.42313	31.11954	14.041744	7.5901318
Ti	12.50	2341.0294	194.55882	46.029412	16.470588	8.3823529
Fe-b	1.09	1230285.5	214915.55	40512.072	13067.548	5520.3089
Cu	1.45	4395.5929	214.22491	37.180538	12.027802	5.4450186

Correction Ratio For B Sample = 1270919 / 1301020 = 1.0118474

Figure A.10: Corrected Elemental Intensity Values For Specimen S850

APPENDIX B:

RELATIVE SENSITIVITY FACTORS RESULTS PRESENTED IN GRAPHICAL FORM

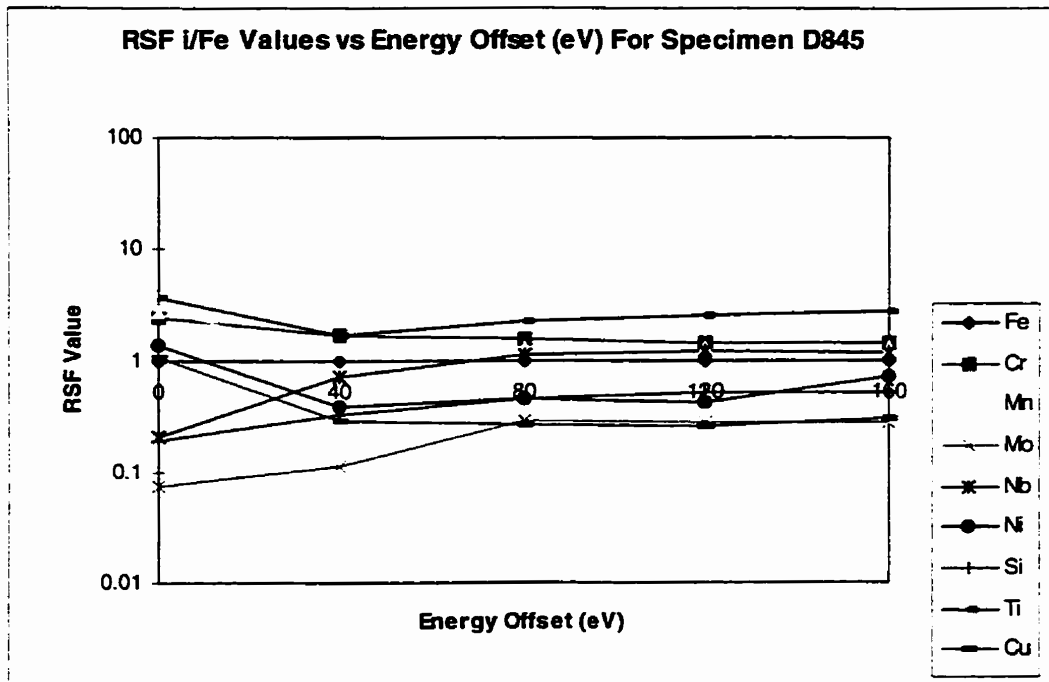

Figure B.1: RSF Values (Calculated With Respect To Iron) Versus Energy For Sample D 845

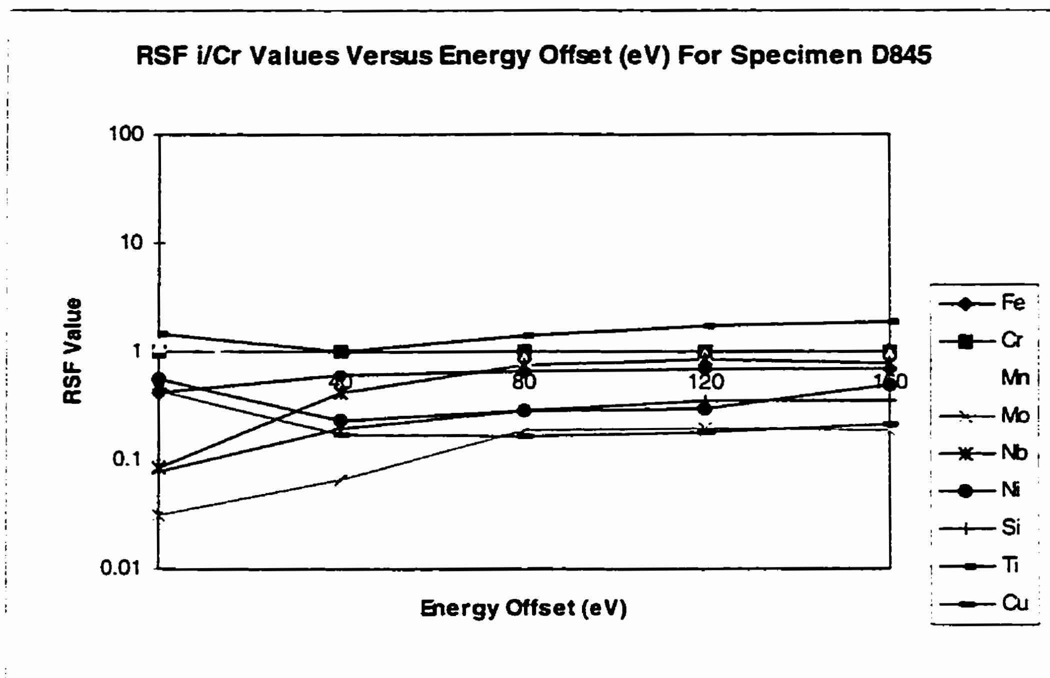

Figure B.2: RSF Values (Calculated With Respect To Chromium) Versus Energy For Sample D 845

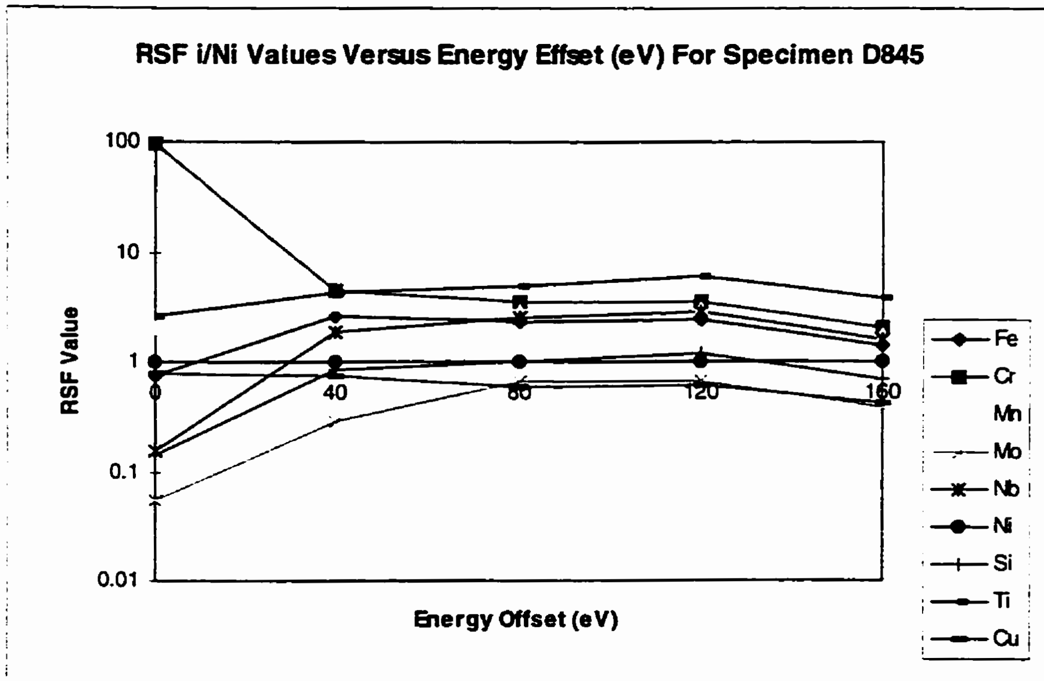

Figure B.3: RSF Values (Calculated With Respect To Nickel) Versus Energy For Sample D 845

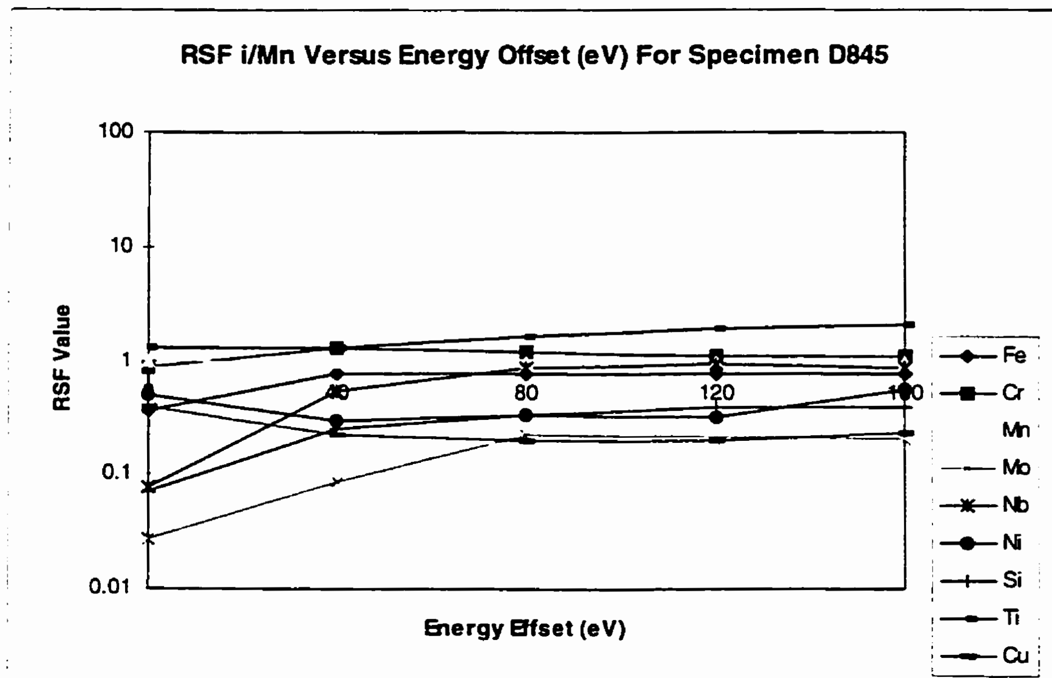

Figure B.4: RSF Values (Calculated With Respect To Manganese) Versus Energy For Sample D 845

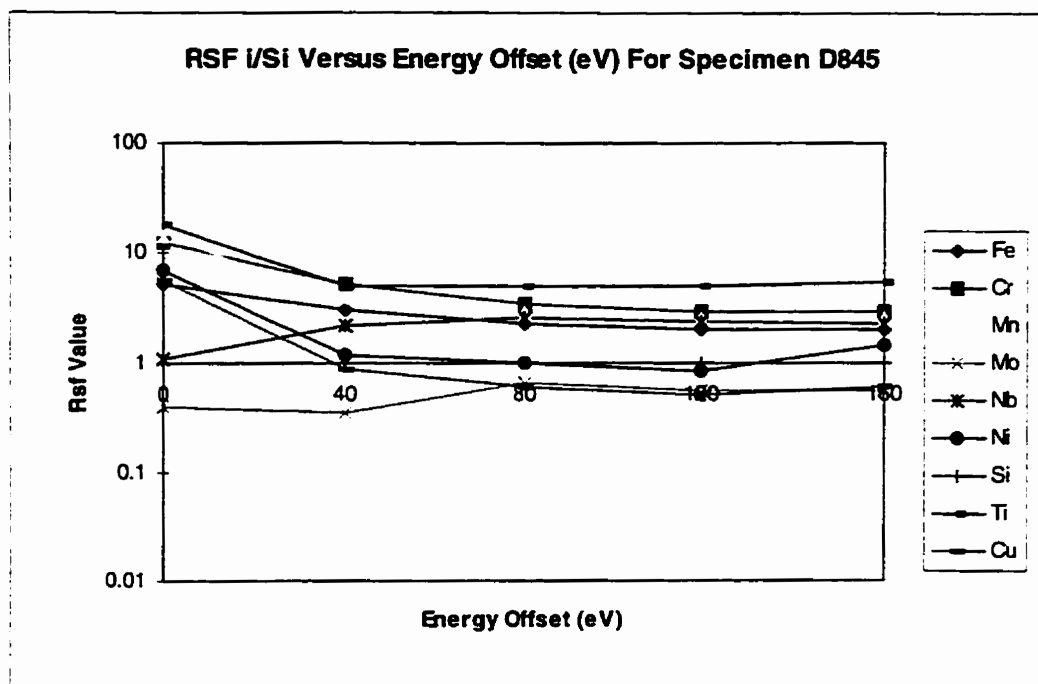

Figure B.5: RSF Values (Calculated With Respect To Silicon) Versus Energy For Sample D 845

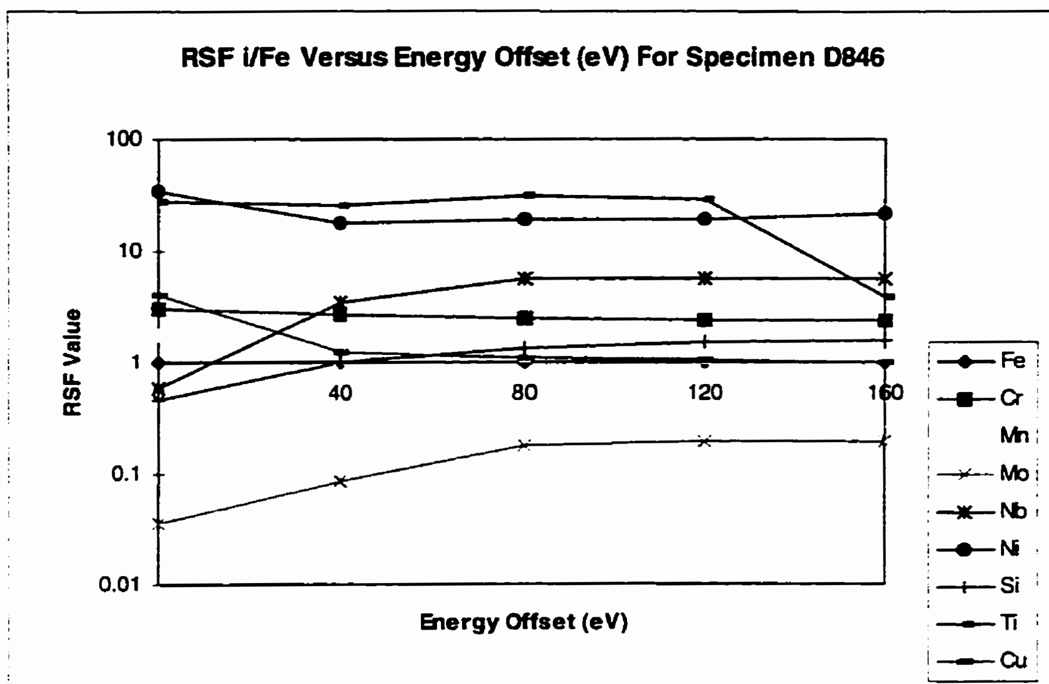

Figure B.6: RSF Values (Calculated With Respect To Iron) Versus Energy For Sample D 846

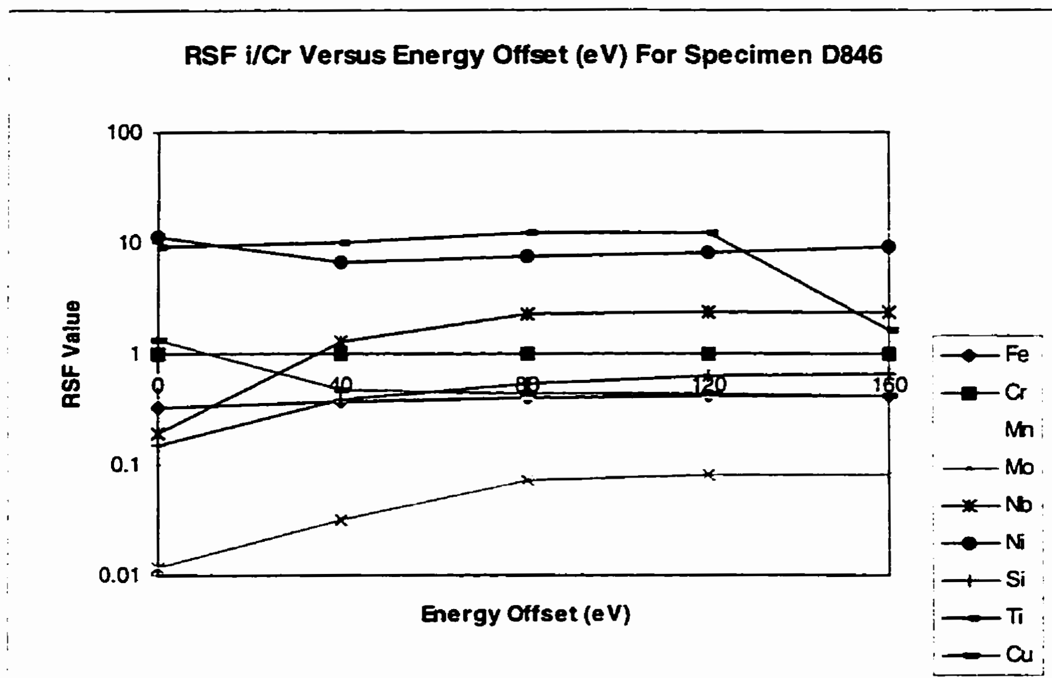

Figure B.7: RSF Values (Calculated With Respect To Chromium) Versus Energy For Sample D 846

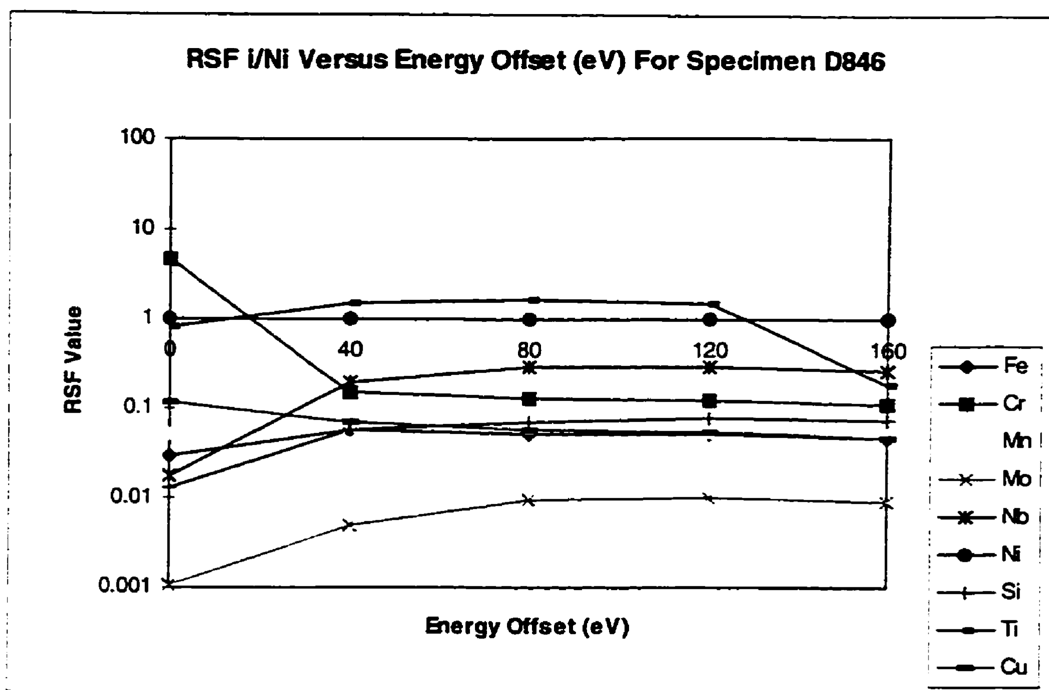

Figure B.8: RSF Values (Calculated With Respect To Nickel) Versus Energy For Sample D 846

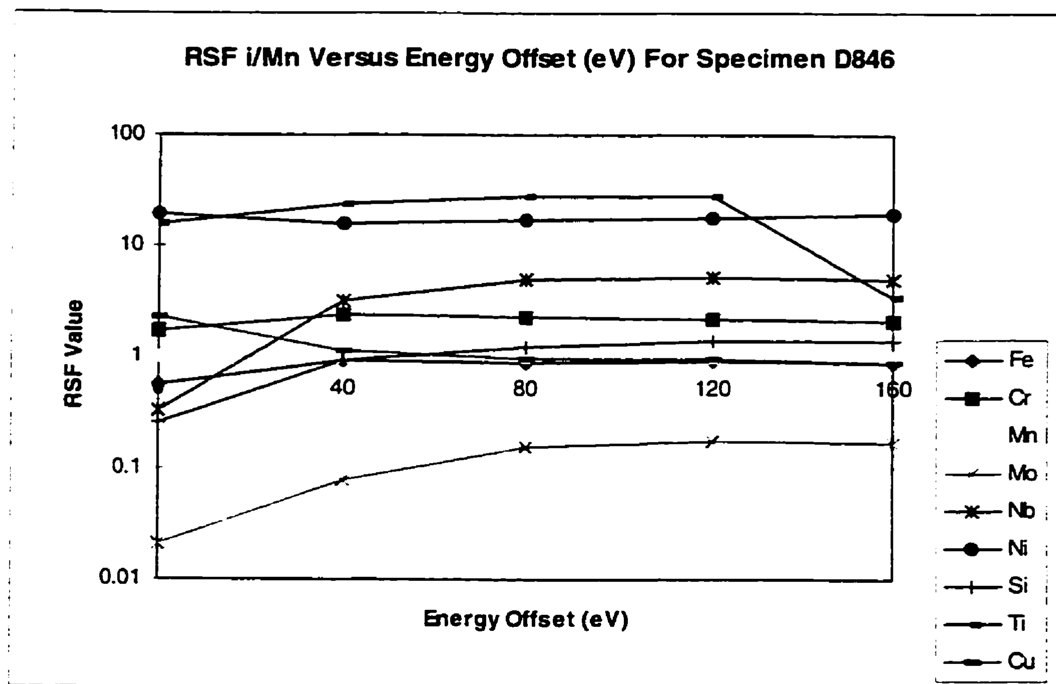

Figure B.9: RSF Values (Calculated With Respect To Manganese) Versus Energy For Sample D 846

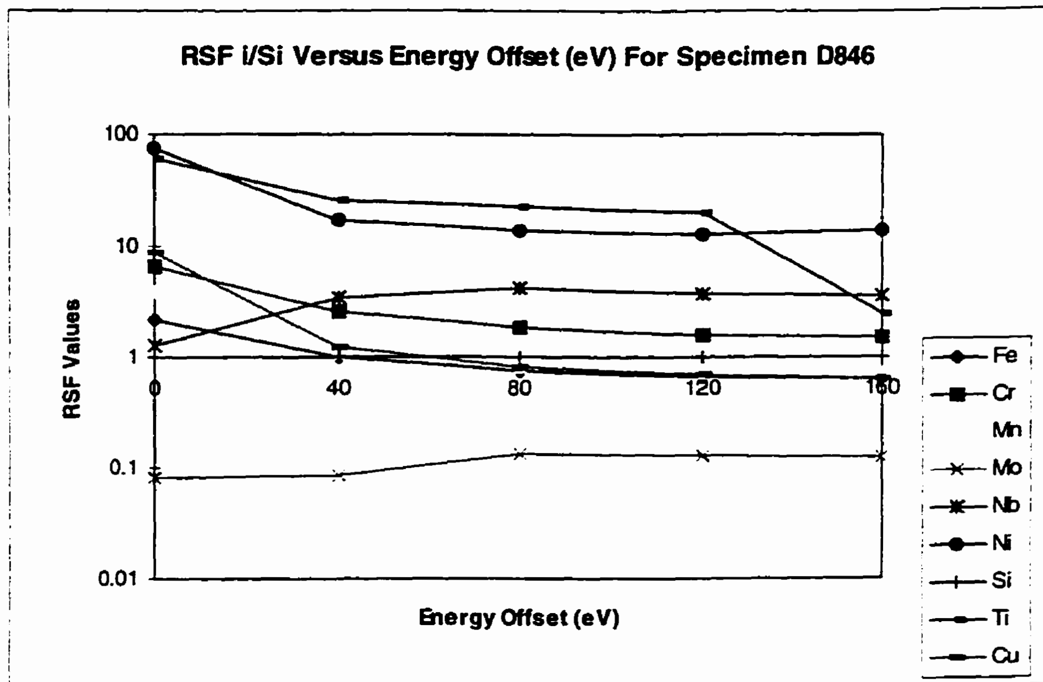

Figure B.10: RSF Values (Calculated With Respect To Silicon) Versus Energy For Sample D 846

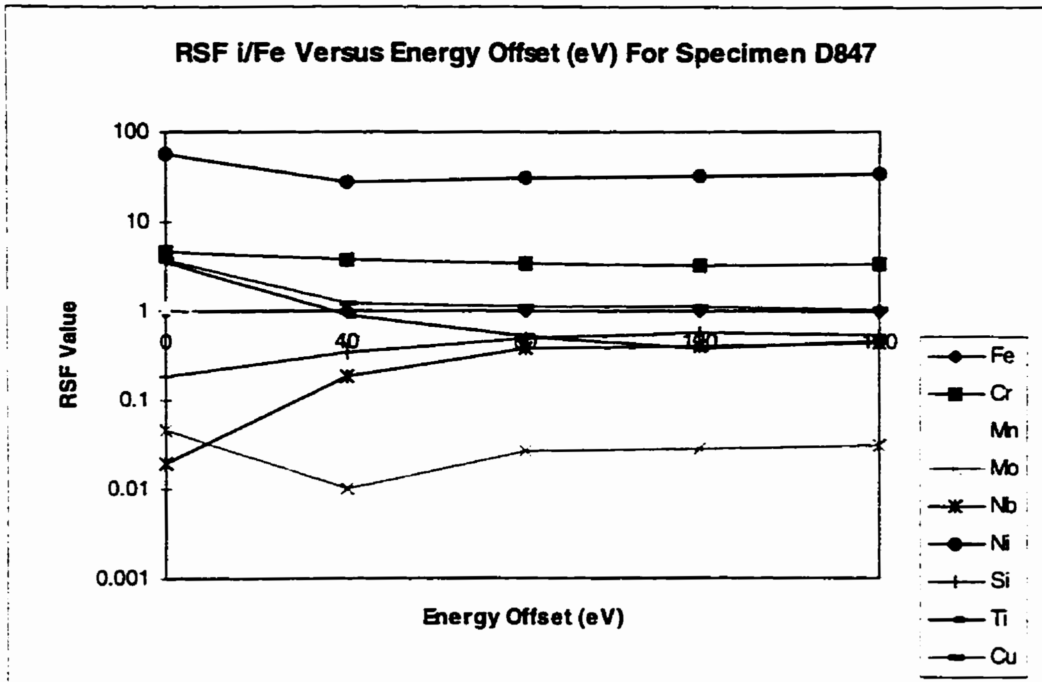

Figure B.11: RSF Values (Calculated With Respect To Iron) Versus Energy For Sample D 847

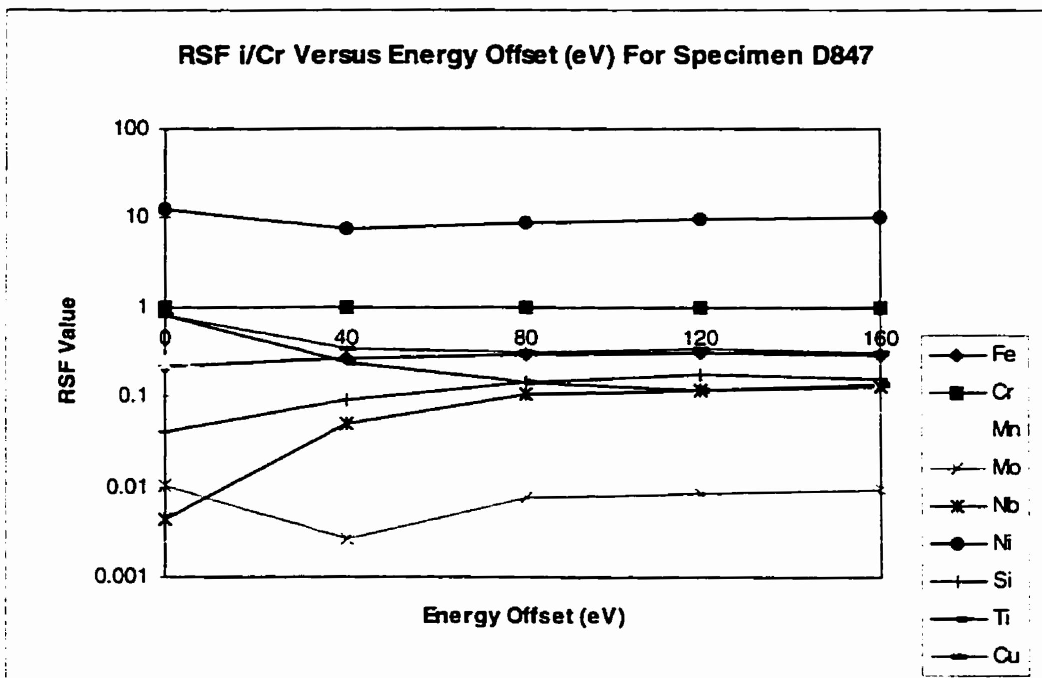

Figure B.12: RSF Values (Calculated With Respect To Chromium) Versus Energy For Sample D 847

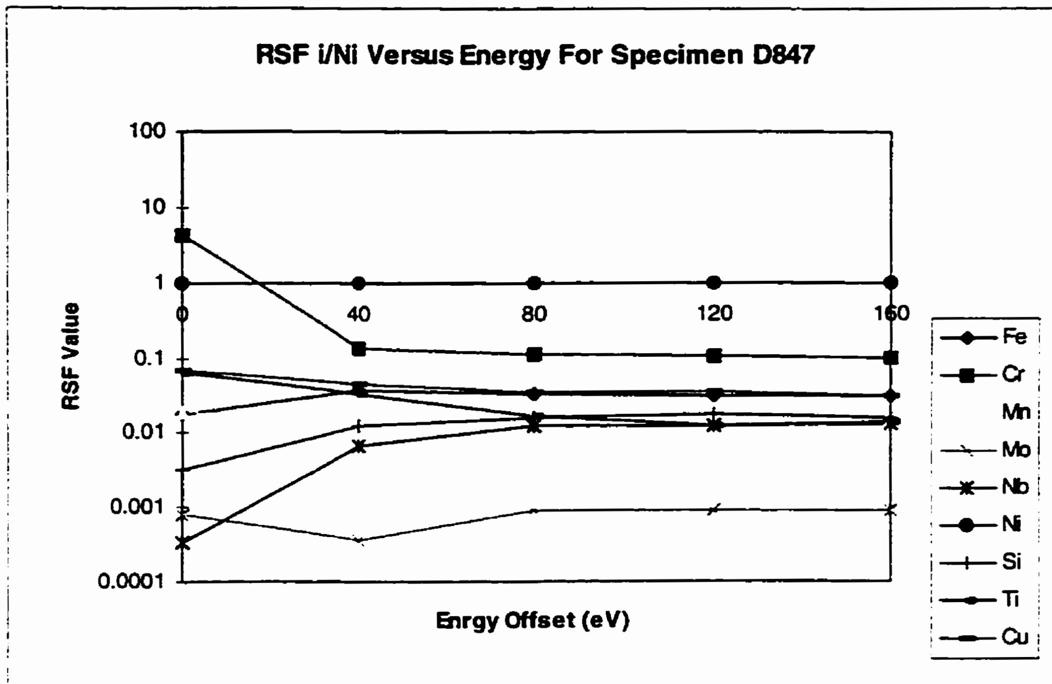

Figure B.13: RSF Values (Calculated With Respect To Nickel) Versus Energy For Sample D 847

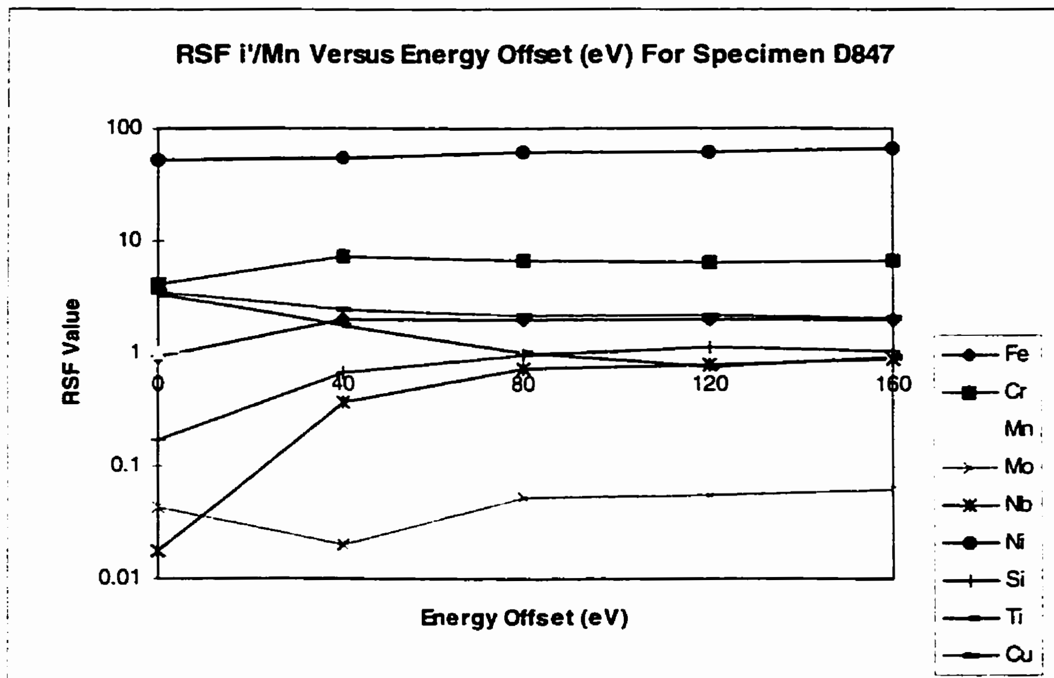

Figure B.14: RSF Values (Calculated With Respect To Manganese) Versus Energy For Sample D 847

NOTE TO USERS

Page(s) not included in the original manuscript are unavailable from the author or university. The manuscript was microfilmed as received.

UMI

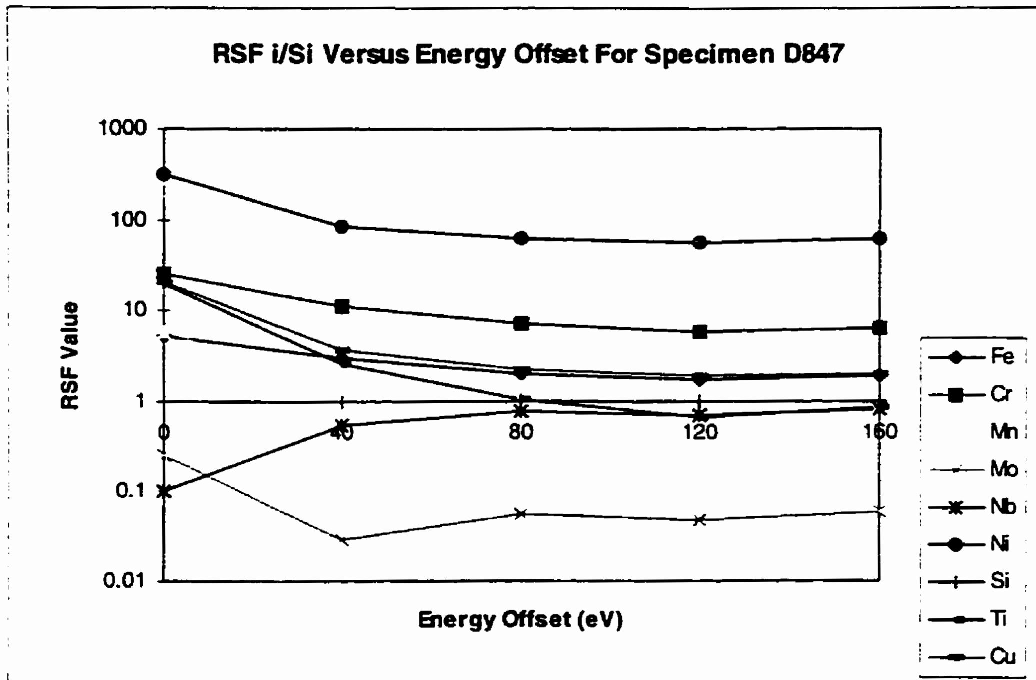

Figure B.15: RSF Values (Calculated With Respect To Silicon) Versus Energy For Sample D 847

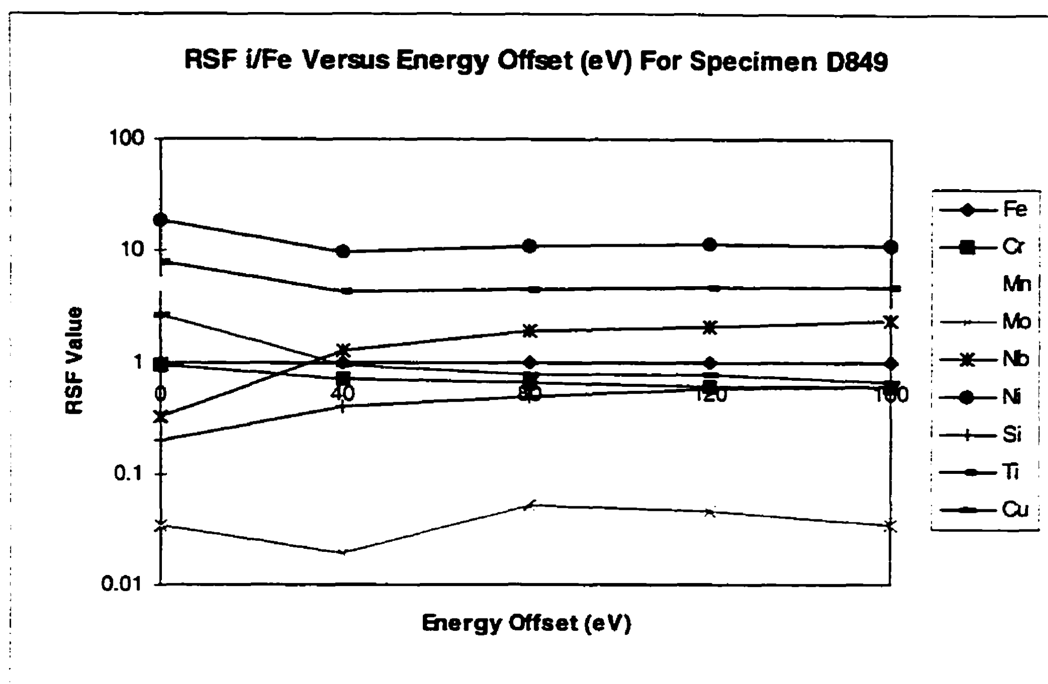

Figure B.16: RSF Values (Calculated With Respect To Iron) Versus Energy For Sample D 849

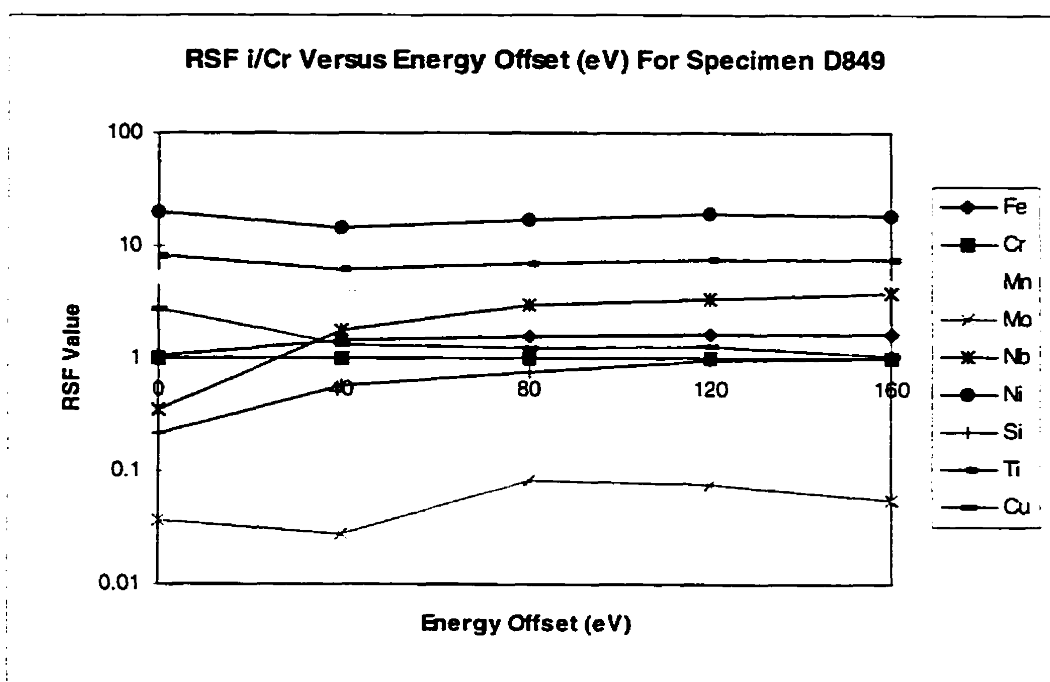

Figure B.17: RSF Values (Calculated With Respect To Chromium) Versus Energy For Sample D 849

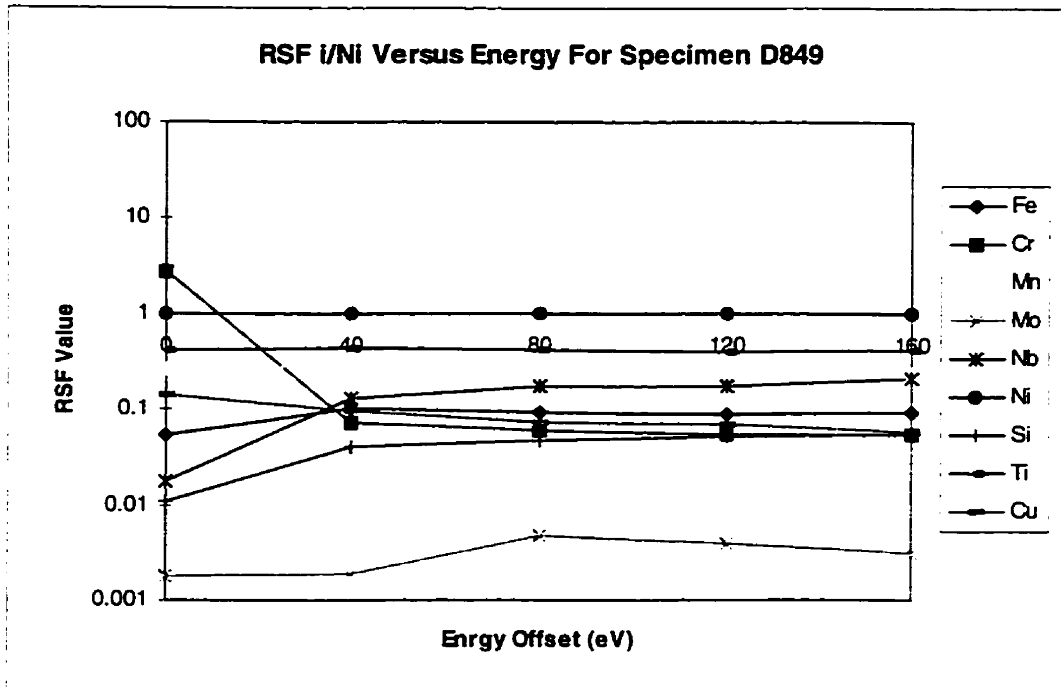

Figure B.18: RSF Values (Calculated With Respect To Nickel) Versus Energy For Sample D 849

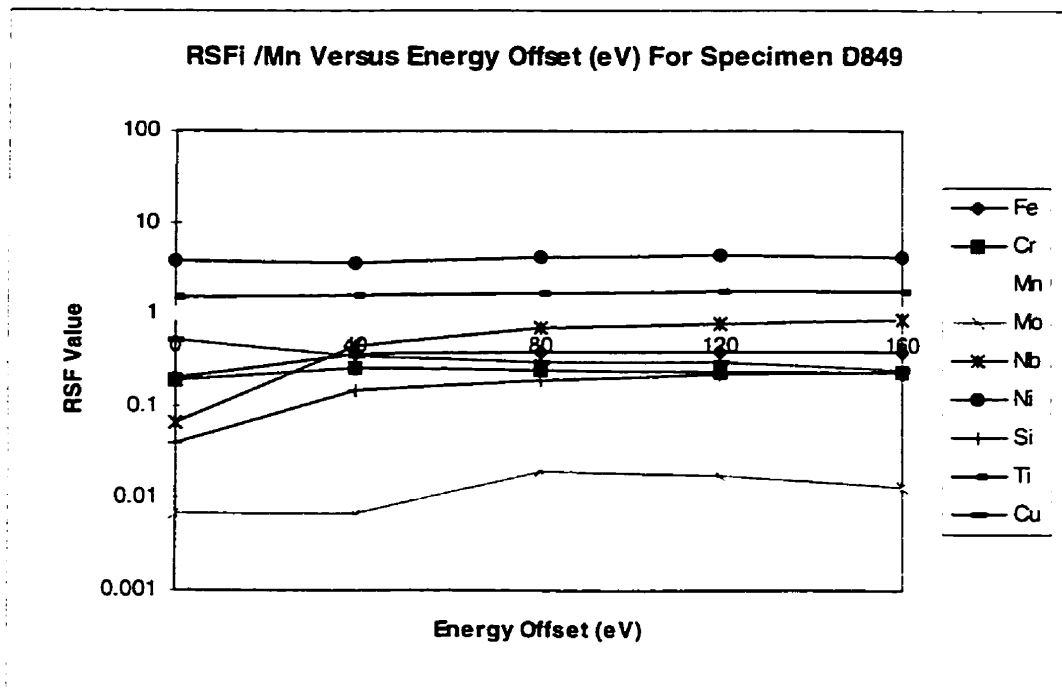

Figure B.19: RSF Values (Calculated With Respect To Manganese) Versus Energy For Sample D 849

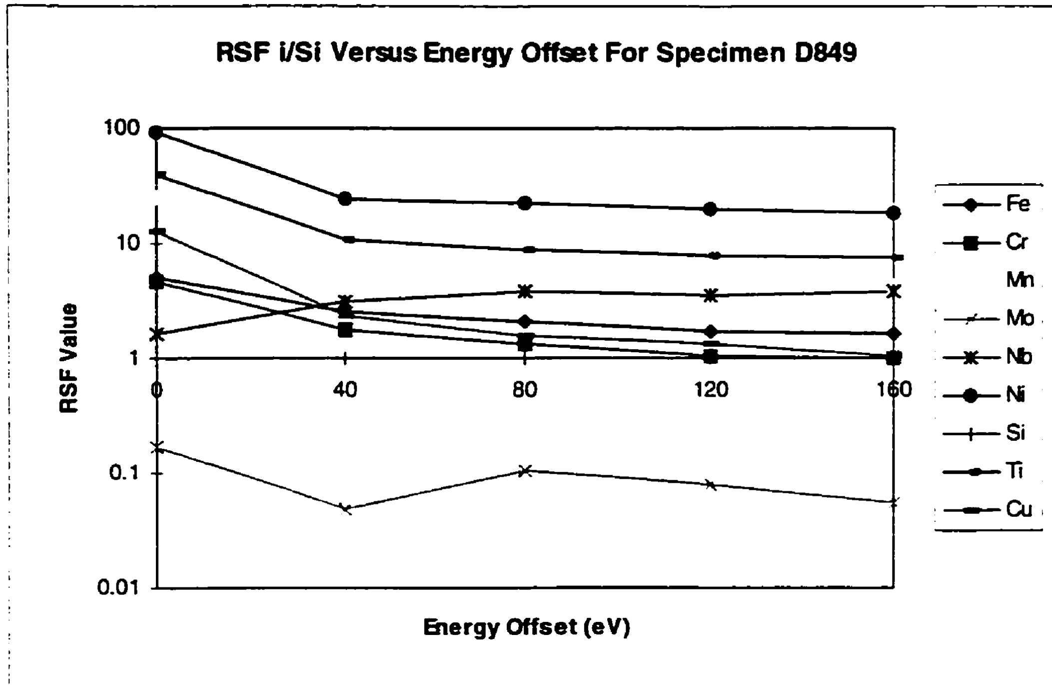

Figure B.20: RSF Values (Calculated With Respect To Silicon) Versus Energy For Sample D 849

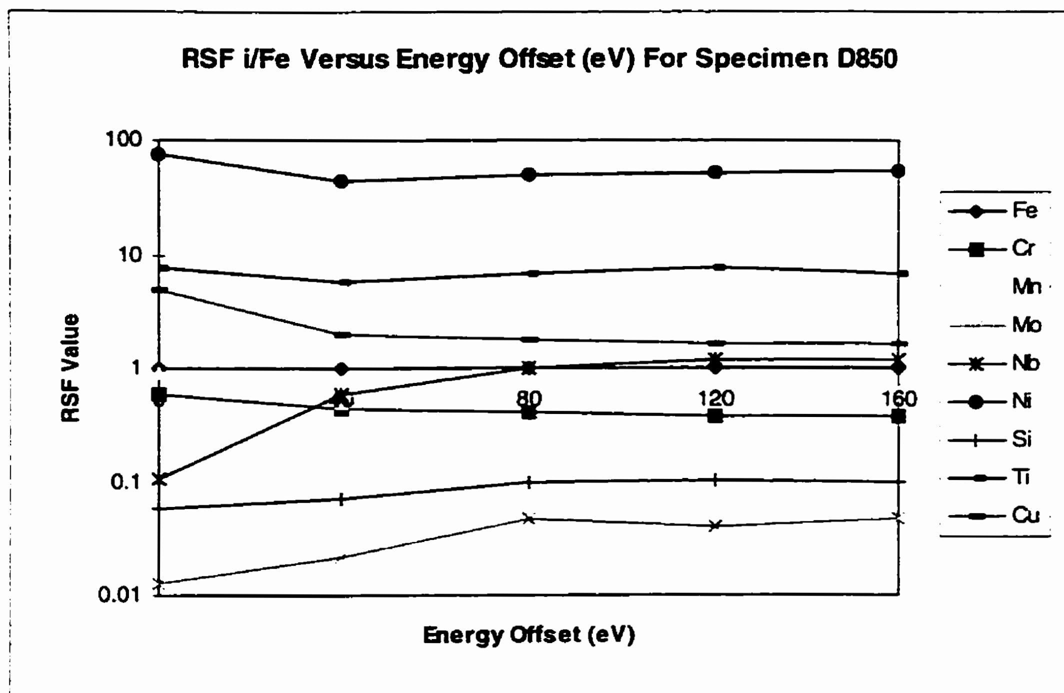

Figure B.21: RSF Values (Calculated With Respect To Iron) Versus Energy For Sample D 850

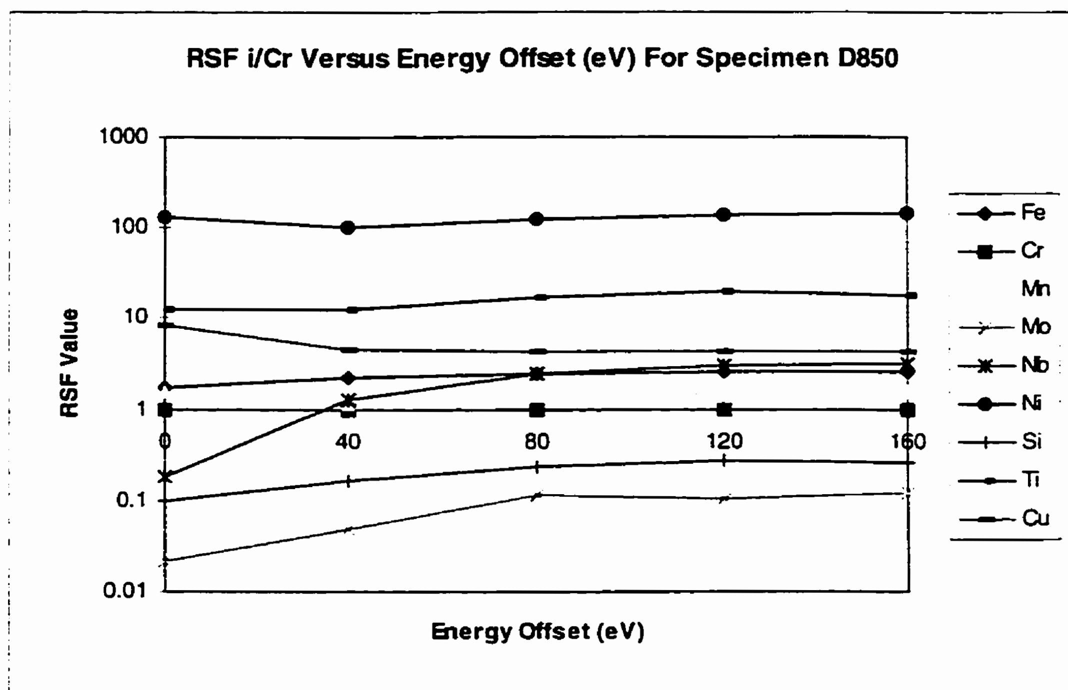

Figure B.22: RSF Values (Calculated With Respect To Chromium) Versus Energy For Sample D 850

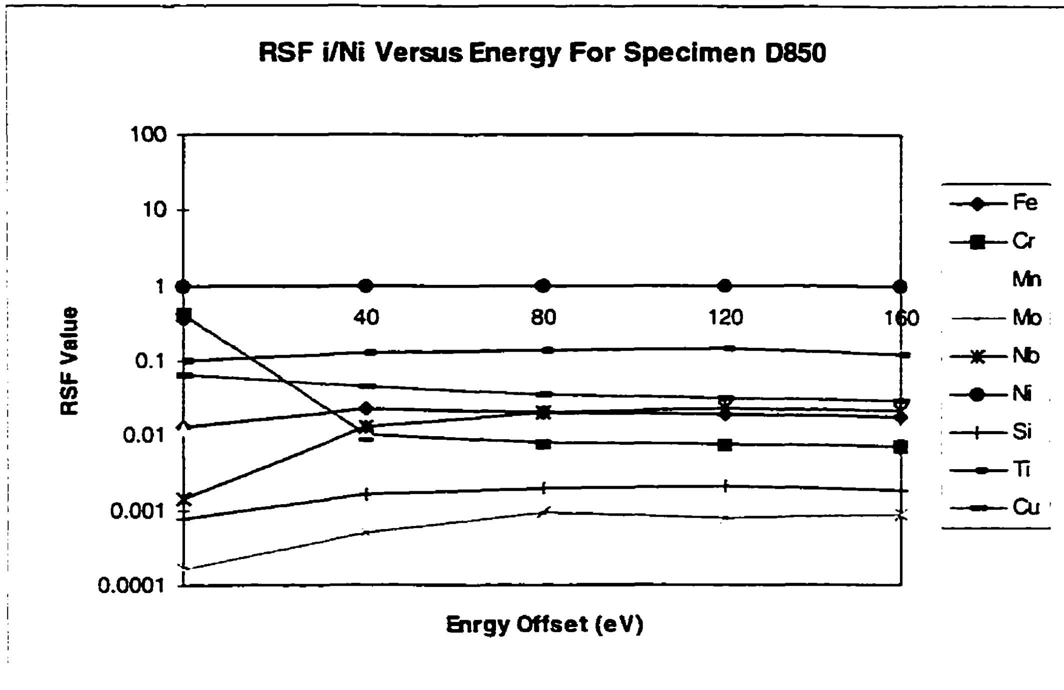

Figure B.23: RSF Values (Calculated With Respect To Nickel) Versus Energy For Sample D 850

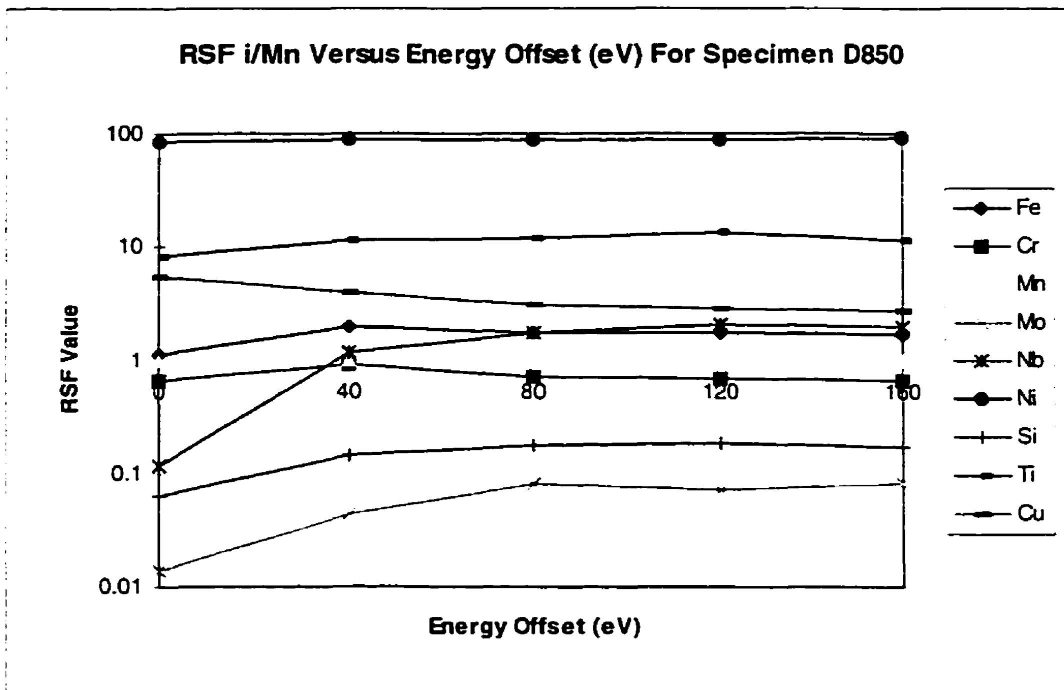

Figure B.24: RSF Values (Calculated With Respect To Manganese) Versus Energy For Sample D 850

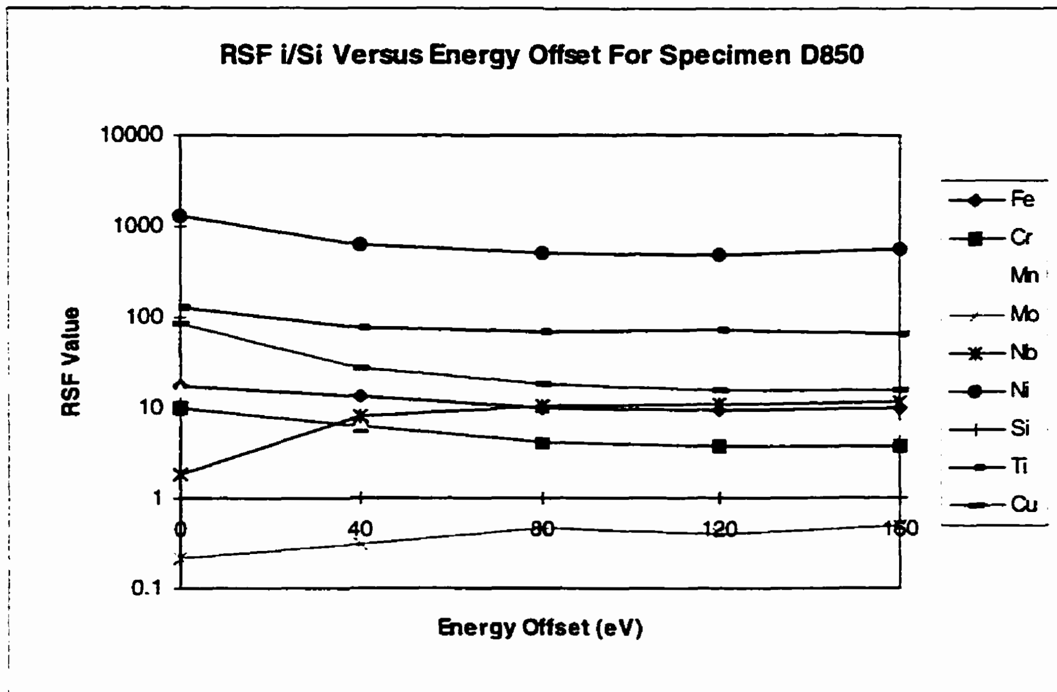

Figure B.25: RSF Values (Calculated With Respect To Silicon) Versus Energy For Sample D 850

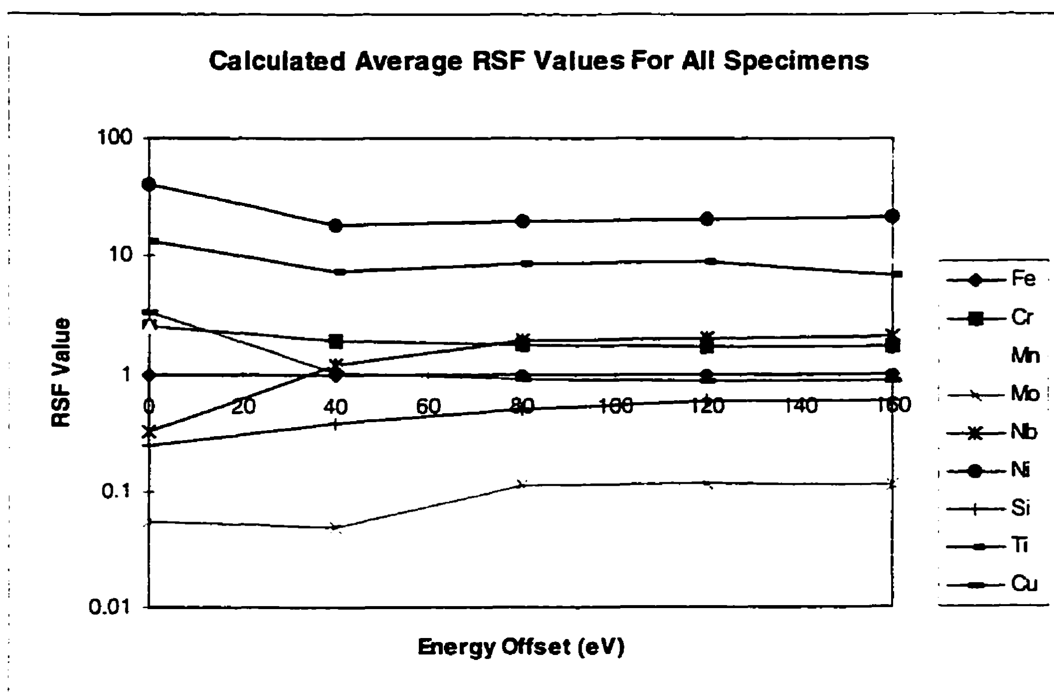

Figure B.26: Average RSF Values Calculated From All Alloys of Both Data Sets

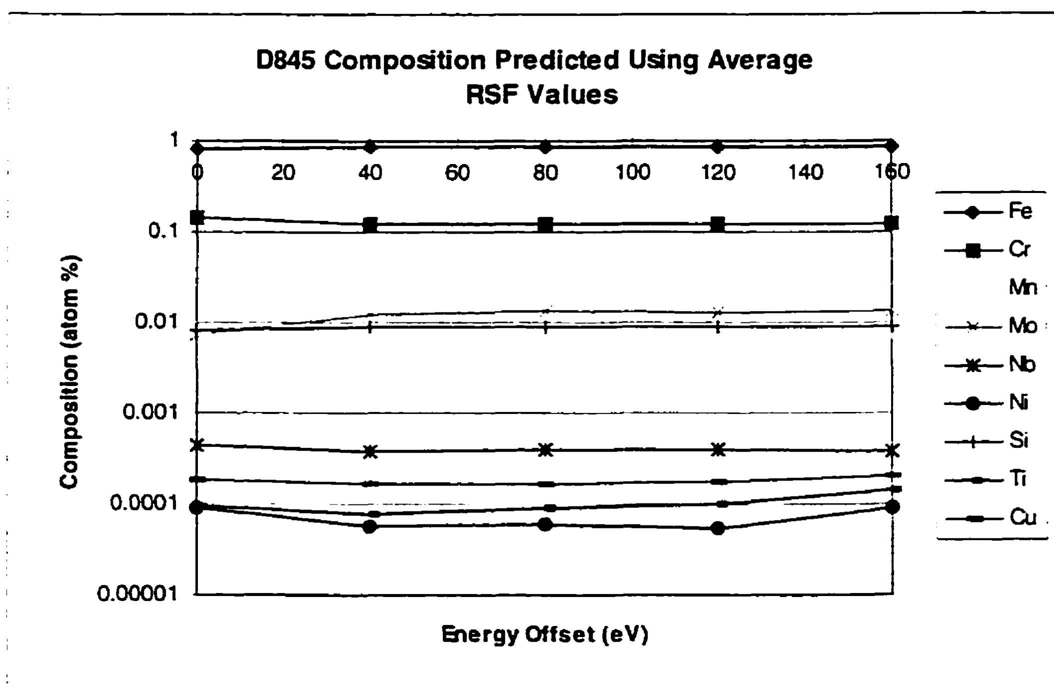

Figure B.27: Composition of D845 Predicted Using Average RSF Values

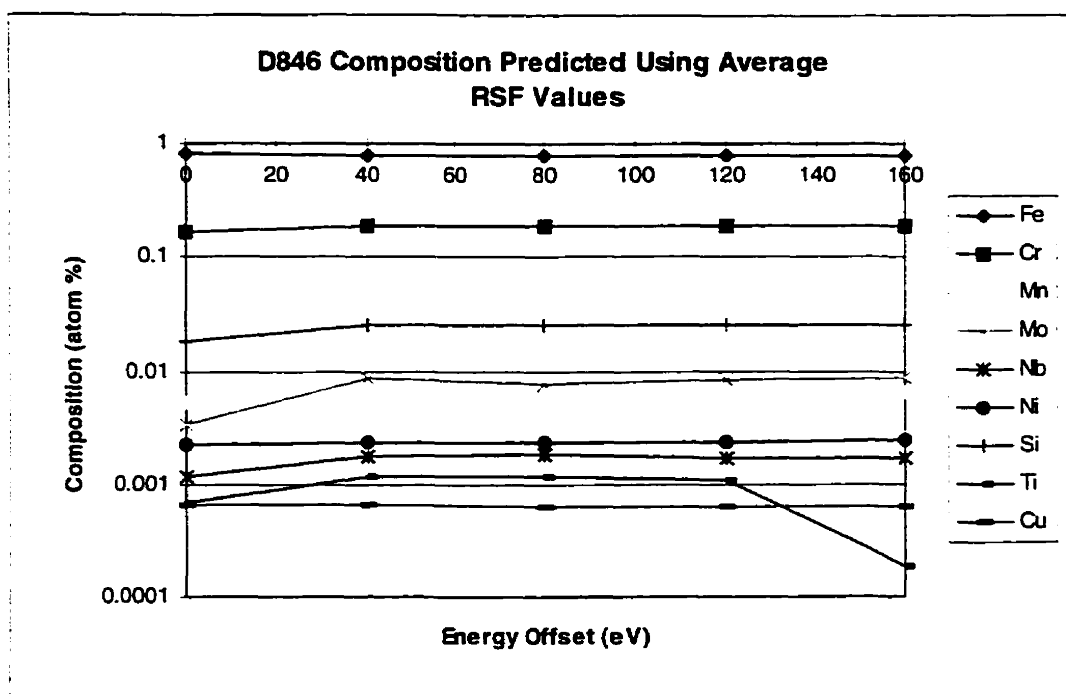

Figure B.28: Composition of D846 Predicted Using Average RSF Values

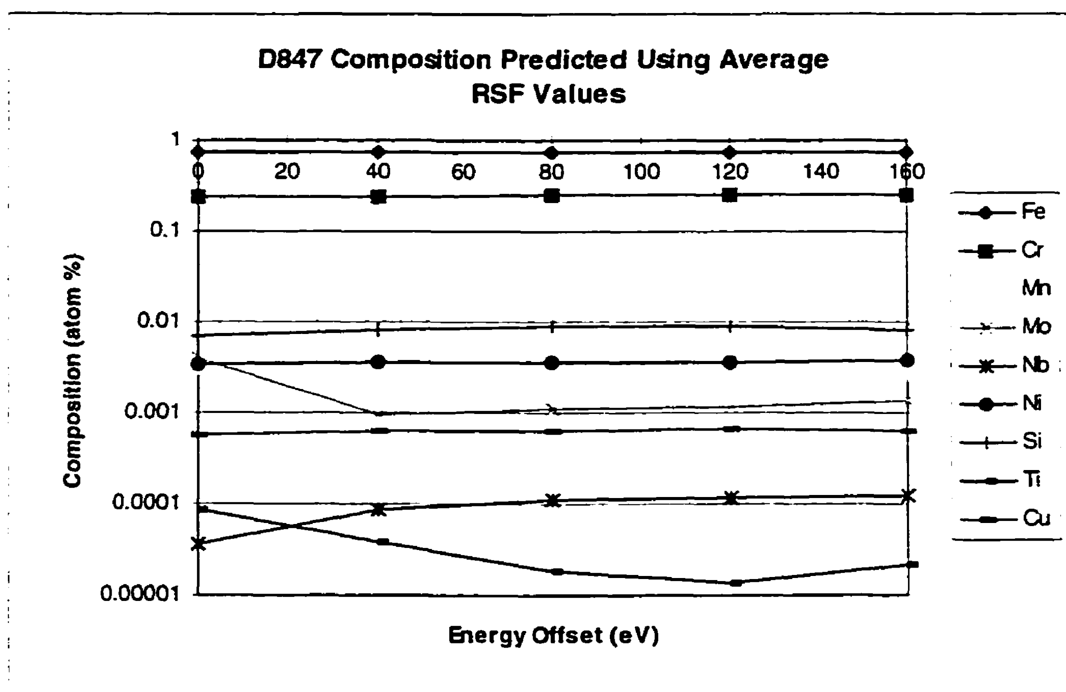

Figure B.29: Composition of D847 Predicted Using Average RSF Values

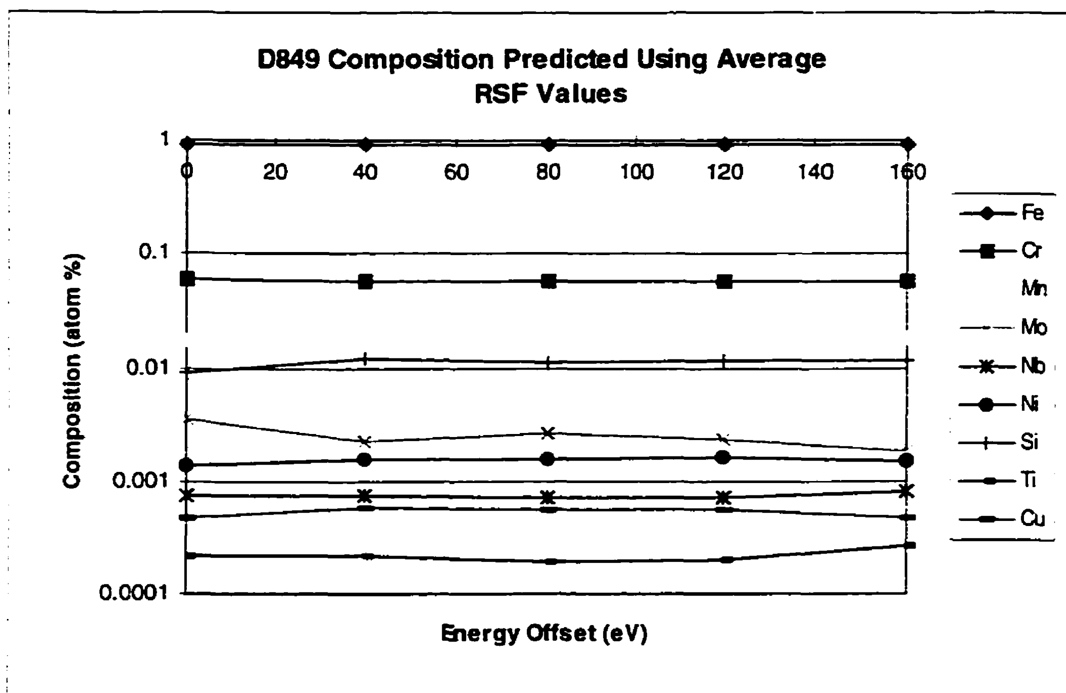

Figure B.30: Composition of D849 Predicted Using Average RSF Values

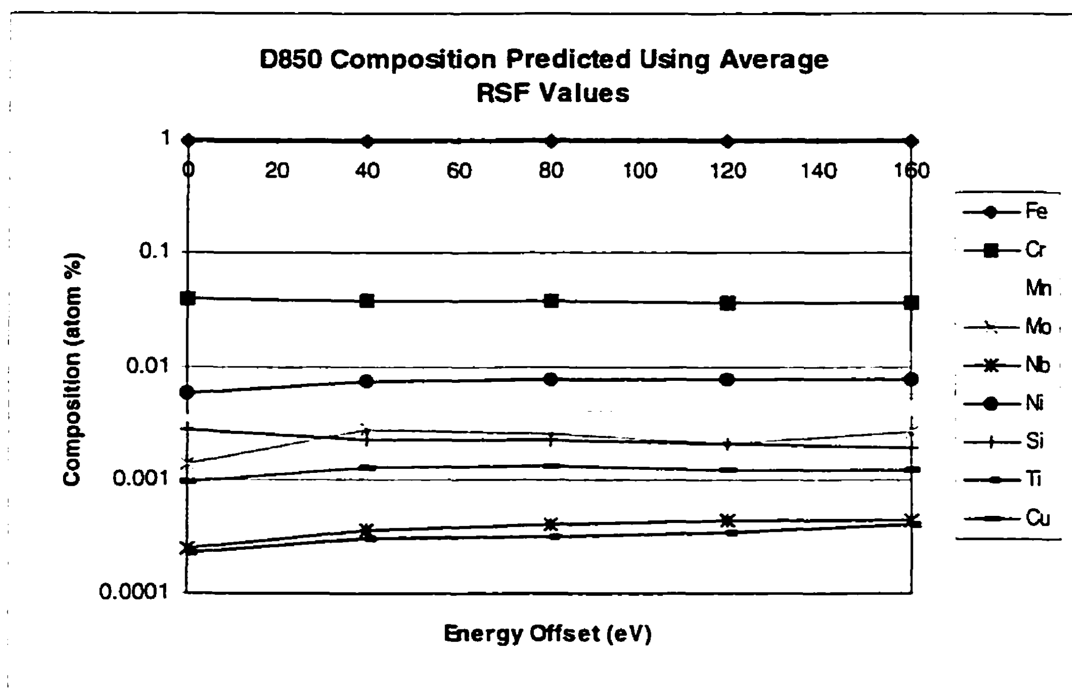

Figure B.31: Composition of D850 Predicted Using Average RSF Values

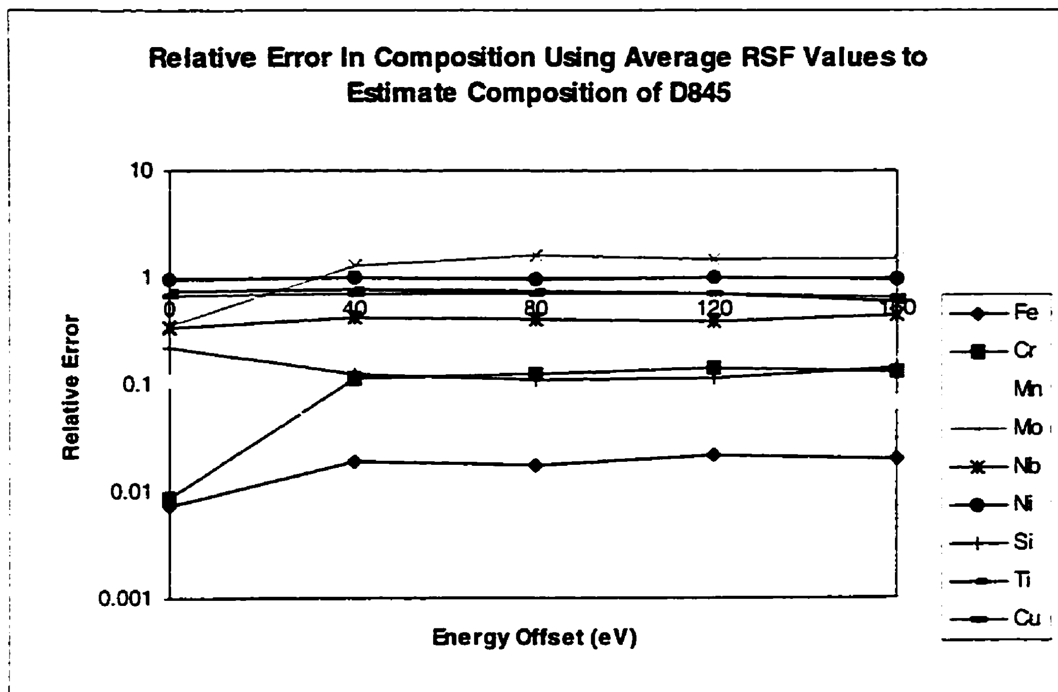

Figure B.32: Relative Error In D845 Composition Predicted Using Average RSF Values

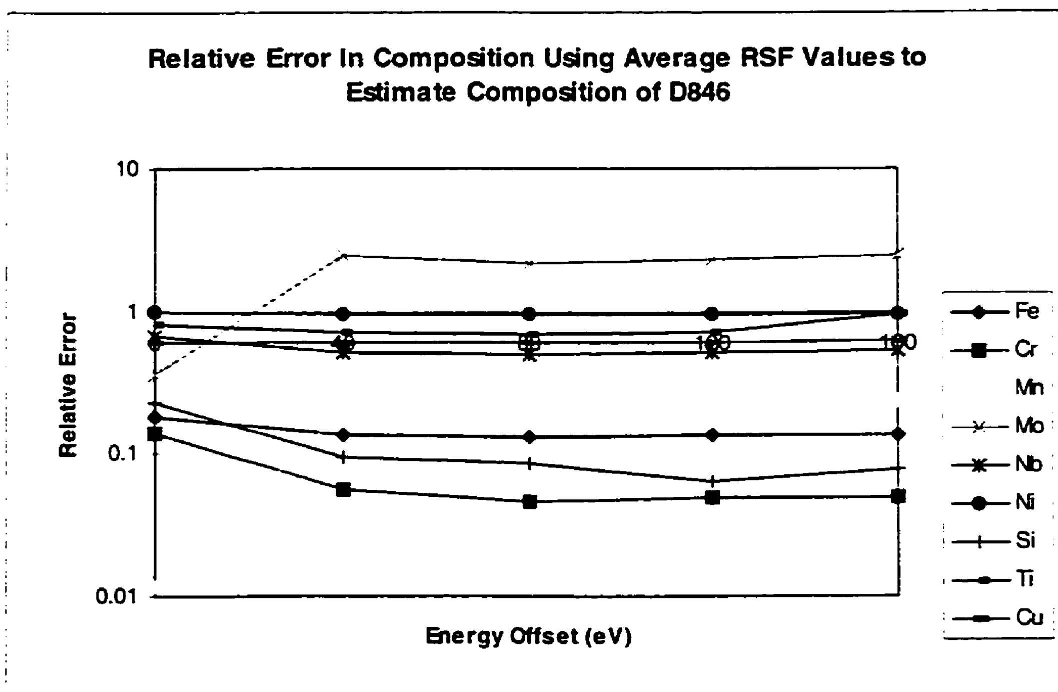

Figure B.33: Relative Error In D846 Composition Predicted Using Average RSF Values

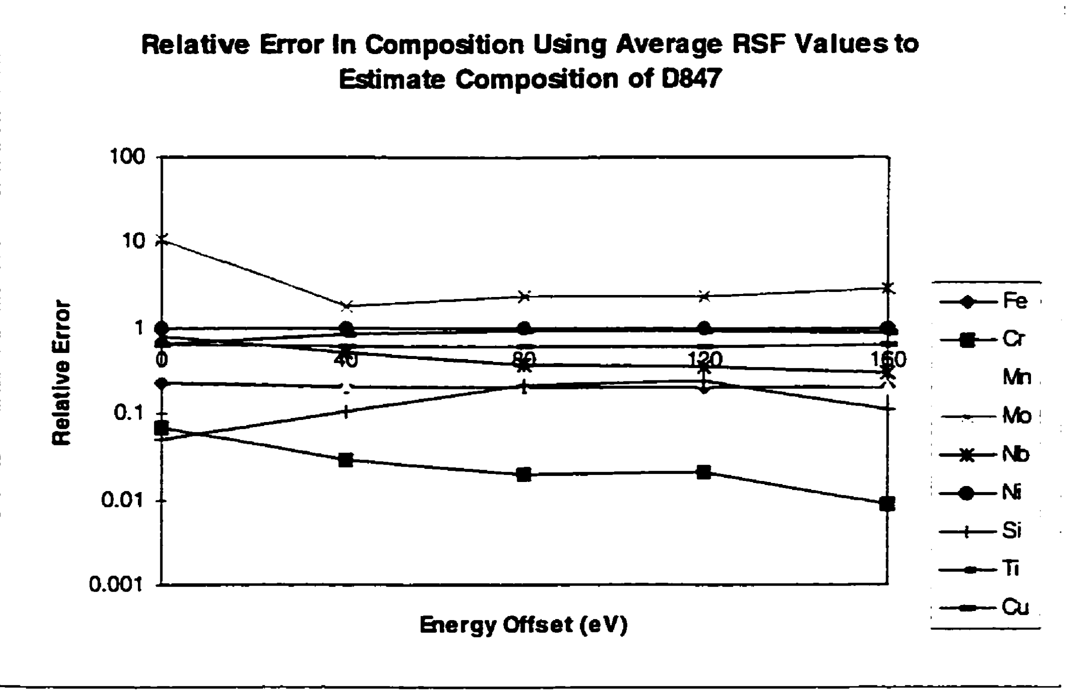

Figure B.34: Relative Error In D847 Composition Predicted Using Average RSF Values

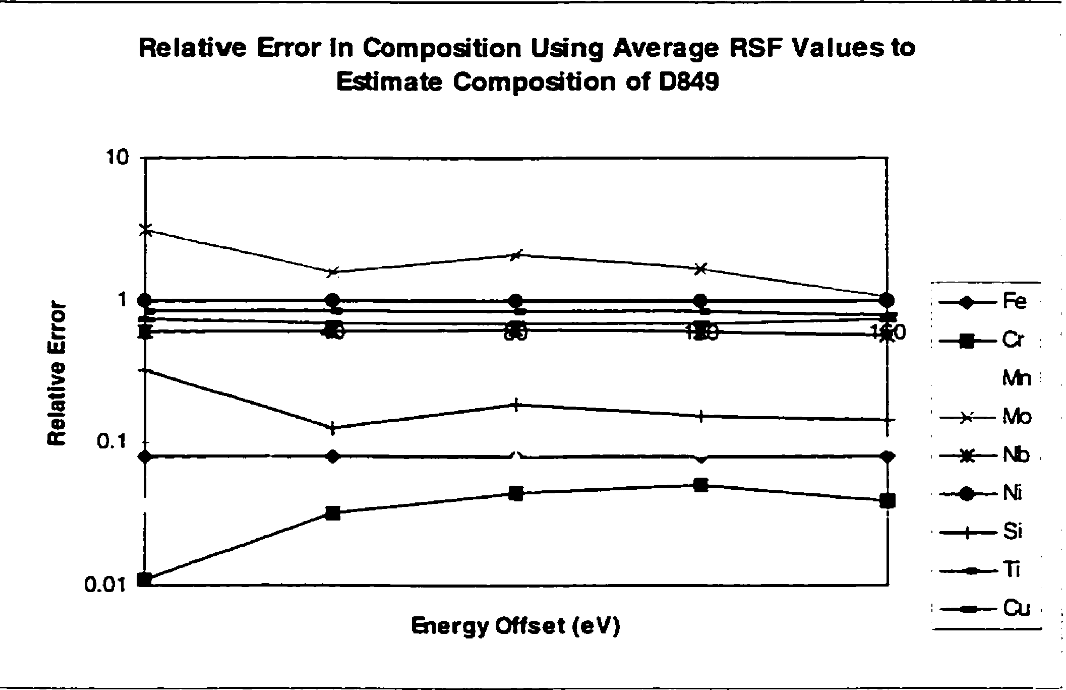

Figure B.35: Relative Error In D849 Composition Predicted Using Average RSF Values

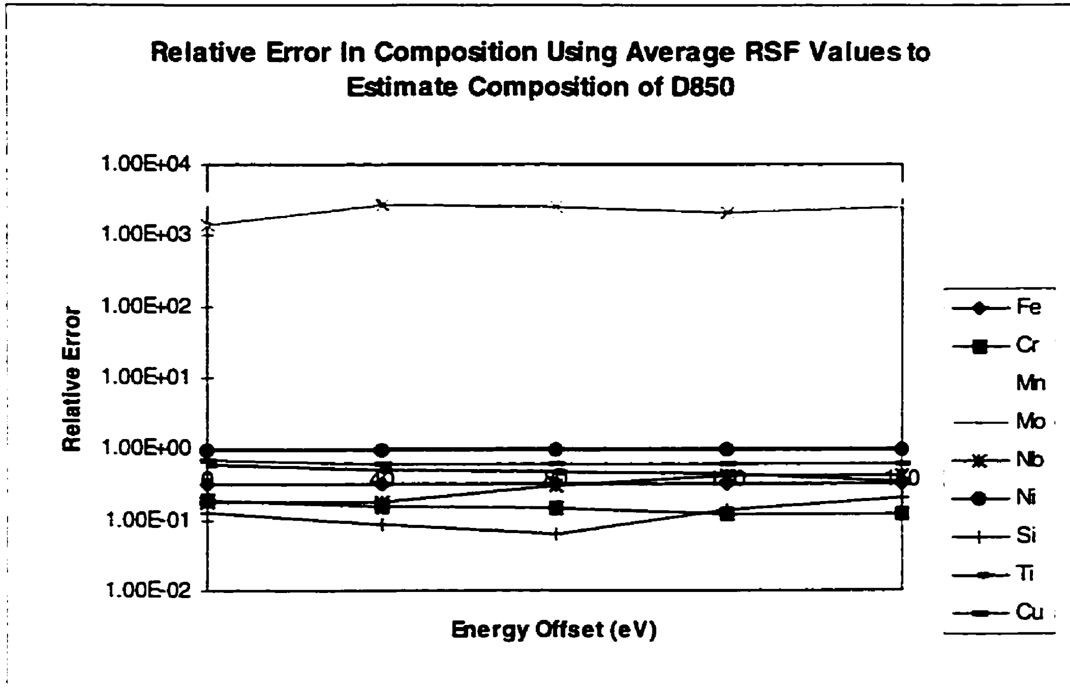

Figure B.36: Relative Error In D850 Composition Predicted Using Average RSF Values

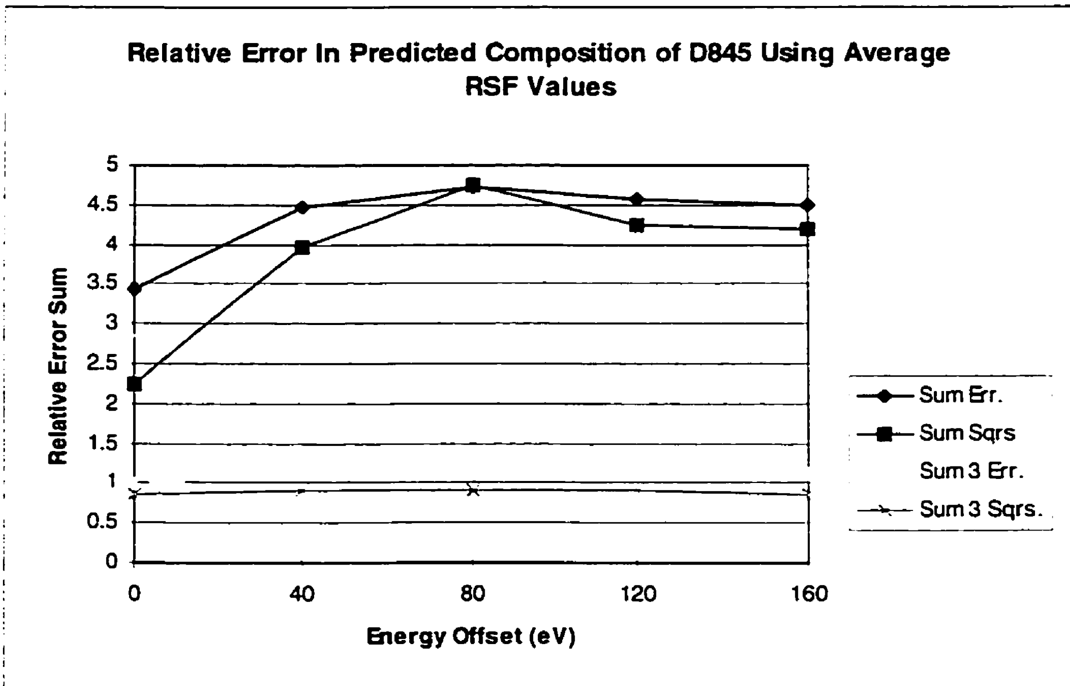

Figure B.37: Sum of Errors In D845 Composition Predicted Using Average RSF Values

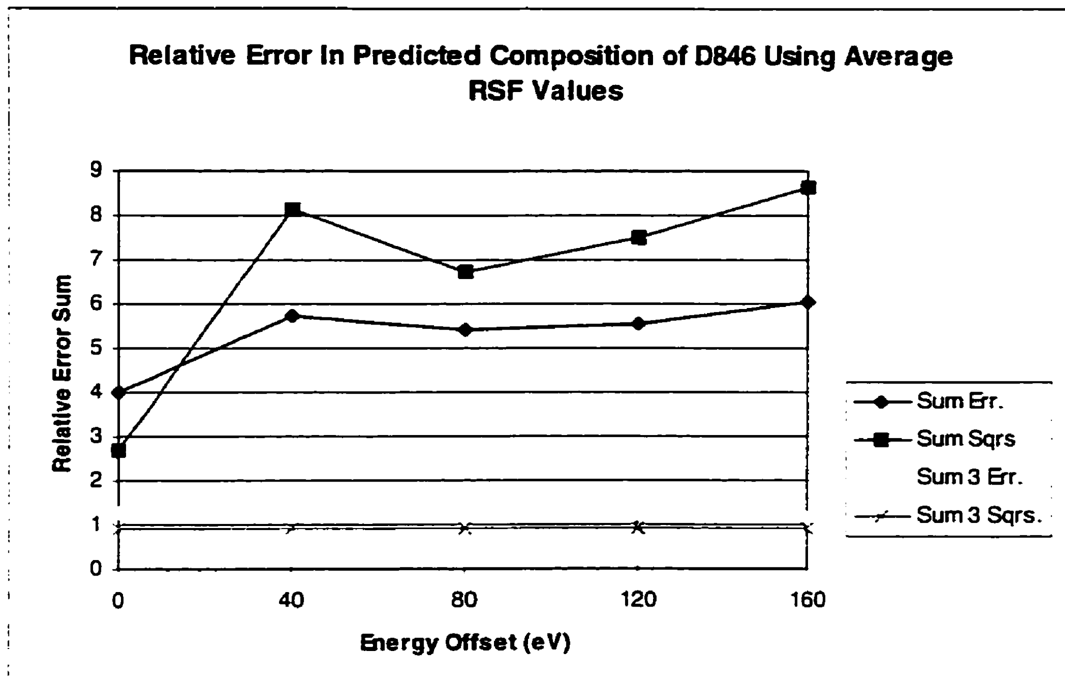

Figure B.38: Sum of Errors In D846 Composition Predicted Using Average RSF Values

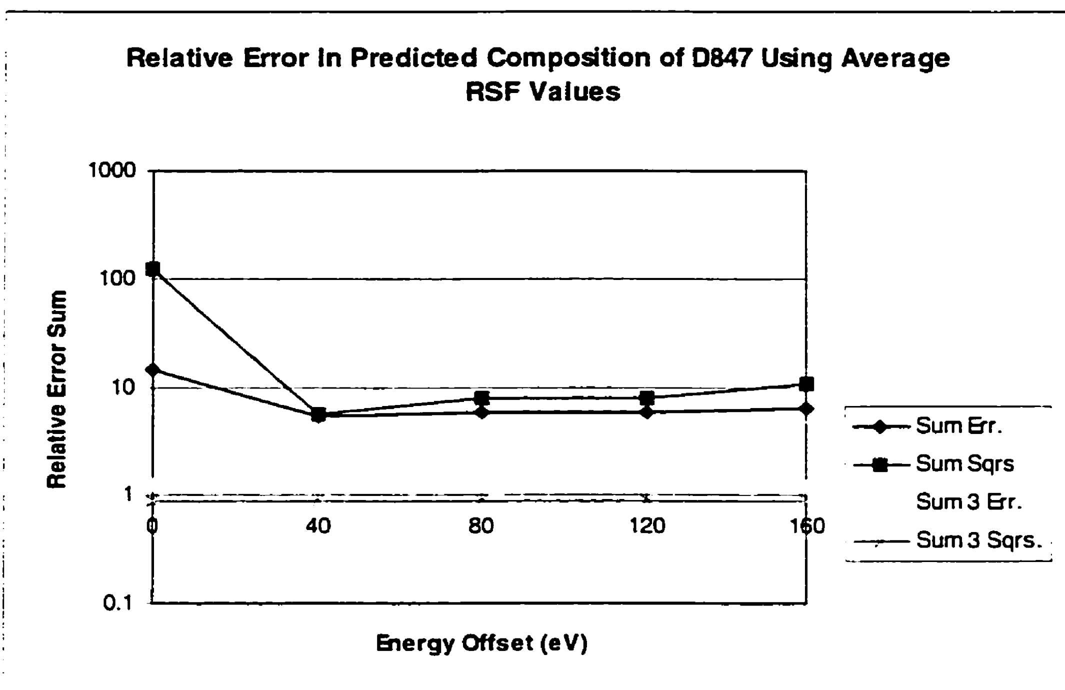

Figure B.39: Sum of Errors In D847 Composition Predicted Using Average RSF Values

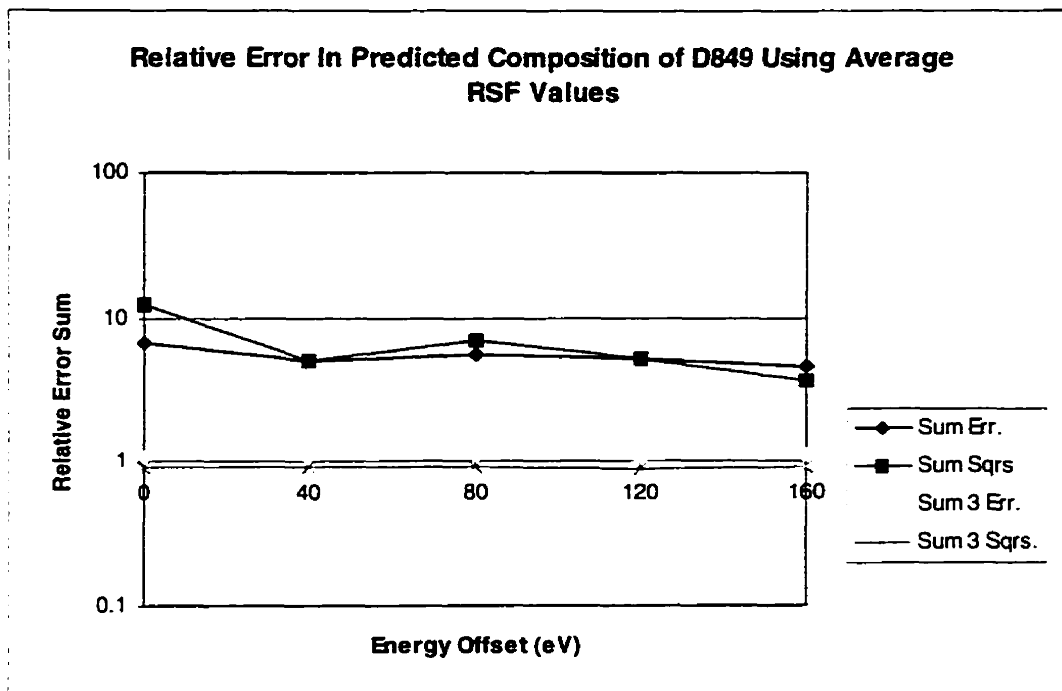

Figure B.40: Sum of Errors In D849 Composition Predicted Using Average RSF Values

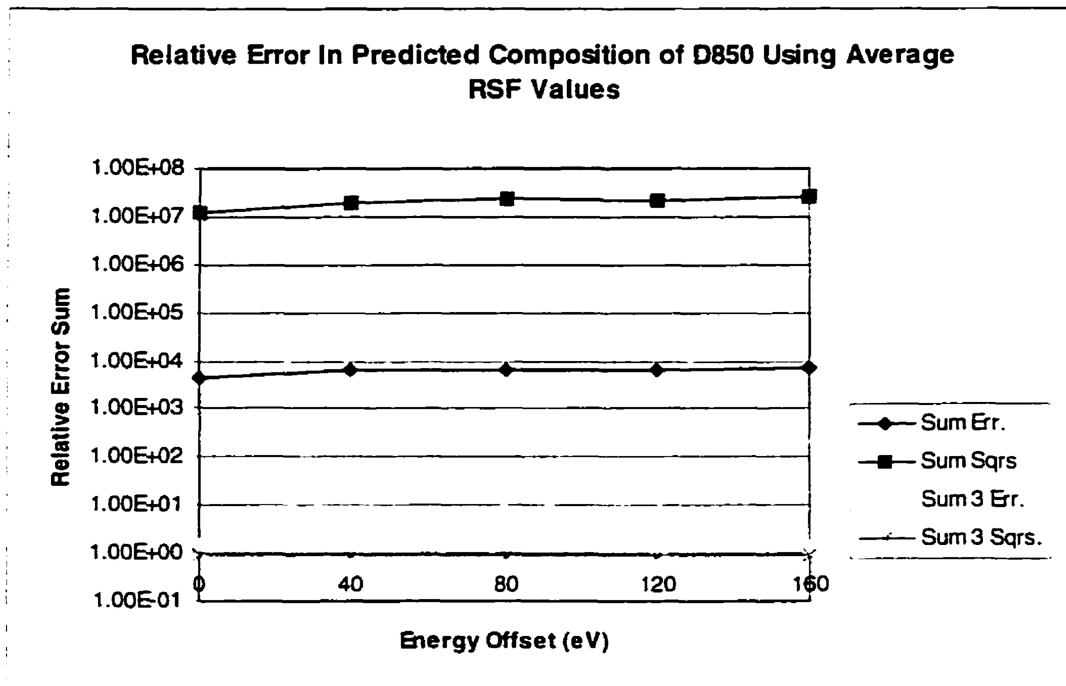

Figure B.41: Sum of Errors In D845 Composition Predicted Using Average RSF Values

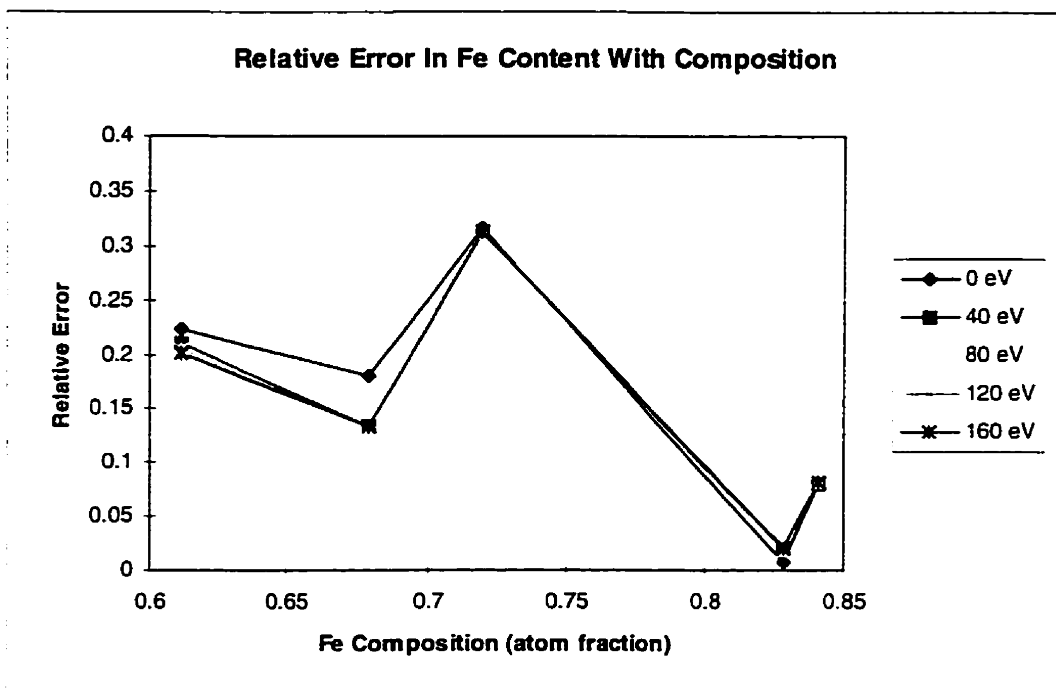

Figure B.42: Relative Error In Predicted Fe Content Versus Elemental Fe Composition

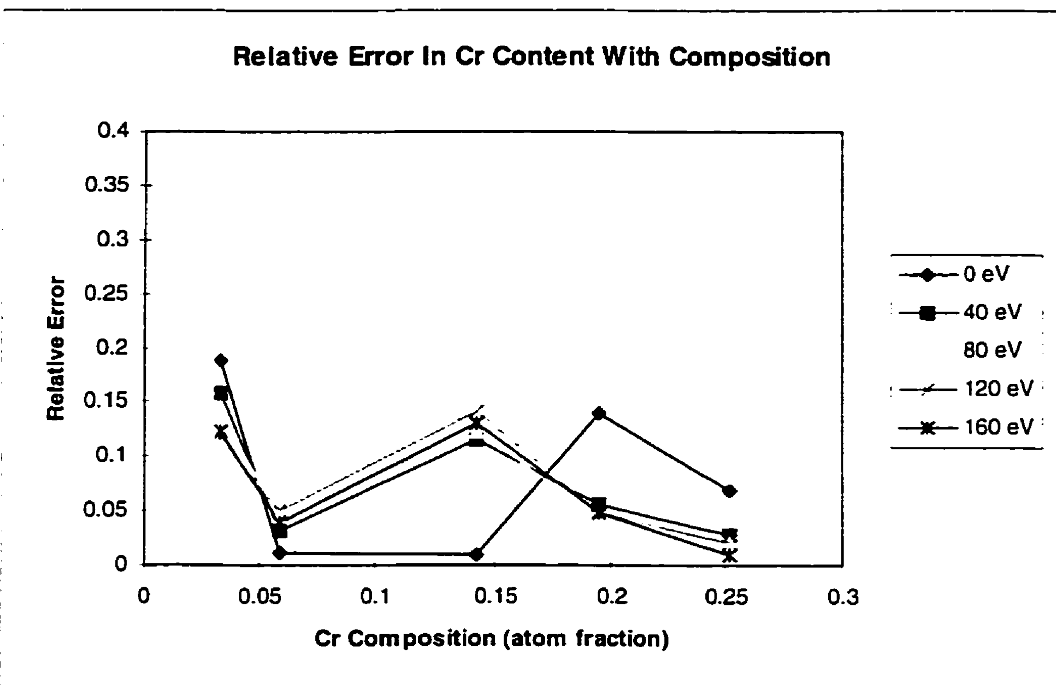

Figure B.43: Relative Error In Predicted Cr Content Versus Elemental Cr Composition

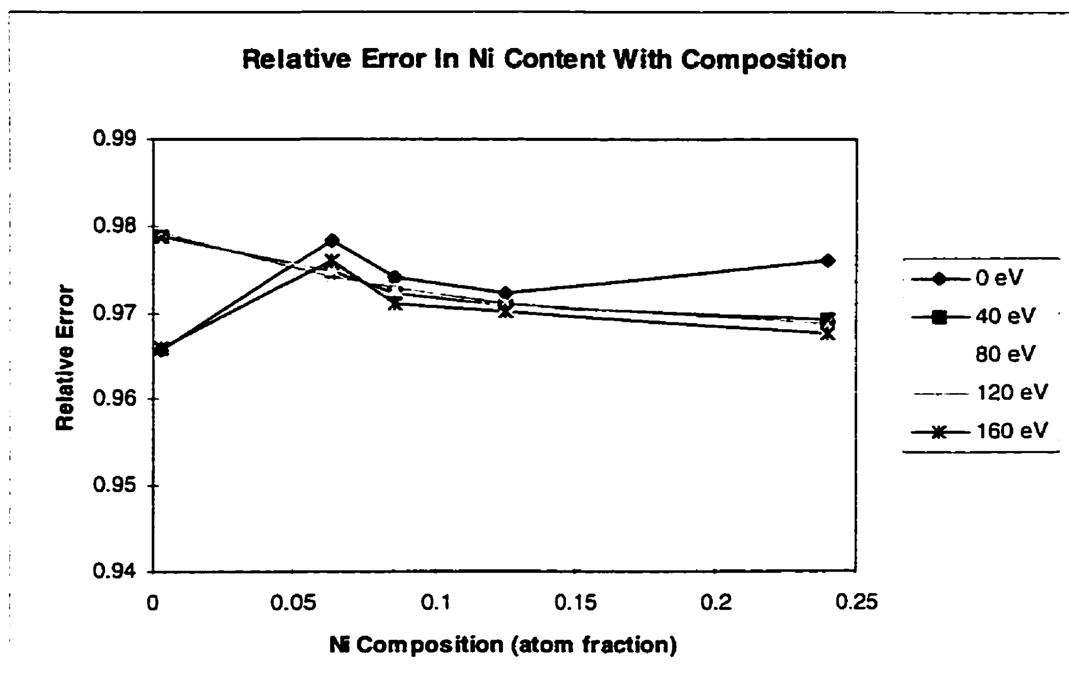

Figure B.44: Relative Error In Predicted Ni Content Versus Elemental Ni Composition

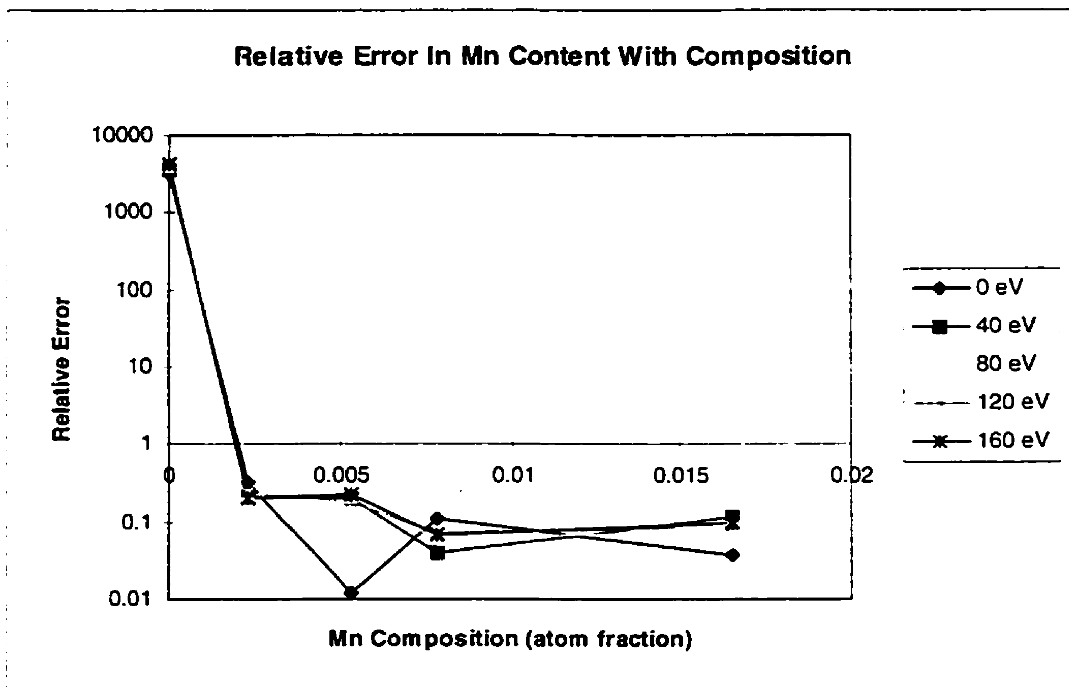

Figure B.45: Relative Error In Predicted Mn Content Versus Elemental Mn Composition

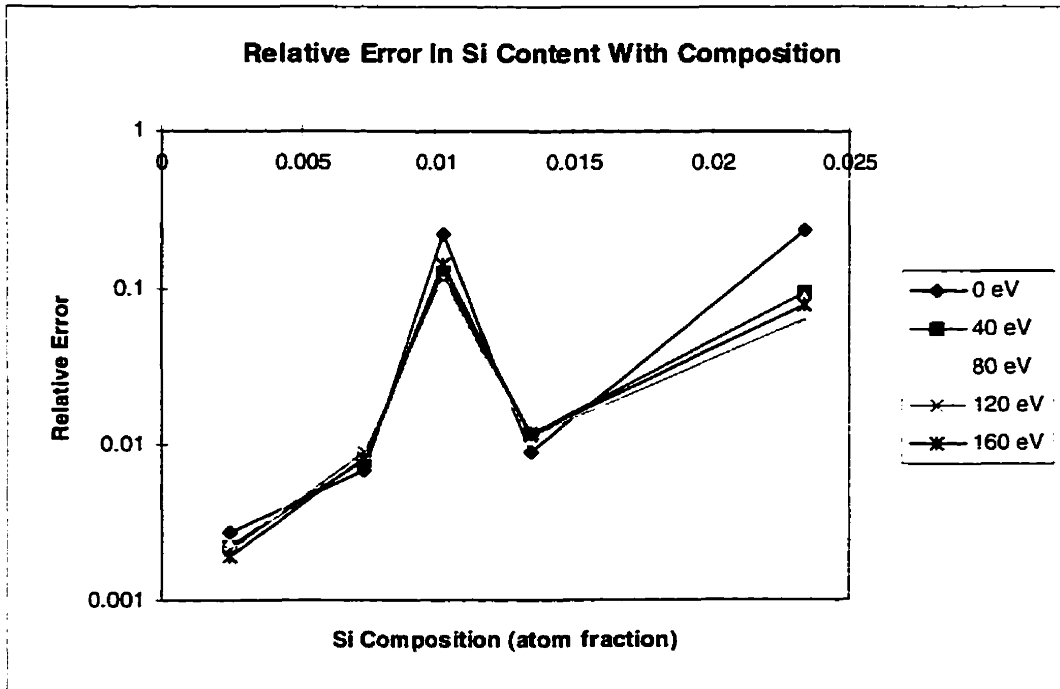

Figure B.46: Relative Error In Predicted Si Content Versus Elemental Si Composition

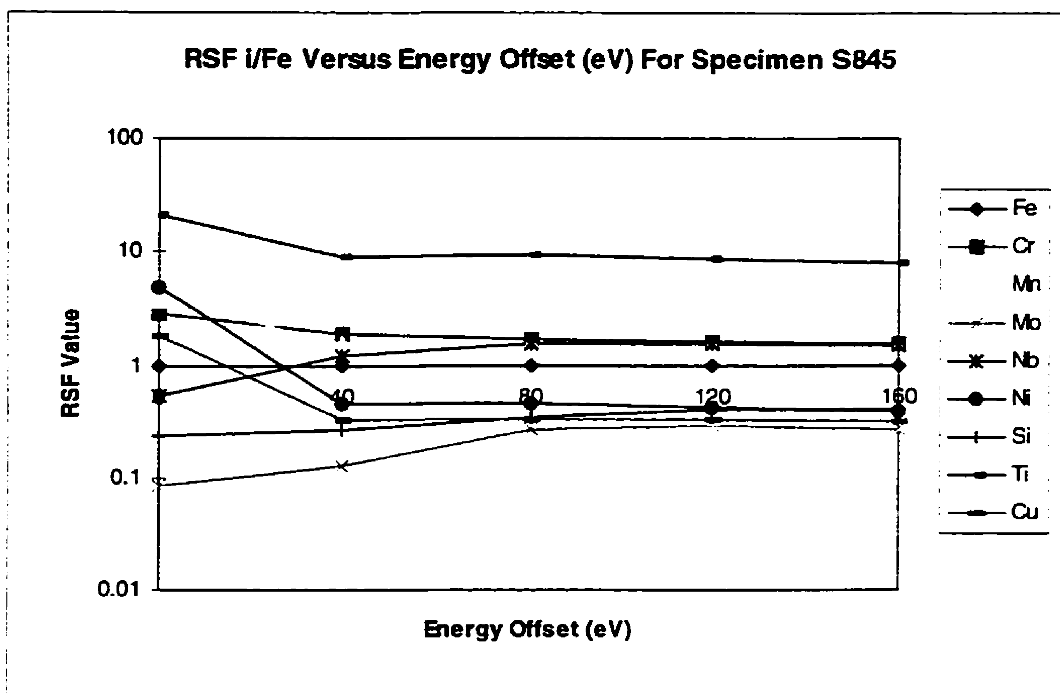

Figure B.47: RSF Values (Calculated With Respect To Iron) Versus Energy For Sample S 845

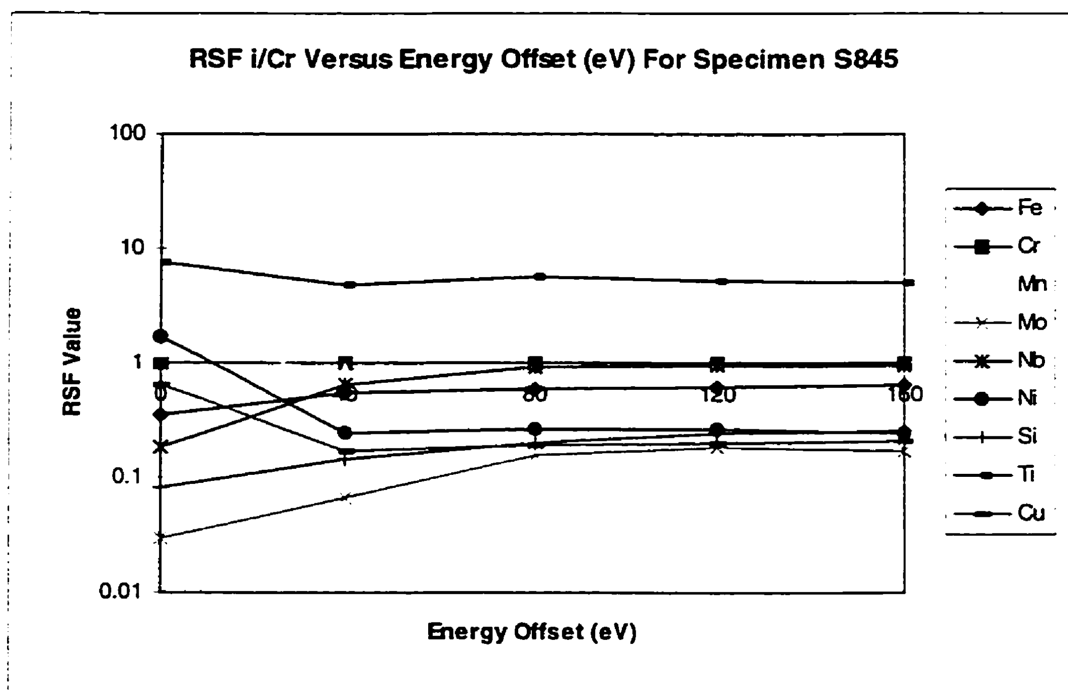

Figure B.48: RSF Values (Calculated With Respect To Chromium) Versus Energy For Sample S 845

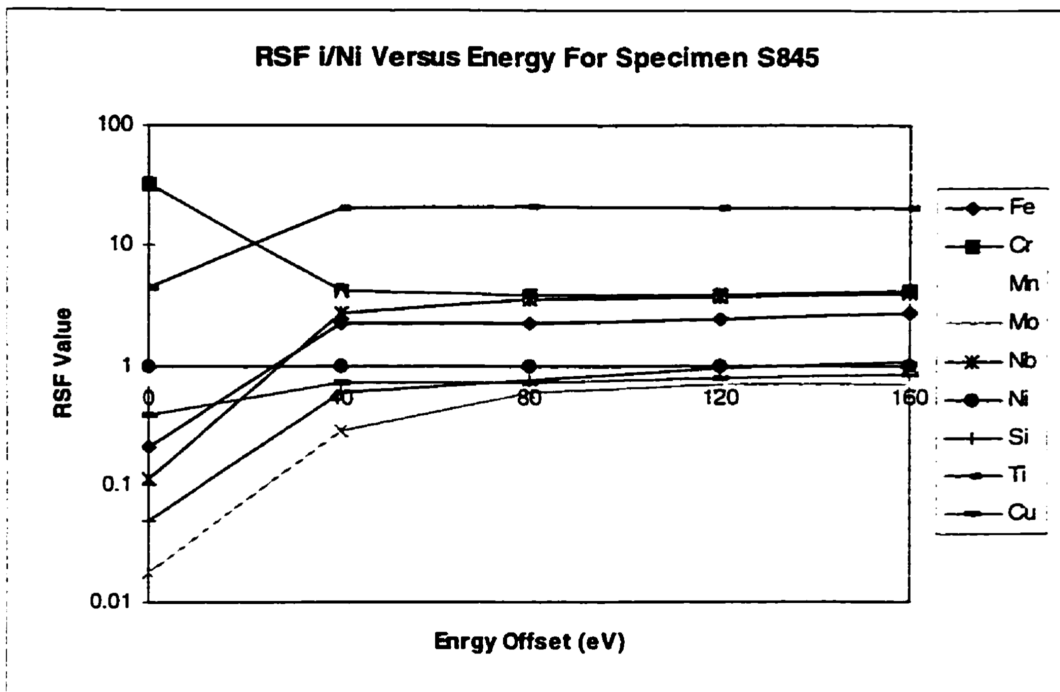

Figure B.49: RSF Values (Calculated With Respect To Nickel) Versus Energy For Sample S 845

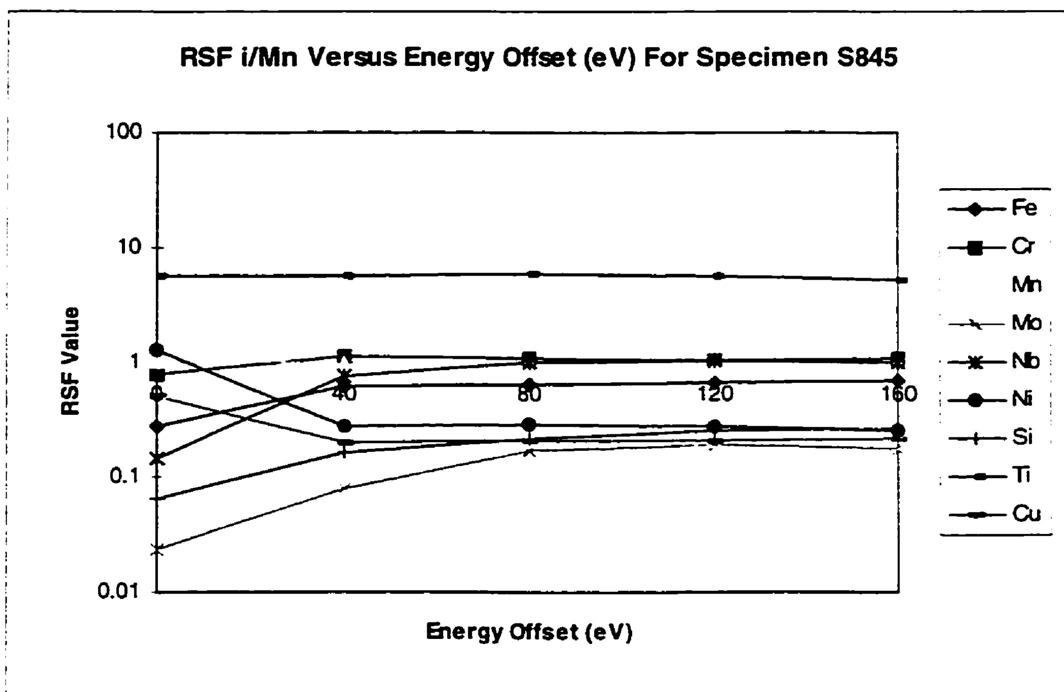

Figure B.50: RSF Values (Calculated With Respect To Manganese) Versus Energy For Sample S 845

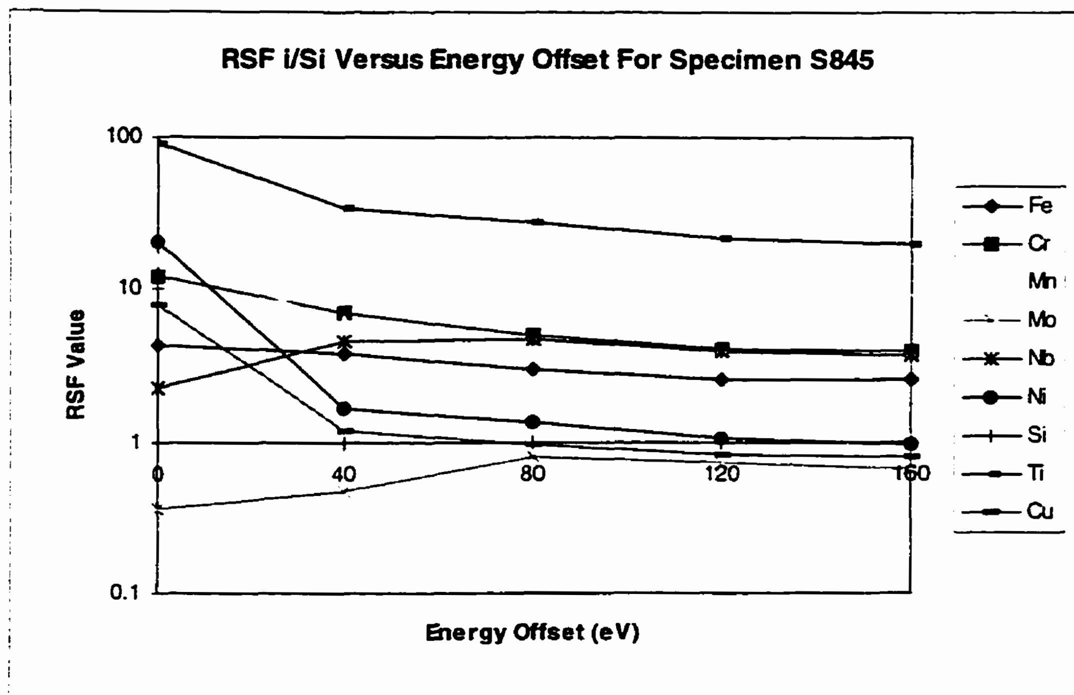

Figure B.51: RSF Values (Calculated With Respect To Silicon) Versus Energy For Sample S 845

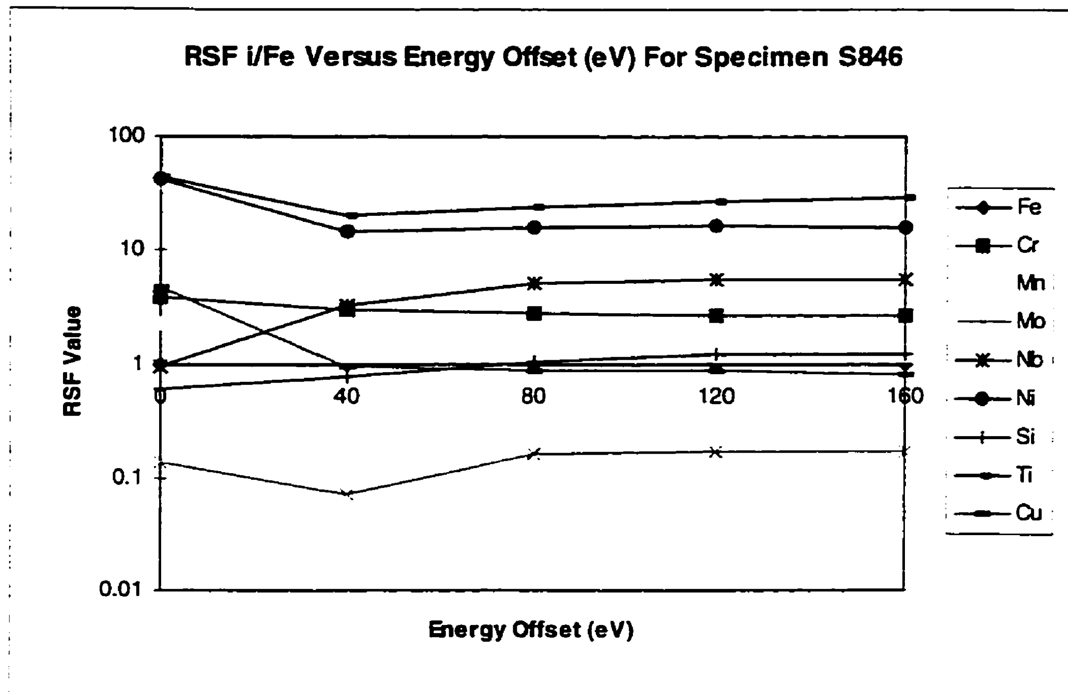

Figure B.52: RSF Values (Calculated With Respect To Iron) Versus Energy For Sample S 846

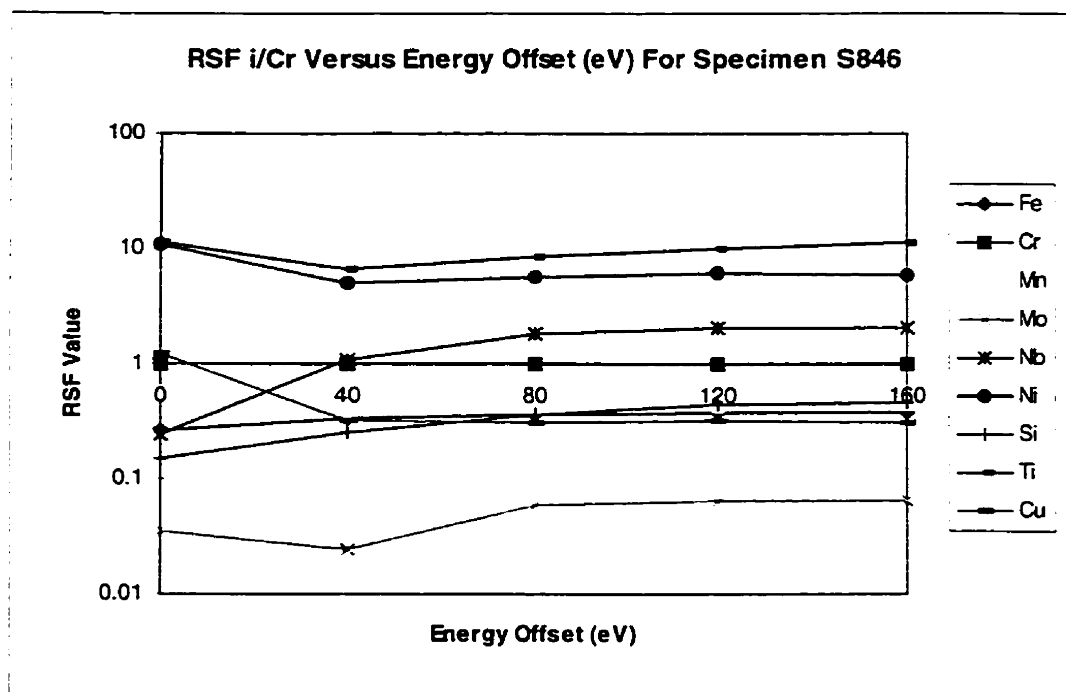

Figure B.53: RSF Values (Calculated With Respect To Chromium) Versus Energy For Sample S 846

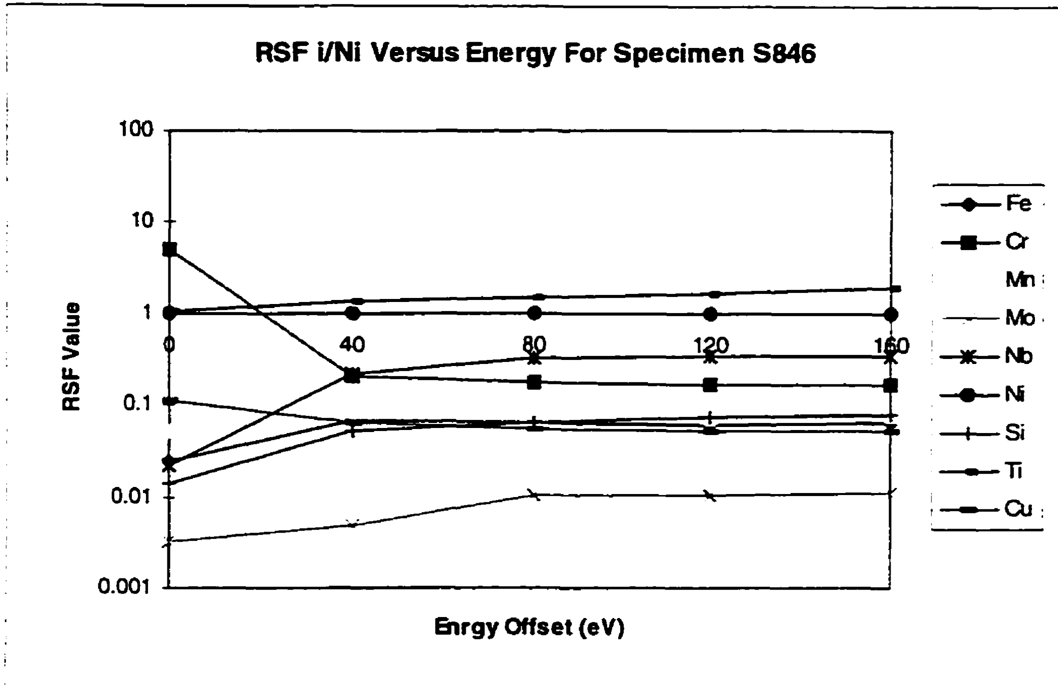

Figure B.54: RSF Values (Calculated With Respect To Nickel) Versus Energy For Sample S 846

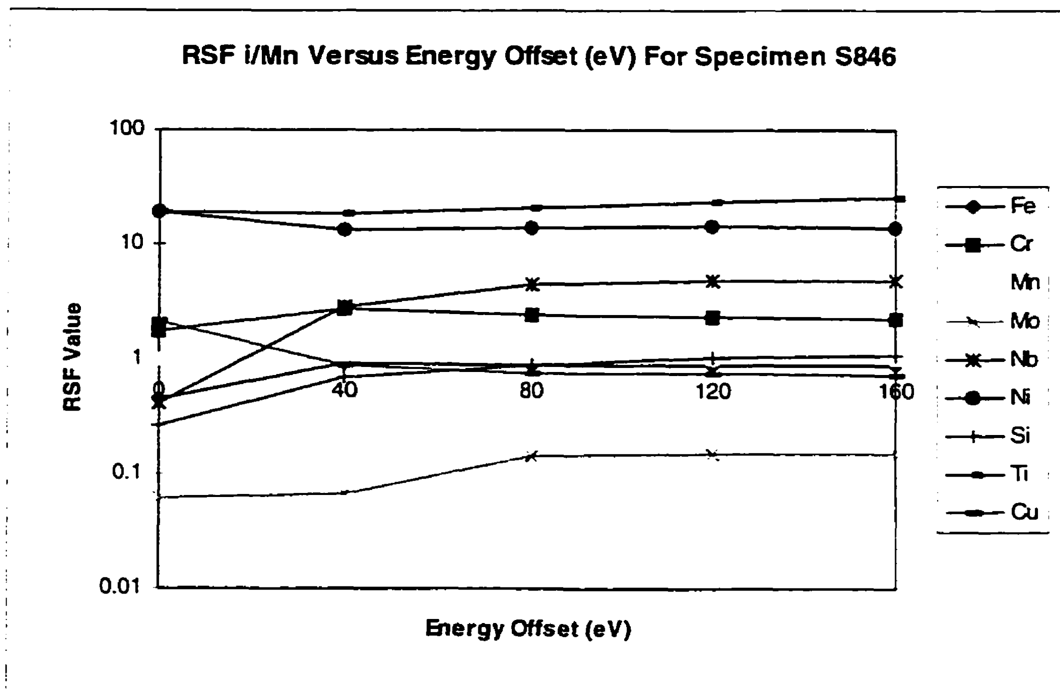

Figure B.55: RSF Values (Calculated With Respect To Manganese) Versus Energy For Sample S 846

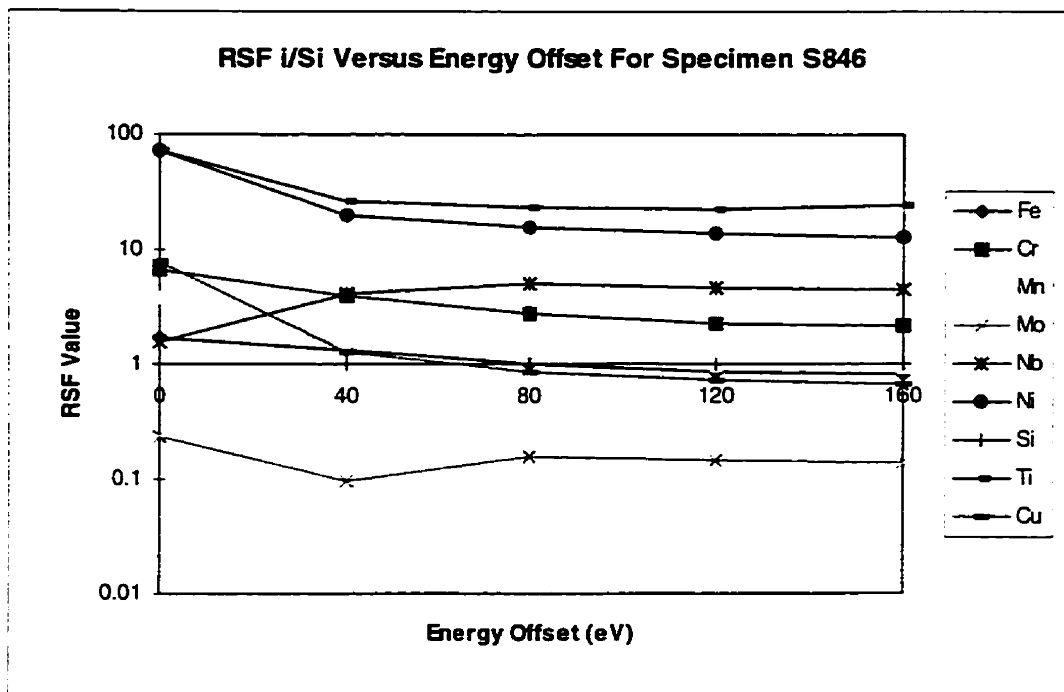

Figure B.56: RSF Values (Calculated With Respect To Silicon) Versus Energy For Sample S 846

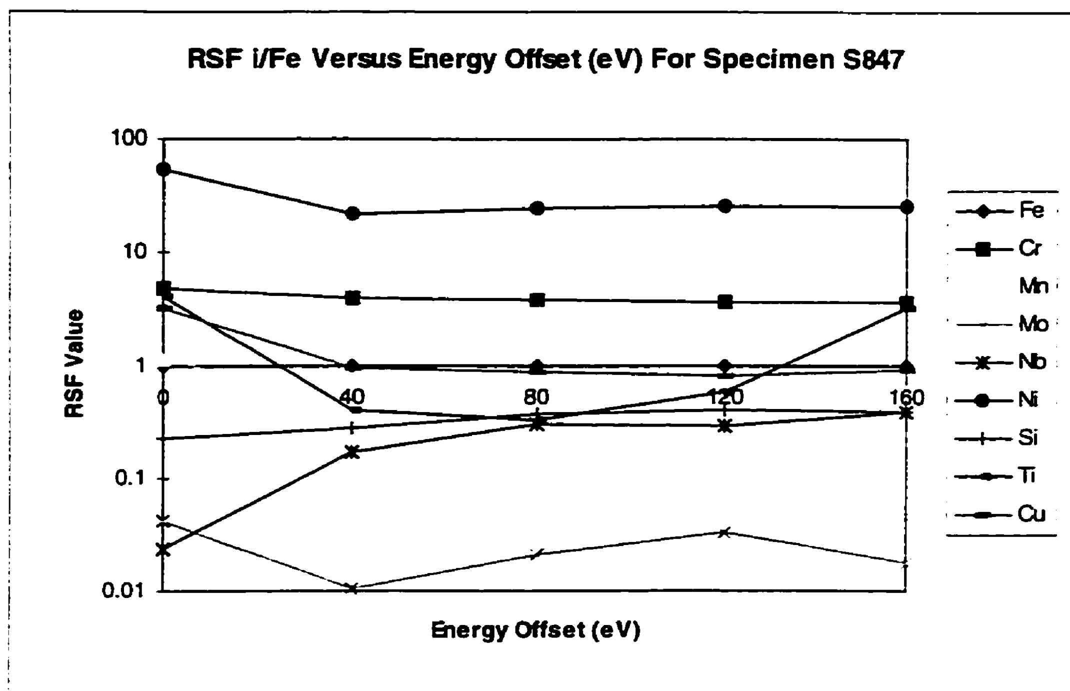

Figure B.57: RSF Values (Calculated With Respect To Iron) Versus Energy For Sample S 847

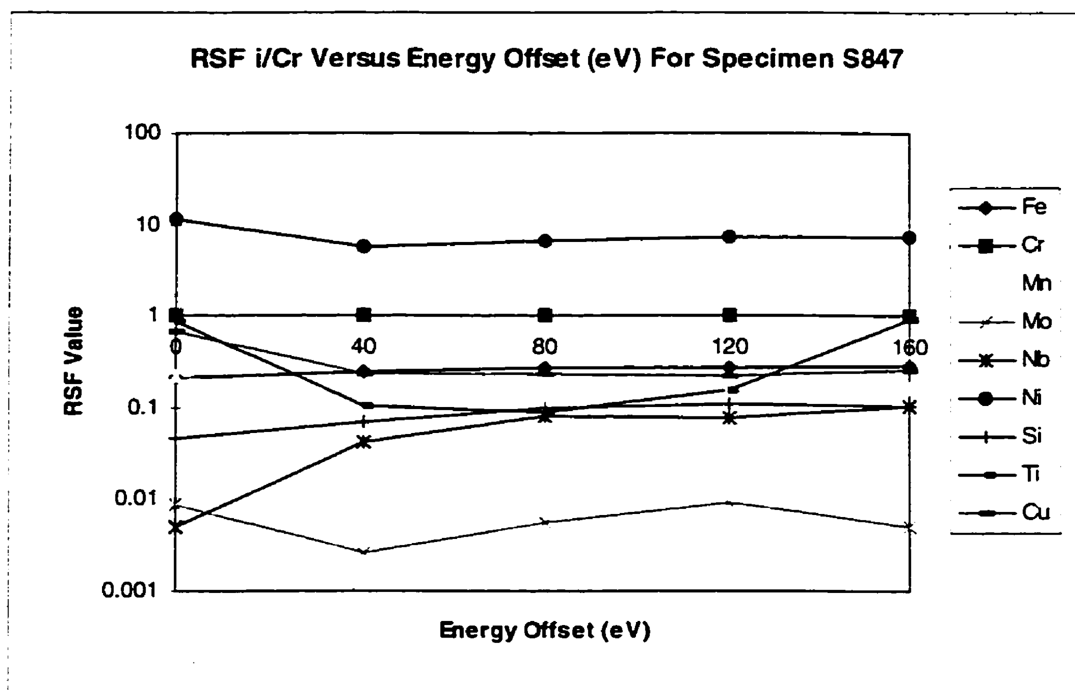

Figure B.58: RSF Values (Calculated With Respect To Chromium) Versus Energy For Sample S 847

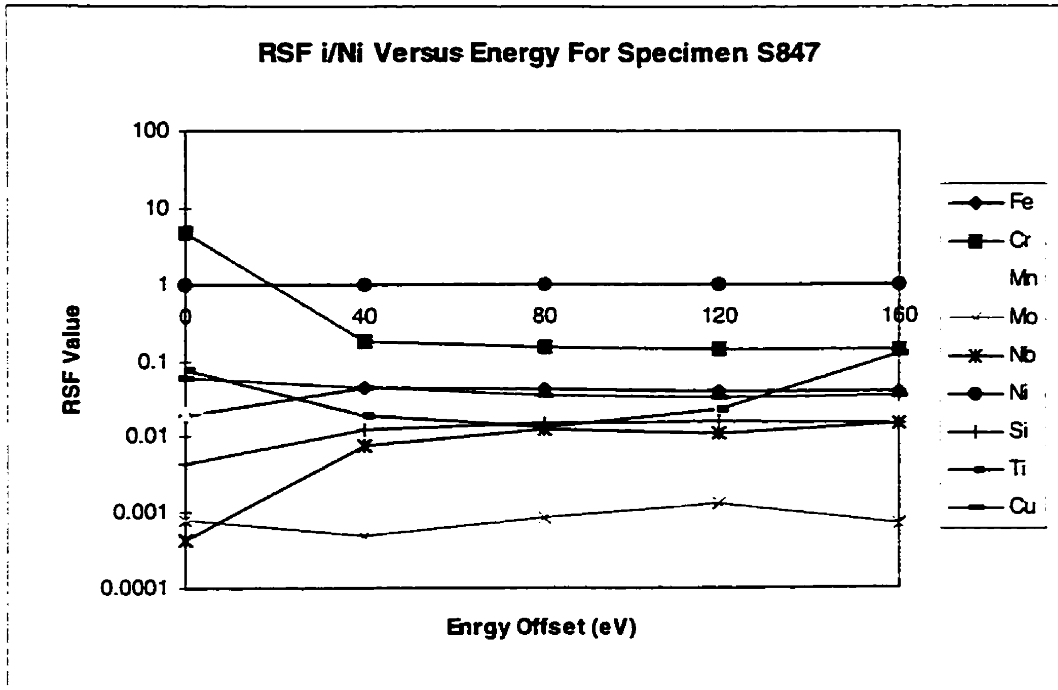

Figure B.59: RSF Values (Calculated With Respect To Nickel) Versus Energy For Sample S 847

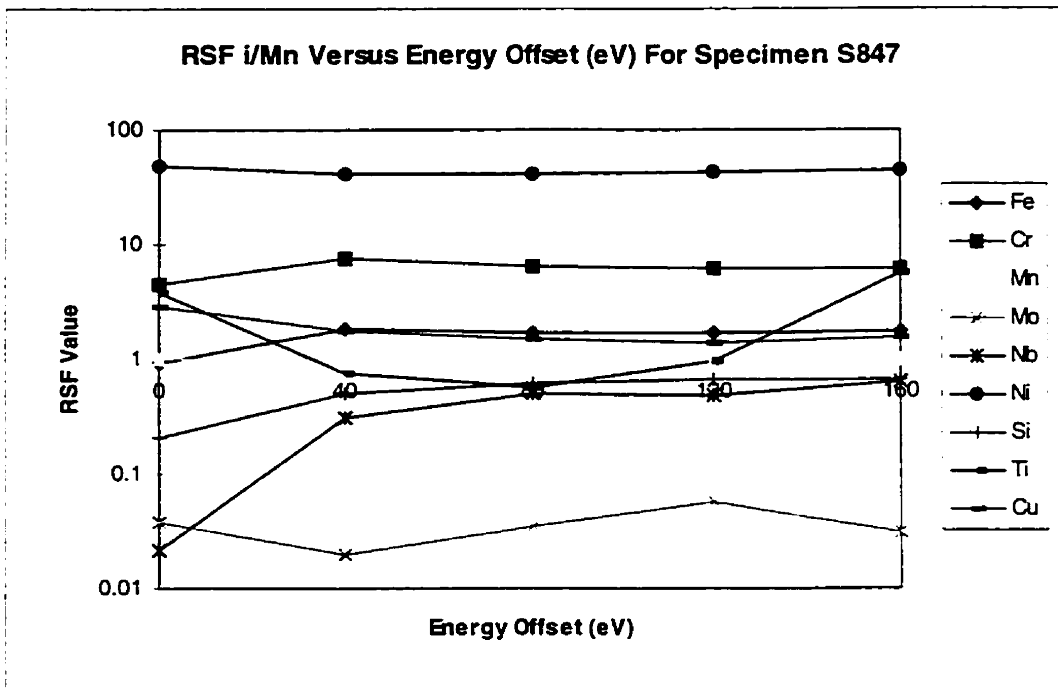

Figure B.60: RSF Values (Calculated With Respect To Manganese) Versus Energy For Sample S 847

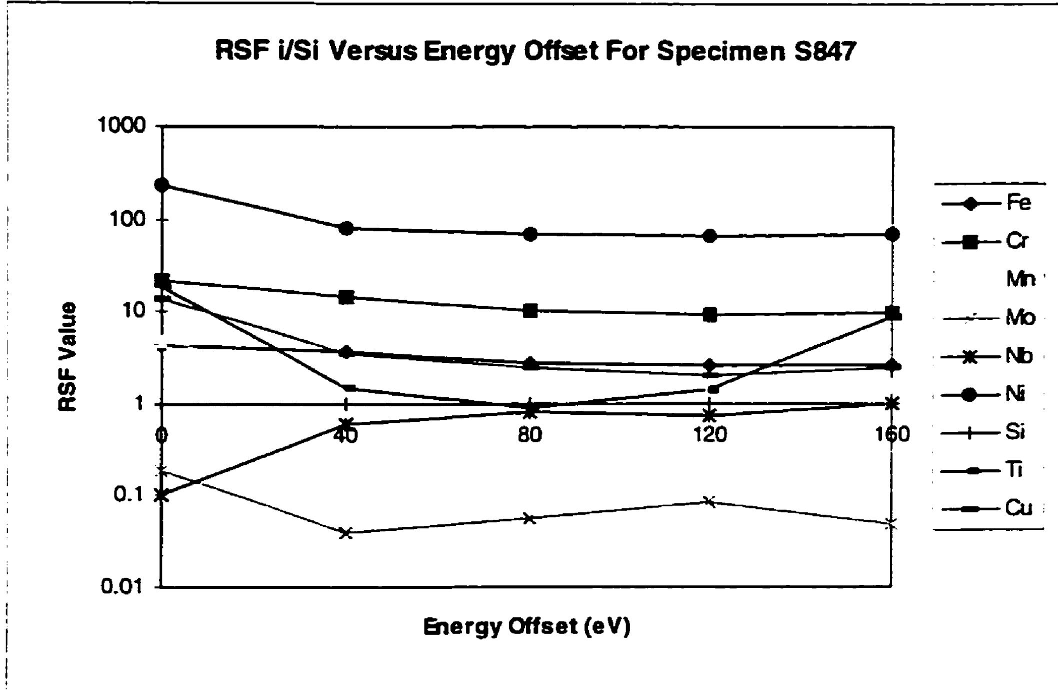

Figure B.61: RSF Values (Calculated With Respect To Silicon) Versus Energy For Sample S 847

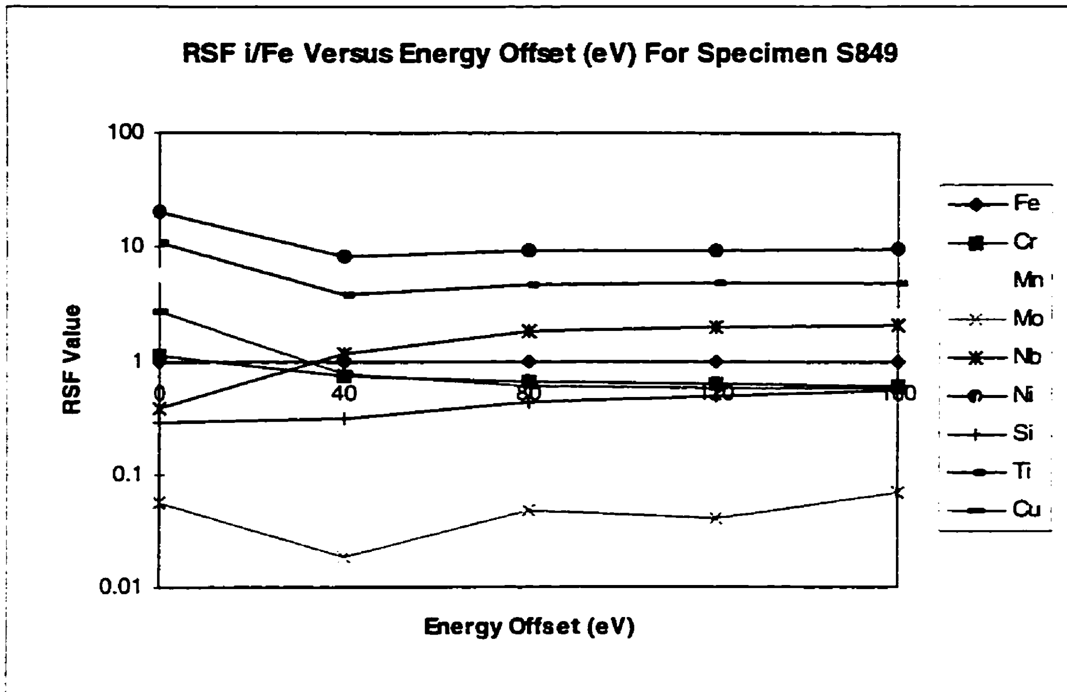

Figure B.62: RSF Values (Calculated With Respect To Iron) Versus Energy For Sample S 849

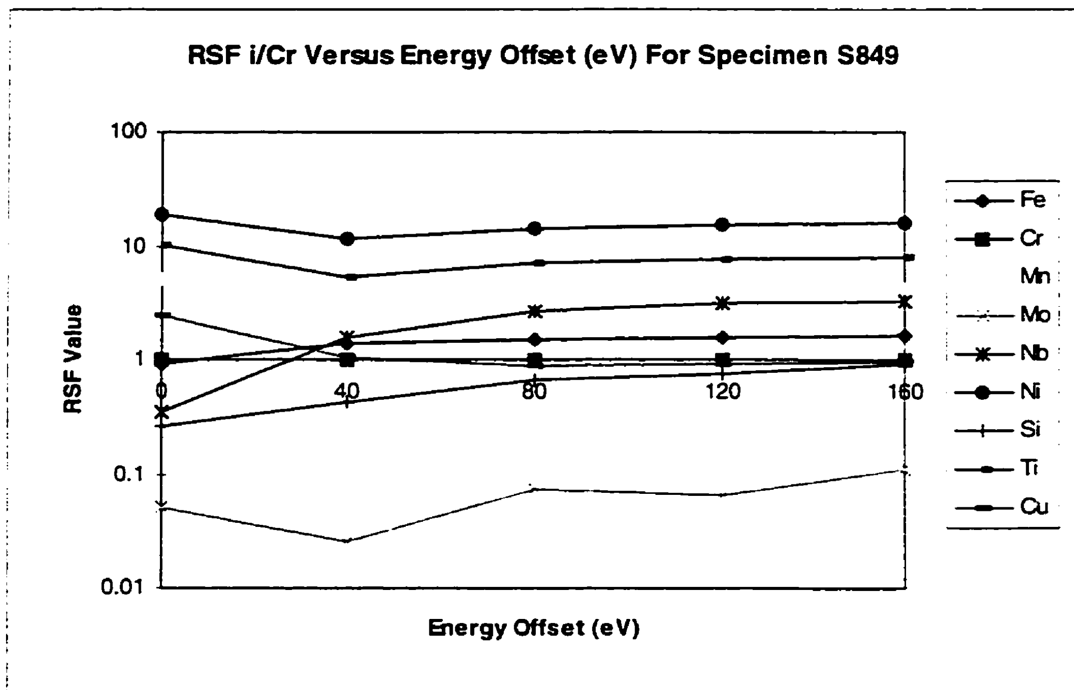

Figure B.63: RSF Values (Calculated With Respect To Chromium) Versus Energy For Sample S 849

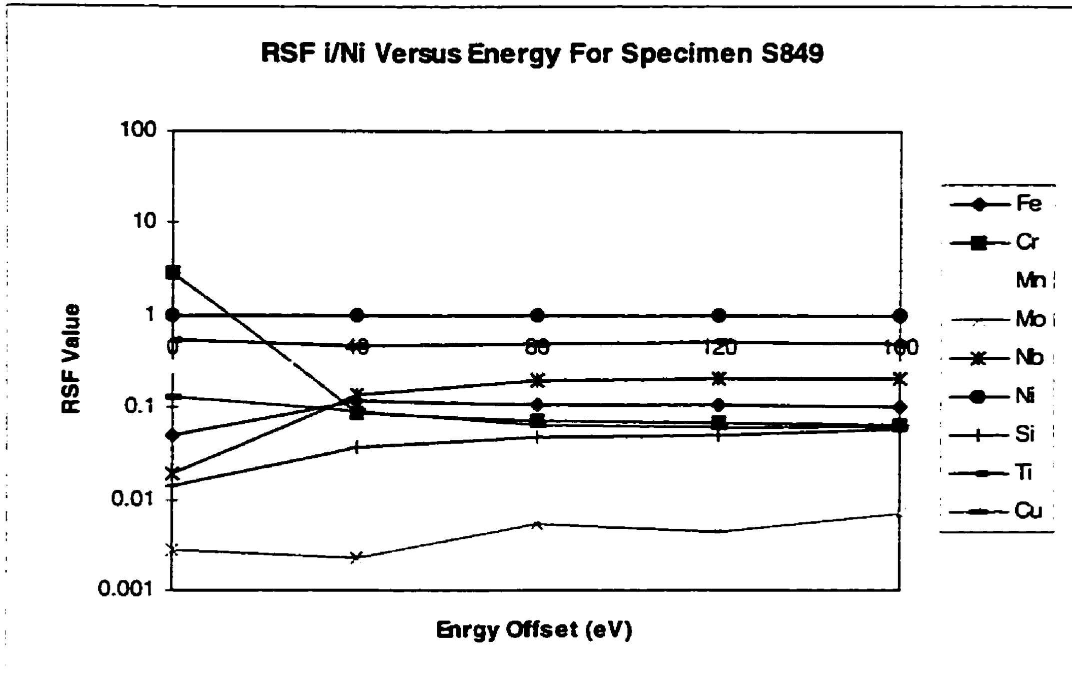

Figure B.64: RSF Values (Calculated With Respect To Nickel) Versus Energy For Sample S 849

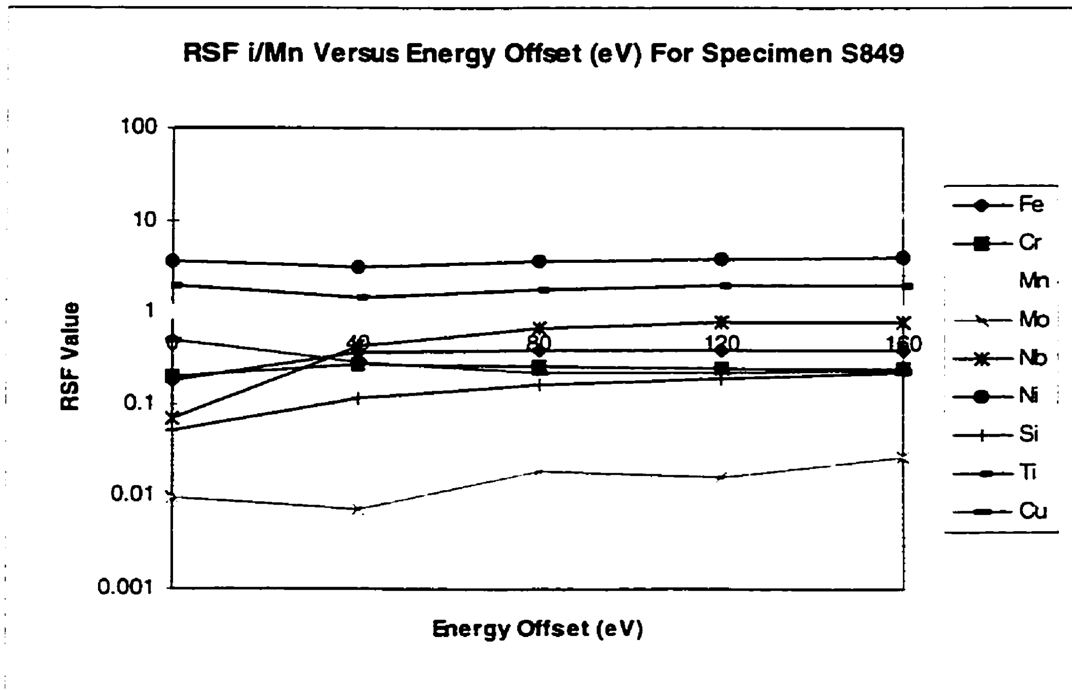

Figure B.65: RSF Values (Calculated With Respect To Manganese) Versus Energy For Sample S 849

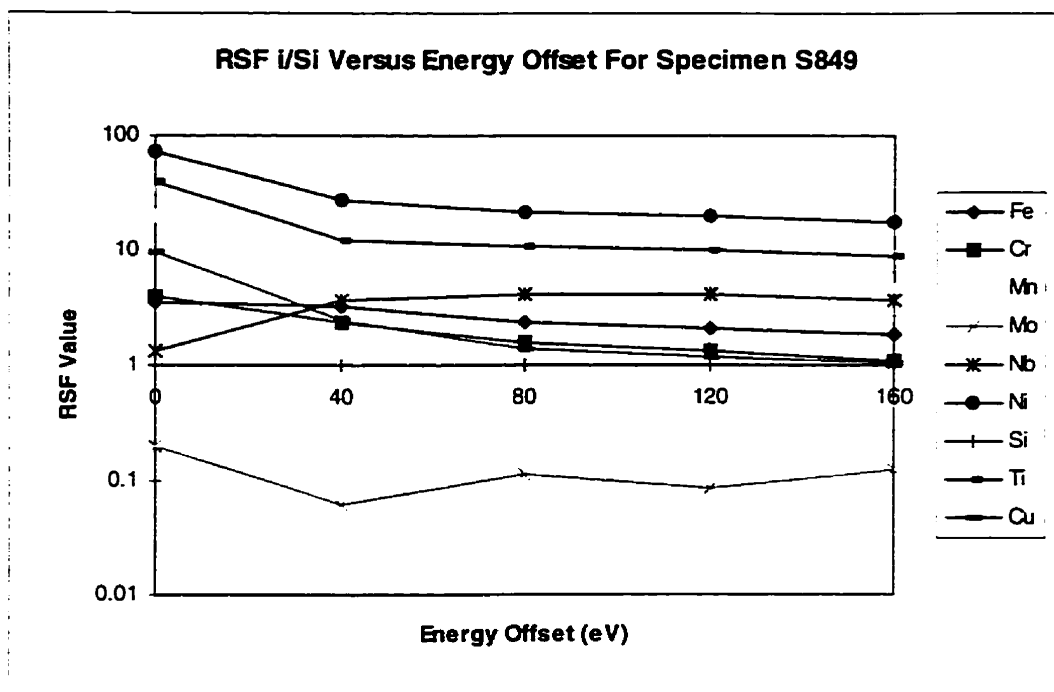

Figure B.66: RSF Values (Calculated With Respect To Silicon) Versus Energy For Sample S 849

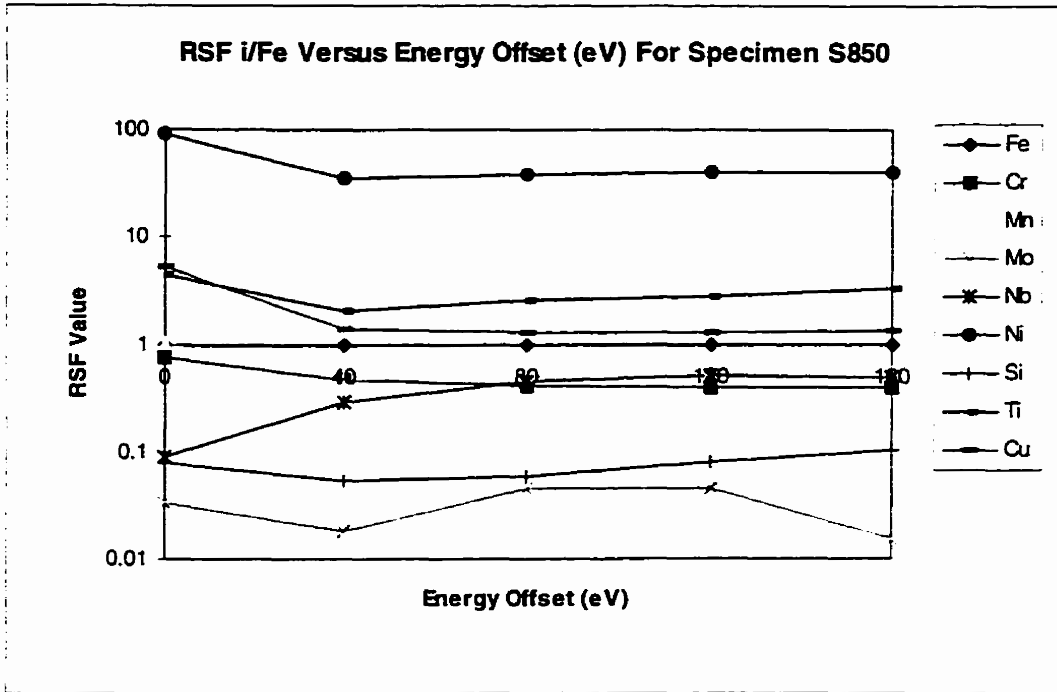

Figure B.67: RSF Values (Calculated With Respect To Iron) Versus Energy For Sample S 850

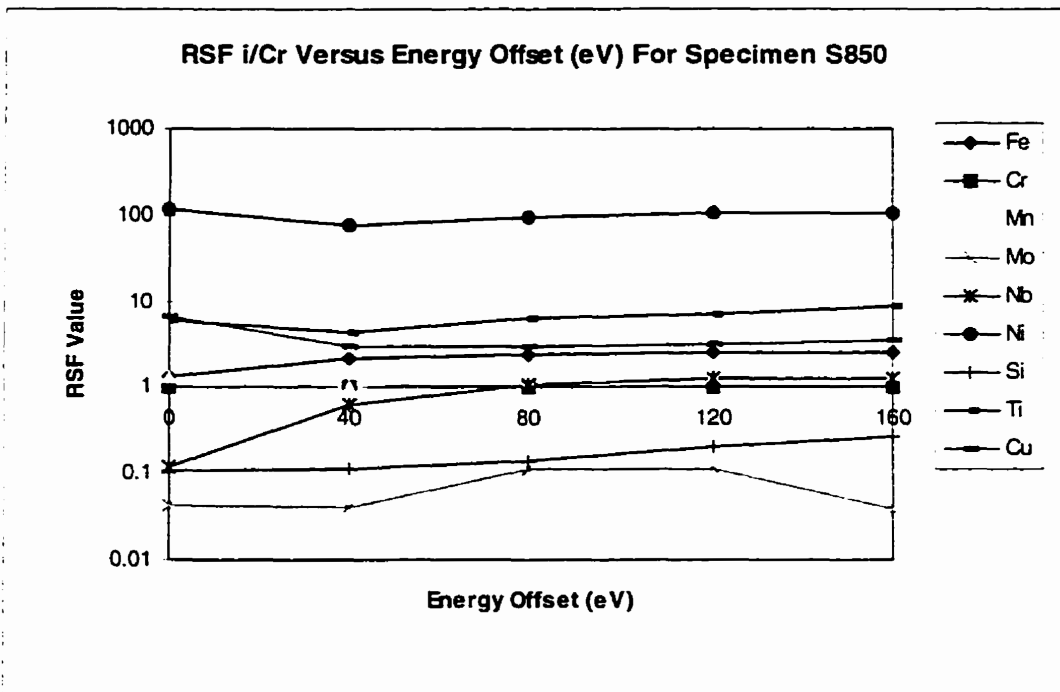

Figure B.68: RSF Values (Calculated With Respect To Chromium) Versus Energy For Sample S 850

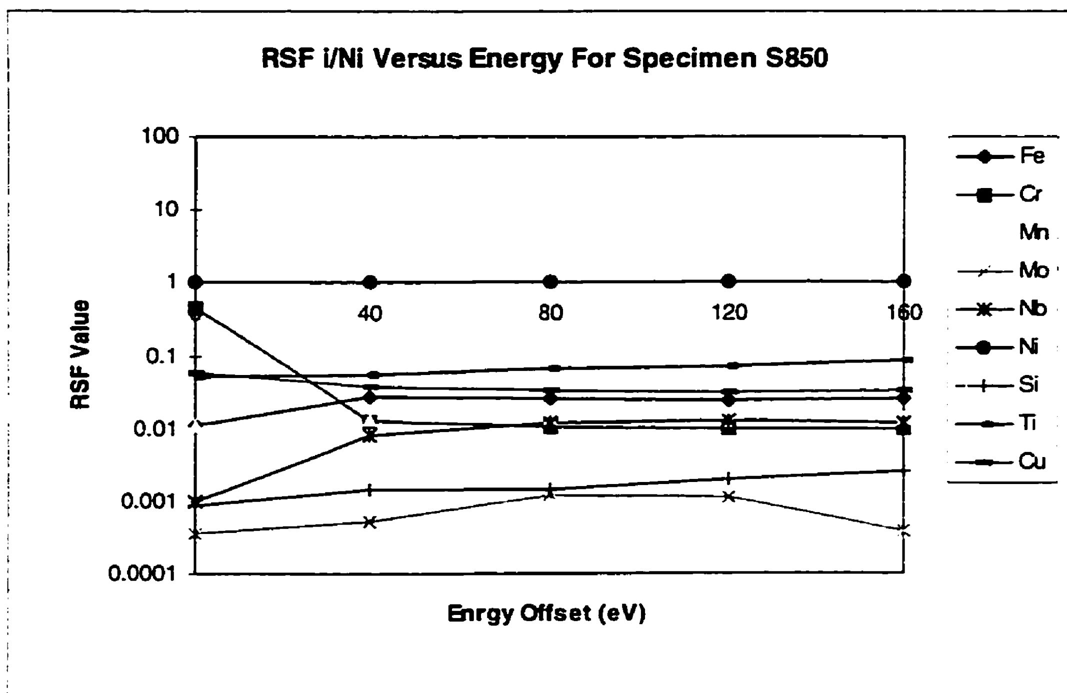

Figure B.69: RSF Values (Calculated With Respect To Nickel) Versus Energy For Sample S 850

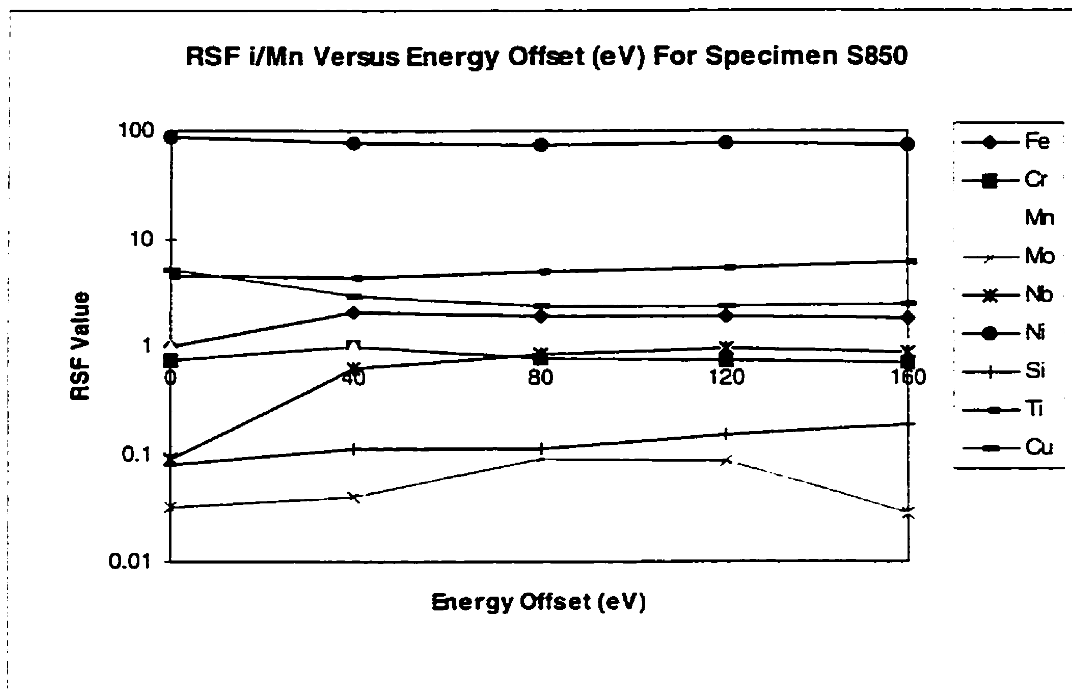

Figure B.70: RSF Values (Calculated With Respect To Manganese) Versus Energy For Sample S 850

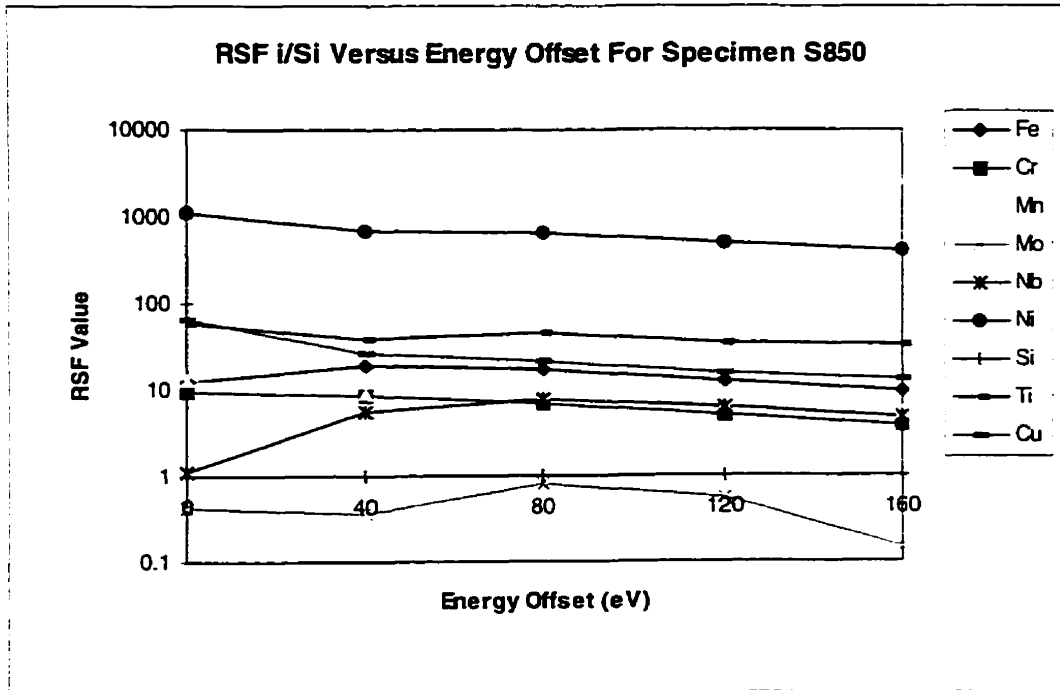

Figure B.71: RSF Values (Calculated With Respect To Silicon) Versus Energy For Sample S 850

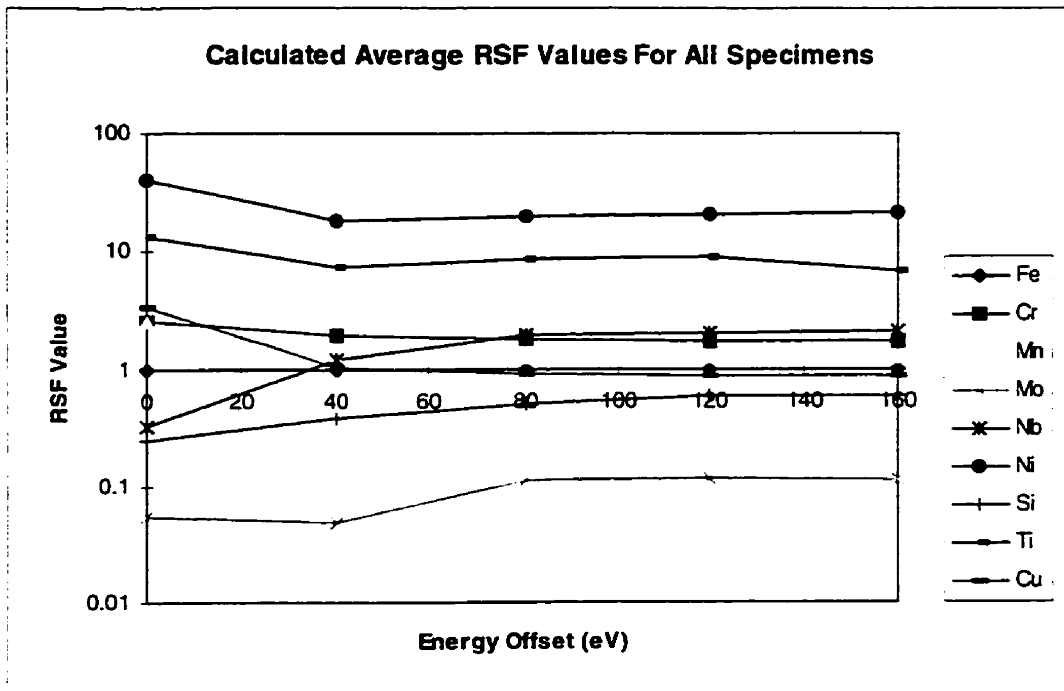

Figure B.72: Average RSF Values Calculated From All Alloys of Both Data Sets

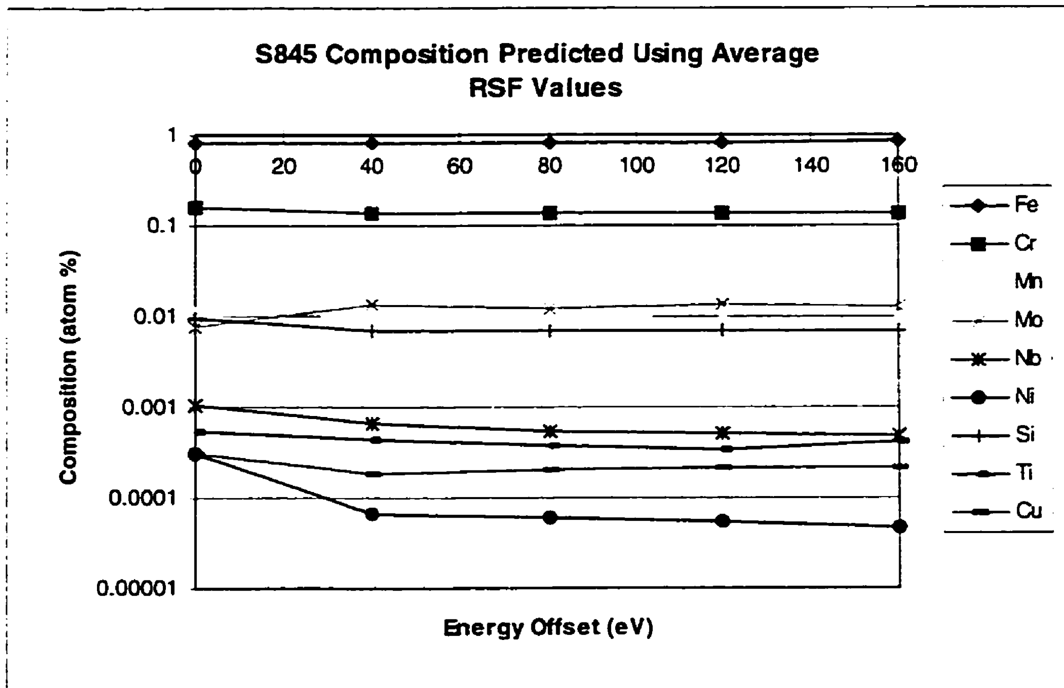

Figure B.73: Composition of S845 Predicted Using Average RSF Values

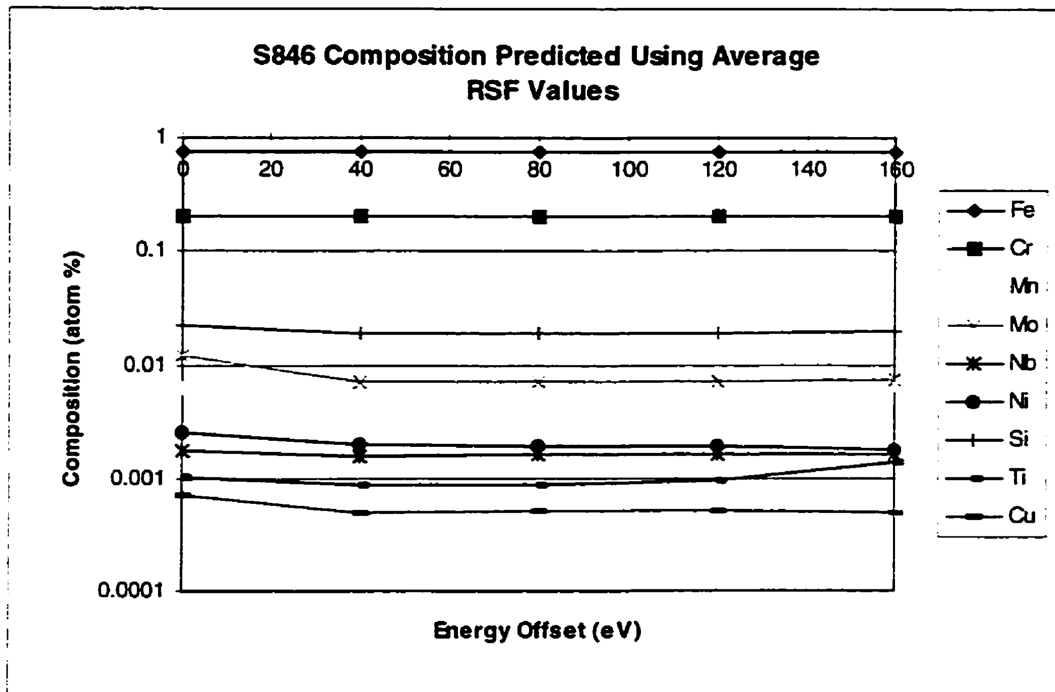

Figure B.74: Composition of S846 Predicted Using Average RSF Values

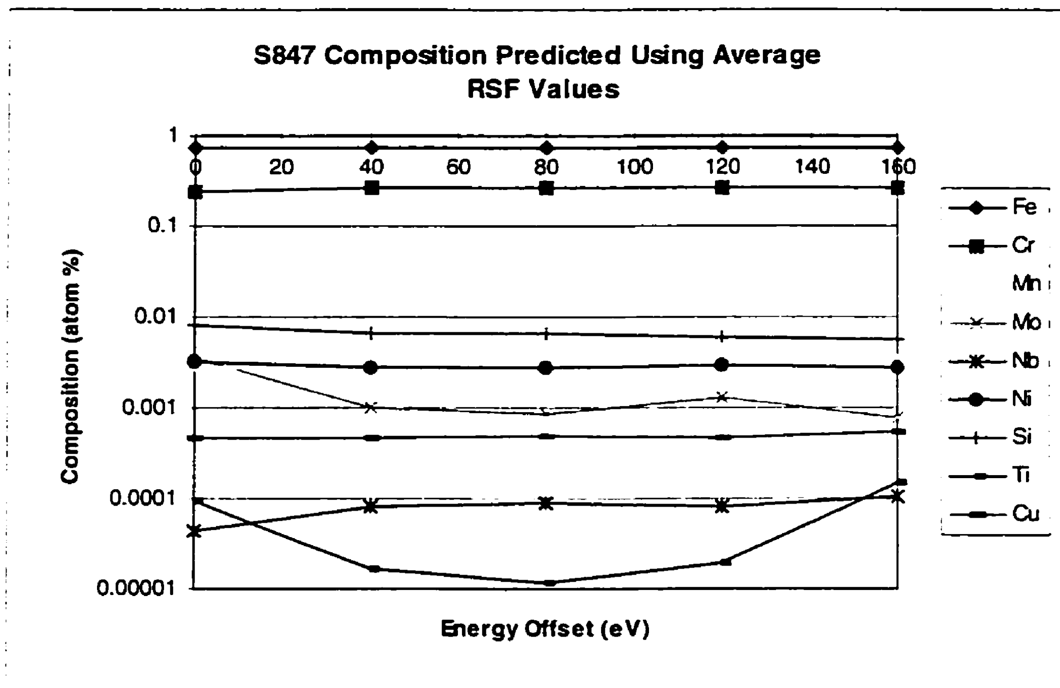

Figure B.75: Composition of S847 Predicted Using Average RSF Values

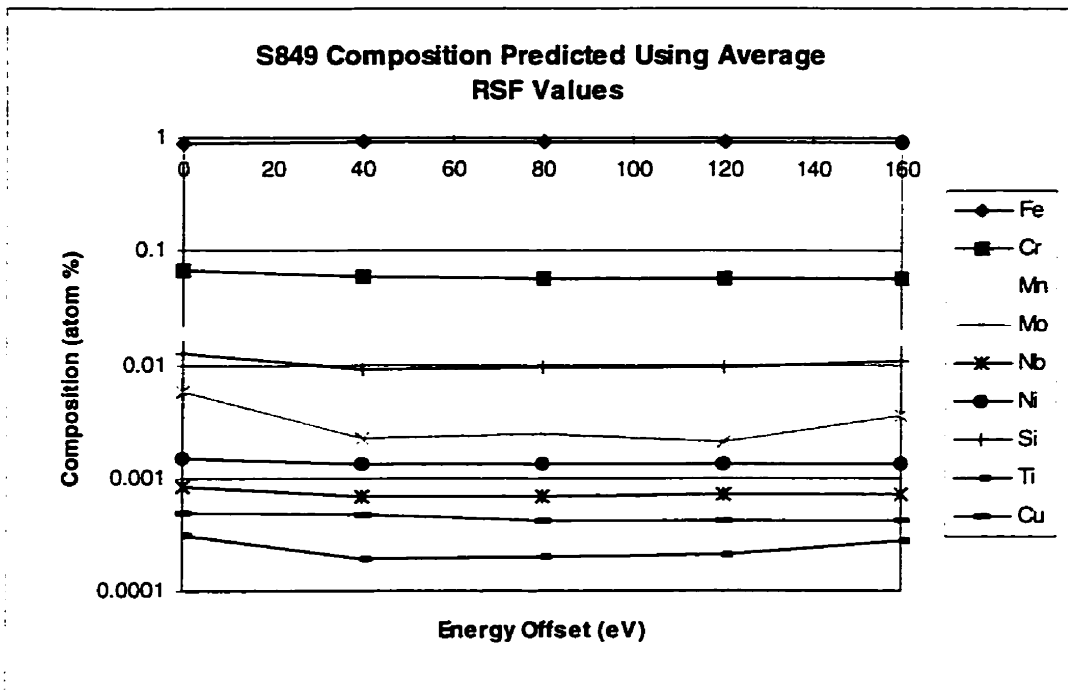

Figure B.76: Composition of S849 Predicted Using Average RSF Values

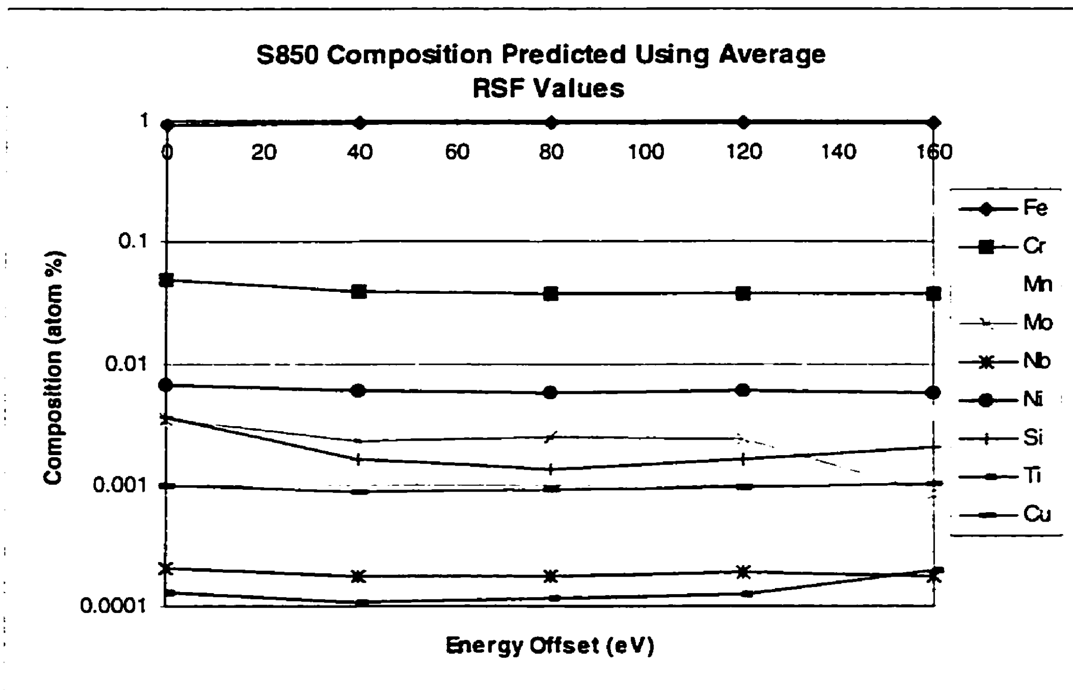

Figure B.77: Composition of S850 Predicted Using Average RSF Values

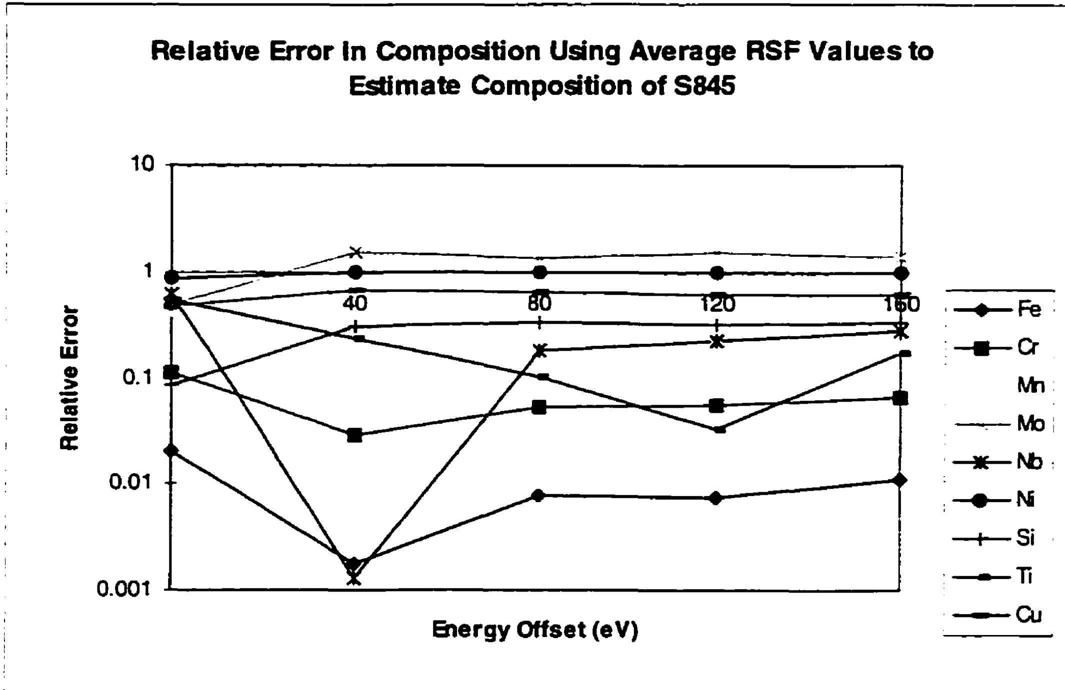

Figure B.78: Relative Error In S845 Composition Predicted Using Average RSF Values

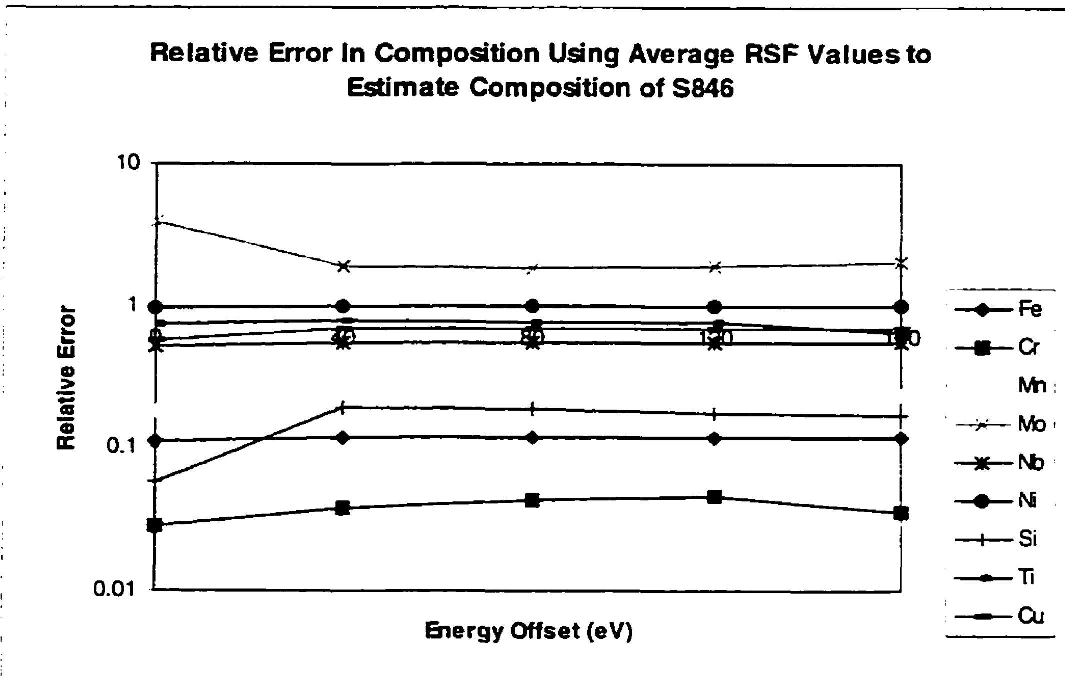

Figure B.79: Relative Error In S846 Composition Predicted Using Average RSF Values

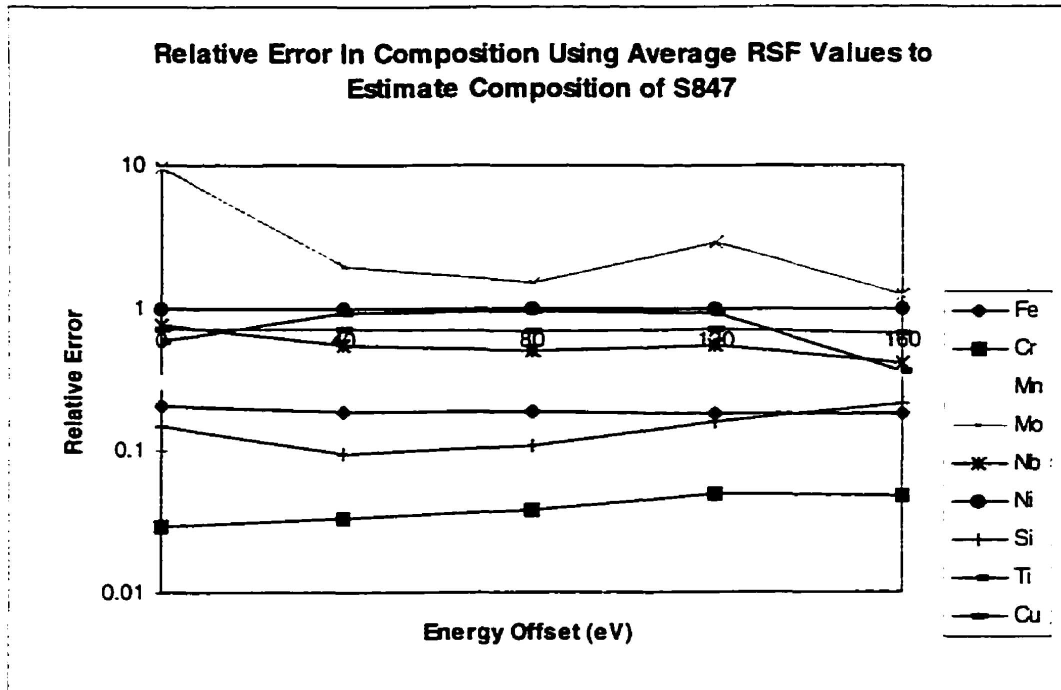

Figure B.80: Relative Error In S847 Composition Predicted Using Average RSF Values

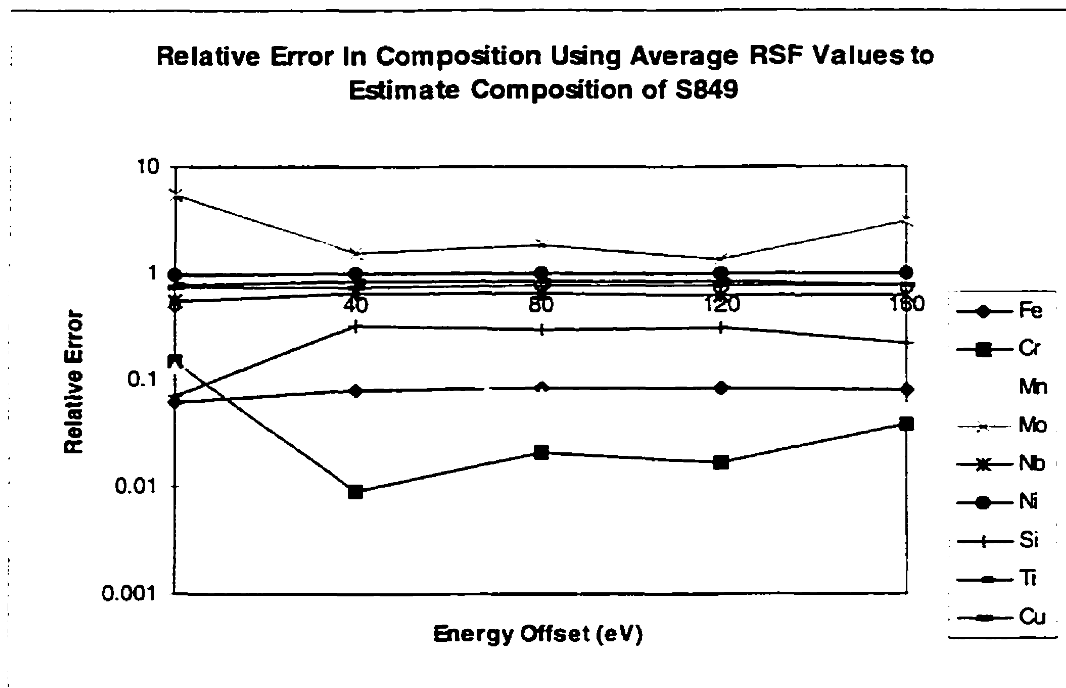

Figure B.81: Relative Error In S849 Composition Predicted Using Average RSF Values

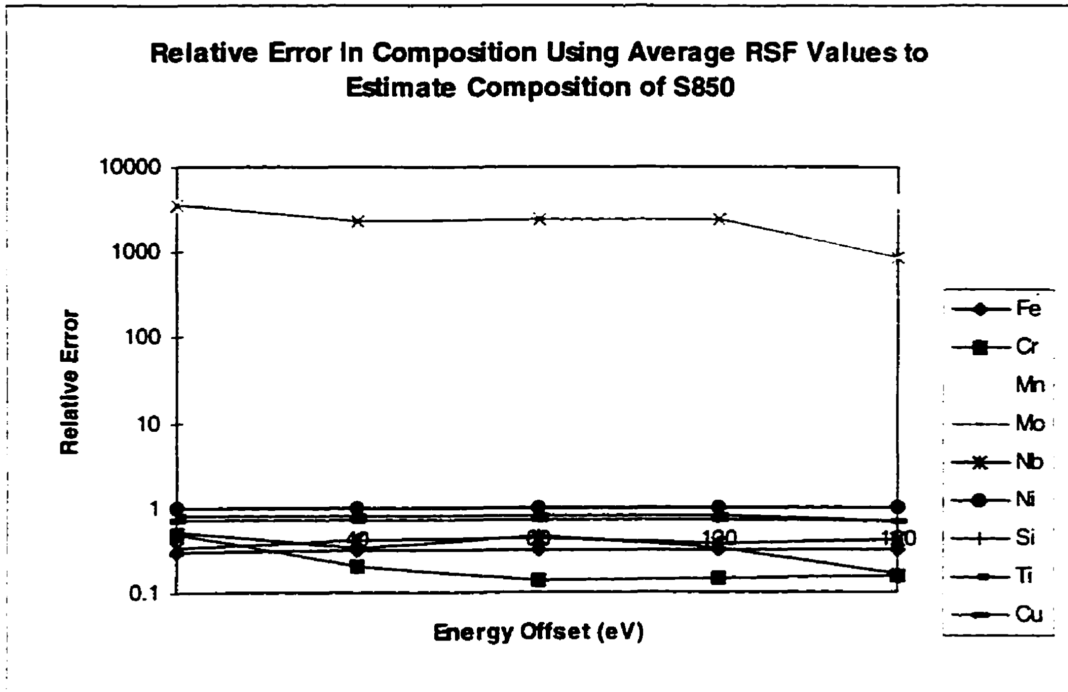

Figure B.82: Relative Error In S850 Composition Predicted Using Average RSF Values

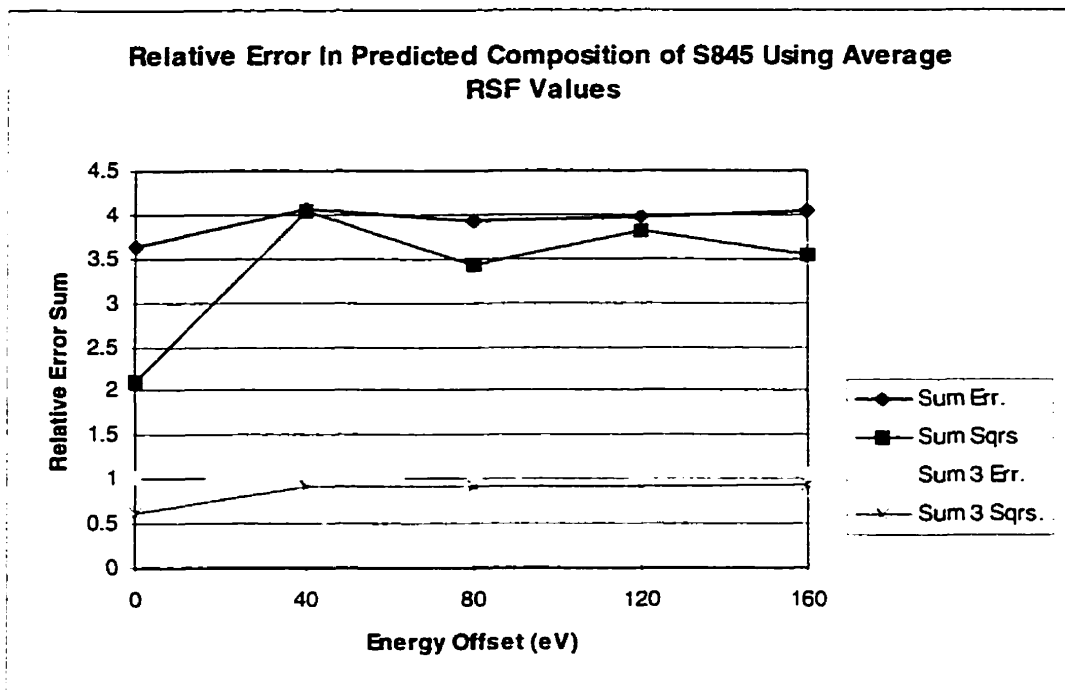

Figure B.83: Sum of Errors In S845 Composition Predicted Using Average RSF Values

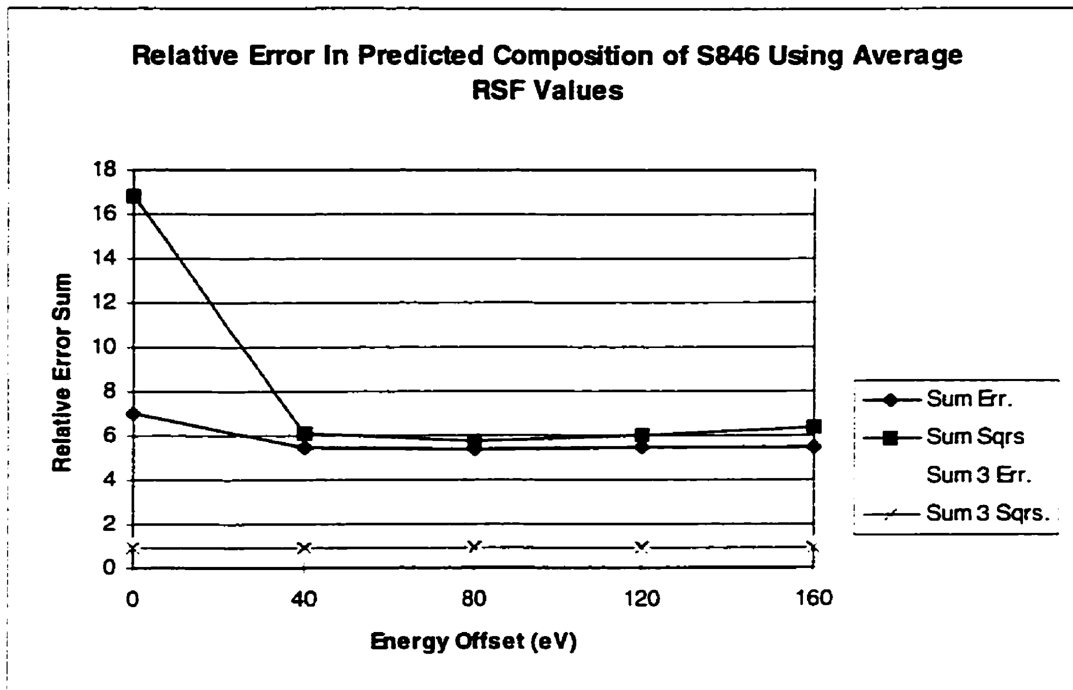

Figure B.84: Sum of Errors In S846 Composition Predicted Using Average RSF Values

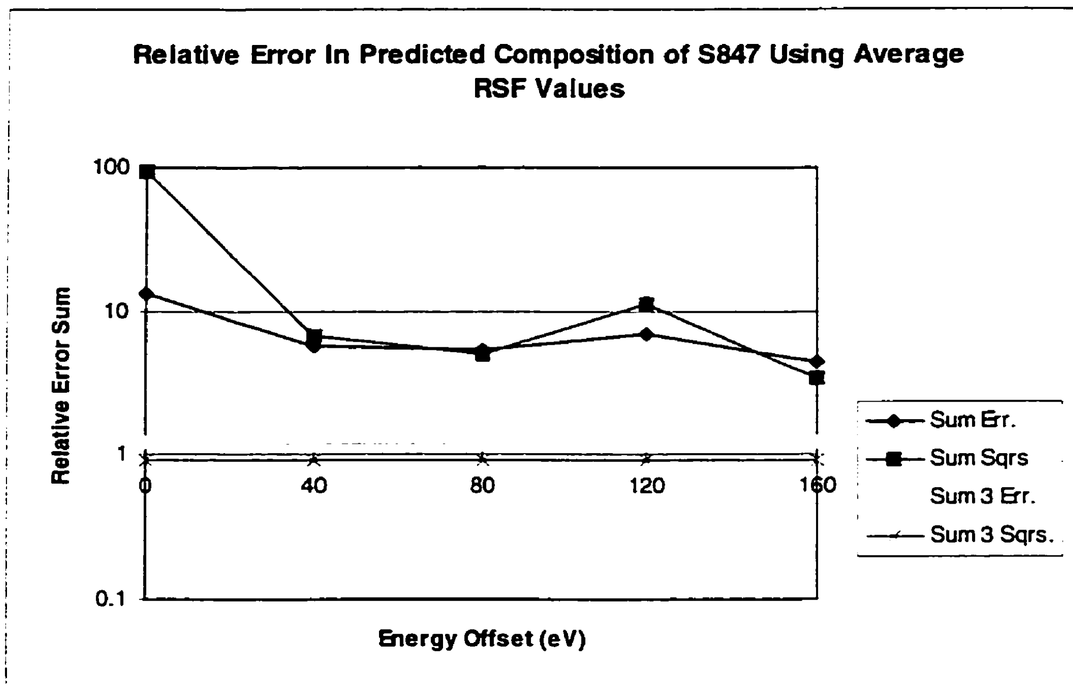

Figure B.85: Sum of Errors In S847 Composition Predicted Using Average RSF Values

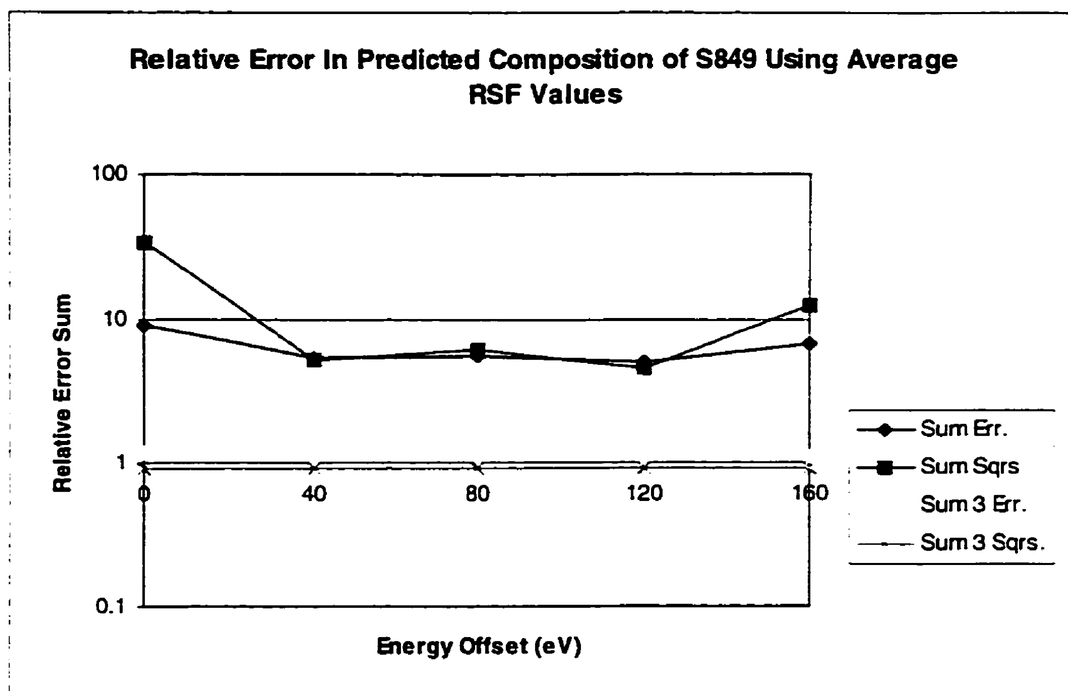

Figure B.86: Sum of Errors In S849 Composition Predicted Using Average RSF Values

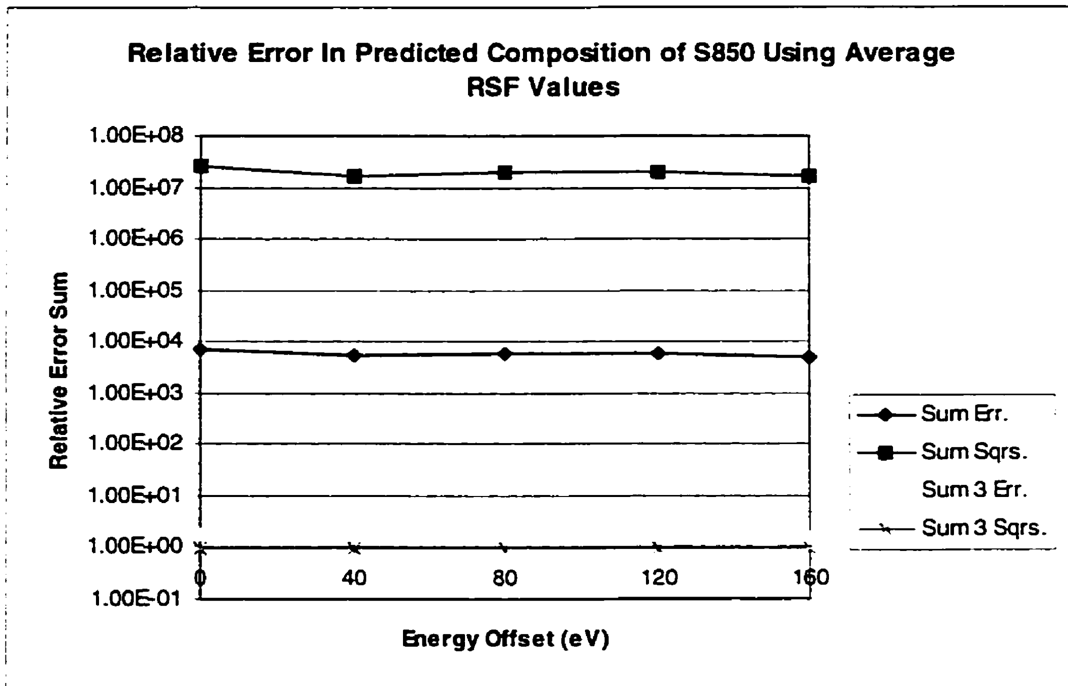

Figure B.87: Sum of Errors In S850 Composition Predicted Using Average RSF Values

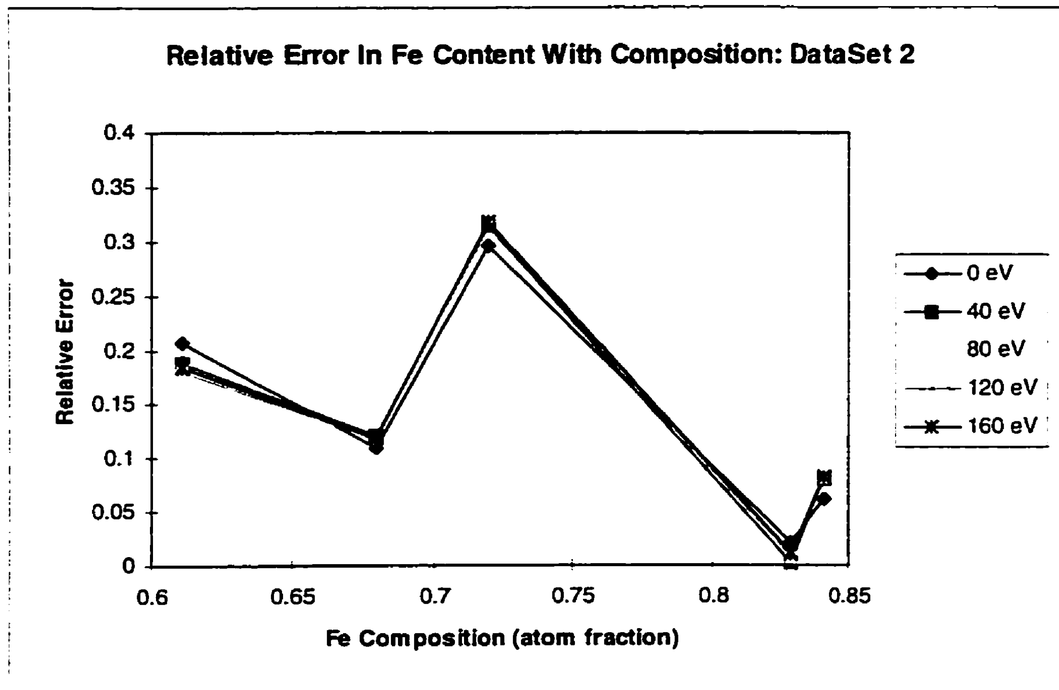

Figure B.88: Relative Error In Predicted Fe Content Versus Elemental Fe Composition

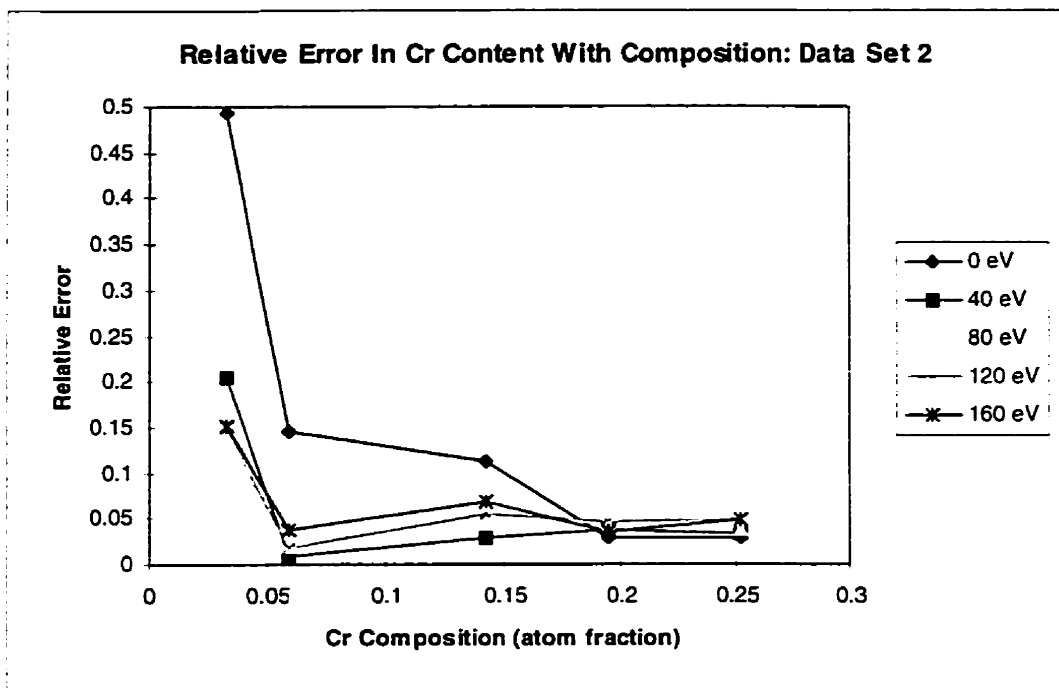

Figure B.89: Relative Error In Predicted Cr Content Versus Elemental Cr Composition

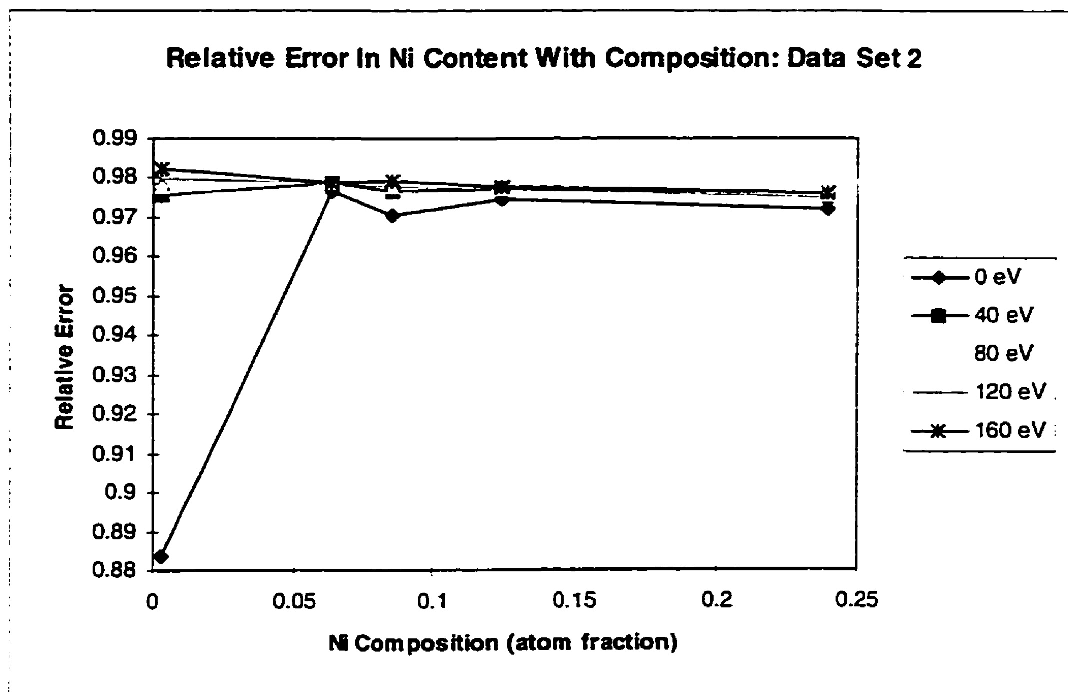

Figure B.90: Relative Error In Predicted Ni Content Versus Elemental Ni Composition

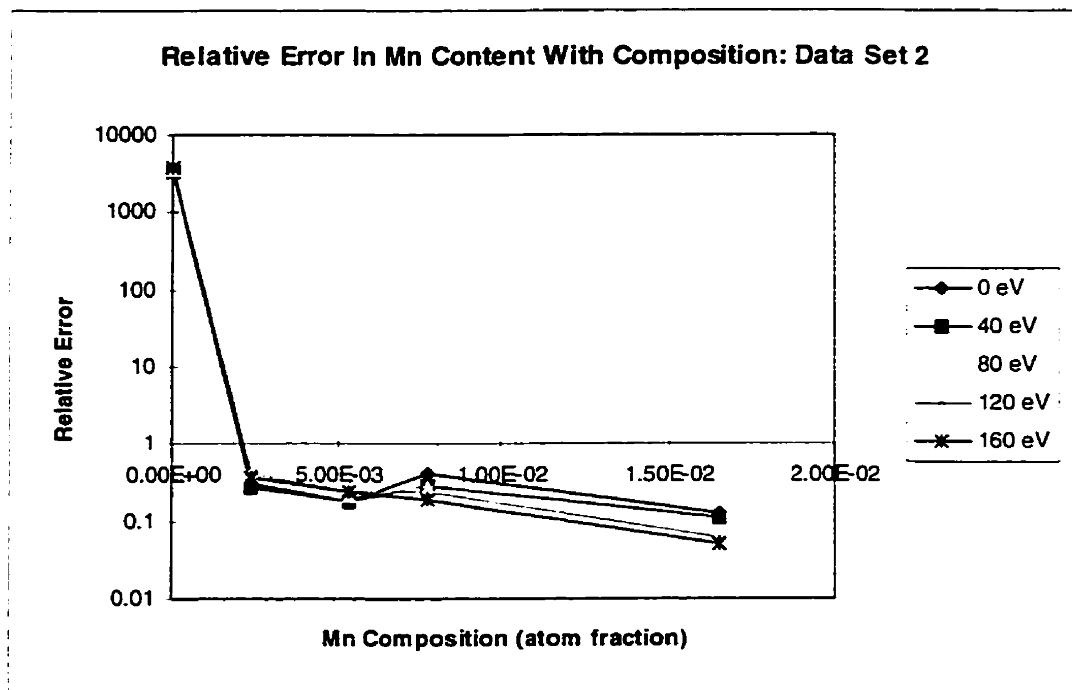

Figure B.91: Relative Error In Predicted Mn Content Versus Elemental Mn Composition

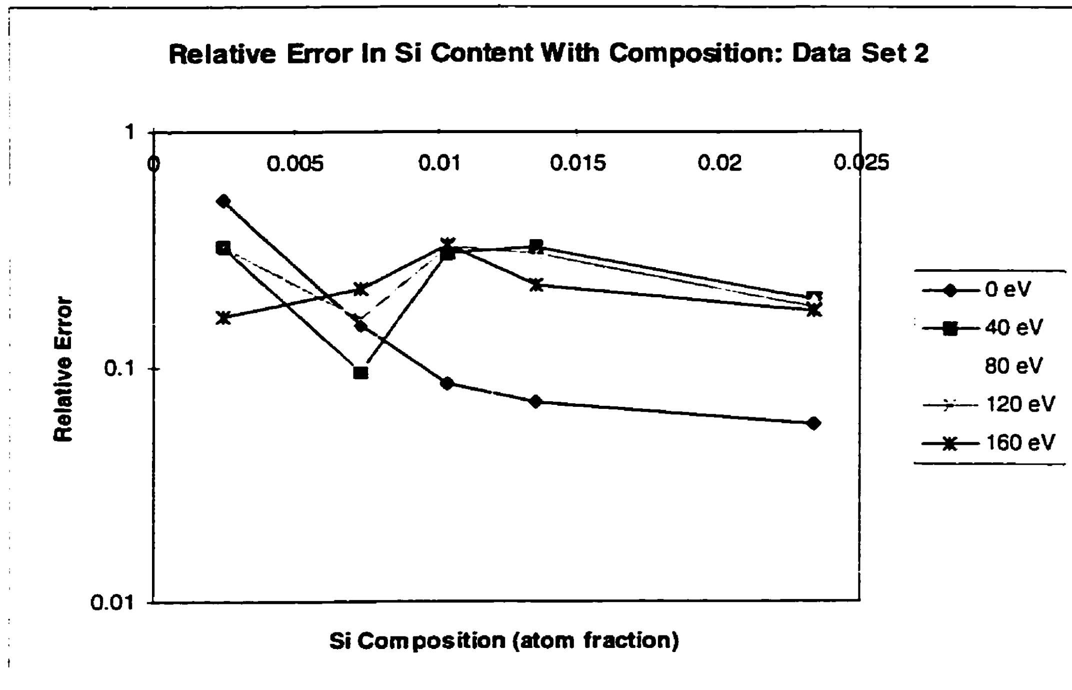

Figure B.92: Relative Error In Predicted Si Content Versus Elemental Si Composition

APPENDIX C:

BOND BREAKING MODEL RESULTS PRESENTED IN GRAPHICAL FORM

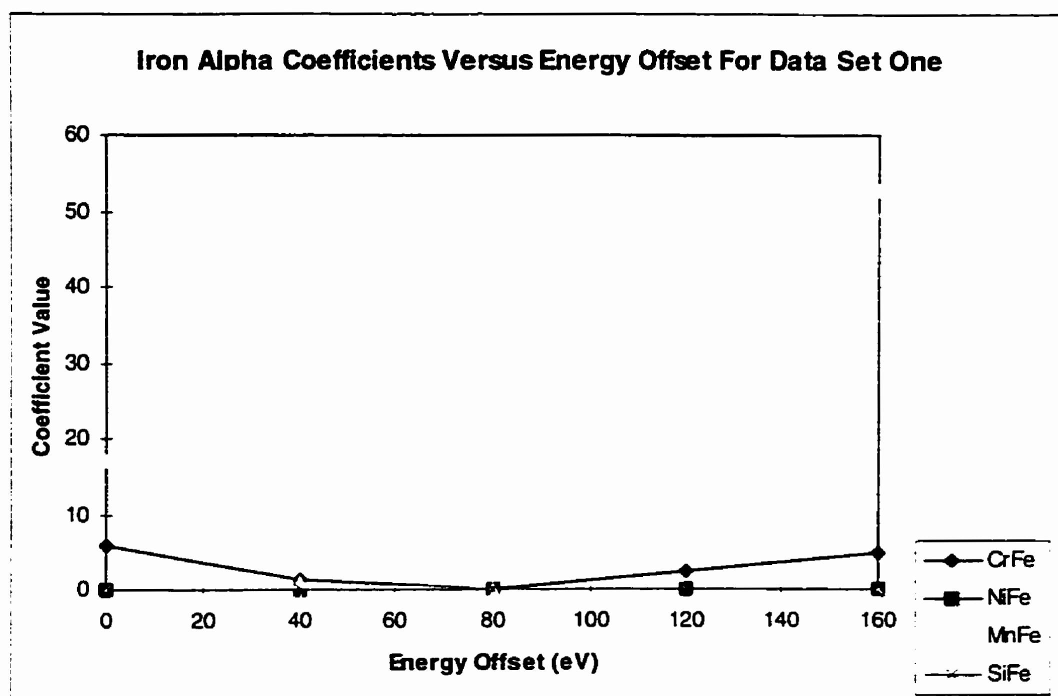

Figure C.1: Iron Relative Emission Coefficients For Data Set 1

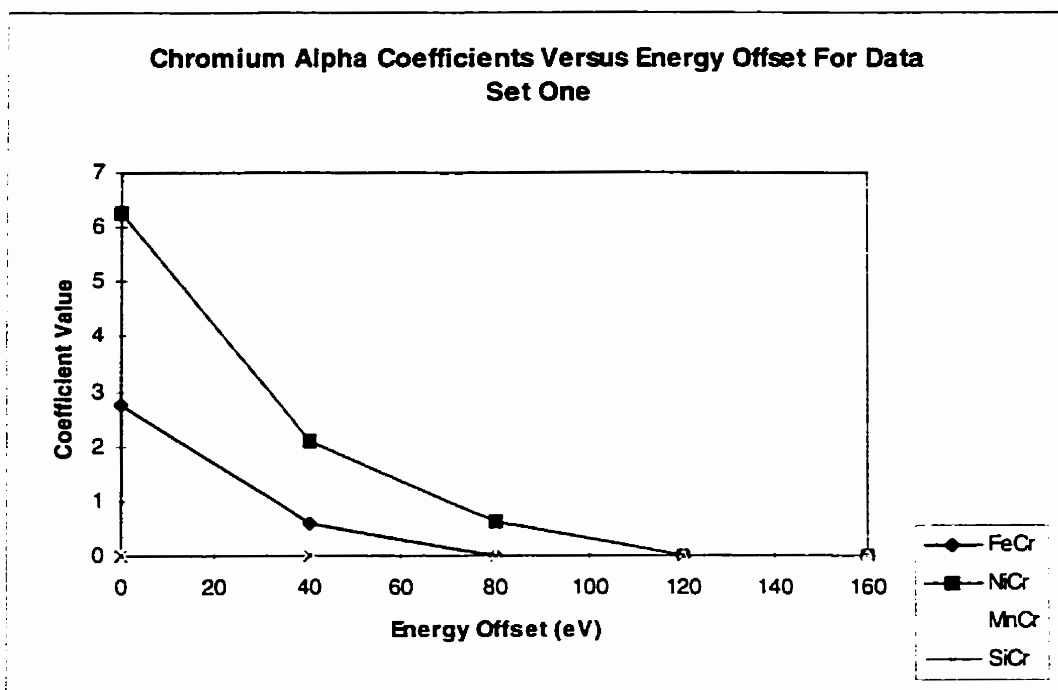

Figure C.2: Chromium Relative Emission Coefficients For Data Set 1

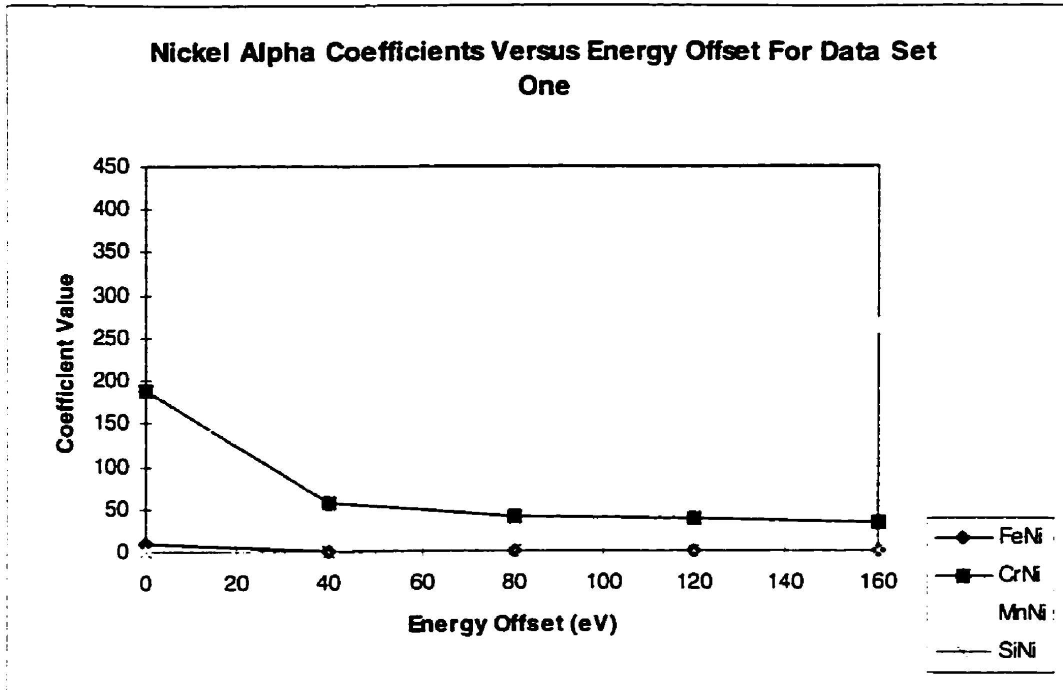

Figure C.3: Nickel Relative Emission Coefficients For Data Set 1

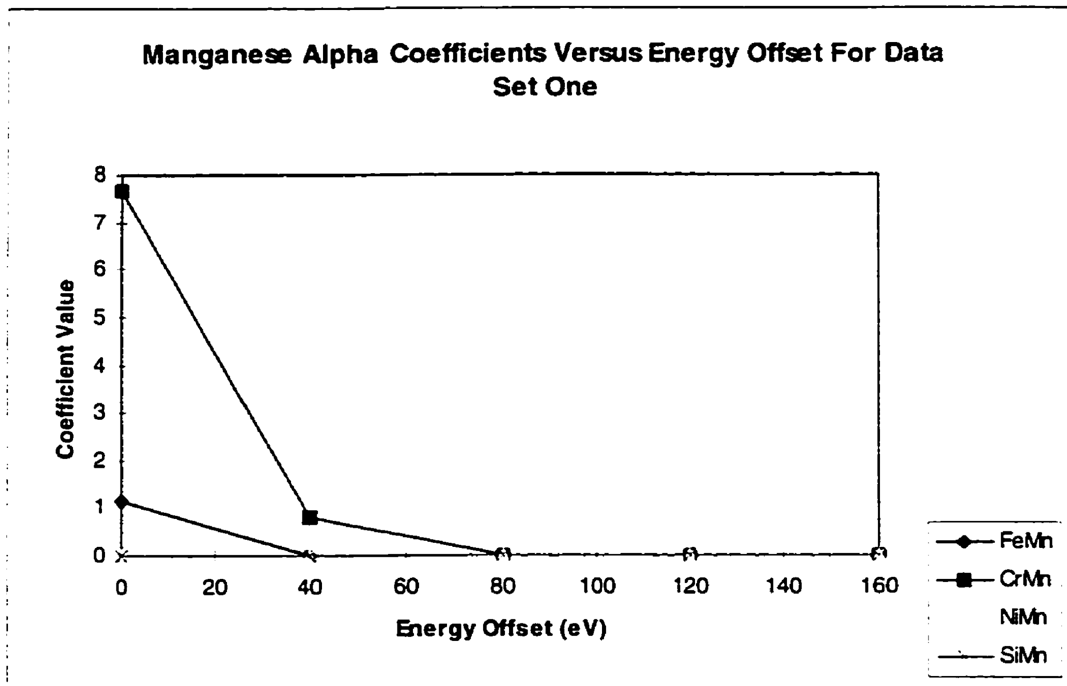

Figure C.4: Manganese Relative Emission Coefficients For Data Set 1

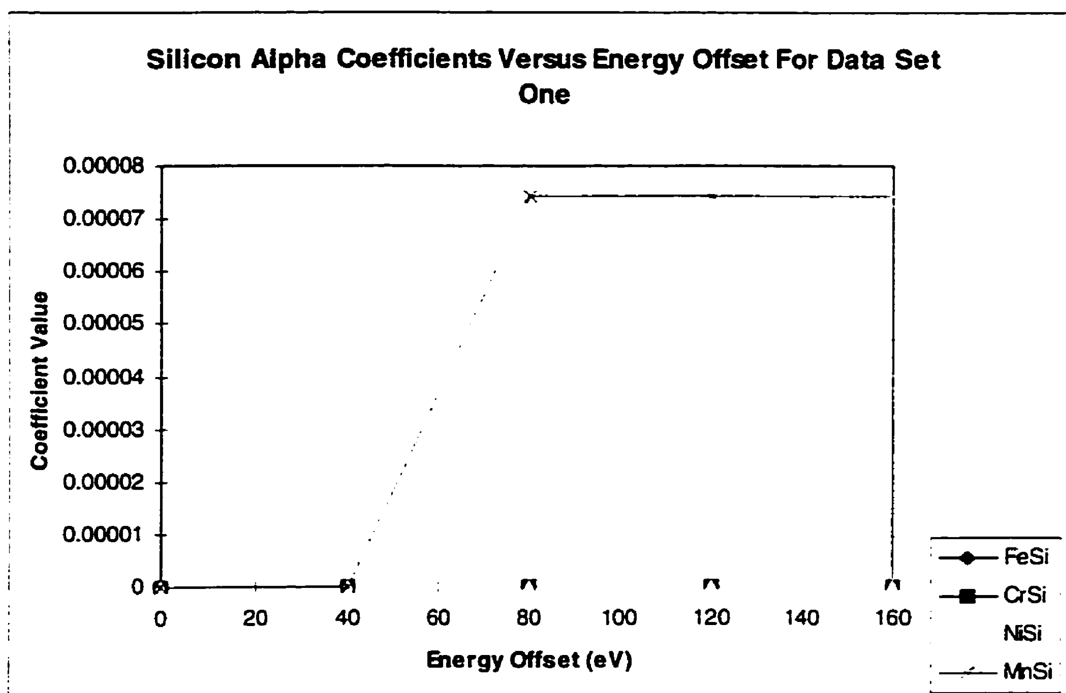

Figure C.5: Silicon Relative Emission Coefficients For Data Set 1

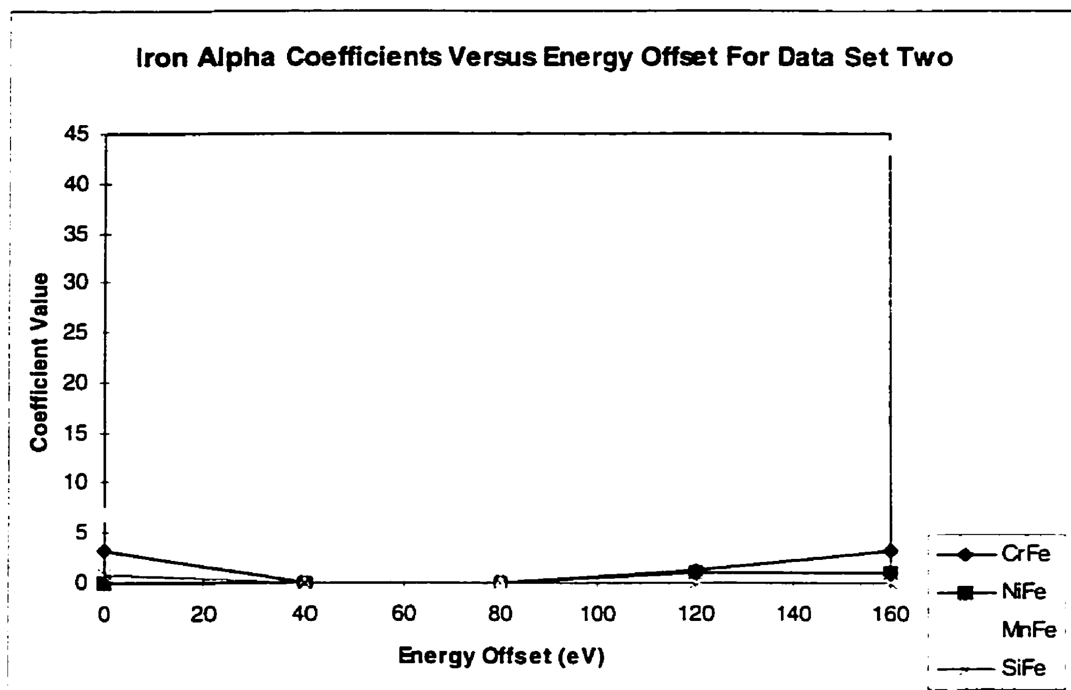

Figure C.6: Iron Relative Emission Coefficients For Data Set 2

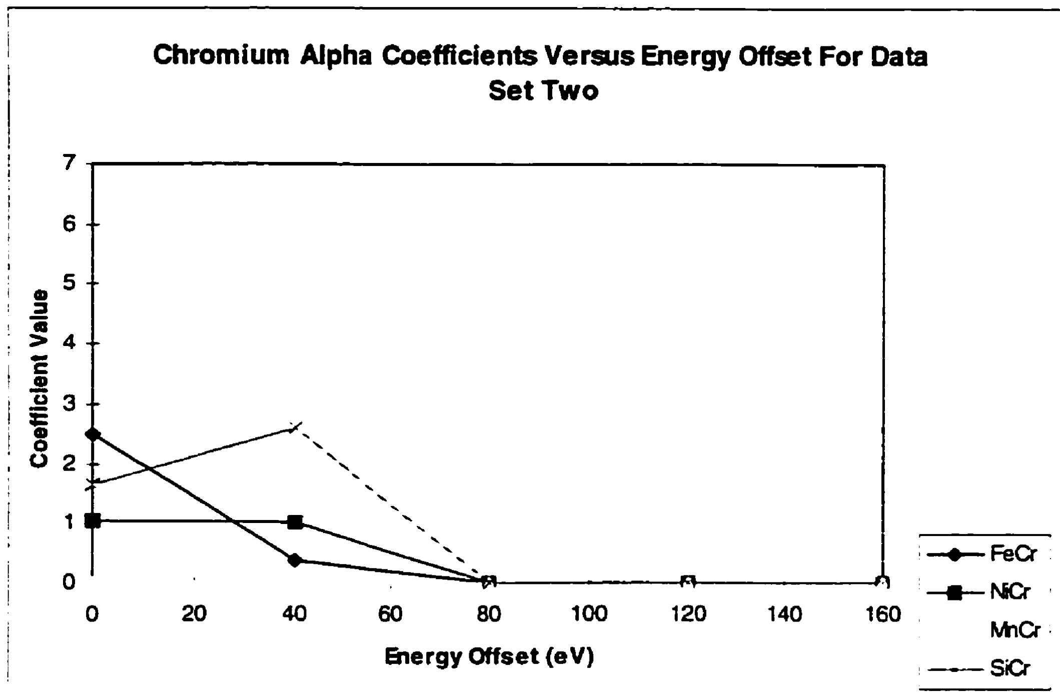

Figure C.7: Chromium Relative Emission Coefficients For Data Set 2

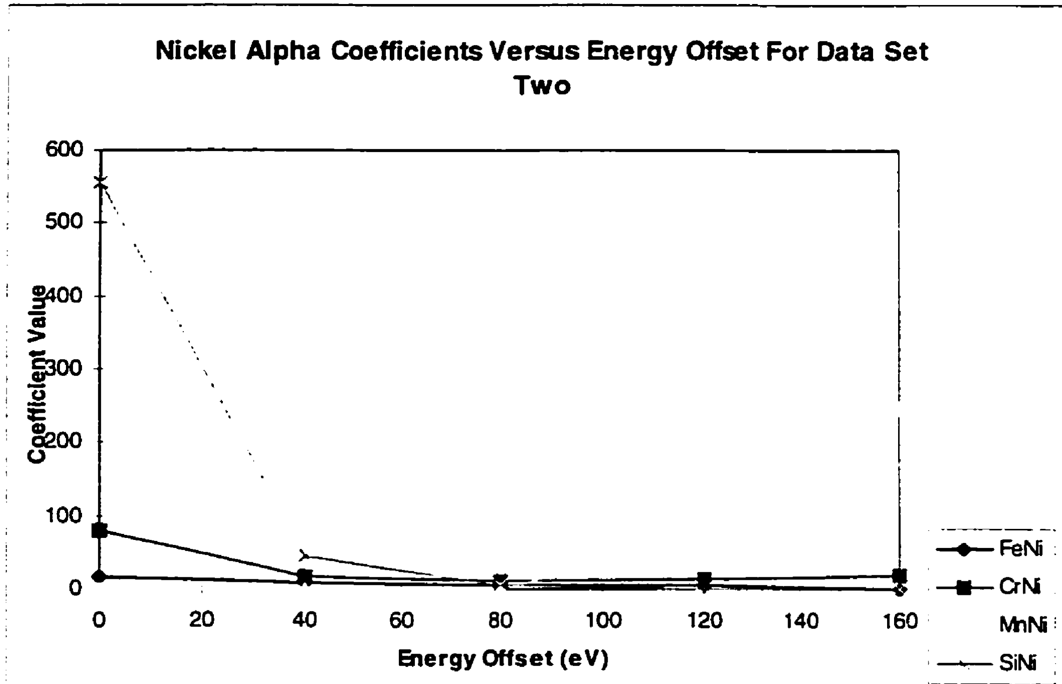

Figure C.8: Nickel Relative Emission Coefficients For Data Set 2

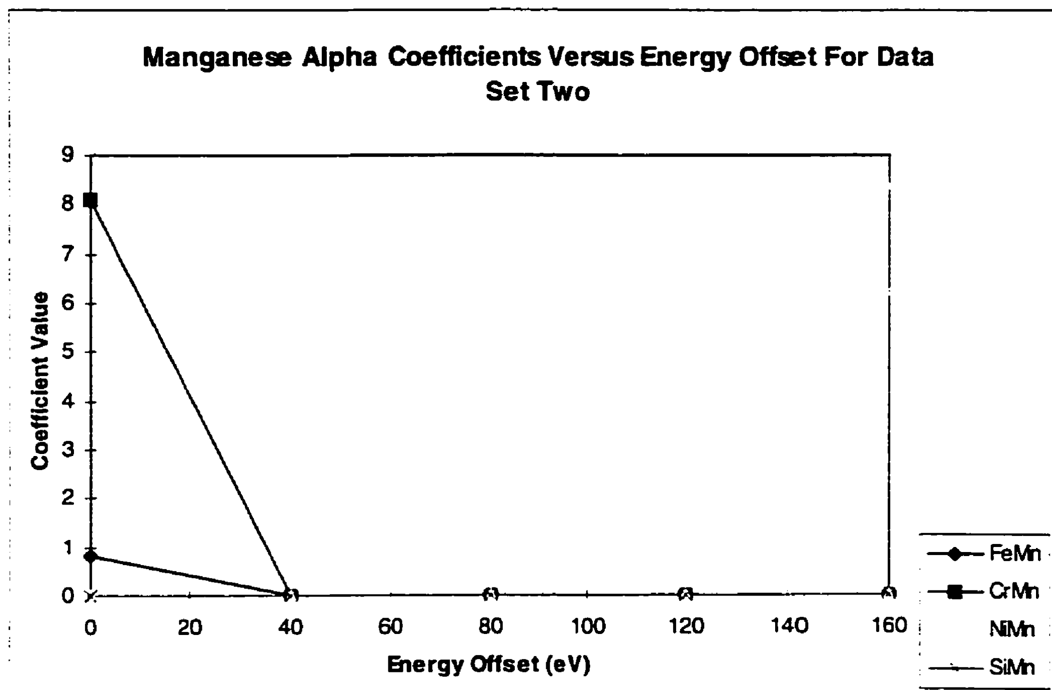

Figure C.9: Manganese Relative Emission Coefficients For Data Set 2

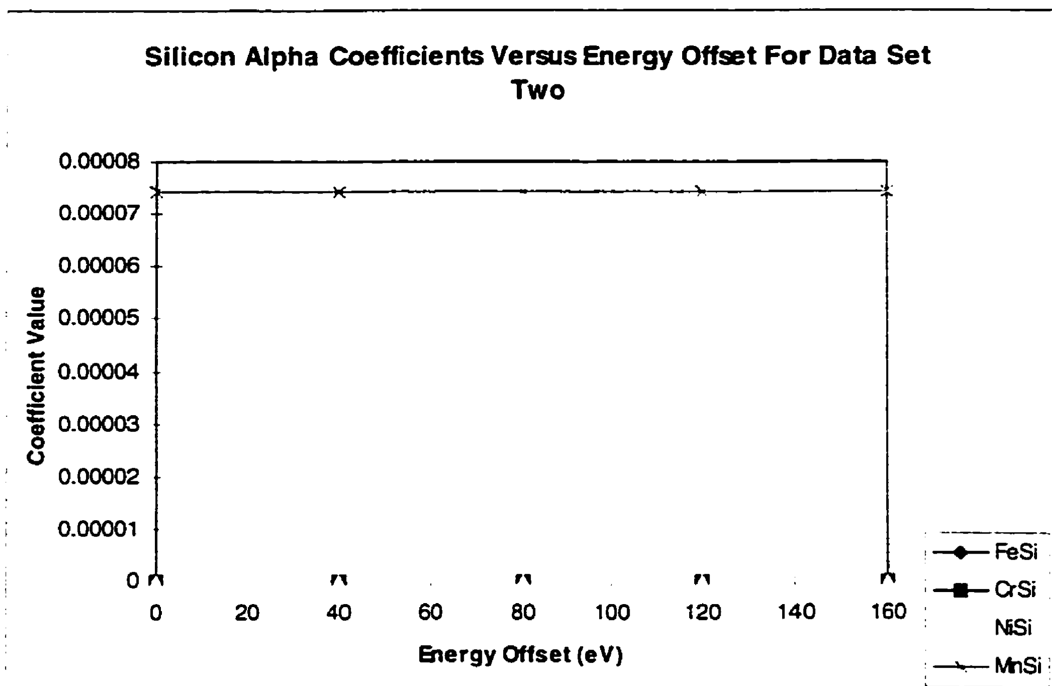

Figure C.10: Silicon Relative Emission Coefficients For Data Set 2

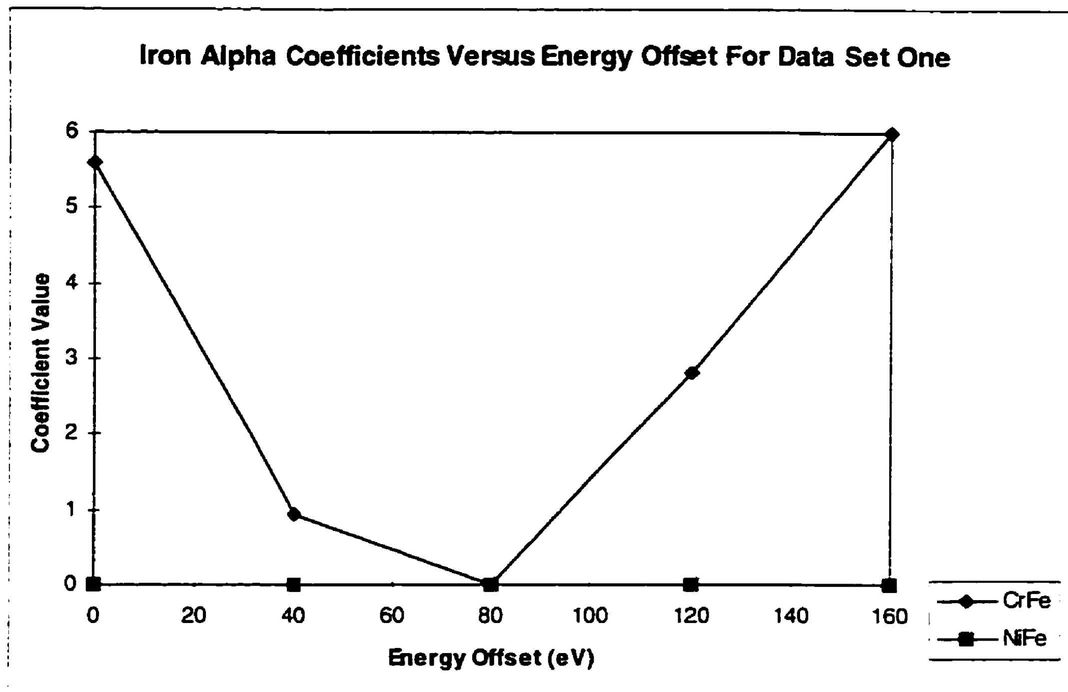

Figure C.11: Iron Relative Emission Coefficients For Data Set 1 - Three Element Model

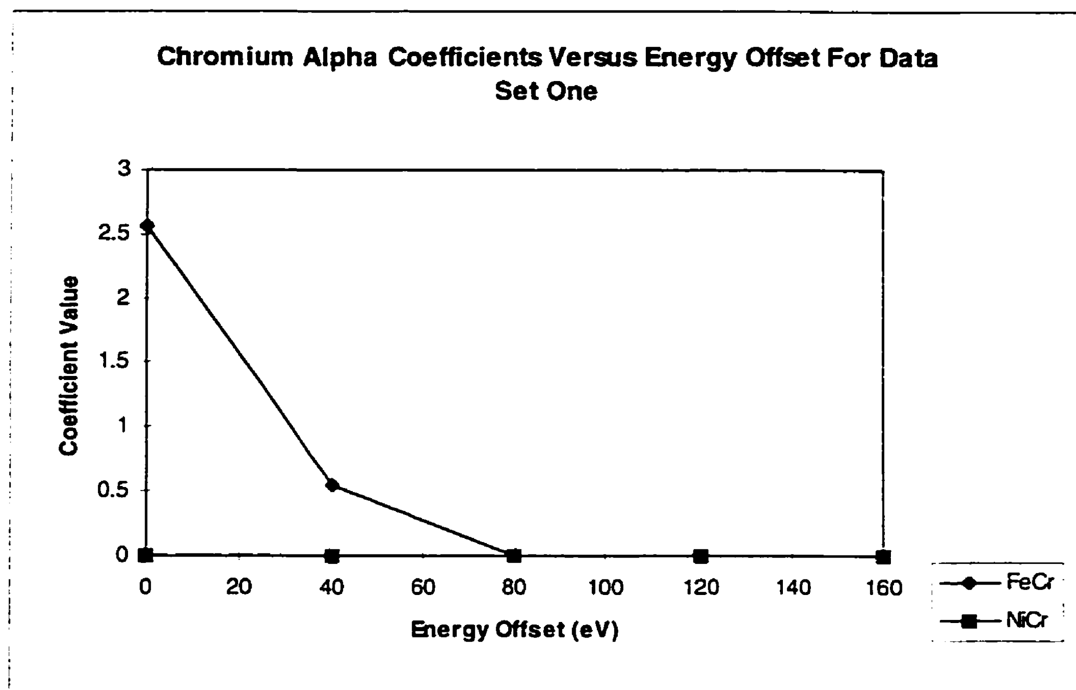

Figure C.12: Chromium Relative Emission Coefficients For Data Set 1 - Three Element Model

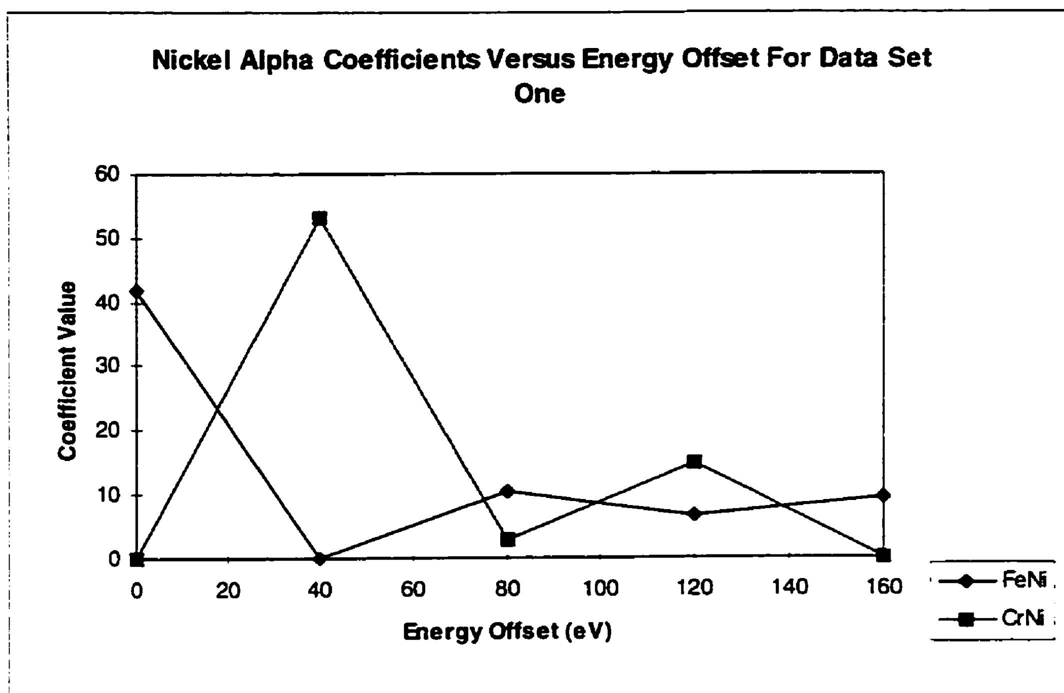

Figure C.13: Nickel Relative Emission Coefficients For Data Set 1 - Three Element Model

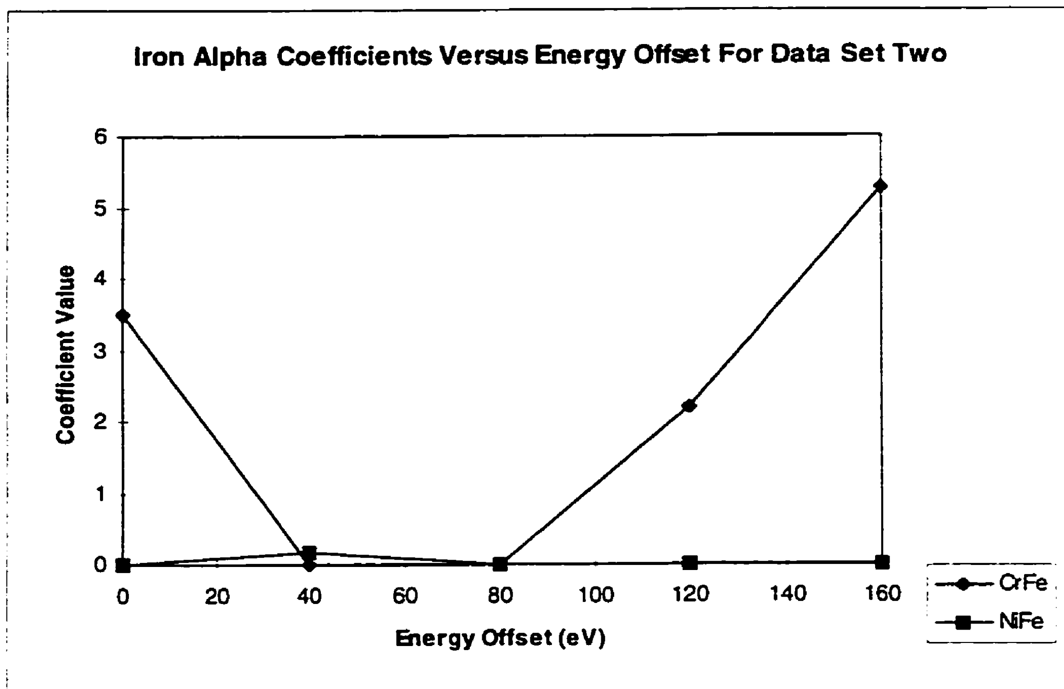

Figure C.14: Iron Relative Emission Coefficients For Data Set 2 - Three Element Model

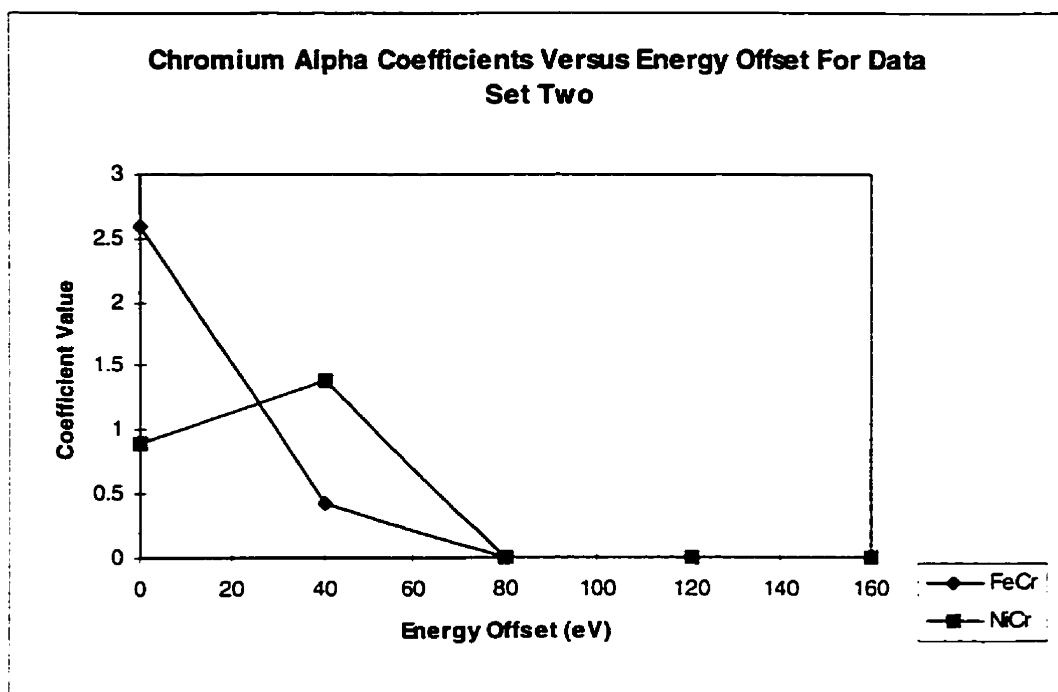

Figure C.15: Chromium Relative Emission Coefficients For Data Set 2 - Three Element Model

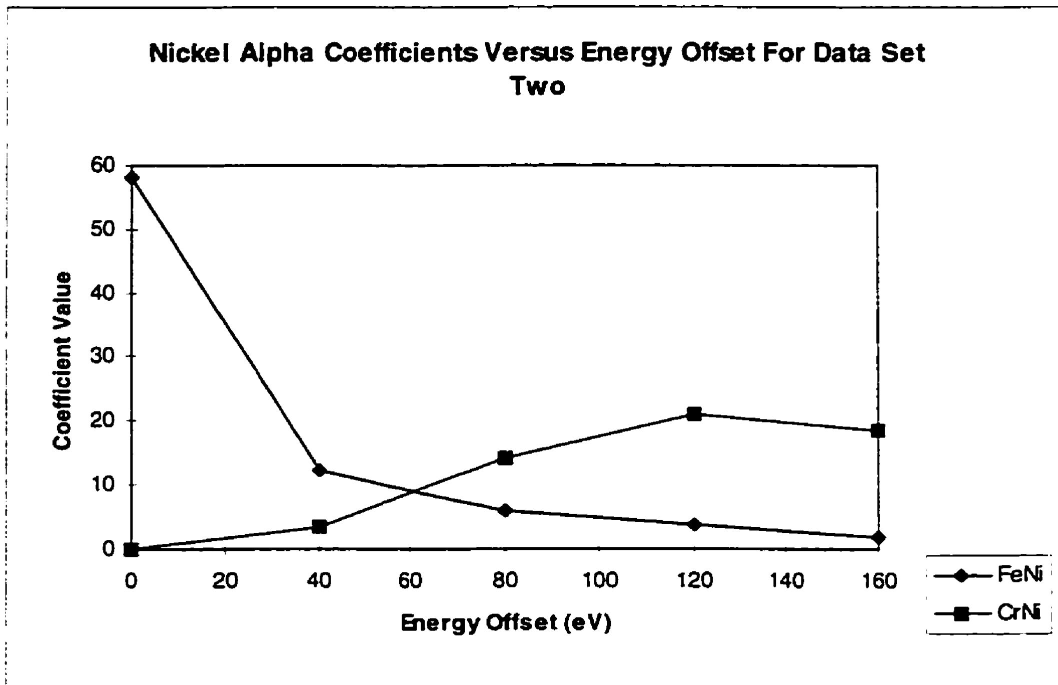

Figure C.16: Nickel Relative Emission Coefficients For Data Set 2 - Three Element Model

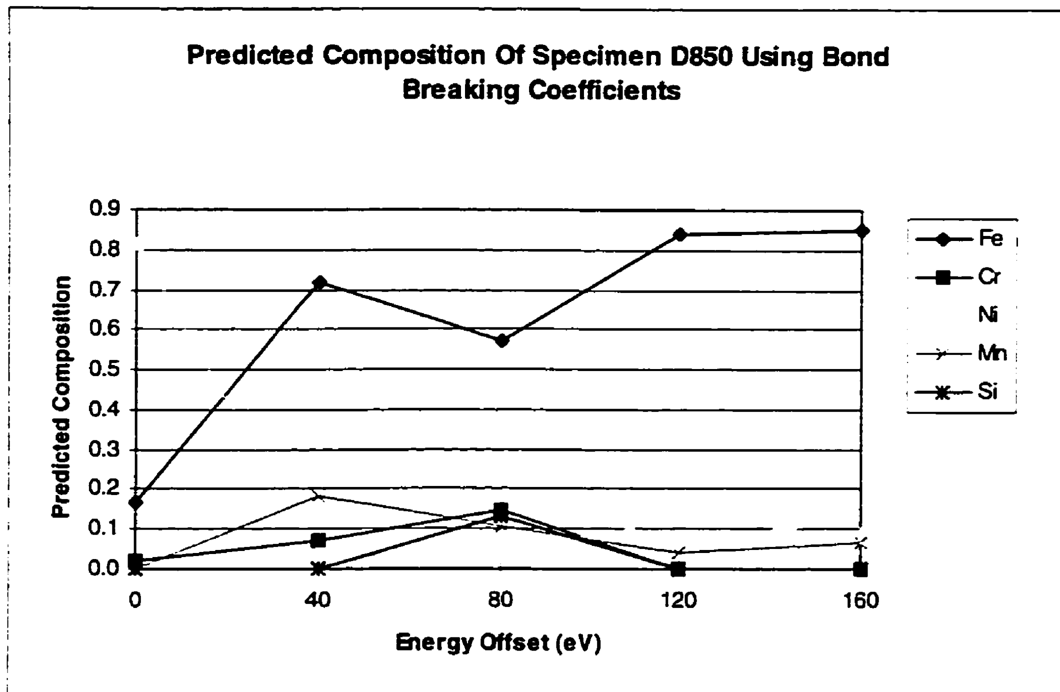

Figure C.17: D850 Composition Predicted Using 5 Element Bond Breaking Data - Data Set 1

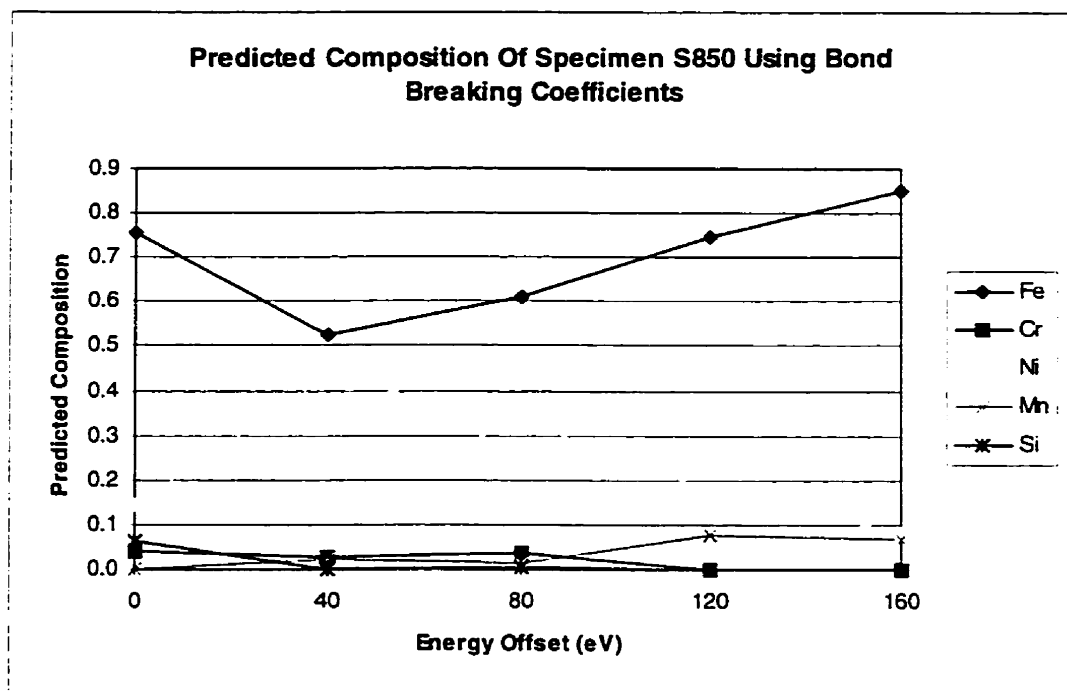

Figure C.18: D850 Composition Predicted Using 5 Element Bond Breaking Data - Data Set 2

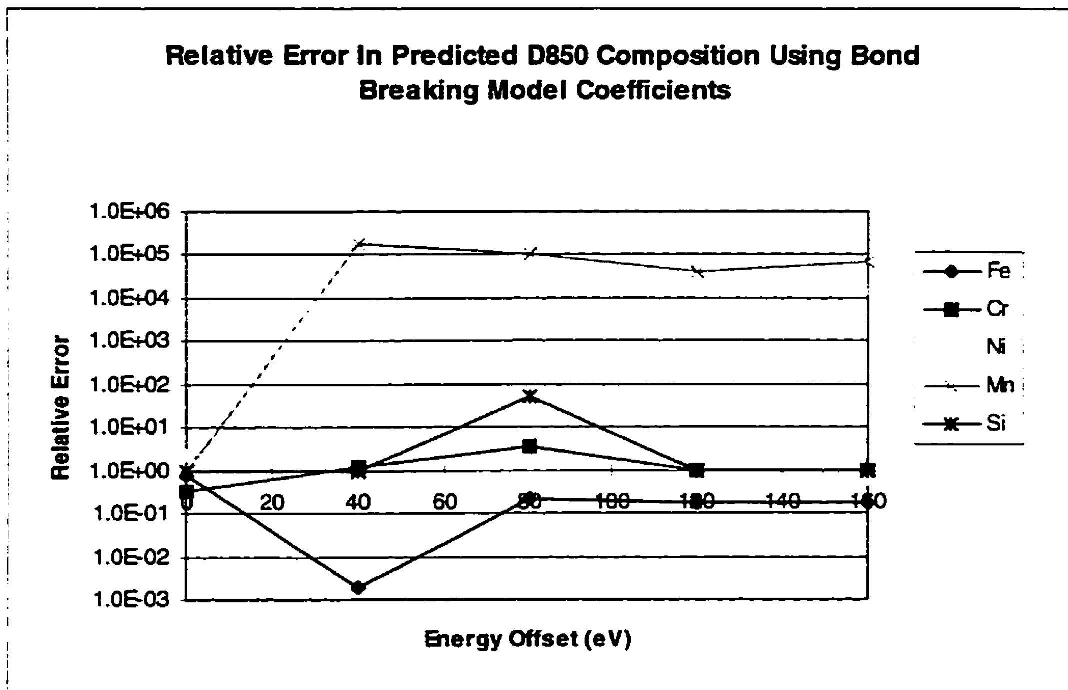

Figure C.19: Error In Predicted D850 Composition - 5 Element Analysis of Data Set 1

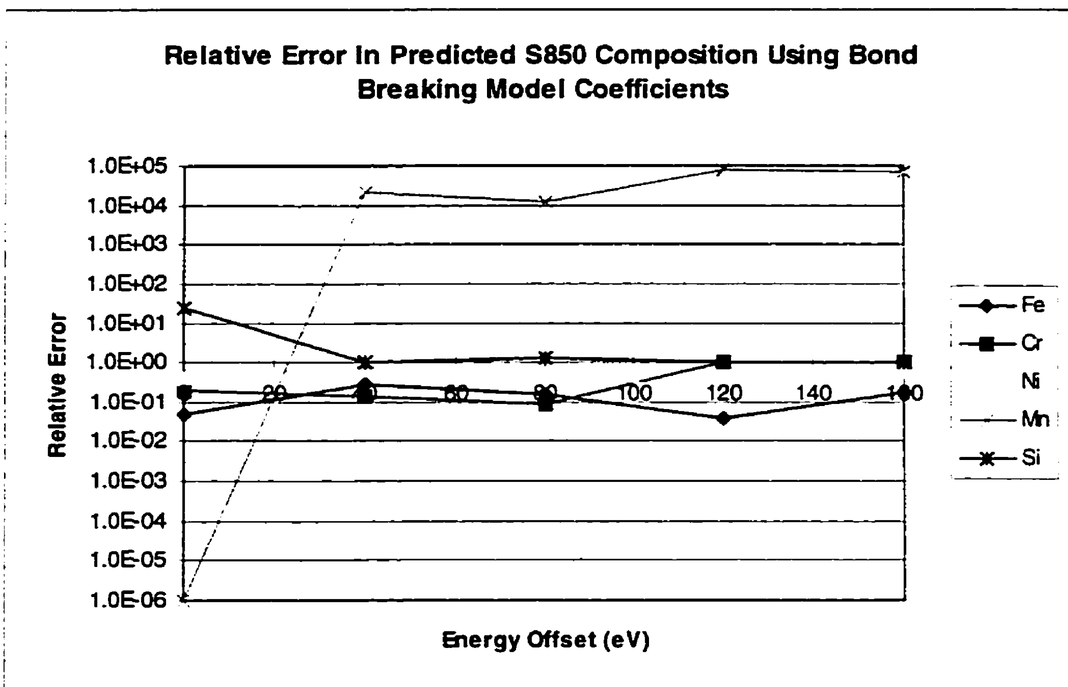

Figure C.20: Error In Predicted D850 Composition - 5 Element Analysis of Data Set 2

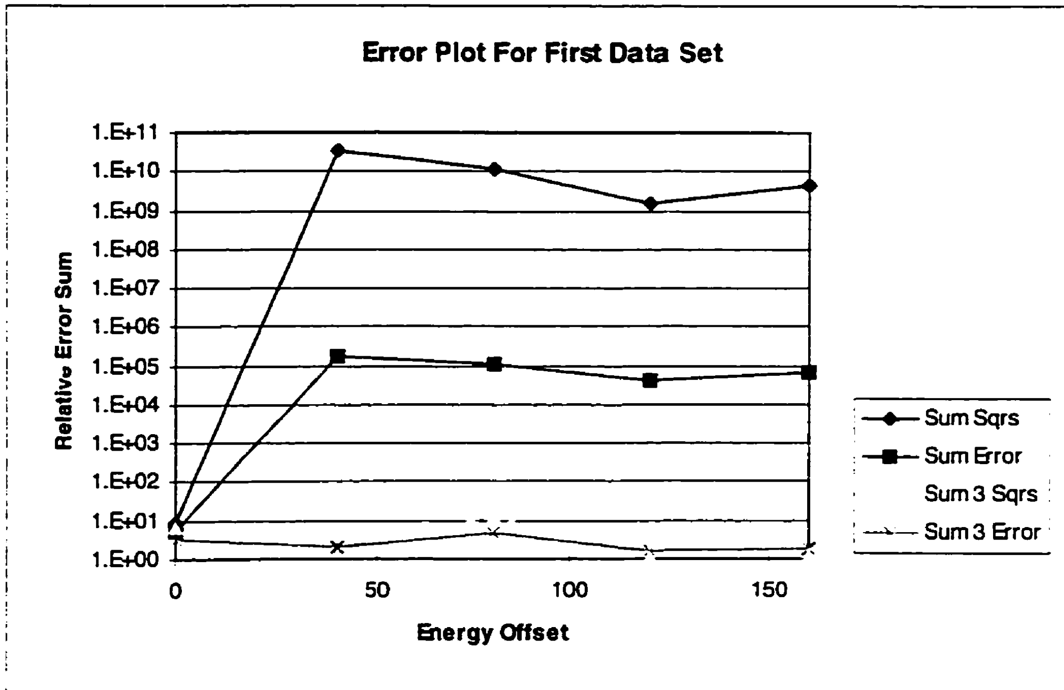

Figure C.21: Sum of Relative Errors In Predicted D850 Composition for 5 Element Analysis of Data Set 1

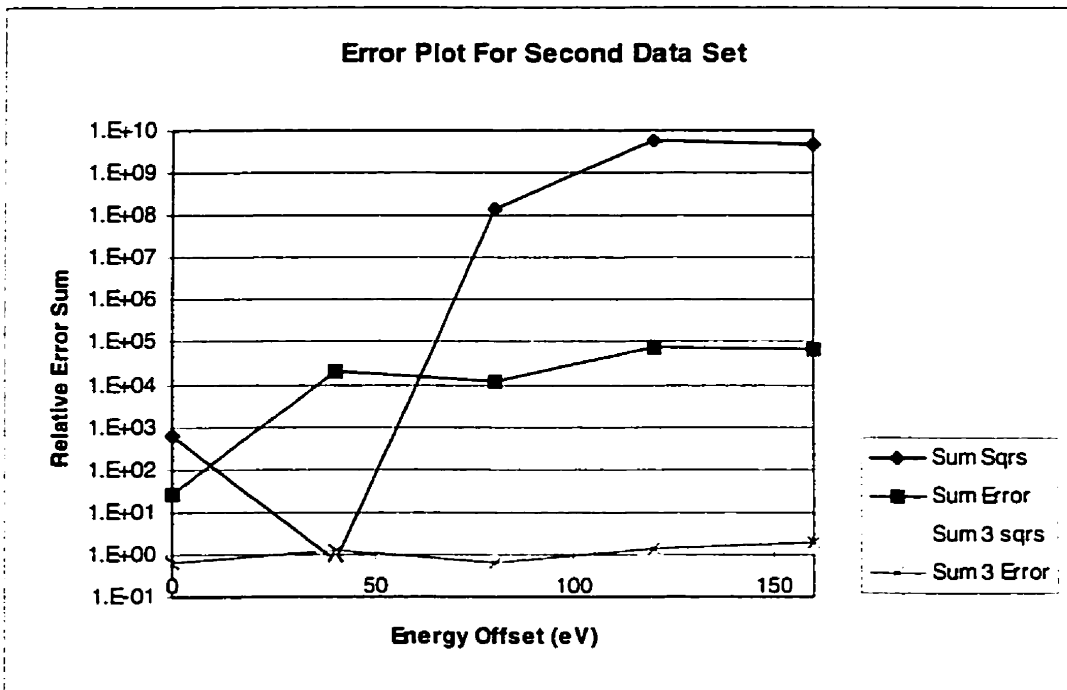

Figure C.22: Sum of Relative Errors In Predicted D850 Composition for 5 Element Analysis of Data Set 2

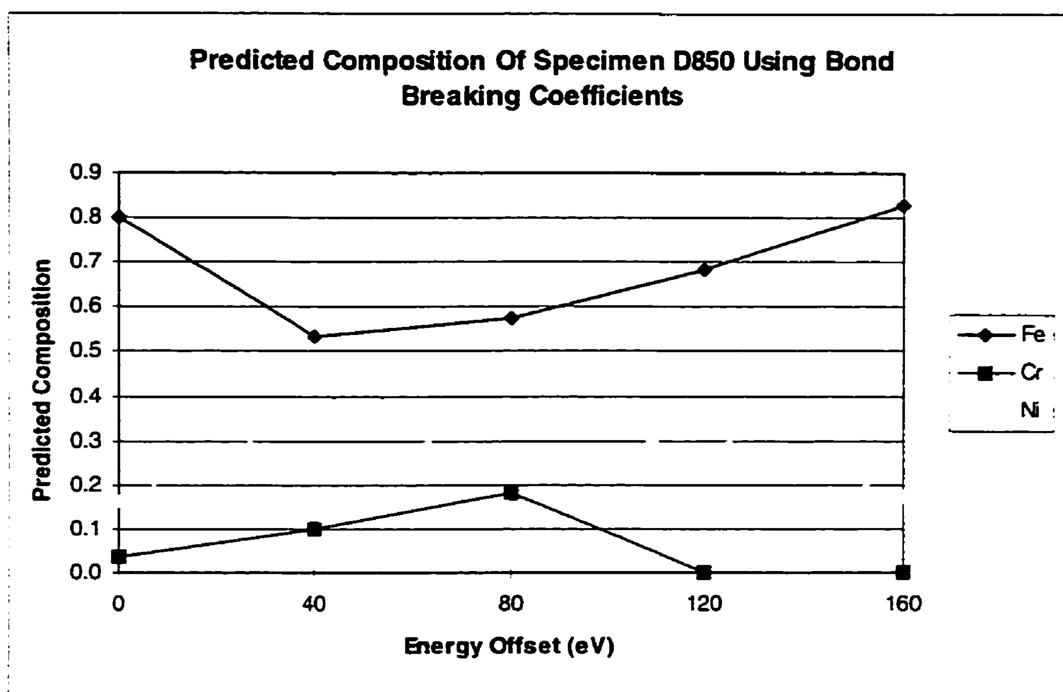

Figure C.23: D850 Composition Predicted Using 3 Element Bond Breaking Data - Data Set 1

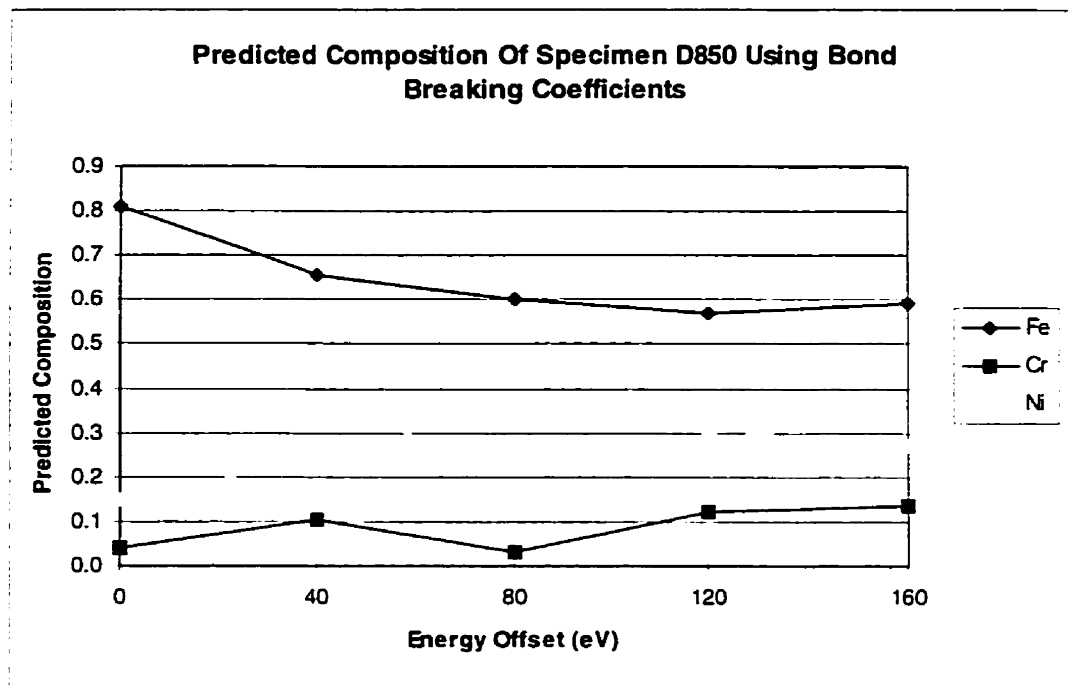

Figure C.24: D850 Composition Predicted Using 3 Element Bond Breaking Data - Data Set 2

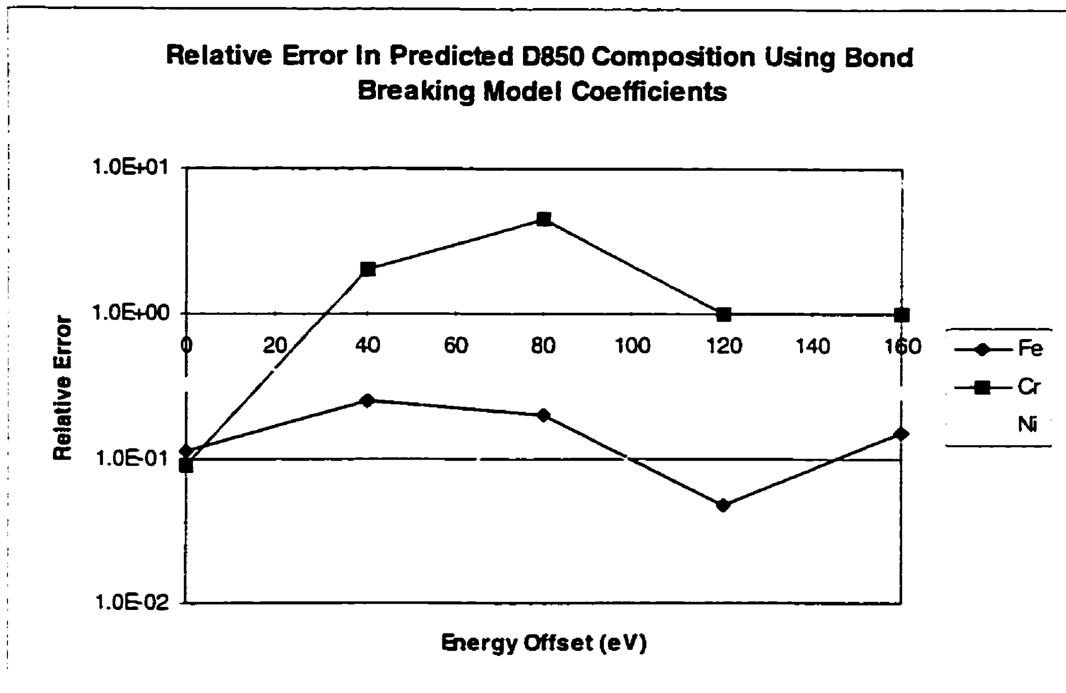

Figure C.25: Error In Predicted D850 Composition - 3 Element Analysis of Data Set 1

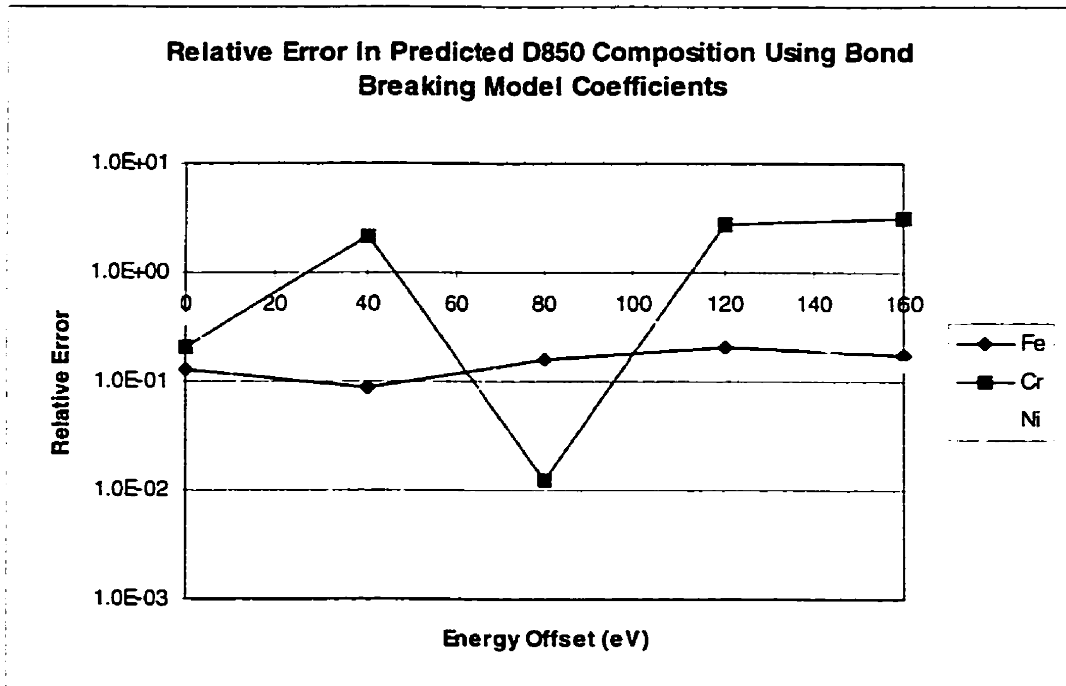

Figure C.26: Error In Predicted D850 Composition - 3 Element Analysis of Data Set 2

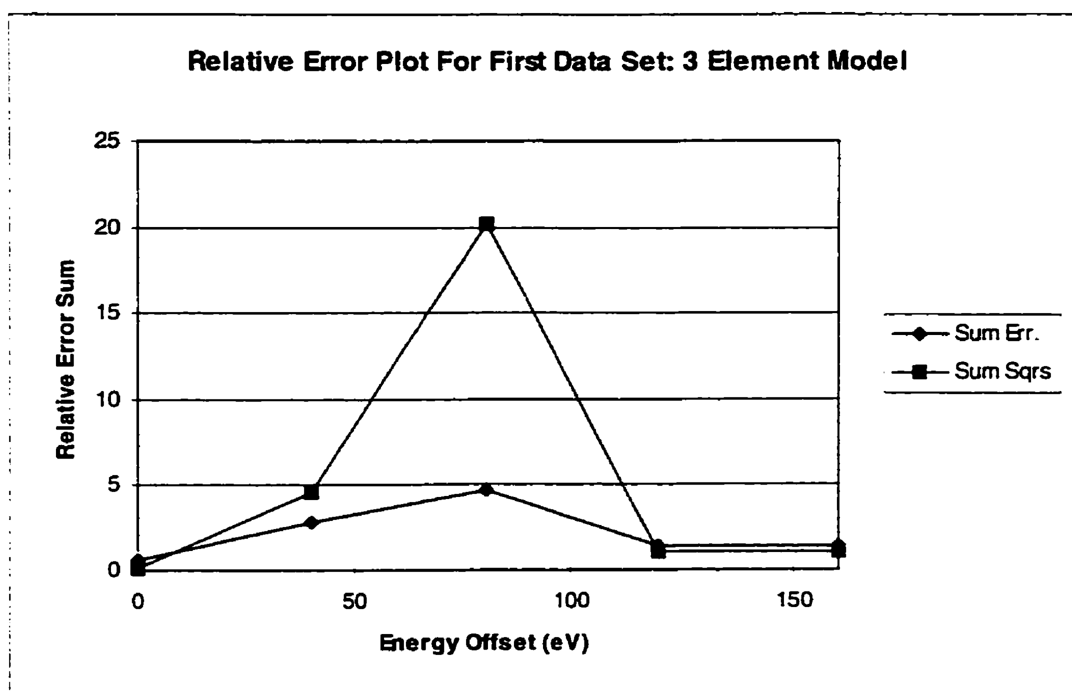

Figure C.27: Sum of Relative Errors In Predicted D850 Composition for 3 Element Analysis of Data Set 1

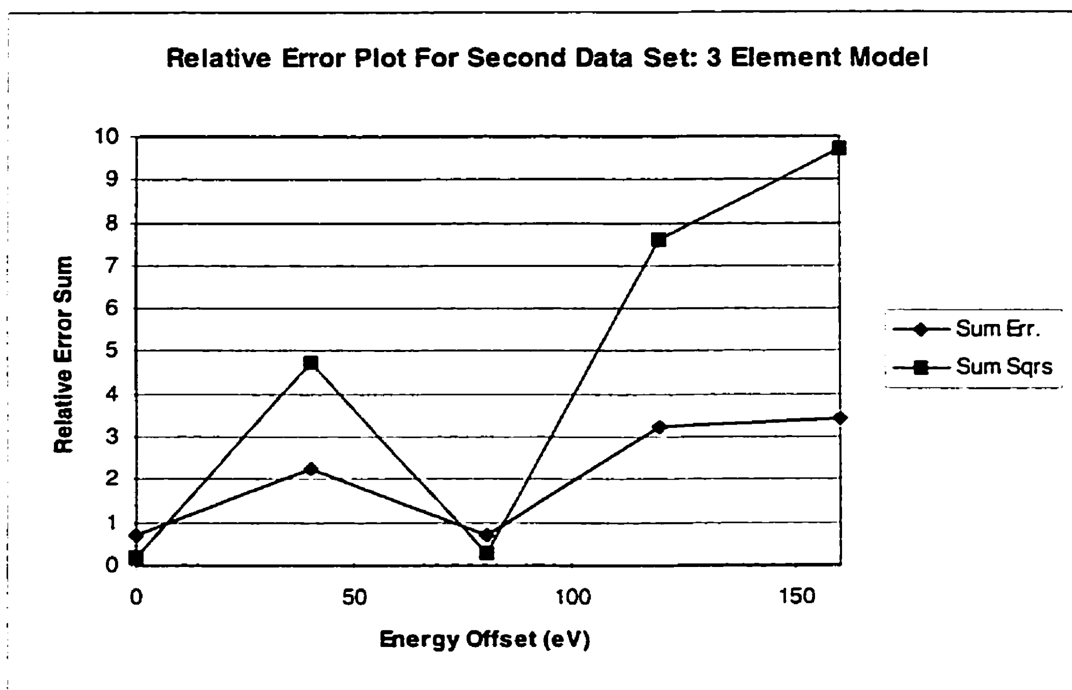

Figure C.28: Sum of Relative Errors In Predicted D850 Composition for 3 Element Analysis of Data Set 2

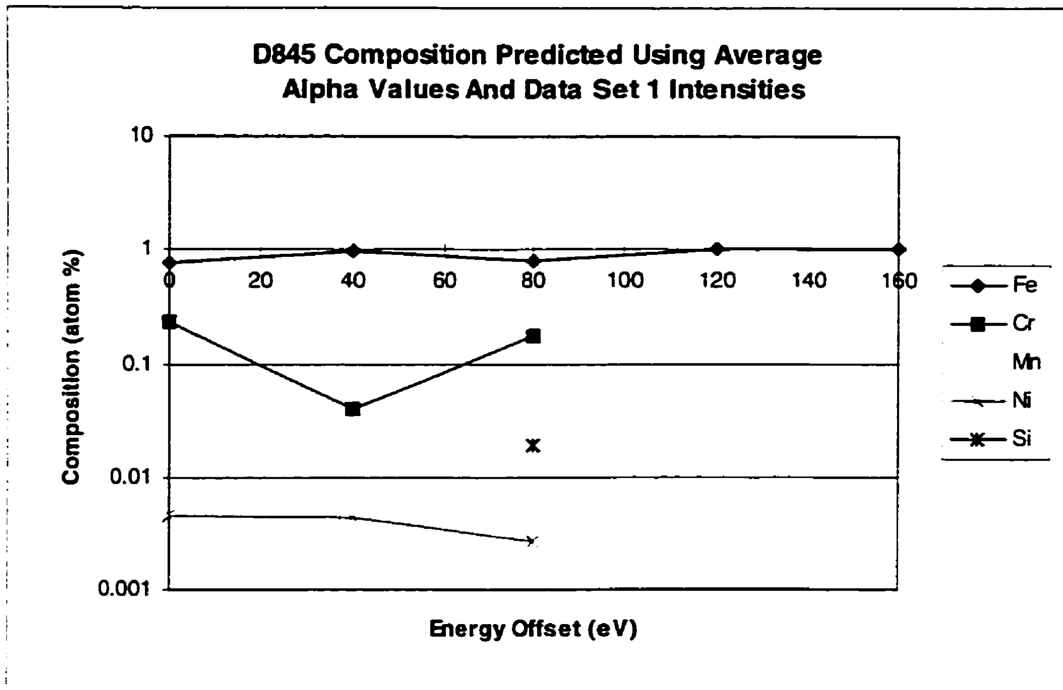

Figure C.29: Composition Of D845 Predicted Using Average Alpha Values

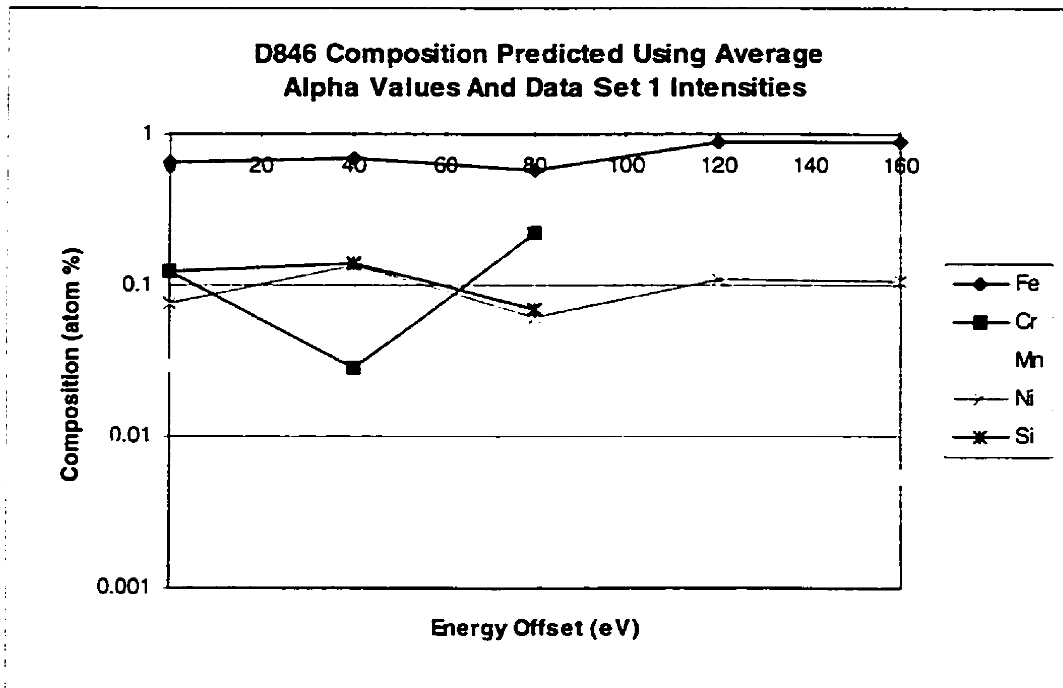

Figure C.30: Composition Of D846 Predicted Using Average Alpha Values

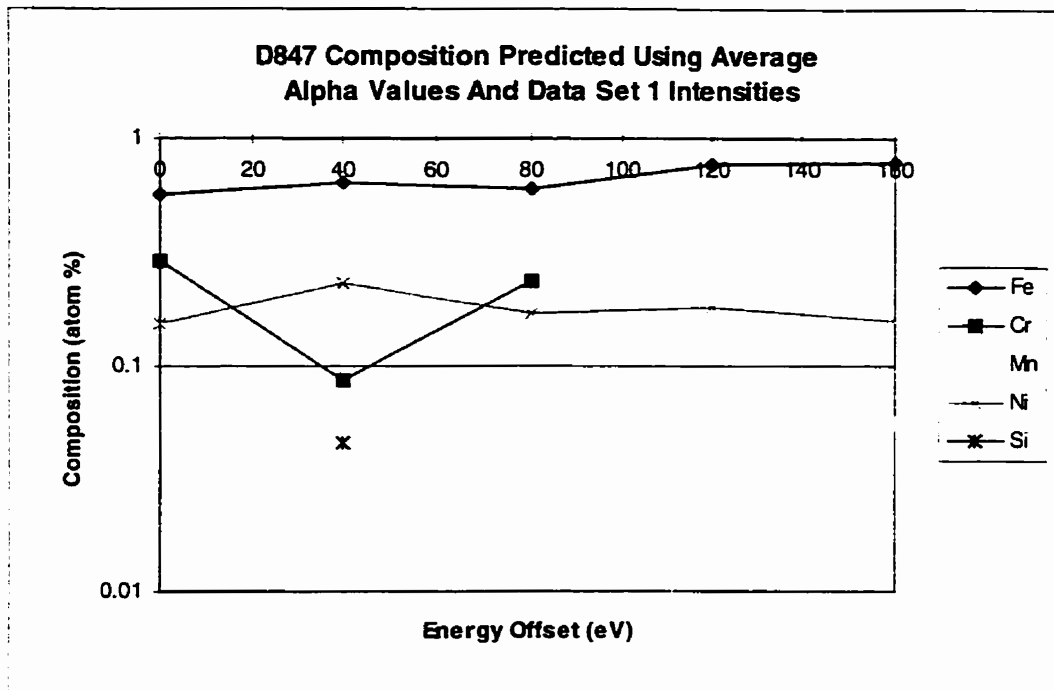

Figure C.31: Composition Of D847 Predicted Using Average Alpha Values

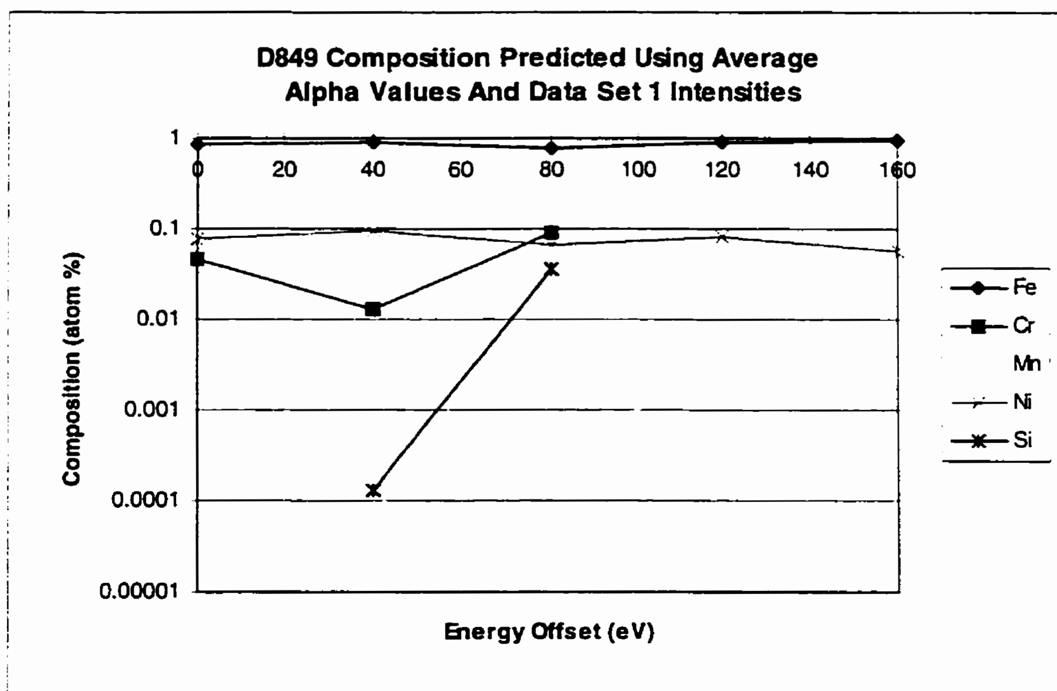

Figure C.32: Composition Of D849 Predicted Using Average Alpha Values

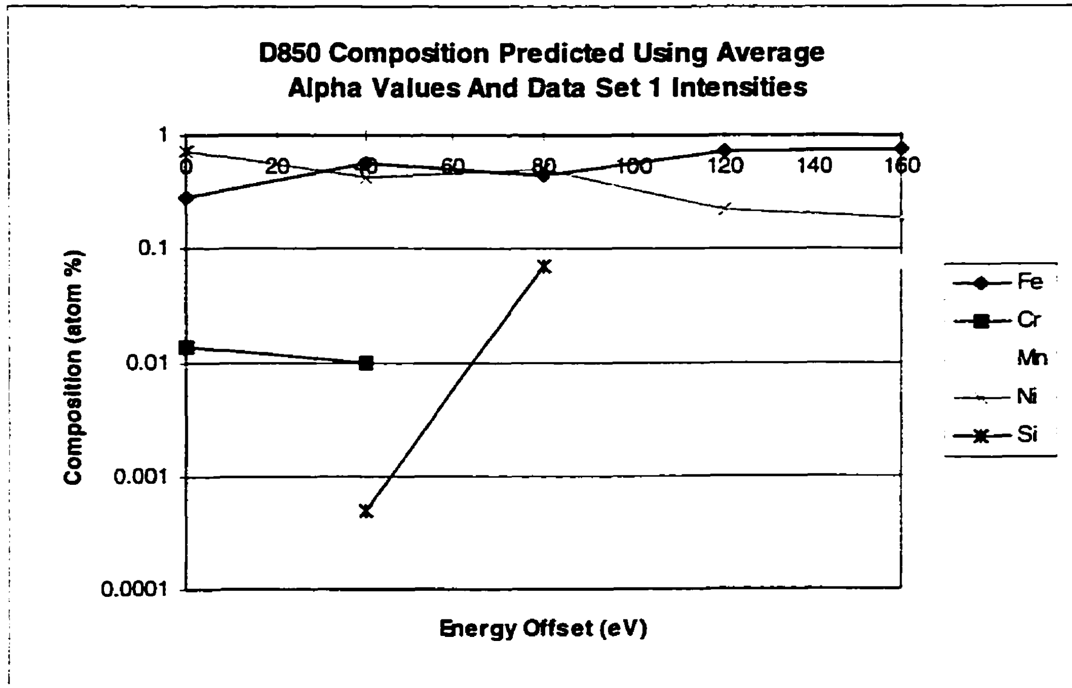

Figure C.33: Composition Of D850 Predicted Using Average Alpha Values

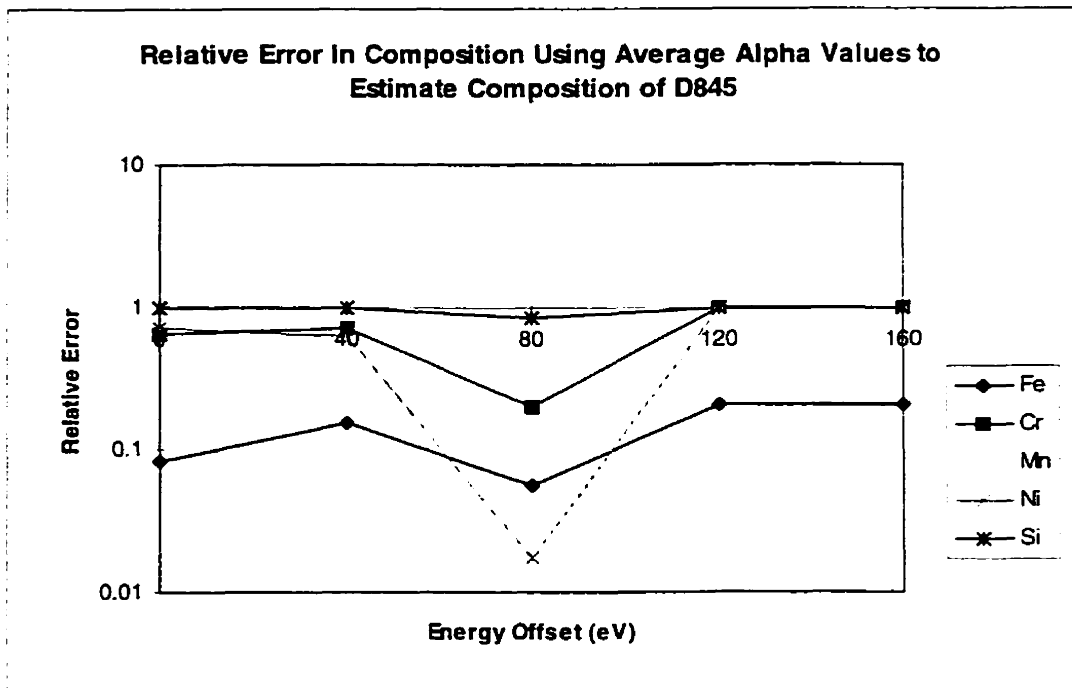

Figure C.34: Relative Error In D845 Composition Predicted Using Average Alpha Values

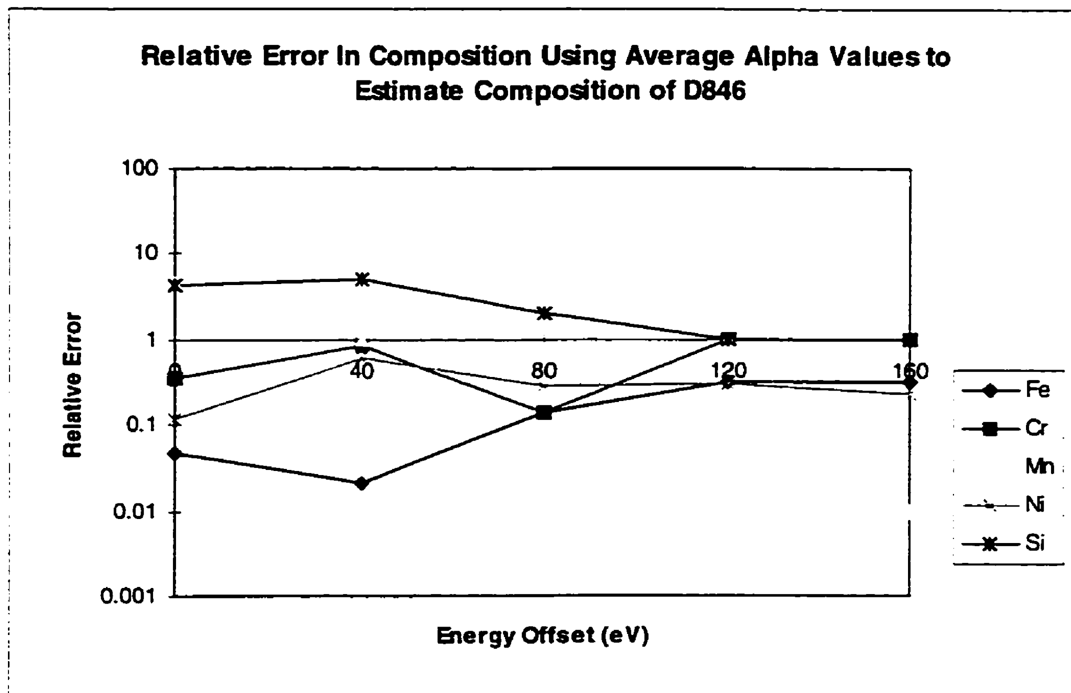

Figure C.35: Relative Error In D846 Composition Predicted Using Average Alpha Values

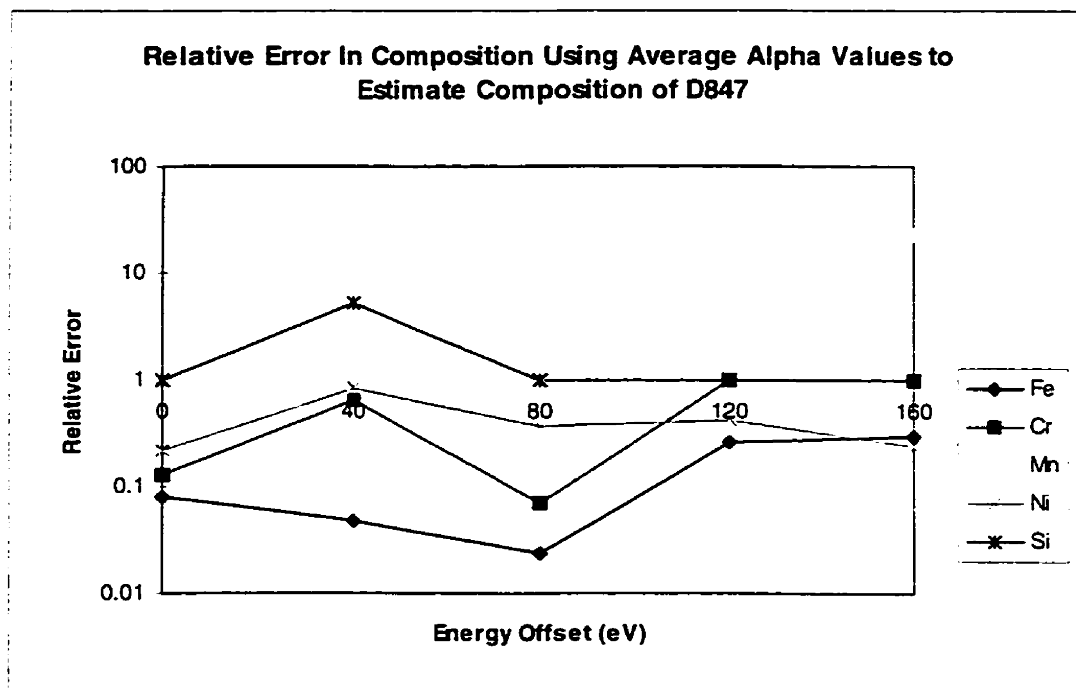

Figure C.36: Relative Error In D847 Composition Predicted Using Average Alpha Values

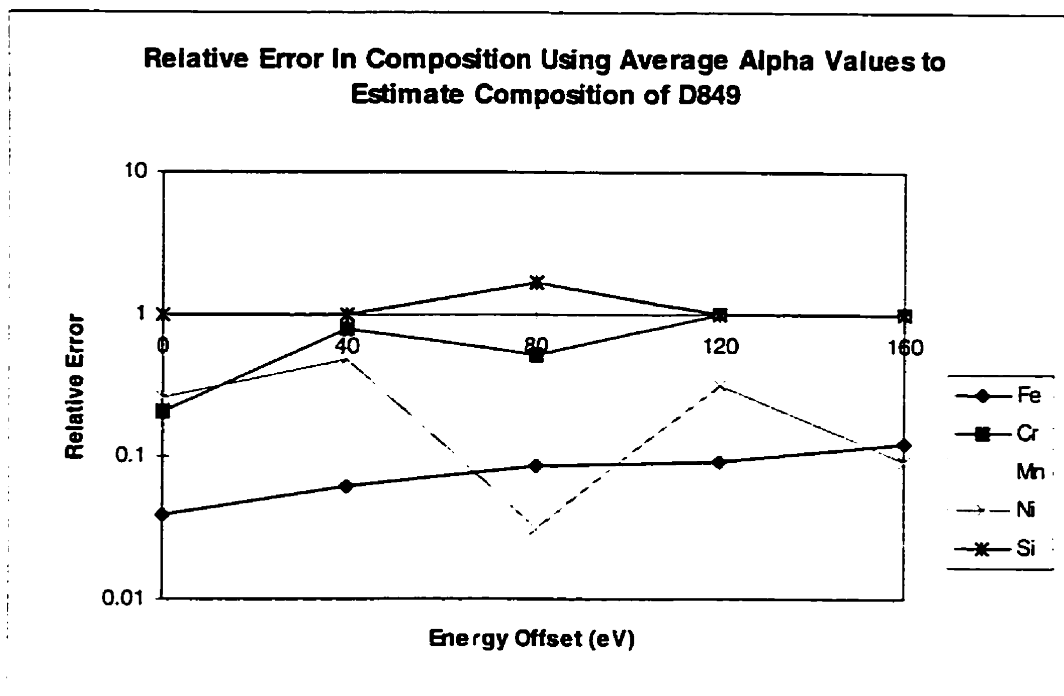

Figure C.37: Relative Error In D849 Composition Predicted Using Average Alpha Values

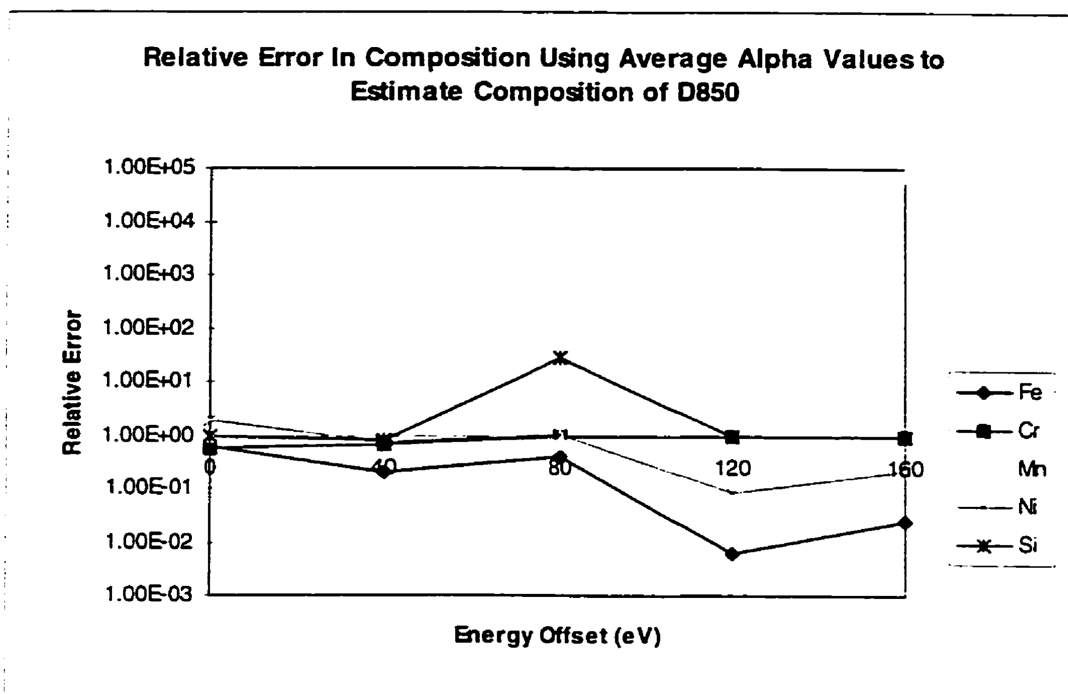

Figure C.38: Relative Error In D850 Composition Predicted Using Average Alpha Values

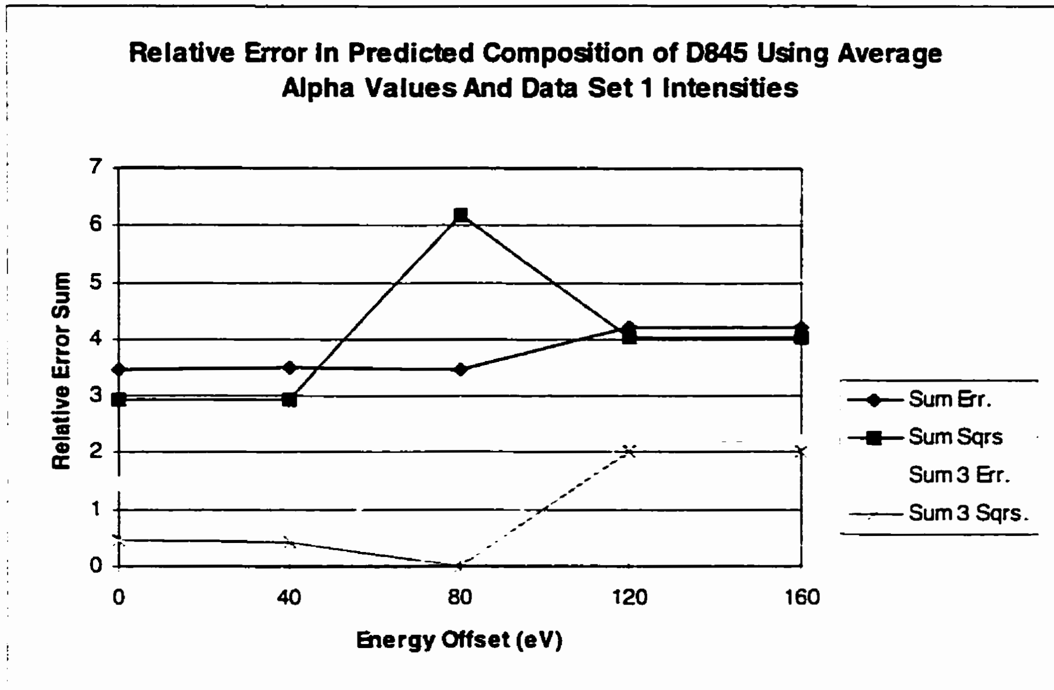

Figure C.39: Sum of Errors In D845 Composition Predicted Using Average Alpha Values

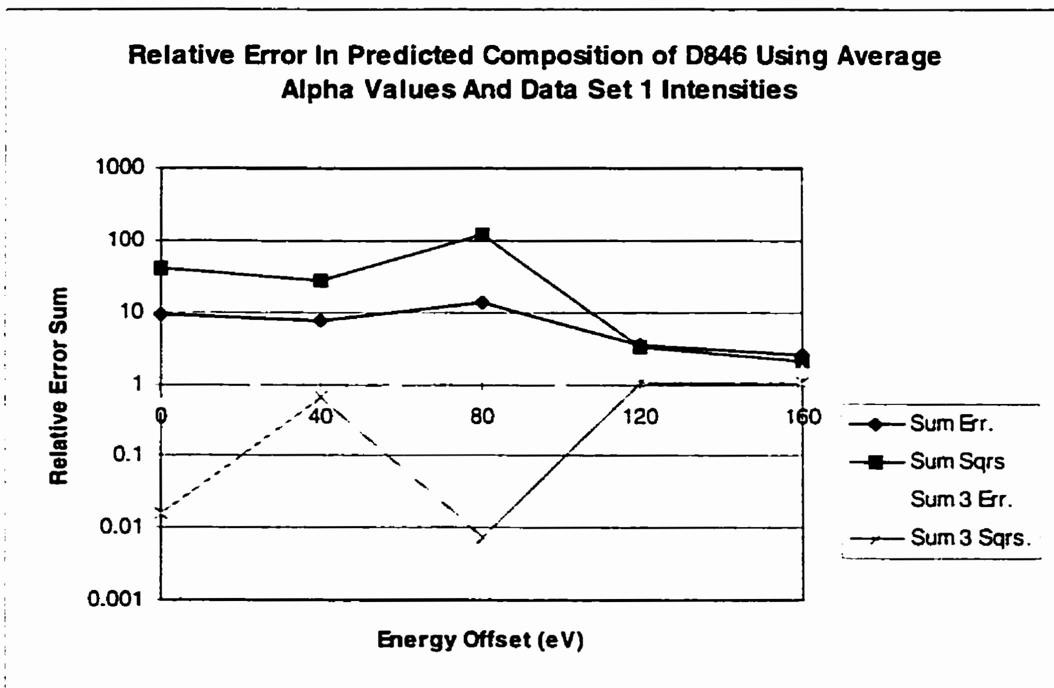

Figure C.40: Sum of Errors In D846 Composition Predicted Using Average Alpha Values

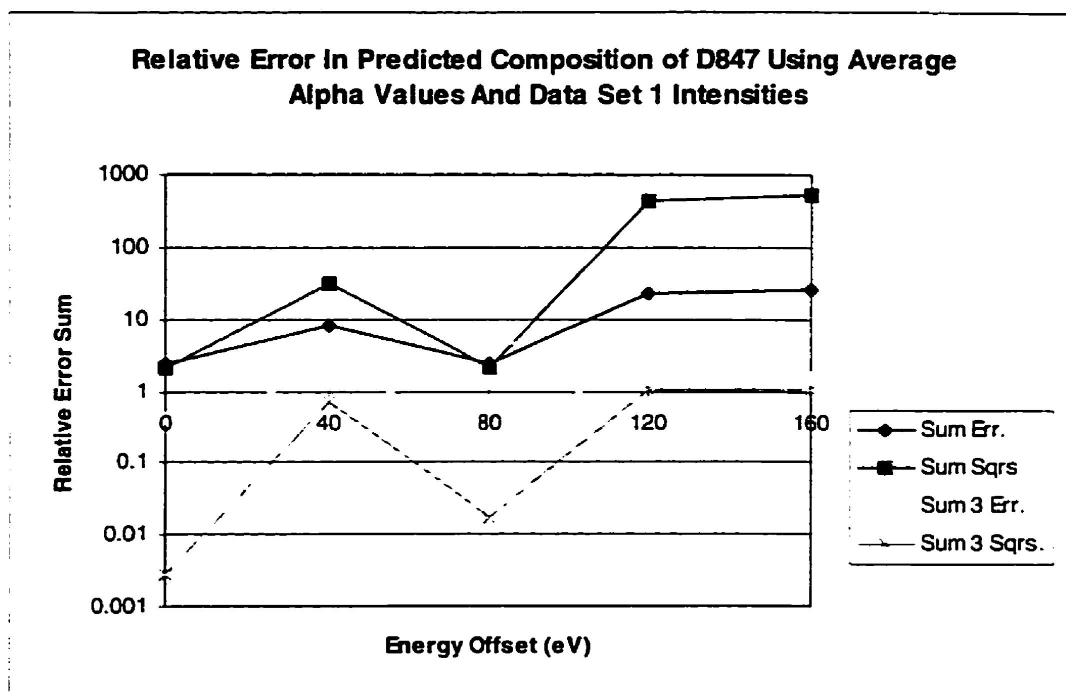

Figure C.41: Sum of Errors In D847 Composition Predicted Using Average Alpha Values

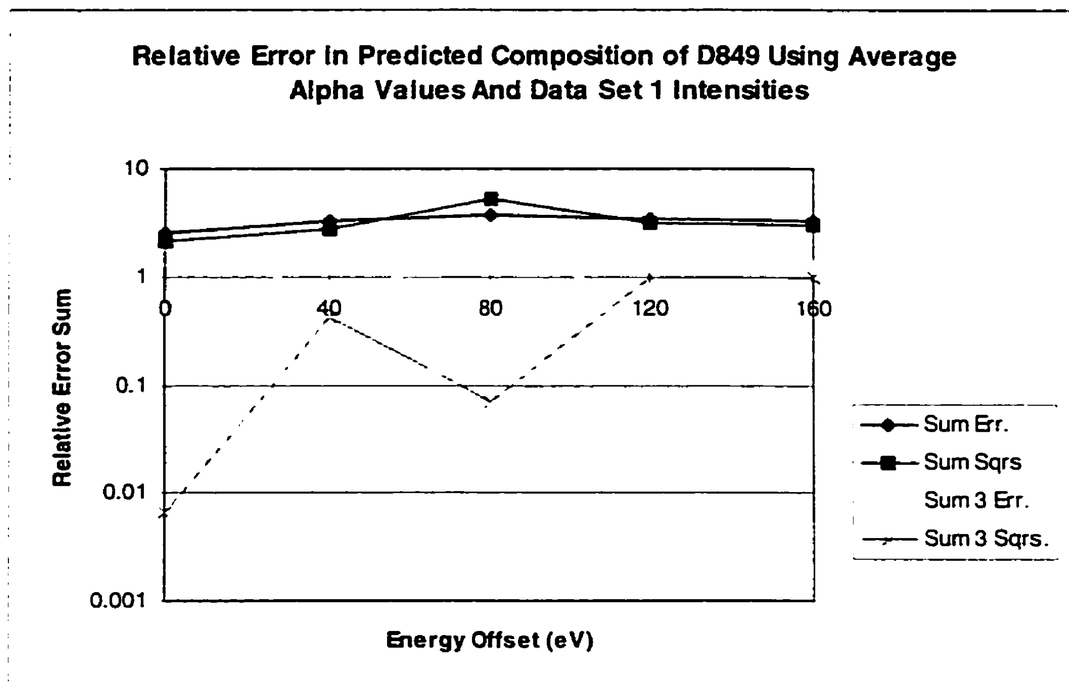

Figure C.42: Sum of Errors In D849 Composition Predicted Using Average Alpha Values

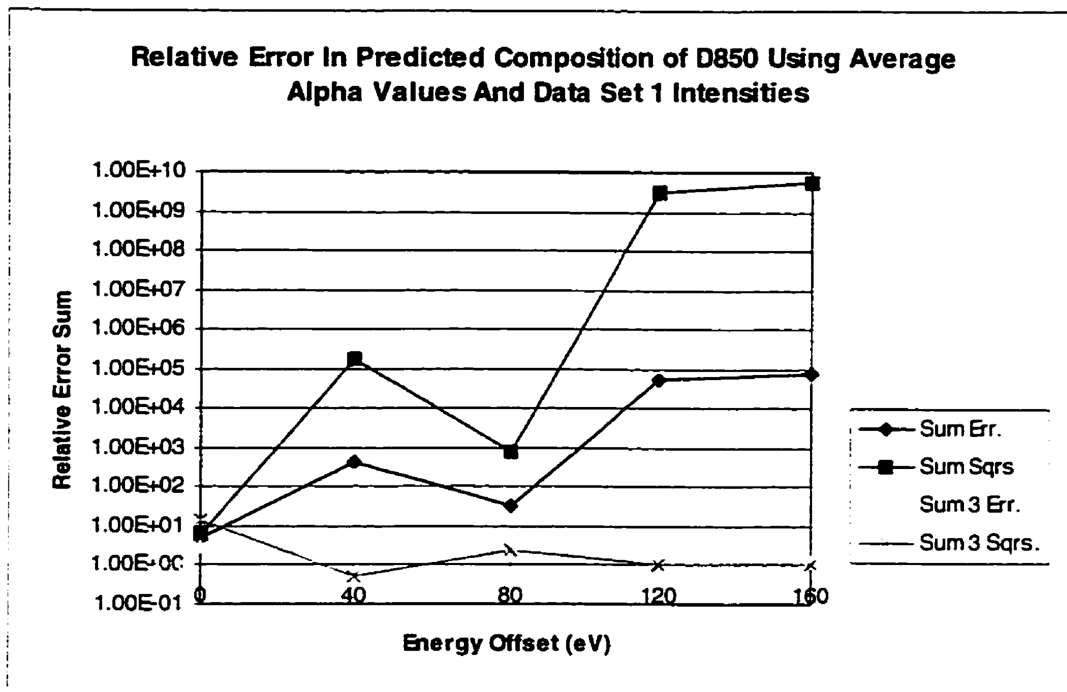

Figure C.43: Sum of Errors In D850 Composition Predicted Using Average Alpha Values

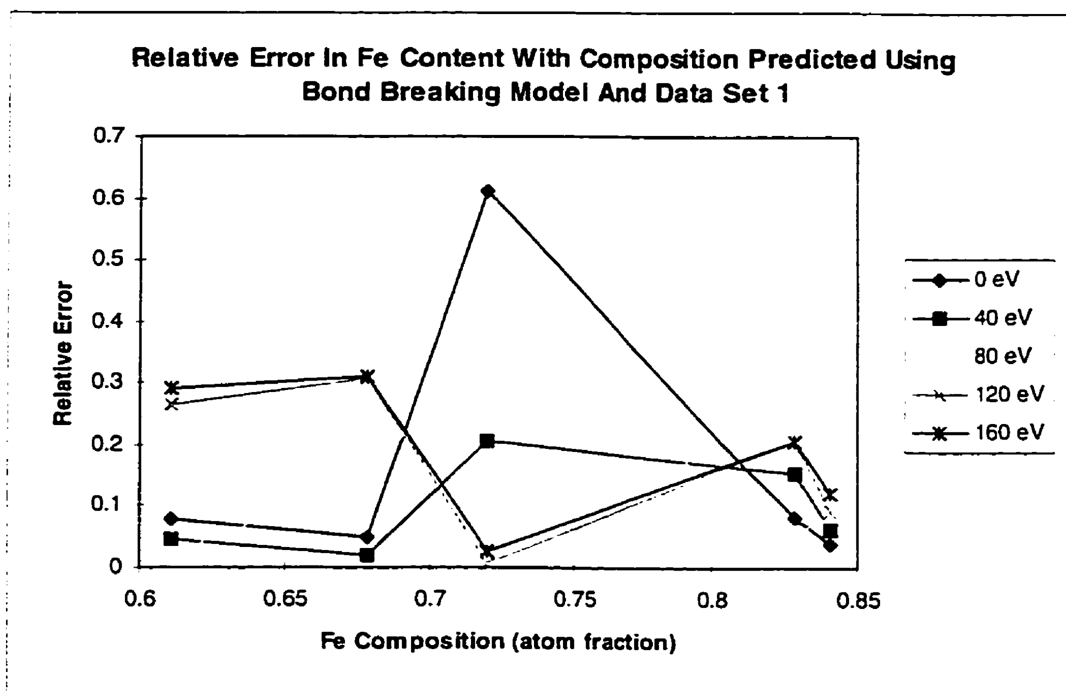

Figure C.44: Relative Error In Predicted Fe Content Versus Elemental Fe Composition

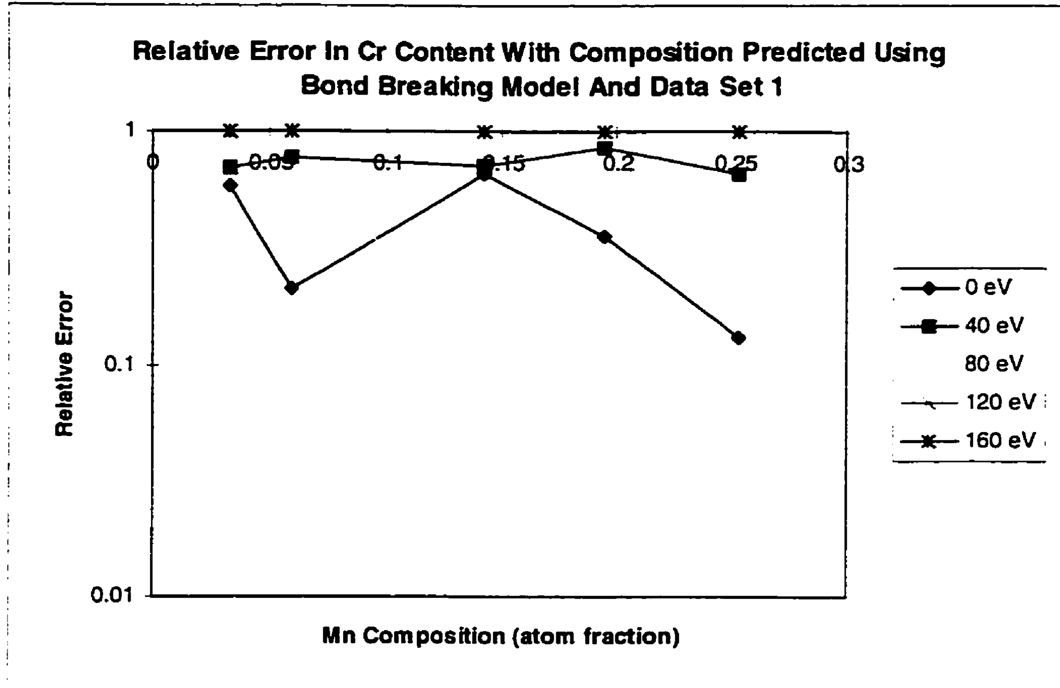

Figure C.45: Relative Error In Predicted Cr Content Versus Elemental Cr Composition

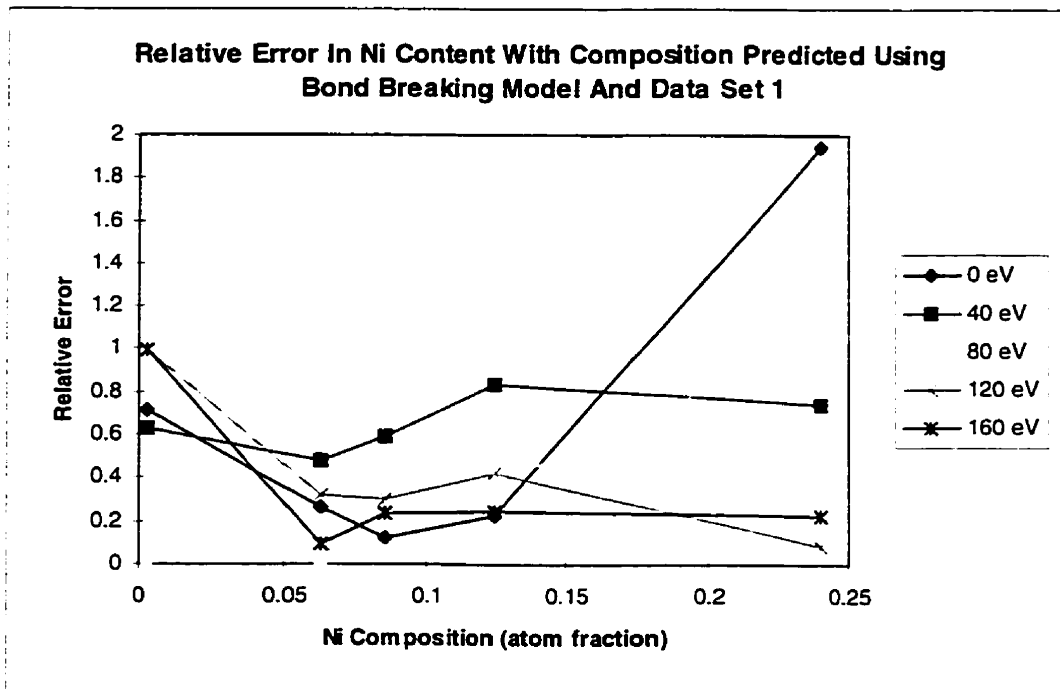

Figure C.46: Relative Error In Predicted Ni Content Versus Elemental Ni Composition

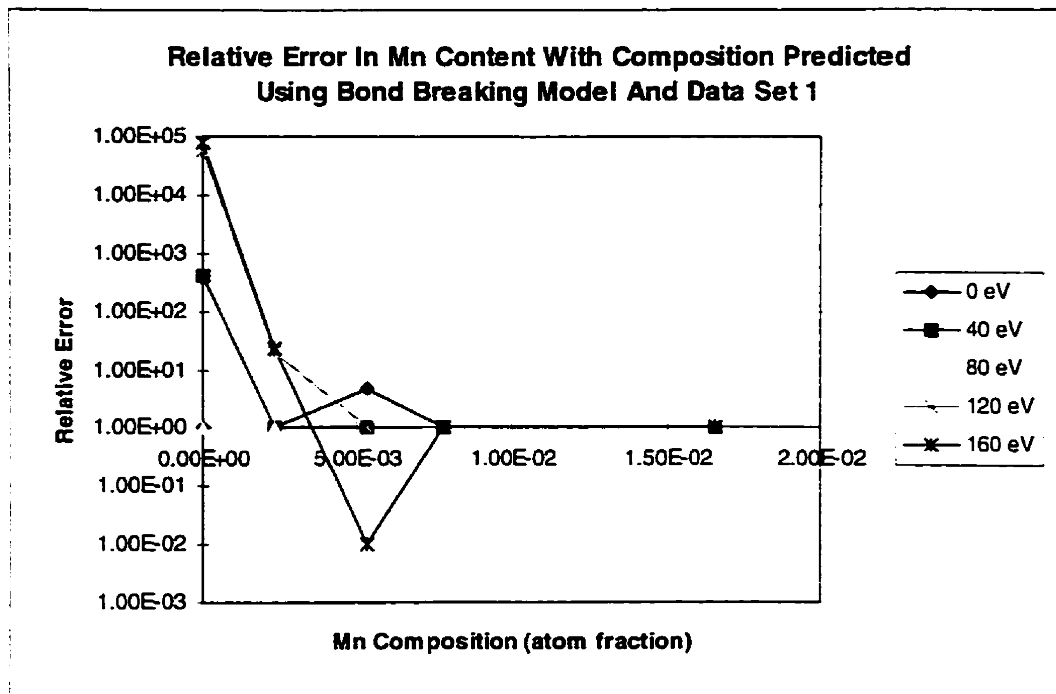

Figure C.47: Relative Error In Predicted Mn Content Versus Elemental Mn Composition

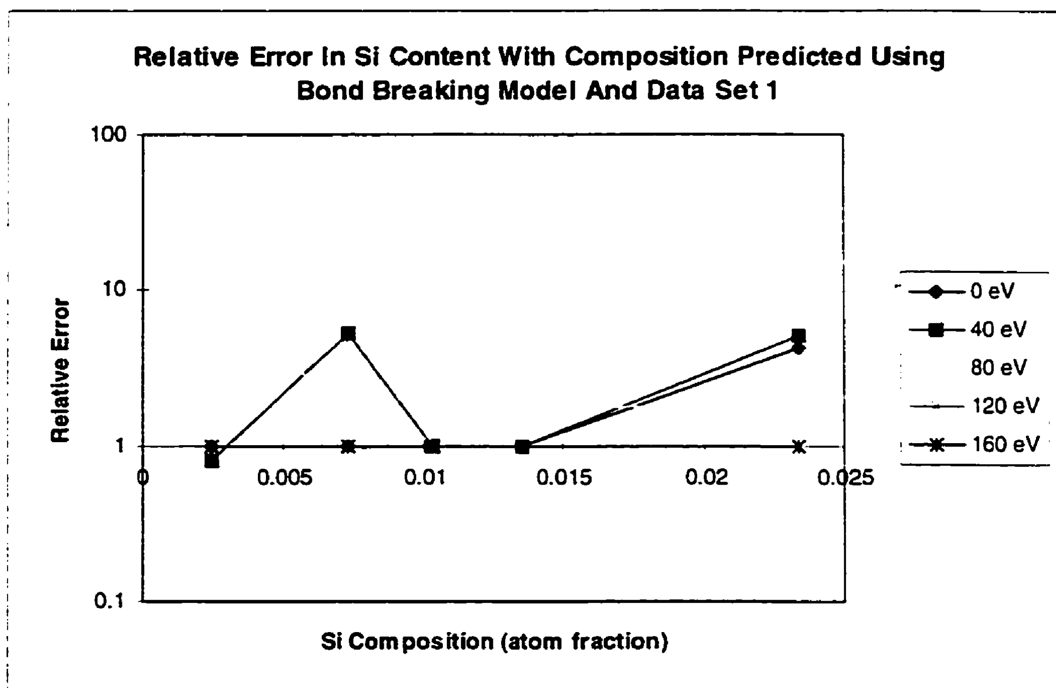

Figure C.48: Relative Error In Predicted Si Content Versus Elemental Si Composition

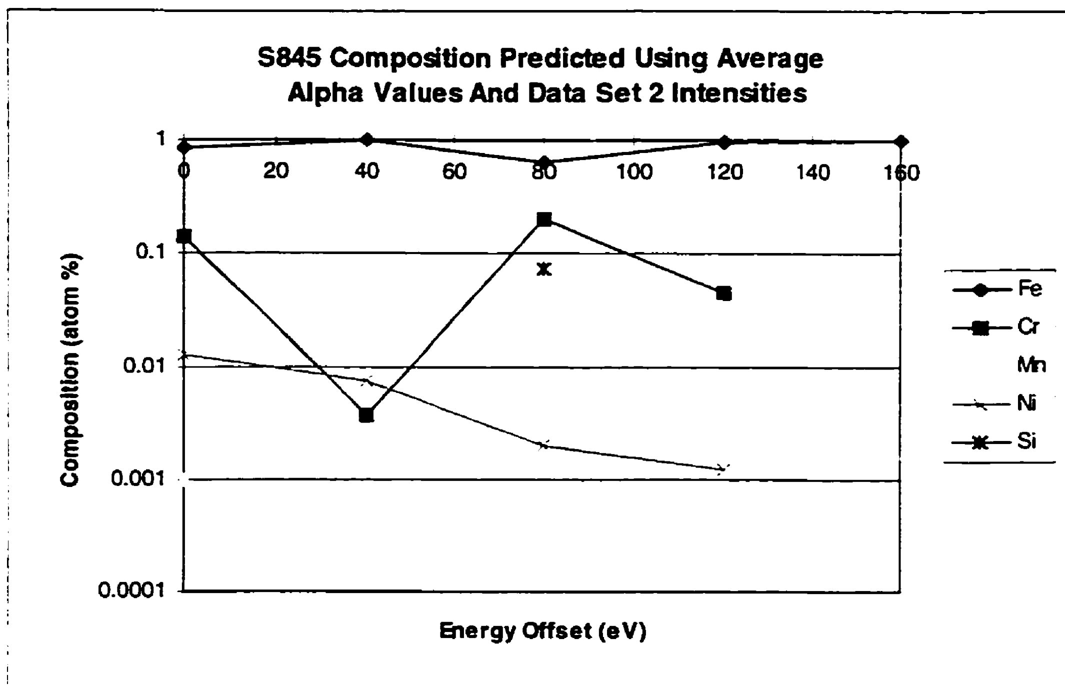

Figure C.49: Composition Of S845 Predicted Using Average Alpha Values

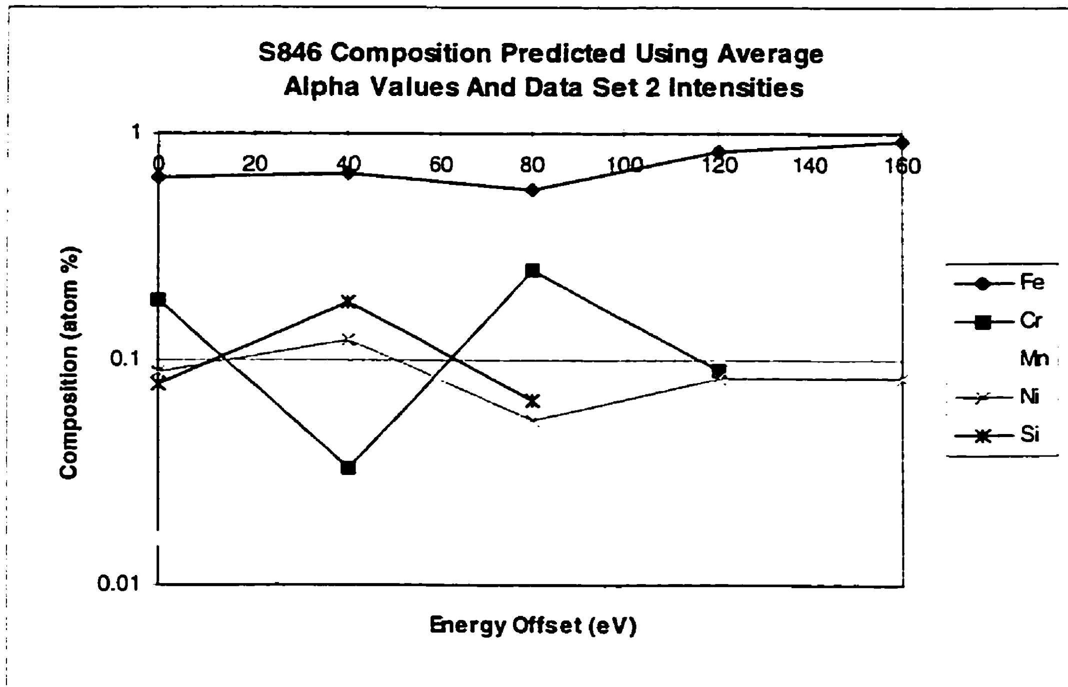

Figure C.50: Composition Of S846 Predicted Using Average Alpha Values

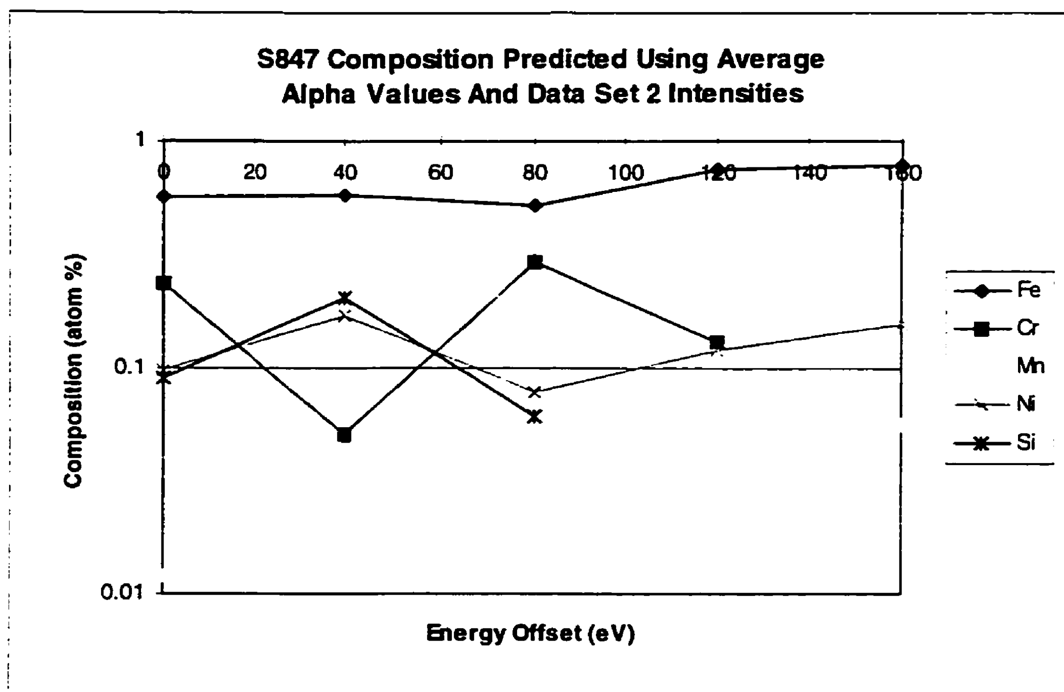

Figure C.51: Composition Of S847 Predicted Using Average Alpha Values

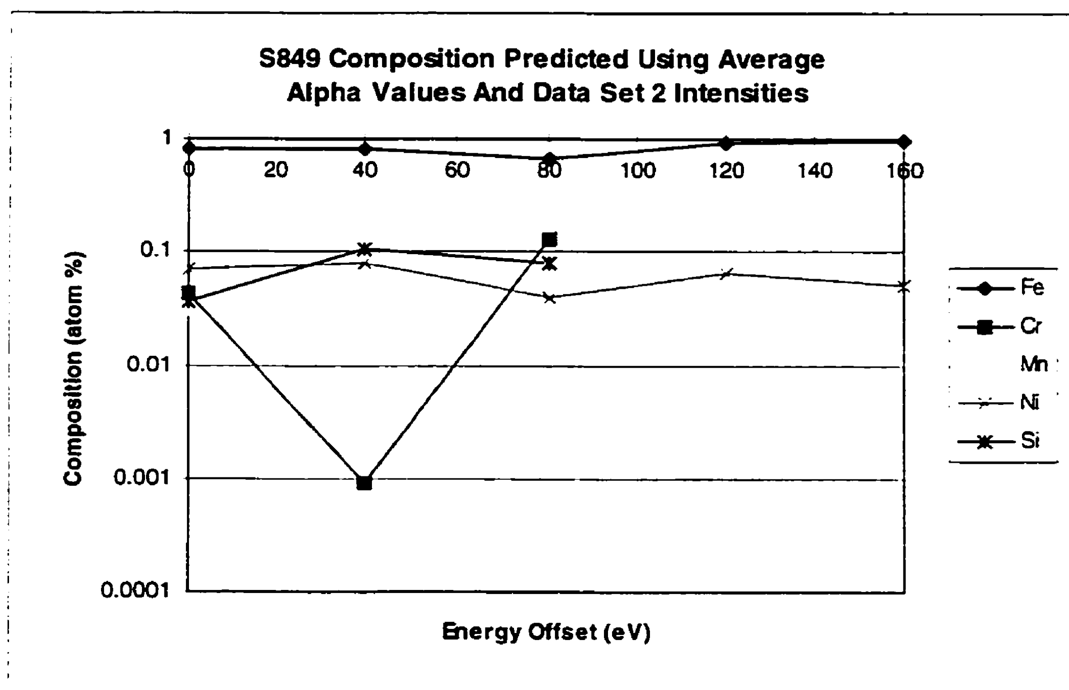

Figure C.52: Composition Of S849 Predicted Using Average Alpha Values

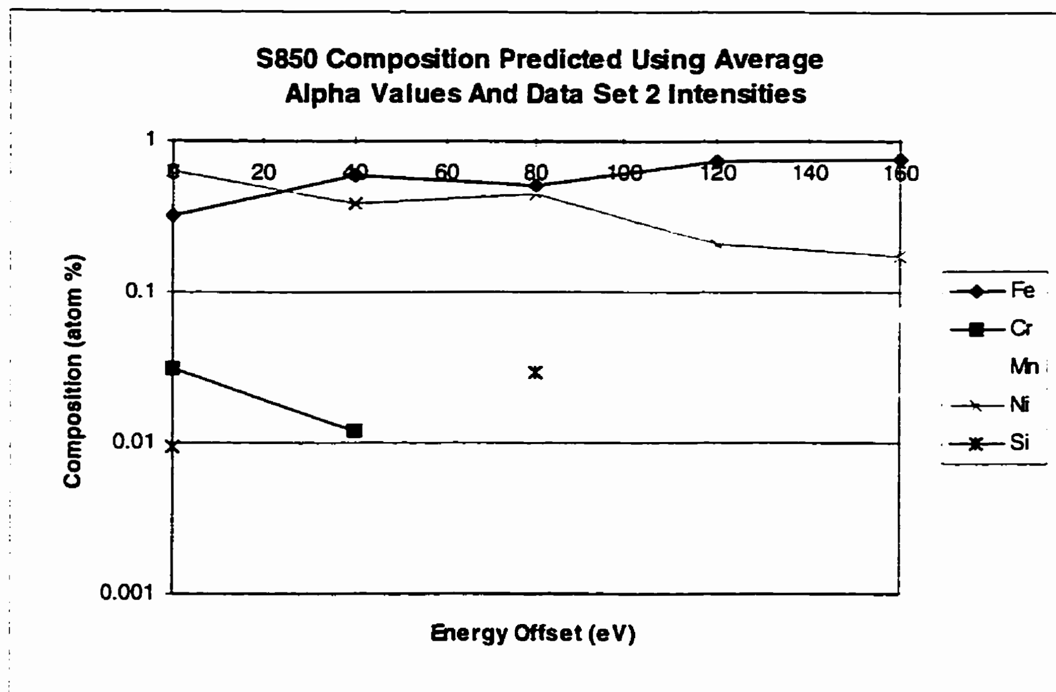

Figure C.53: Composition Of S850 Predicted Using Average Alpha Values

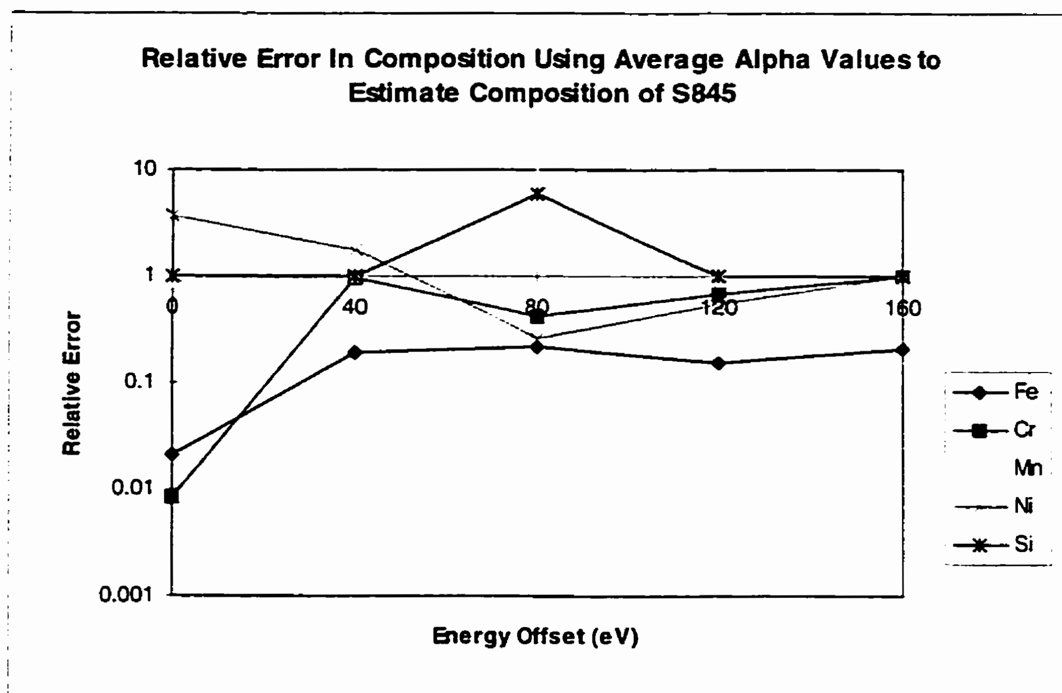

Figure C.54: Relative Error In S845 Composition Predicted Using Average Alpha Values

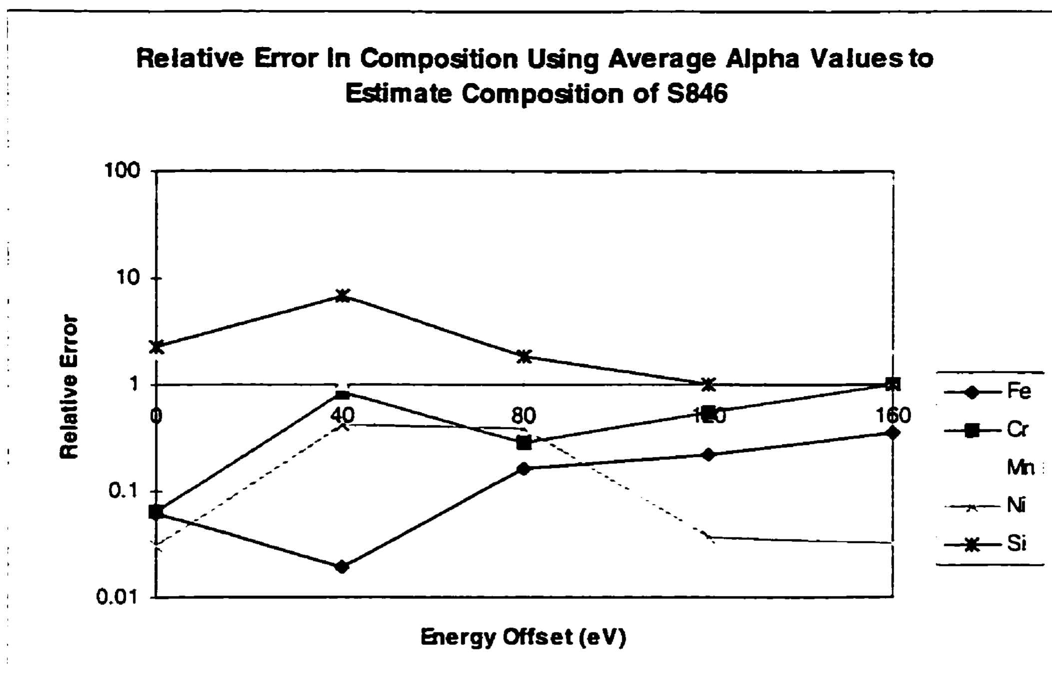

Figure C.55: Relative Error In S846 Composition Predicted Using Average Alpha Values

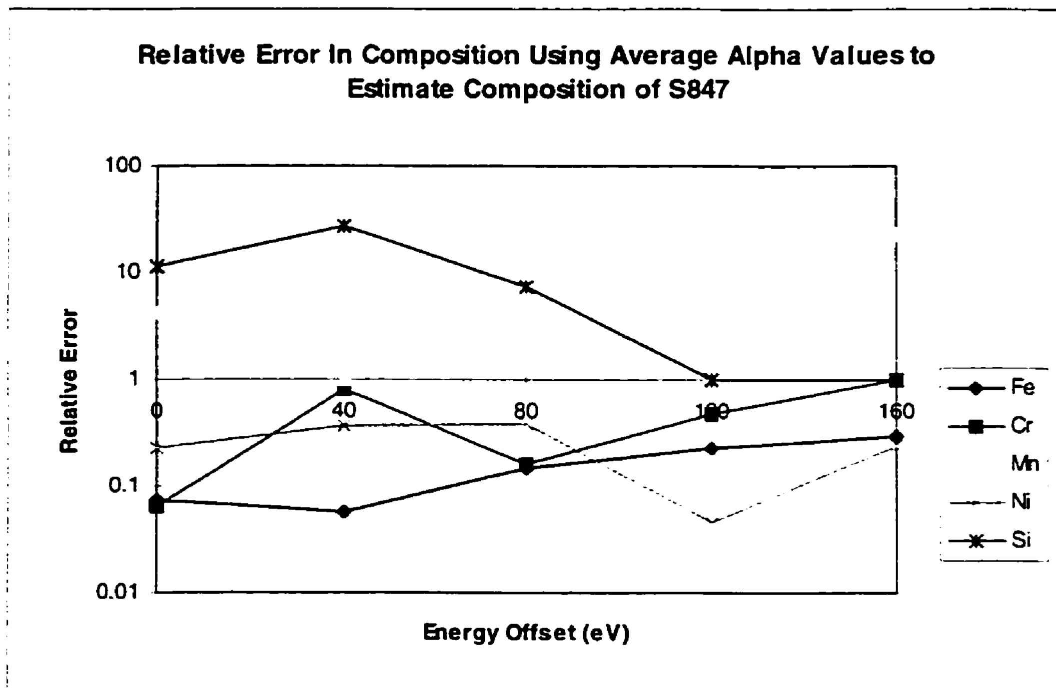

Figure C.56: Relative Error In S847 Composition Predicted Using Average Alpha Values

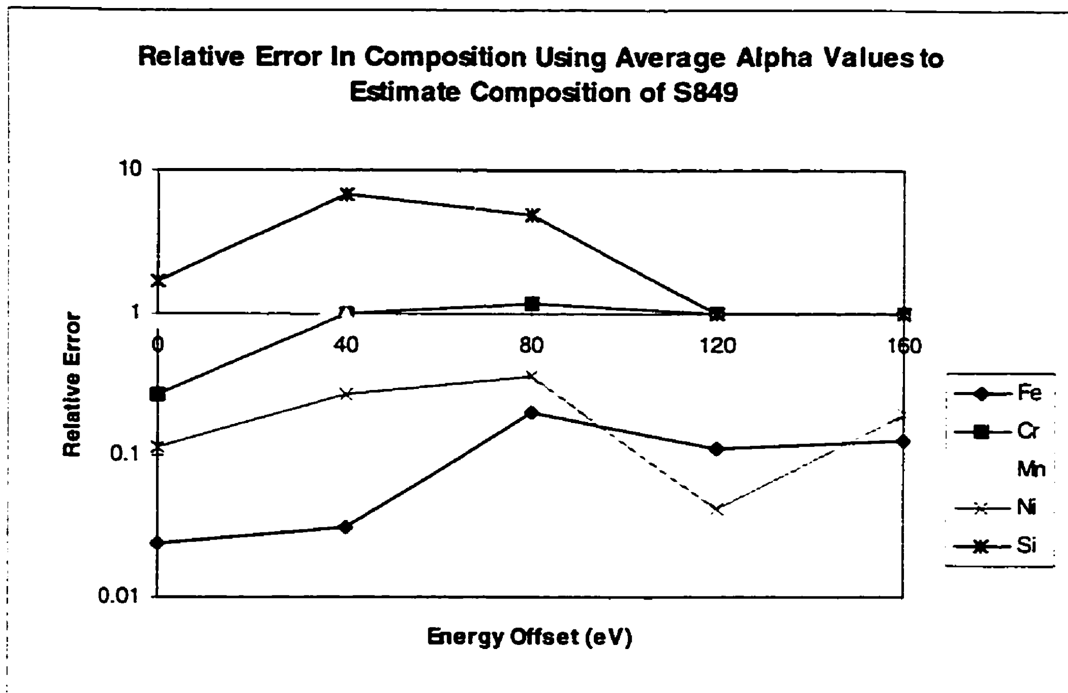

Figure C.57: Relative Error In S849 Composition Predicted Using Average Alpha Values

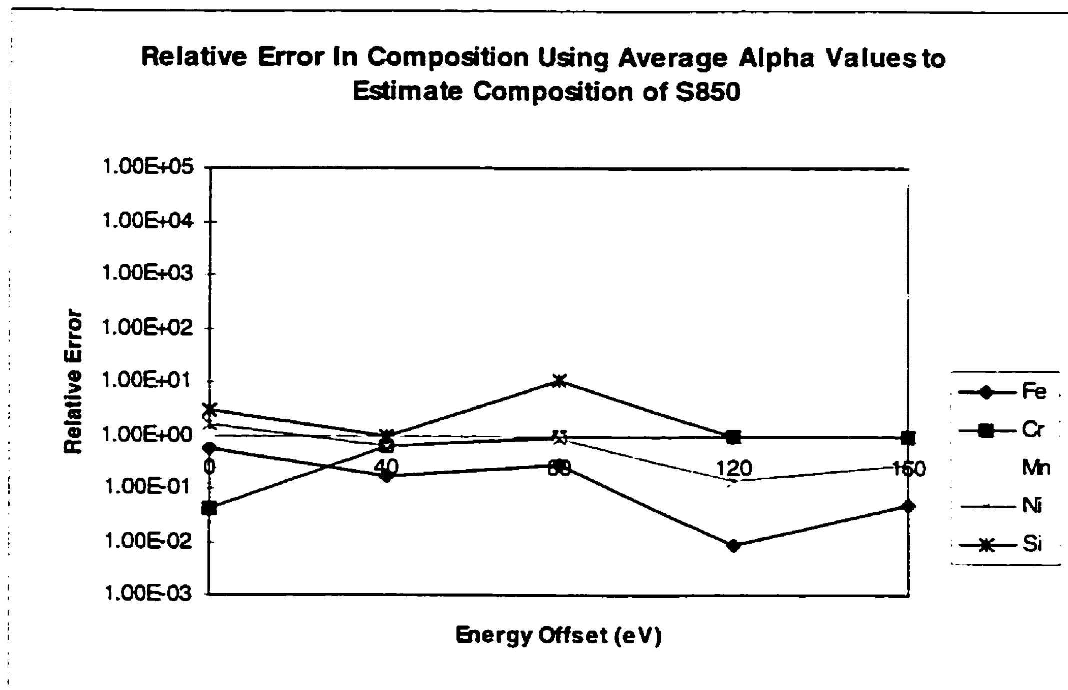

Figure C.58: Relative Error In S850 Composition Predicted Using Average Alpha Values

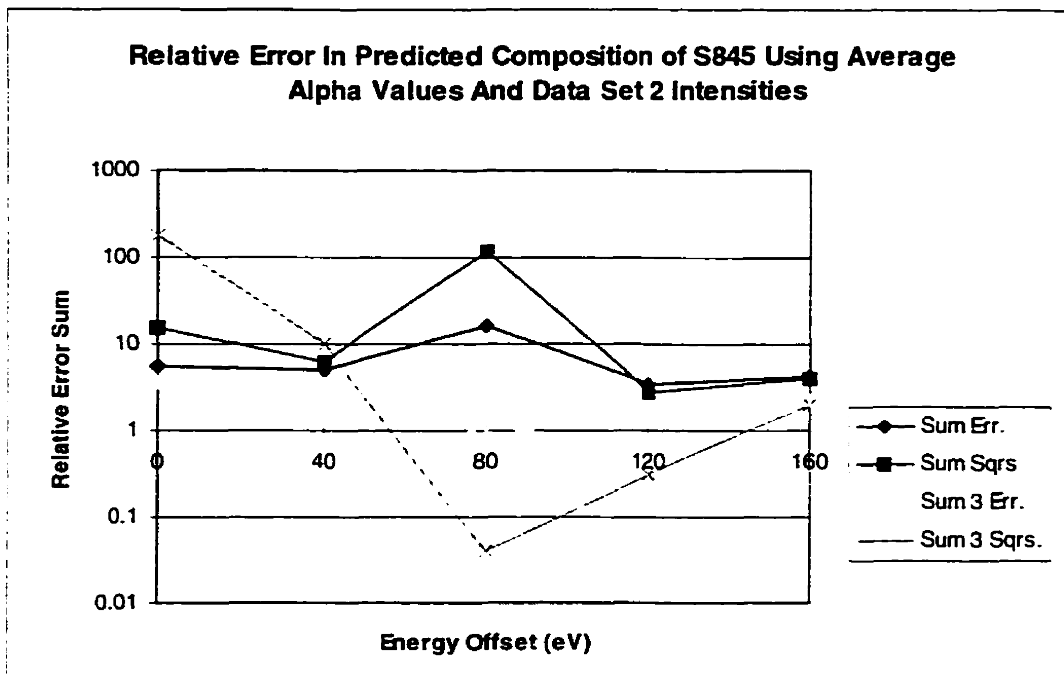

Figure C.59: Sum of Errors In S845 Composition Predicted Using Average Alpha Values

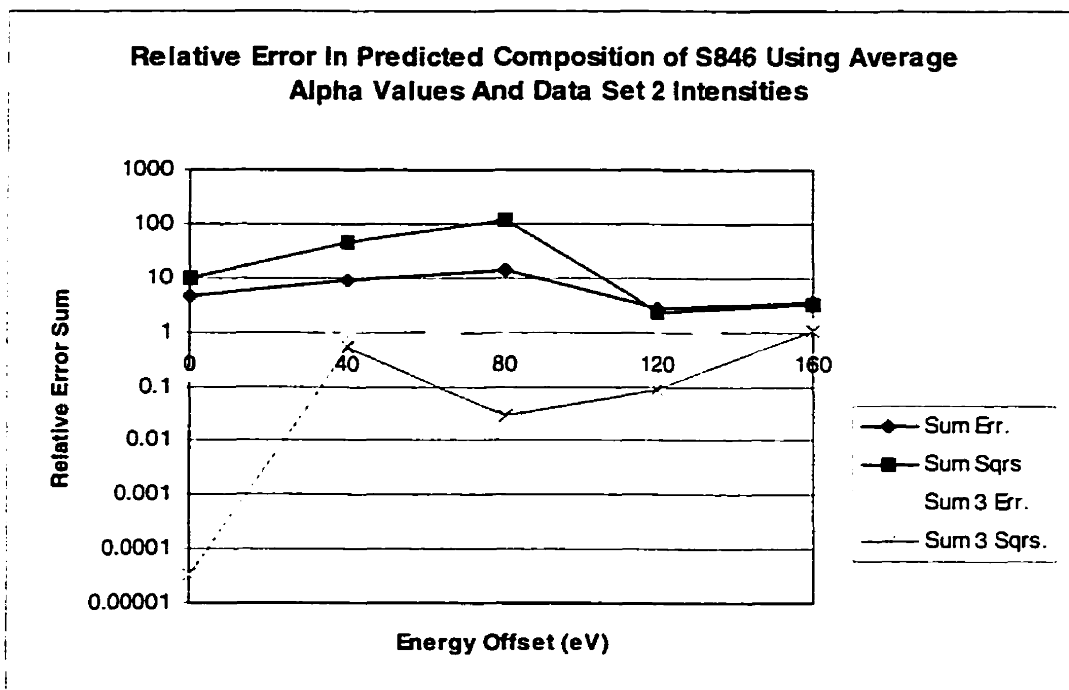

Figure C.60: Sum of Errors In S846 Composition Predicted Using Average Alpha Values

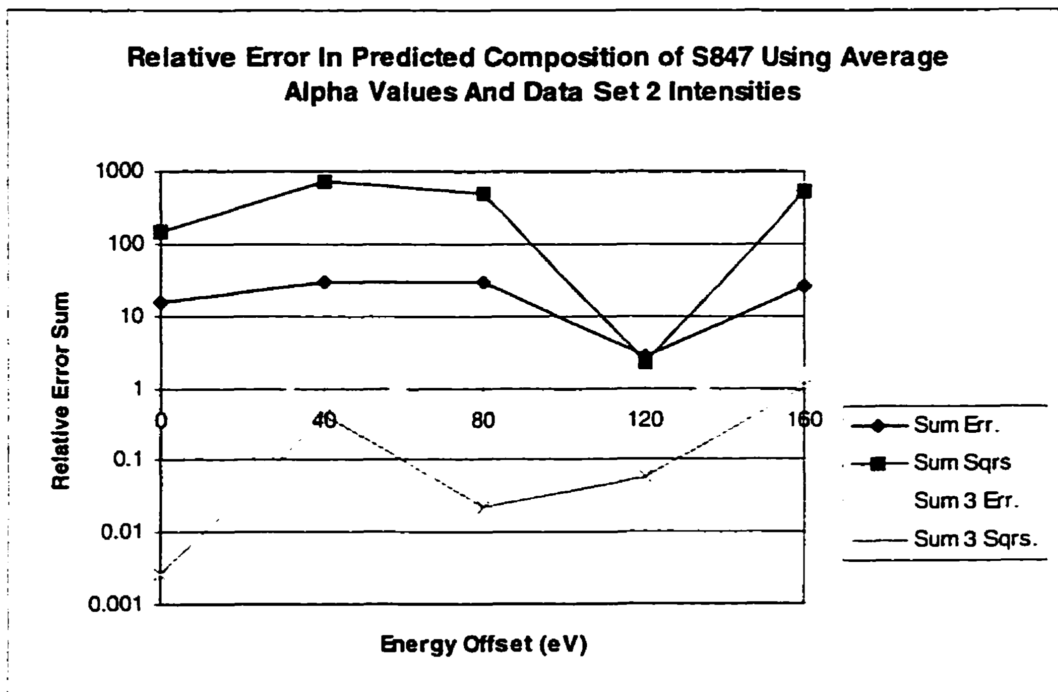

Figure C.61: Sum of Errors In S847 Composition Predicted Using Average Alpha Values

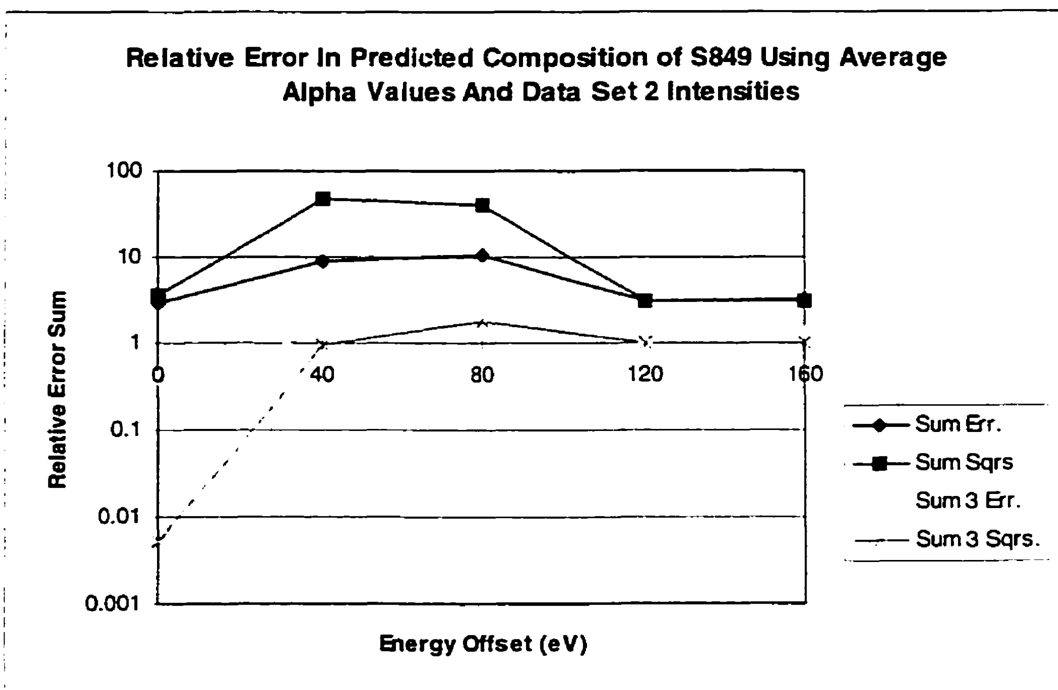

Figure C.62: Sum of Errors In S849 Composition Predicted Using Average Alpha Values

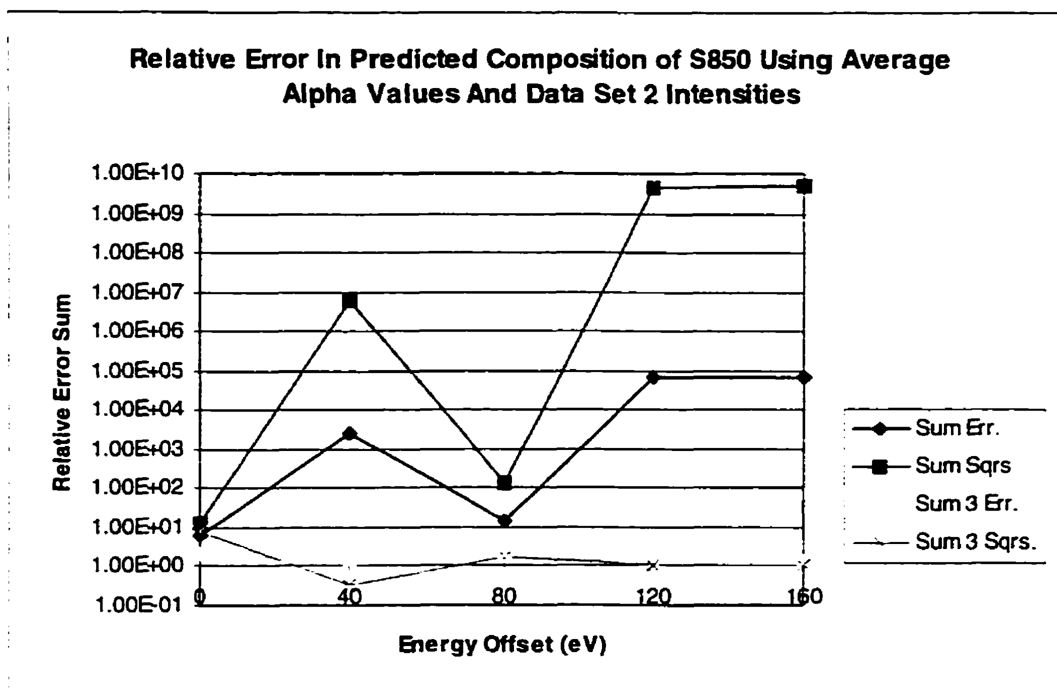

Figure C.63: Sum of Errors In S850 Composition Predicted Using Average Alpha Values

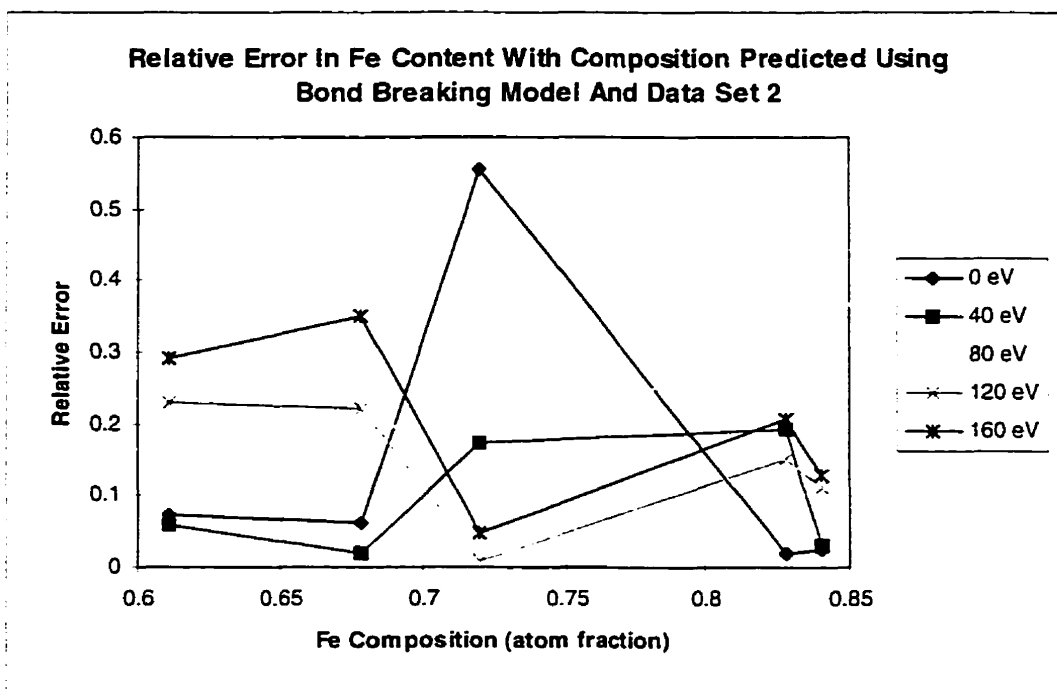

Figure C.63: Relative Error In Predicted Fe Content Versus Elemental Fe Composition

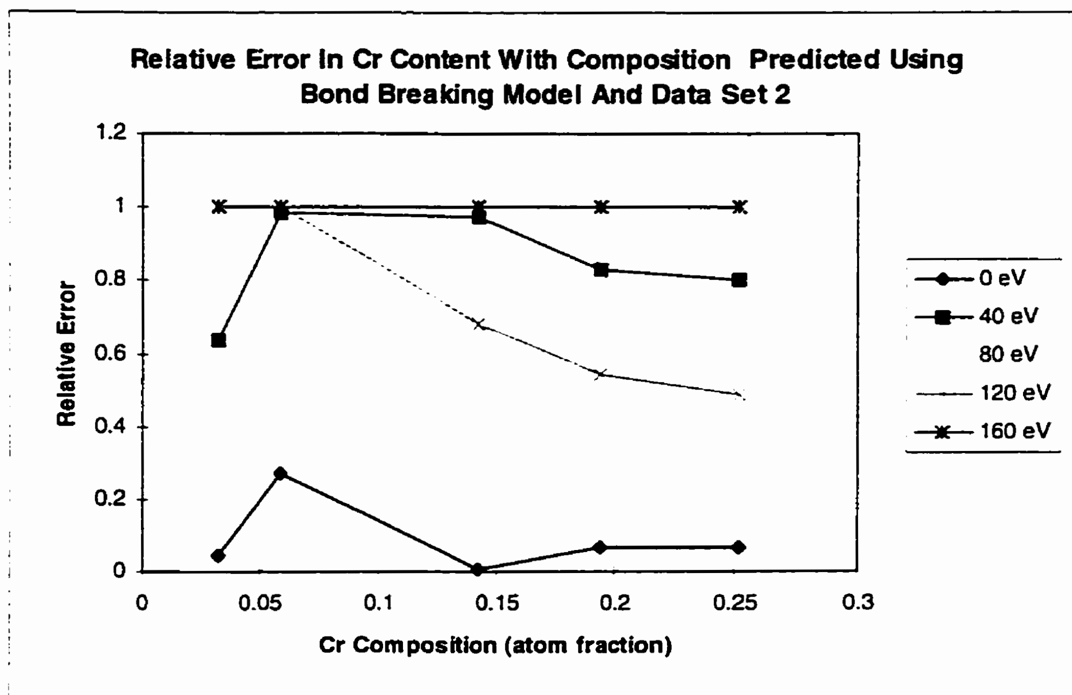

Figure C.64: Relative Error In Predicted Cr Content Versus Elemental Cr Composition

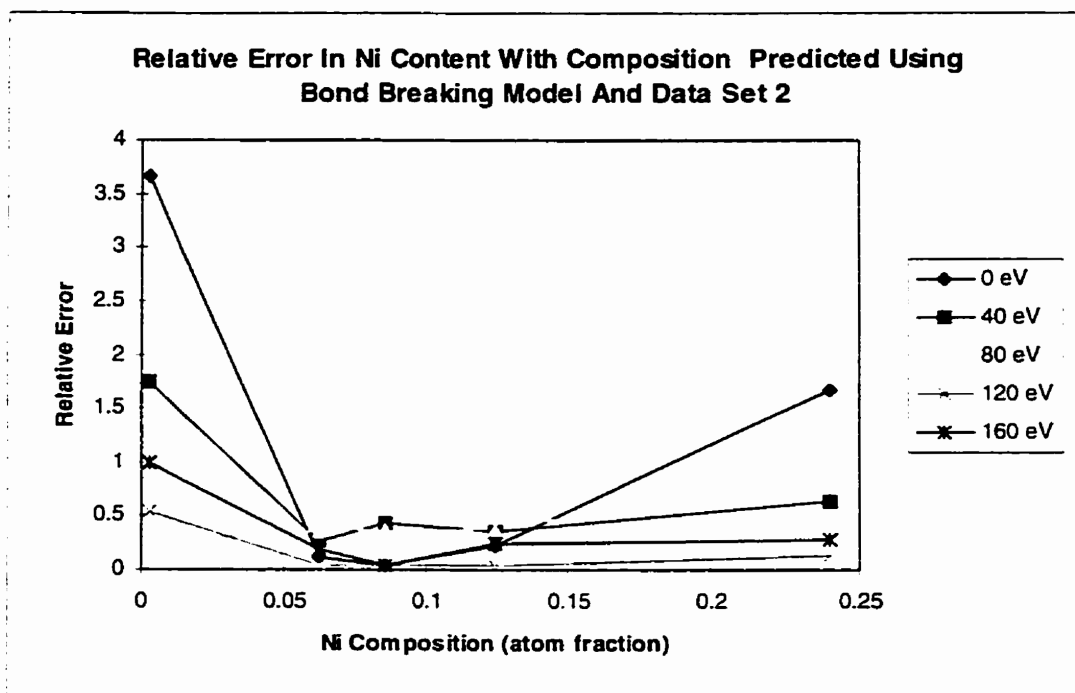

Figure C.65: Relative Error In Predicted Ni Content Versus Elemental Ni Composition

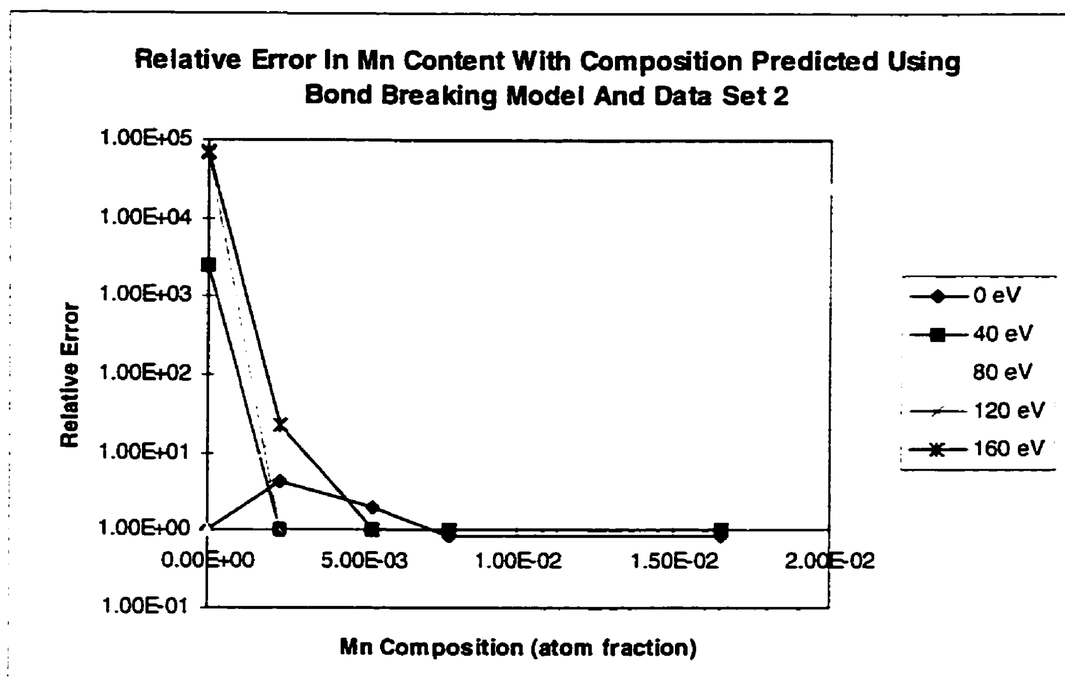

Figure C.66: Relative Error In Predicted Mn Content Versus Elemental Mn Composition

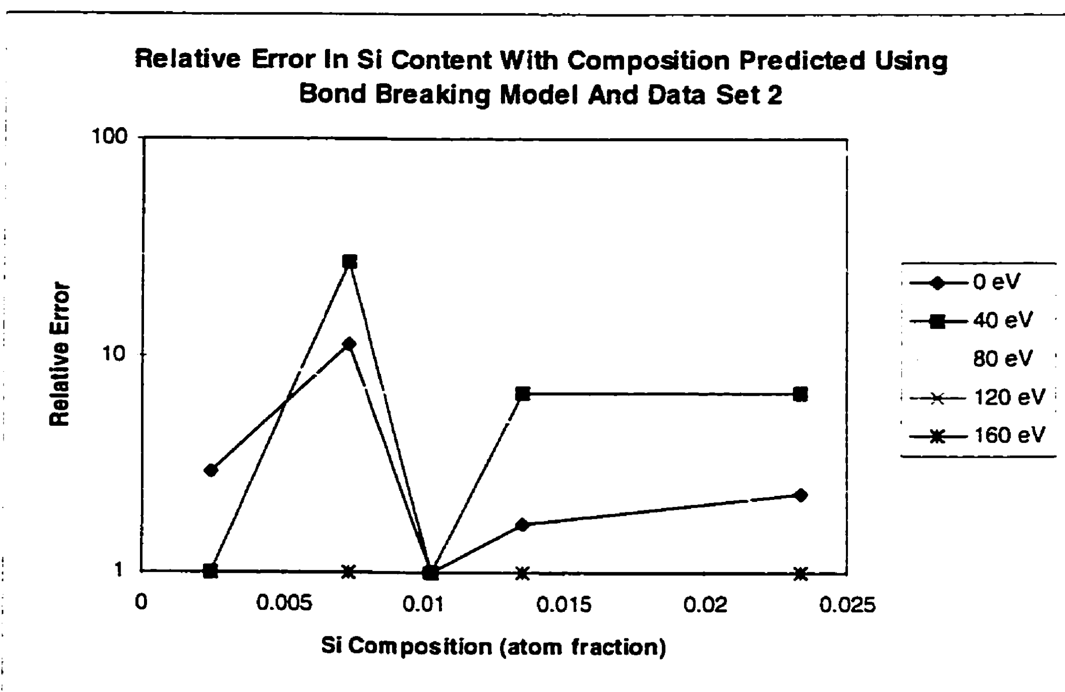

Figure C.67: Relative Error In Predicted Si Content Versus Elemental Si Composition

BIBLIOGRAPHY

1. Benninghoven, A., Rudenauer, F.G., Werner, H.W., Secondary Ion Mass Spectrometry, John Wiley & Sons Inc., New York, 1987

2. Thompson, J.J., Phil. Mag. **20**, 252 (1910)

3. Woodcock, K.S.,Phys. Rev. **38**, 1696 (1931)

4. Herzog, R.F.K, Viehbock, F.P., Phys. Rev. **76**, 855L (1949)

5. Liebl, H.J., Herzog, R.F.K., J. Appl. Phys., **34**, 2893 (1963)

6. Honig, R.E., Secondary Ion Mass Spectrometry (SIMS V), Benninghoven, A., Colton, R.J., Somins, D.S., and Werner, H.W., (Editors), Springer-Verlag, Berlin, p2 (1986)

7. Castaing, R., Slodzian, G., J. Microscopic., **1**, 395, (1962)

8. Liebl, H.J., J. Appl. Phys., **38**, 5277 (1967)

9. Krohn V.E., Ringo, G.R., Appl. Phys. Lett. **27**, 479 (1975)

10. Levvi - Setti, R., Wang, Y.L., Crow, G., J. Phys. 45, C9-147 (1984)

11. Honig, R.E., Advances in Mass Spectroscopy, Waldron, J.D. (Editor), Pergamon Press, London, p162 (1959)

12. Gnaser, H., Fleischhauer, J., Hofer, W.O., Appl. Phys. Lett. A, **37**, 211, (1985)

13. Blaise, G., Scanning Electron. Micros., 1985/I, P31 (1985)

14. Becker, C.H., Gillen, K.T., Anal. Chem., **56**, 1671 (1984)

15. Becker, C.H., Gillen, K.T., Appl. Phys. Letters, 45, 1063 (1984)

16. Wilson, R.G., Stevie, F.A., Magee, C.W., Secondary Ion Mass Spectrometry: A Practical Handbook For Depth Profiling And Bulk Impurity Analysis, John Wiley & Sons Inc., New York, 1989

17. Degreve, F., Lang, J.M., Secondary Ion Mass Spectrometry (SIMS V), Benninghoven, A., Colton, R.J., Somins, D.S., and Werner, H.W., (Editors),

Springer-Verlag, Berlin, p388, 1986

18. ASM Handbook, "Volume 10: Materials Characterization", ASM Press, 1986

19. Van der Voorst, W., Ph.D Thesis, University of Antwerp, 1984

20. Lodding, A., "Inorganic Mass Spectrometry", Chemical Analysis, Vol. 95. Adams, F., Gijbels, R., Van Grieken, R. (Editors) John Wiley & Sons

21. Liebl, H., Scanning, **3**, 79-89 (1980)

22. Von Ardenne, M., Tabellen Der Elektronenphysik, Ionenphysik Und Ubermikroskopie, Deutscher Verlag der Wissenschaften, 544, Berlin (1956)

23. Liebl, H., Secondary Ion Mass Spectrometry, (SIMS 2), Benninghoven, A., Evans, C.A., Powell, R.A., Shimizu, R.,and storms, H.A., (Editors), Springer-Verlag, Berlin, p176 (1979)

24. Williams, P., Lewis, R.K., Evans, C.A., and Hanley,P.R., Anal. Chem., **49**, 1399 (1977)

25. Liebl, H.J., Int. J. Mass Spectrom. Ion Phys., **22**, 237 (1976)

26. Storms, H.A., Brown, K.F., Stein, J.D., Analytical Chemistry, Vol. 49, No.13, Nov., 2023 (1977)

27. Liebl, H.J., "Ion Optics for Surface analysis - Low Energy Ion Beams"Inst. Phys. Conf. Ser. No. 38, 226 (1977)

28. Gourgout, J,M., Cameca News, No.2, Cameca S.A., Courbevoie/ France (1977)

29. Herzog, R.F.K, "Trace Analysis By Mass Spectrometry", Hearn, A.J. Editor, Acadamy Press New York & London, 57-99 (1972)

30. Werner, H.W., Proceedings Conference on Electron and Ion Spectroscopy of Solids, Ghent, Belgium, Fiermans, L., Vennik, J., Dekeyser, W. (Editors), Plenum Press, New York, 324, 1978

31. Mount, G., The Detection of Hydrogen In Steel By SIMS, Masters degree Thesis, University of Western Ontario (1993)

32. McHugh, J.A., NBS Spec. Publ. 427, Workshop on Secondary Ion Mass Spectrometry (SIMS) and Ion Microprobe Mass Analysis held at Gaithersburg, Maryland, September 16-18, 1974 (Issued October, 1975)

33. Winograd, N., Secondary Ion Mass Spectrometry, (SIMS 2), Benninghoven, A., Evans, C.A., Powell, R.A., Shimizu, R.,and storms, H.A., (Editors), Springer-Verlag, Berlin, p2 (1979)

34. Strydom, H.J., Botha, A.P., Strydom, C.A., Vermaak, J.S., Secondary Ion Mass Spectrometry, (SIMS 7), Benninghoven, A., McKeegan, K.D., Storms, H.A., Werner, H.W., (Editors), John Wiley & Sons Inc., New York, 1990

35. Smith, Steven P., Secondary Ion Mass Spectrometry, (SIMS 9), Benninghoven, A., Nilhei, Y., Shimuzu, R., Werner, H.W., (Editors), John Wiley & Sons Inc., New York, 1994

36. Hayashi, S., Yonezawa, H., Homma, Y., Tohjou, F., Yoshioka, Y., Okuno, K., et. Al., Secondary Ion Mass Spectrometry, (SIMS 10) Benninghoven, A., Hagenhoff, B., Werner,H.W., (Editors), John Wiley & Sons Inc., New York, 1997

37. Schneiders, A., Schroder-Oeynhausen, F., Burkhardt, B., Kotter, F., Mollers, R., Wiedmann, L., Benninghoven, A., Secondary Ion Mass Spectrometry, (SIMS 10) Benninghoven, A., Hagenhoff, B., Werner,H.W., (Editors), John Wiley & Sons Inc., New York, 1997

38. Montfort, S.A., Candy, J.M., Oakley A.E., Taylor, G.A., Poole, D.M., et. Al. Secondary Ion Mass Spectrometry, (SIMS 8), Benninghoven, A., Janssen, K.T.F., Tumpner, J., Werner,H.W., (Editors), John Wiley & Sons Inc., New York, 1992

39. Ausserer, W.A., Ling, Y.C., Chandra, S., Morrison, G.H., Secondary Ion Mass Spectrometry, (SIMS 7), Benninghoven, A., McKeegan, K.D., Storms, H.A., Werner, H.W., (Editors), John Wiley & Sons Inc., New York, 1990

40. Nakada, Y., Koutsuka, T., Mine, K., Suga, H., Secondary Ion Mass Spectrometry, (SIMS 9), Benninghoven, A., Nilhei, Y., Shimuzu, R., Werner, H.W., (Editors), John Wiley & Sons Inc., New York, 1994

41. Smith, S.P., Landstrass, M.I., Wilson, R.G., Secondary Ion Mass Spectrometry, (SIMS 8), Benninghoven, A., Janssen, K.T.F., Tumpner, J., Werner,H.W., (Editors), John Wiley & Sons Inc., New York, 1992

42. Gries, W.H., Secondary Ion Mass Spectrometry, (SIMS 9), Benninghoven, A., Nilhei, Y., Shimuzu, R., Werner, H.W., (Editors), John Wiley & Sons Inc., New York, 1994

43. Homma, Y., Secondary Ion Mass Spectrometry, (SIMS 9), Benninghoven, A., Nilhei, Y., Shimuzu, R., Werner, H.W., (Editors), John Wiley & Sons Inc., New York, 1994

44. Homma, Y., Secondary Ion Mass Spectrometry, (SIMS 7), Benninghoven, A., McKeegan, K.D., Storms, H.A., Werner, H.W., (Editors), John Wiley & Sons Inc., New York, 1990 p119

45. Simons, D.S., Chi, P.H., Kahora, P.M., Lux, G.E., Moore, J.L., Novak, S.W., Secondary Ion Mass Spectrometry, (SIMS 7), Benninghoven, A., McKeegan, K.D., Storms, H.A., Werner, H.W., (Editors), John Wiley & Sons Inc., New York, 1990

46. Homma, Y., Yoshioka, Y., Okuno, K., Hayashi, S., Okamoto, Y., Maruo, T., et. Al., Secondary Ion Mass Spectrometry, (SIMS 10) Benninghoven, A., Hagenhoff, B., Werner,H.W., (Editors), John Wiley & Sons Inc., New York, 1997

47. Yamamoto, A., Usui, Y., Matsumara, T., Shimomura, J., Secondary Ion Mass Spectrometry, (SIMS 9), Benninghoven, A., Nilhei, Y., Shimuzu, R., Werner, H.W., (Editors), John Wiley & Sons Inc., New York, 1994

48. Slodzian, G., Secondary Ion Mass Spectrometry, (SIMS 3), Benninghoven, A., Giber, J., Laslo, J., Riedel, M., Werner, H.W., (Editors), Springer-Verlag, Berlin, p115 (1982)

49. Piven, J.C., J. Microsc. Spectrosc. Electron., **7**, 277-290 (1982)

50. Piven, J.C., Roques-Carmes, C., Slodzian, G., Int. J. Mass Spectrom. Ion Phys., **26**, 293 (1979)

51. Piven, J.C., Roques-Carmes, C., J. Appl. Phys., **8**, 51, (1980)

52. Roques-Carmes, C., Piven, J.C., Secondary Ion Mass Spectrometry, (SIMS 2), Benninghoven, A., Evans, C.A., Powell,R.A., Shimizu, R.,and storms, H.A., (Editors), Springer-Verlag, Berlin, p161 (1979)

53. Slodzian, G., Lorin, J.C., Havette, A., J. de Phys. Lett. **44**, 555, (1981)

54. Slodzian, G., Phys. Rev. B., Condensed Matter, **49**, Iss. 14, pp9344-9356, 1994

55. Lasdon, L.S., Waren, A.D., Jain, A., Ratner, M., ACM Trans on Mathematical Software, **4** No. 1, 34-50 (1975)

56. Press, W.H., Flannery, B.P., Teukolsky, S.A., Vetterling, W.T., "Numerical Rescipes In C", Cambridge University Press, U.S.A., 324-328 (1988)

57. Werner, H.W., Surf. Interface Anal., **2**, 56, (1980)

58. van der Heide, P.A.W., Zhang, Min, Mount, G.R., McIntyre N.S., Surface And Interface Analysis, **21**, 747-757, (1994)

59. van der Heide, P.A.W., Zhang, Min, Mount, G.R., McIntyre N.S., Sodervall, U., Odelius, H., Lodding, A., Secondary Ion Mass Spectrometry, (SIMS 10), Benninghoven, A., Hagenhoff, B., Werner,H.W., (Editors), John Wiley & Sons Inc., New York, 1997

60. Lodding, A., van der Heide, P.A.W., Sodervall, U., Brown, J.D., Secondary Ion Mass Spectrometry, (SIMS 9), Benninghoven, A., Nilhei, Y., Shimuzu, R., Werner, H.W., (Editors), John Wiley & Sons Inc., New York, 1994

61. van der Heide, P.A.W., Secondary Ion Mass Spectrometry, (SIMS 10) Benninghoven, A., Hagenhoff, B., Werner,H.W., (Editors), John Wiley & Sons Inc., New York, 1997

62. van der Heide, P.A.W., Ramamuthy, S., McIntyre N.S., Surface and Interface Analysis, **23**, 163-170, (1995)

63. Piven, J.C., Pellerin, F., Roques-Carmes, C., Le Gressus, C., 4th International Conference on Solid Surfaces and 3rd European Conference on Surface Science, Cannes, p.283 (1980)

64. Certificate of Analysis: Standard Reference Materials D845-D850 Spectrographic Stainless Steel Standards, National Bureau of Standards, January 19, 1966

65. CRC Handbook of Chemistry and Physics, 74th Edition, Lide, D.R., Frederikse, H.P.R., (Editors), CRC Press, Boca Raton (1993-1994)

66. Newbury, D.E., Heinrich, K.F.J., Myklebust, R.L., "Errors Observed In Quantitative Ion Probe Microanalysis", Surface Analysis Techniques For Metallurgucal Applications, ASTM STP 569, American Society For Testing and Material, 1976, p. 101-113

IMAGE EVALUATION TEST TARGET (QA-3)

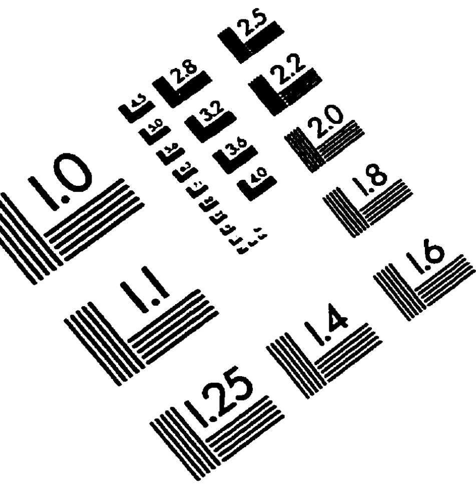

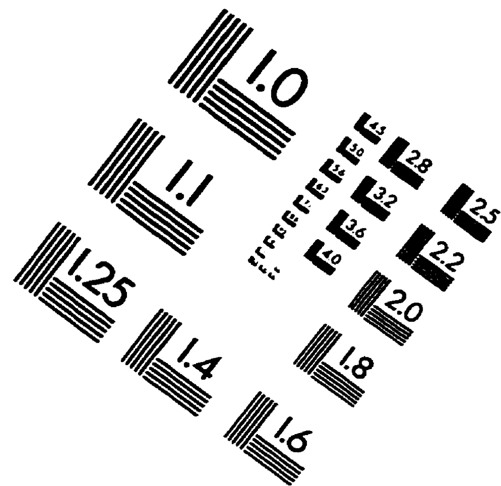

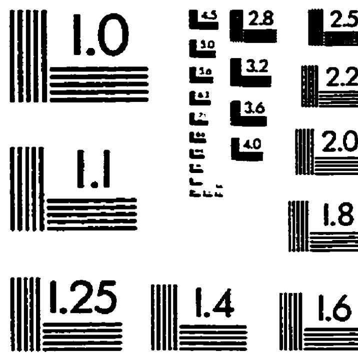

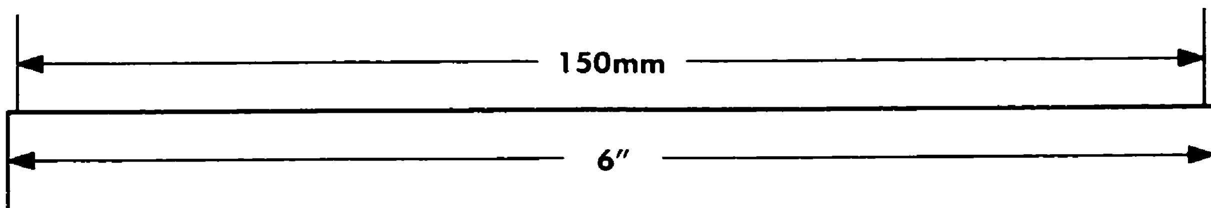

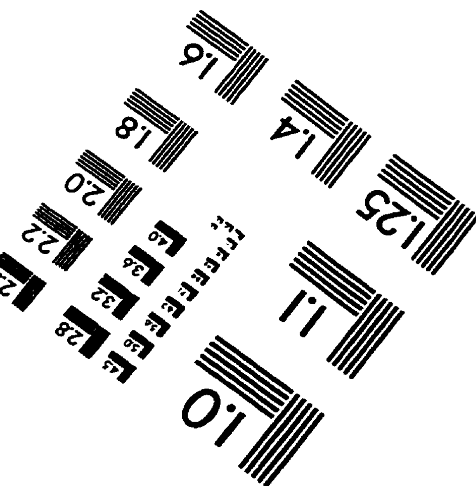

APPLIED IMAGE, Inc
1653 East Main Street
Rochester, NY 14609 USA
Phone: 716/482-0300
Fax: 716/288-5989

© 1993, Applied Image, Inc., All Rights Reserved